MEASUREMENT OF CHARM AND BEAUTY CROSS SECTIONS IN PHOTOPRODUCTION USING EVENTS WITH MUONS AND DIJETS AT HERA

Dissertation
zur Erlangung des Doktorgrades
des Department Physik
der Universität Hamburg

Vorgelegt von
Mira Krämer
aus Engelskirchen

Hamburg 2009

Gutachter der Dissertation:	Prof. Dr. Robert Klanner PD Dr. Andreas Meyer
Gutachter der Disputation:	Prof. Dr. Robert Klanner PD Dr. Olaf Behnke
Datum der Disputation:	23. Juli 2009
Vorsitzender des Prüfungsausschusses:	Prof. Dr. Dieter Horns
Vorsitzender des Promotionsausschusses:	Prof. Dr. Robert Klanner
Dekan der MIN Fakultät:	Prof. Dr. Heinrich Graener
Leiter des Department Physik:	Prof. Dr. Joachim Bartels

Abstract

A measurement of open charm and beauty cross sections in photoproduction using dijet events containing a muon at the *ep* collider HERA is presented. The analysed data are collected with the H1 detector in the years 2006 and 2007, corresponding to an integrated luminosity of 179 pb^{-1}. Events are selected, which contain at least two jets with transverse momenta of $p_t^{jet1(2)} > 7(6)$ GeV in the pseudorapidity region $-2.5 < \eta^{jet1(2)} < 2.5$. A muon with a minimal transverse momentum of $p_t^{\mu} > 2.5$ GeV in the pseudorapidity range $-1.3 < \eta^{\mu} < 1.5$ is required. The muon is associated to one of the two selected jets. The method used to determine the fraction of events containing charm or beauty is based on the transverse momentum of the muon relative to its associated jet and the impact parameter of the muon track with respect to the primary vertex. Differential cross sections for charm and beauty are measured as a function of the transverse momentum of the muon, the pseudorapidity of the muon, the transverse momentum of the highest p_t jet, the azimuthal angular separation of the two selected jets and the observable x_{γ}^{obs}. Double differential cross sections for charm and beauty are measured in the region of direct and resolved processes.

Kurzfassung

Ziel dieser Analyse ist die Messung von Charm und Beauty Wirkungsquerschnitten in *ep* Kollisionen bei HERA. Die Messung erfolgt im kinematischen Bereich der Photoproduktion mit Hilfe von Zweijet-Ereignissen, die ein Myon beinhalten. Die analysierten Daten wurden mit dem H1 Detektor in den Jahren 2006 und 2007 aufgezeichnet. Die zur Verfügung stehende integrierte Luminosität beträgt 179 pb^{-1}. Es werden Ereignisse selektiert, die mindestens zwei Jets mit einem minimalen Transversalimpuls von $p_t^{jet1(2)} > 7(6)$ GeV im Rapiditätsbereich $-2.5 < \eta^{jet1(2)} < 2.5$ aufweisen. Ein Myon mit einem Transversalimpuls von mindestens $p_t^{\mu} > 2.5$ GeV im Rapiditätsbereich $-1.3 < \eta^{\mu} < 1.5$ wird zusätzlich gefordert. Dieses Myon wird einem der beiden Jets mit den höchsten Transversalimpulsen zugeordnet. Die hier verwendete Methode zur Bestimmung des Anteils von Ereignissen mit Charm und Beauty Kandidaten beruht zum einen auf dem relativen Transversalimpuls des Myons zu dem ihm zugeordneten Jet und zum anderen auf dem Stoßparameter der Myonspur in Bezug auf den Primärvertex. Differentielle Wirkungsquerschnitte von Charm und Beauty werden als Funktion des Transversalimpulses des Myons, seiner Pseudorapidität, dem Transversalimpuls des führenden Jets, dem azimutalen Winkel zwischen den beiden selektierten Jets, sowie der Observablen x_{γ}^{obs} bestimmt. Zusätzlich werden doppelt differentielle Wirkungsquerschnitte für Charm und Beauty in direkten und aufgelösten Prozessen gemessen.

Contents

Chapter 1

Introduction

The idea that all matter is composed of fundamental building blocks was first conceived of by Greek philosophers such as Democritus and Leucippus, more than two thousand years ago. This idea remained untested until the 20th century. In the beginning of the 1900s, experiments to investigate subatomic structures were performed and led to the development of physical models such as the Rutherford model. In the 1950s, the invention of bubble chambers and spark chambers revolutionised elementary particle physics. A large number of hadrons and their resonances were discovered. Since physicists prefer the idea of fundamental particles, they began immediately to classify the discovered 'particle zoo'. In 1963, the 'quark model' was introduced independently by Murray Gell-Mann and George Zweig. Here, the hadrons can be classified as combinations of quark-antiquark pairs, which are called mesons, or as combinations of three quarks, the baryons. At this time, only three quarks were known, namely the *up*, *down* and *strange* quarks. In the years to follow, three further quark flavours - *beauty*, *charm* and *top* - were introduced to solve inconsistencies of the developing theory. The experimental evidences of the new quarks were found several years later. The charm quark was discovered in 1974 by two groups independently: by the group around Samuel C. C. Ting in Brookhaven and Burton Richter in Stanford. Three years later, in 1977, the experiment E288 at Fermilab discovered the beauty quark. Finally, the top quark was discovered in 1995 by the experiments CDF and D0 at Fermilab. The force between the quarks can be described by strong interactions. The most accepted theory of strong interactions, namely *Quantum Chromodynamics* (QCD), is an important part of the Standard Model of particle physics. The strong interaction is one of the four fundamental forces and describes the interaction between the quarks via the exchange of gluons, the gauge bosons of the strong interaction. The quark and gluons carry colour and interact with each other. The gluons can also interact with other gluons, which can be explained theoretically by the non-Abelian colour symmetry group, which is the basis of QCD. This leads to a running strong coupling constant α_s, which decreases with the energy scale and increases with the distance, causing the principle of colour confinement. Due to confinement, quarks cannot be observed directly, but only through hadronisation. Their experimental observation is therefore based on the investigation of jets, which consist of colour-neutral hadrons.

The electron proton collisions at HERA provide an opportunity to study the structure of the proton as well as the properties of strong interactions. Due to the running of α_s, the energy scale at which α_s is evaluated plays a crucial role in QCD calculations. At HERA, several hard scales are relevant, for example the virtuality of the photon Q^2, transverse momentum p_t and the mass m_q of the quarks. This multi-scale problem complicates the situation, since the perturbative expansion cannot be optimized for all scales at once. The simultaneous occurrence of scales in the same heavy quark production process allows important insights into the nature of QCD and especially further investigations of the calculation schemes. The results obtained at HERA are crucial for the development of QCD theories as well as for the upcoming LHC project, where proton proton collisions are studied. At LHC, the main background to the signals from expected new physics will be heavy flavour physics including jets. To obtain clear signals, the background needs to be understood very well.

Recent analyses at HERA and other colliders show that charm and beauty production is in general reasonably well understood. QCD NLO calculations are able to predict the measurement in most of the distributions, but in some regions, e.g. for resolved processes, further investigations are needed to improve the theory as well as to reduce the experimental uncertainties.

In this analysis, a measurement of charm and beauty dijet muon cross sections in photoproduction using HERA II data is performed. The aim of this analysis is to contribute to the present understanding of heavy quark production by investigating the exclusive final state. The increase in the amount of data collected by a factor of 3.5 compared to the HERA I analyses, provides not only significant improvements of the statistical precision, but also a better understanding of the H1 detector. The beauty cross sections are measured in an extended phase space compared to previous results. For the first time, charm dijet muon cross sections are determined simultaneously. In addition, the charm and beauty cross sections are measured in the regions of direct and resolved processes separately. Events containing at least two jets are selected, with the further requirement of a muon associated to one of these jets. The muon is selected to analyse semi-leptonic decays, while the two jets represent a heavy quark antiquark pair. The experimental method to separate the contributions from the different quark flavours is based on a combination of two variables, which are sensitive to the quark flavours. These two variables are p_t^{rel}, which is the transverse momentum of the selected muon relative to the associated jet axis, and the impact parameter δ, which reflects the distance between the selected muon track and the primary vertex.

This thesis is organised as follows. Chapter 2 presents the theoretical framework of heavy quark production at HERA. General aspects of QCD as well as special properties of the perturbative QCD predictions used in this analysis are discussed. At the end of this chapter, recent heavy flavour measurements performed at HERA and other colliders are reviewed to motivate the presented analysis. In chapter 3, the experimental apparatus is described briefly. The main focus is on the detector components relevant for this analysis. Chapter 4 provides a detailed overview of the event reconstruction procedures used for the tracks and jets, which are very important for this analysis. In this chapter, investigations concerning the resolutions of the track measurement are included. In addition, the tuning of the vertex detector simulation is presented. This detector component plays an important role in this analysis, since it allows to measure primary and secondary vertices with a high precision. It is thus possible to measure the impact parameter distribution of muons, which is sensitive to the different quark flavours. Chapter 5 contains the selection details of the analysed event sample and control distributions. In chapter 6, the methods are presented, which separate the quark flavours. The consistency and details of the methods are investigated. The cross section measurements and their systematic uncertainties are presented in chapter 7. Finally, the obtained results are summarized and compared to previous measurements at HERA.

Chapter 2

Heavy Quark Photoproduction

2.1 Quantum Chromodynamics

Quantum Chromodynamics (QCD) describes the strong interaction between colour charged particles in terms of a *Quantum Field Theory* (QFT). The strong interaction is similar in its concept to *Quantum Electrodynamics* (QED) which describes the interaction between charged particles with photons as gauge bosons. One of the main difference is the gauge group, since QED is based on the Abelian gauge group $U(1)$ and QCD on the non-Abelian $SU(3)$ colour symmetry group. This leads to additional terms in the Lagrangian of the QCD which cause an interaction between the QCD gauge bosons, the gluons [1]. For the same reason the gluons carry colour charge. Therefore, in most of the cases a gluon exchange leads to colour changes of the participating quarks. The self-interaction of the gluons has considerable consequences since it causes a contrary behaviour of the strong coupling constant α_s in comparison to the electromagnetic fine structure constant. The strong coupling constant is very large at low momentum transfers and decreases towards higher energies. This behaviour leads to *asymptotic freedom* at high energies and the so-called *confinement* at low energies. In the case of asymptotic freedom the partons behave like free particles at high energies. As a consequence of confinement, the large coupling constant causes the partons to be bound into colour neutral states, the hadrons. The running coupling constant of the strong interaction is depicted in figure 2.1.

Perturbative QCD (pQCD) cross sections for particle scattering are calculated as a power series in α_s. The large value of α_s is causing problems in the perturbative series, since quark and gluon loop diagrams can give large contributions beyond *Leading Order* (LO). An integration of all particle momenta p in the loop has to be performed, to determine these contributions. As always in QFT, some of the loop diagrams diverge. The logarithmically divergent integrals have to be renormalized, which means that they have to be removed by a finite number of counterterms. In the renormalization procedure an arbitrary dimensionless renormalization scale μ_R is introduced. In practice this scale is chosen close to the physical scales which characterise the studied process. In theory, it is required that every physical observable has to be independent of the arbitrary choice of μ_R. At the scale $\mu_R > \Lambda_{QCD}$ in one loop approximation the strong coupling constant can be written as

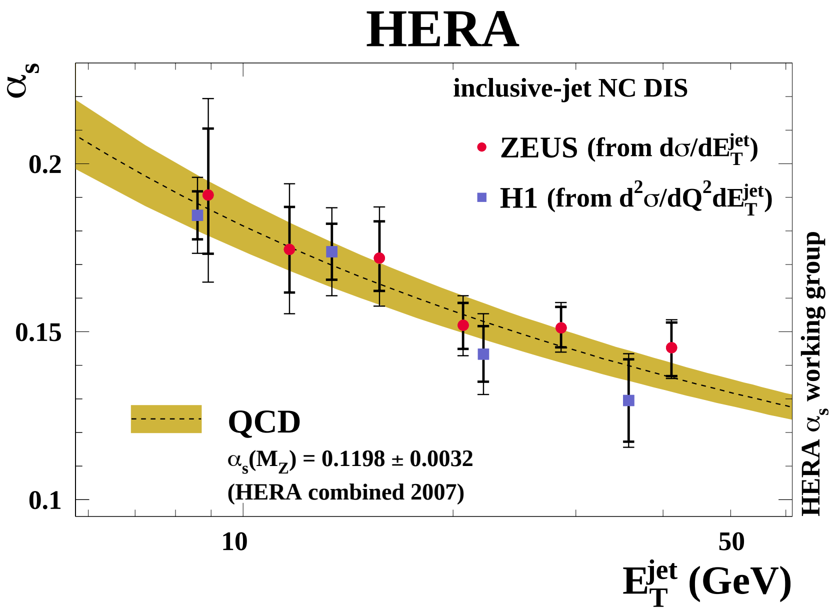

Figure 2.1: The coupling constant α_s of the strong interaction is shown as a function of the transverse jet energy E_T^{jet}. The HERA data (points) are in good agreement with the QCD calculation [2].

$$\alpha_s(\mu_R^2) = \frac{1}{b\ln(\frac{\mu_R^2}{\Lambda_{QCD}^2})}, \quad \text{with} \quad b = \frac{33 - 2n_f}{12\pi}. \tag{2.1}$$

Here n_f stands for the number of active quark flavours with a mass below μ_R. Λ_{QCD} denotes the scale at which α_s gets very large leading to divergences of the perturbative series in α_s. In this case pQCD is no longer applicable. Experimentally Λ_{QCD} is of the order of 200 MeV. Heavy quark production at HERA provides an excellent testing ground for pQCD. The high masses of the heavy quarks in combination with their transverse momenta p_t and/or the virtuality of the exchanged boson Q^2 define a hard scale, which complicates the situation. The perturbative expansion can not be optimized for all scales at once. This so-called multi-scale problem can be treated in different ways according to the relative magnitudes of the present scales.

2.2 Description of *ep* Scattering

The *ep* scattering process $ep \rightarrow lX$ can be described by a single virtual gauge boson exchange. If the boson is either a photon γ or a Z^0, the scattered electron is observed in the final state. This is called a *neutral current* (NC) event with $ep \rightarrow eX$. If the exchanged particle is a $W^{\pm}$ boson, this characterizes a *charged current* (CC) event, $ep \rightarrow \nu_e X$. In figure 2.2 (a) a Feynman diagram for *ep* scattering is depicted, including the kinematic variables. An incoming electron with 4-momentum k is scattered off a proton with 4-momentum P. In the final state a scattered lepton with 4-momentum k' and a hadronic system X with 4-momentum P' is found. The hadronic system is formed by the proton remnant and the scattered parton. The latter is a pointlike constituent of the proton and can be described by the *Quark Parton Model* (QPM) [3], [4].

The squared centre-of-mass energy of the reaction is

$$s = (P + k)^2. \tag{2.2}$$

For unpolarised beams at a given center-of-mass energy the kinematics of inclusive lepton proton scattering can be described by two Lorentz invariant quantities. Usually two of the three variables Q^2, x_{Bj} and y are chosen, which are described in the following. The negative squared 4-momentum transfer at the electron vertex is given by

$$Q^2 = -q^2 = -(k - k')^2. \tag{2.3}$$

It corresponds to the virtuality of the exchanged boson. If the photon is quasi-real ($Q^2 \approx 0$ GeV^2), the production regime is called *photoproduction* (γp). In the case of large Q^2 the regime is called *Deep Inelastic Scattering* (DIS). In this thesis the analysed regime is photoproduction.

The inelasticity y is calculated using the formula:

$$y = \frac{Pq}{Pk} \quad \text{with} \quad 0 \leq y \leq 1. \tag{2.4}$$

The observable y denotes the fraction of the incoming electron energy in the proton rest frame which is carried away by the photon.

The Bjorken scaling variable x_{Bj} is defined as

$$x_{Bj} = \frac{Q^2}{2Pq}, \quad \text{with} \quad 0 \leq x_{Bj} \leq 1. \tag{2.5}$$

In the parton model x_{Bj} stands for the momentum fraction of the proton which is carried by the struck quark (see figure 2.2 (b)).

The squared photon-proton centre-of-mass energy is determined via

$$W^2 = (P + q)^2. \tag{2.6}$$

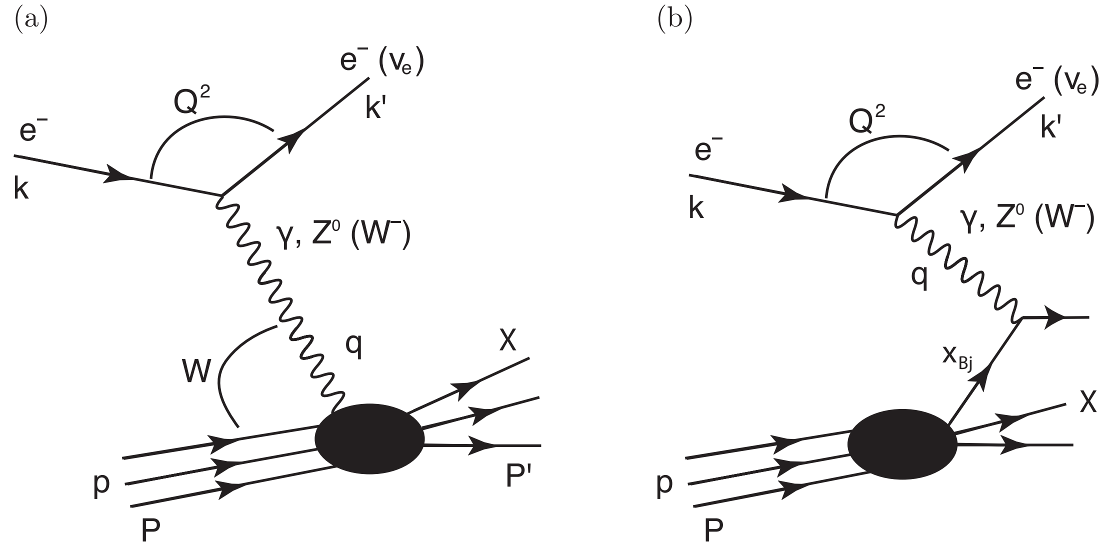

Figure 2.2: Diagram for *ep* scattering including the kinematic variables (a). In (b) *ep* scattering in the parton picture is depicted.

The quantity W^2 corresponds to s in the case of hadron-hadron scattering, if the photon is considered as the hadronic projectile. With the assumption of zero particle masses the product of the centre-of-mass-energy s, inelasticity y and the Bjorken scaling variable x_{Bj} gives the squared 4-momentum transfer Q^2:

$$Q^2 = x_{Bj} ys. \tag{2.7}$$

With the same assumption W^2 is calculated using

$$W^2 = ys - Q^2. \tag{2.8}$$

2.3 Proton Structure

The structure of the proton is parametrised in terms of the structure functions. In the following, the quark parton model is described briefly and the factorization theorem is introduced.

2.3.1 Quark Parton Model

In the picture of the *Quark Parton Model* (QPM) [3], [4] nucleons consist of pointlike, non interacting constituents. These constituents were identified with quarks by J. Bjorken and E. Paschos [5]. A virtual photon is exchanged between the incoming electron and one of these quarks. To derive an approximation to the cross section calculation for *ep* scattering the so-called *infinite momentum frame* is used. Here the proton has an almost lightlike momentum along the collision axis and all transverse momenta can be neglected as well as the proton mass itself. This approximation is valid at high energies as realised at HERA. The momentum fraction of the proton carried by the interacting quark is called the 'longitudinal fraction' x and can be determined by dint of measured electron quantities. In leading order QCD, gluon emission or exchanges during the collision process can be ignored. The cross section for ep scattering can then be determined using the cross section for quasi-elastic electron-quark scattering at a given longitudinal fraction and the probability $f_i(x)dx$ to find a quark at that longitudinal fraction. The probability functions can not be calculated using QCD perturbation theory and have therefore to be determined experimentally. The functions $f_i(x)dx$ are called *Parton Distribution Functions* (PDF). The content of the proton is parametrised by the proton structure functions F_1, F_2 and F_3 which can be extracted from NC DIS cross section measurements. F_3 takes the parity violation of the weak force into account. If Z exchange is negligible, $F_3 = 0$ holds. In the following, this is assumed and therefore only γ exchange is considered. Taking the spin of the particles into account, the double differential cross section as a function of x and Q^2 can be written as

$$\frac{d^2\sigma}{dQ^2dx} = \frac{4\pi\alpha^2}{xQ^4}(xy^2F_1(x,Q^2) + (1-y)F_2(x,Q^2)). \tag{2.9}$$

Both structure functions $F_1(x,Q^2)$ and $F_2(x,Q^2)$ parametrise the proton structure and details of the interaction at the photon-proton vertex. In the QPM for free Dirac quarks, which is also called DIS scheme, the relation between them is described by the Callan-Gross relation [6]:

$$F_2(x,Q^2) = 2xF_1(x,Q^2), \tag{2.10}$$

which is often used to eliminate $F_1(x,Q^2)$. This relation is valid if the interacting parton coming from the proton is a fermion. In the case of bosons $F_1(x,Q^2)$ would be equal to zero since it corresponds to the magnetic form factor.

The proton structure function F_2 can be written in the DIS scheme as

$$F_2(x,Q^2) = x\sum_i e_i^2 f_i(x). \tag{2.11}$$

Here e_i denotes the charge of quark i. In the Bjorken limit, which is defined as $Q^2, p\cdot q \to \infty$ with fixed x, the structure function obeys an approximate *scaling*. Which means, that it depends only on the variable x: $F_2(x,Q^2) \to F_2(x)$. This independence was predicted by J. Bjorken [3]. In this picture, the increase of Q^2 does not disclose any new detail of the quasi-free partons in the proton if once the partons are resolved. Experimental results showed a scaling behaviour at $x \approx 0.1$, which confirms the QPM in good approximation [7]. This scaling behaviour, which is the independence of F_2 on Q^2, is interpreted mainly as a scattering off the valence quarks. This is for example depicted in figure 2.3, where experimental results of the collider experiments H1 and ZEUS at HERA and fixed target experiments of the years 1994-2000 are shown. But already in the early 1970s experimental comparisons of DIS data with the QPM revealed, that only 50% of the proton's momentum is carried by quarks [8], [9]. As illustrated in figure 2.3, for low x a sharp increase of F_2 with increasing Q^2 is found. These observations lead to the conclusion that the QPM does not describe the full proton content. The observable Q^2 is related to the Compton wavelength, which determines the resolution. With increasing Q^2, the Compton wavelength decreases and finer structures of the proton can be resolved. The dependence of F_2 on Q^2 at low x, also denoted as *scaling violations*, is therefore interpreted as an increase of sea quarks produced by gluons, which can be seen due to the better resolution. This leads to a rising ep cross section and at the same time an increasing F_2 towards higher values of Q^2. To take the gluon contributions into account and to describe the proton content successfully, an extension of the quark parton model was necessary. In terms of pQCD the proton structure function F_2 in equation 2.11 can be seen as the zeroth order term in the expansion of F_2 as a power series in α_s. For taking contributions of the order $O(\alpha_s)$ into account, the photon-parton subprocess diagrams shown in figure 2.4 (b) using the massless approach (cf. section 2.6) have to be calculated. The first diagram in figure 2.4 (b) has a collinear divergence since the gluon can be emitted parallel to the quark. To solve this problem these singularities are absorbed by the quark distribution, which becomes scale dependent. In this procedure a factorization scale μ_F is introduced, which defines the scale where the singularities contribute to the quark density.

2.3.2 Factorization Theorem and Structure Functions

The factorization theorem [10] can be considered as a field theoretical realization of the above described parton model. It separates hard and soft processes, the first ones correspond to the short distance part while the latter ones stand for the long distance part. Hard processes are computable in pQCD and describe the interaction of high energy partons. Soft processes can not be determined with perturbative calculations and describe low energy interactions. In this framework the proton structure functions can be described as follows. Let $F_a(x, Q^2)$ be the structure functions of all DIS processes $l + p \rightarrow l' + X$. The general factorization formula according to [11] holds for all orders in perturbation theory. It is proven only for DIS but turned out to be usable for the photoproduction regime as well. It can be written as

$$F_a(x, Q^2) = \sum_{i=q,\bar{q},g} \int_0^1 \frac{dy}{y} f_i(y, Q^2) C_{a,i}\Big(\frac{x}{y}, \alpha_s(Q^2)\Big) + O\Big(\frac{\Lambda^2_{QCD}}{Q^2}\Big). \tag{2.12}$$

The observable $F_a(x, Q^2)$ is factorized into two parts: the universal parton densities, denoted as f_i and the coefficient functions $C_{a,i}$. The first part corresponds to the soft processes where long distance collinear singularities are absorbed. Soft processes are considered to be processes with lower momentum transfers than hard processes. The parton densities cannot be calculated in pQCD. The DGLAP evolution equations (cf. section 2.4) make it possible to determine the dependence on Q^2. The second part of equation 2.12 stands for the hard processes. The coefficient functions describe the short distance subprocess and are computable in

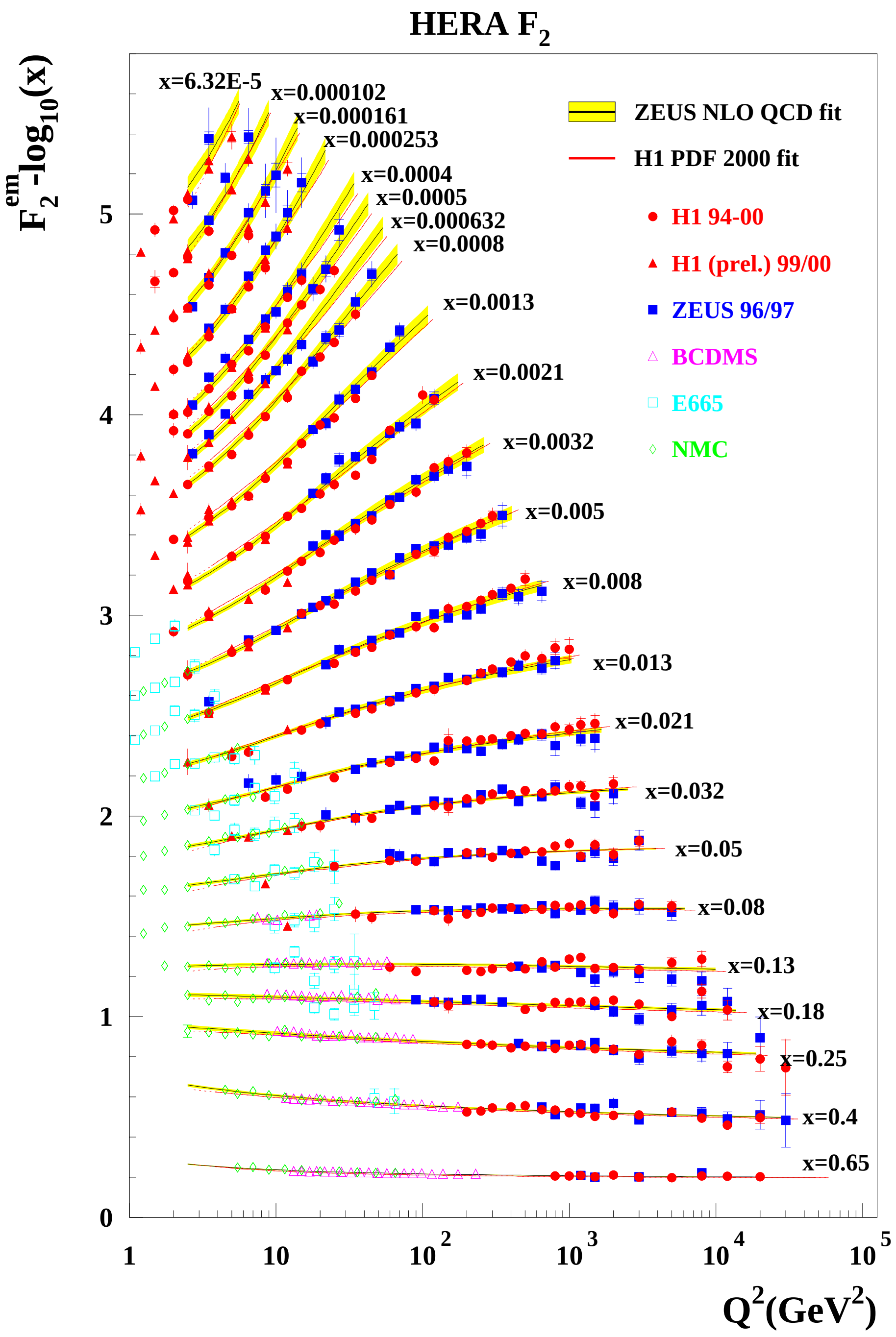

Figure 2.3: Proton structure function F_2 as a function of Q^2 for various values of x. The data is measured by H1, ZEUS and different fixed target experiments using fits based on DGLAP. For a better visibility an offset of $-\log x$ is applied to each data point.

pQCD as a power series in α_s. They are unique to the particular structure function F_a. The added term at the end of equation 2.12 denotes non-perturbative contributions. It contains hadronization effects, multiparton interactions etc. These effects are negligible for sufficiently high Q^2. Since this analysis is performed in photoproduction ($Q^2 \approx 0$ GeV^2), these effects become important. The structure function $F_2(x, Q^2)$ is a special case of equation 2.12. For leading order in α_s and the convenient choice of $\mu_F = Q$ it has the following form:

$$F_2(x, Q^2) = x \sum_{i=q,\bar{q}} e_q^2 \int_0^1 \frac{dy}{y} \Big[f_q(y, Q^2) \Big(\delta\Big(1 - \frac{x}{y}\Big) + \frac{\alpha_s}{2\pi} C_{2,q}\Big(\frac{x}{y}\Big)\Big) + f_g(y, Q^2) \frac{\alpha_s}{2\pi} C_{2,g}\Big(\frac{x}{y}\Big)\Big]. \tag{2.13}$$

The $C_{2,i}$ are the coefficient functions for the observable F_2. This prescription is not unique, since any finite term can be added. Therefore a scheme must be chosen. A very common one is the *modified minimal subtraction* scheme ($\overline{MS}$ factorization scheme), which sets also the renormalization scheme. In the $\overline{MS}$ scheme not all gluon contributions are absorbed in the quark distributions.

Experimentally the parton density functions are determined by a fit to adjust the non-perturbative distributions to the experimental $F_2(x, Q^2)$ data from HERA and fixed targed experiments. The gluon and valence quark distributions of the proton are depicted in figure 2.4 [12]. At low x, the gluon density exceeds the quark distribution by far, which explains the scaling violations in that region. These parton densities are determined from a combined fit of the H1 and ZEUS data from the HERA I period.

The proton distributions functions obtained by the `CTEQ` [13] group are used for this analysis. The `CTEQ6L` set of PDFs is determined in leading order. This set is appropriate for Monte Carlo event generators and achieved using a QCD coupling of $\alpha_s(\mu_R) = 0.118$.

The structure function of the photon F_2^γ has a different behaviour than the structure function of a hadron, for example the proton. The point-like contributions of the resolved processes lead to a rising of F_2^γ towards large values of x. Here x is again the momentum fraction of the photon carried by the interacting parton. The proton structure function behaves contrary and decreases towards large x, as discussed before. The first calculation of the photon structure function in LO QCD was performed by Witten [14]. He neglected the incalculable hadronic-like component which leads to unreliable results at small values of x.

Photon quark density functions have been determined mainly in e^+e^- scattering. The gluon content in the photon can be calculated from F_2^γ measurements with the help of evolution equations. The gluon distribution function increases towards small values of x. This behaviour is in contrast to the quark distribution function of the photon, since it shows a decrease towards small x. The presence of gluons at low x indicates scaling violations which has been shown in F_2^γ measurements summarized for example in [15]. The scaling violation behaviour is contrary to the one of the proton, since the photon consists of less gluons and the resolved photon is dominated by quarks.

There exist several parton distribution functions for the photon. For this analysis the ones calculated by Schuler and Sjöstrand `SaS` [16] are taken. The different photon PDFs differ in the starting scale Q_0 and in the input distributions at this scale. There are experimental

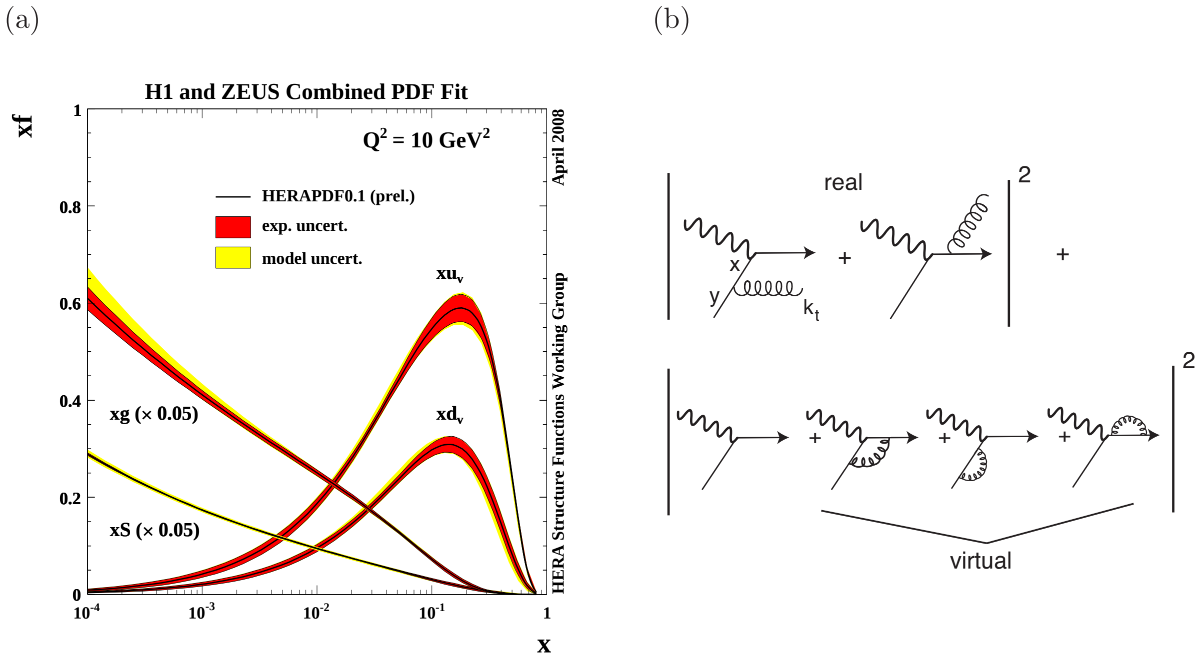

Figure 2.4: Gluon and valence quark densities of the proton in figure (a). The distributions are determined from fits to combined H1 and ZEUS data from the HERA I period [12]. In (b) the leading order $O(\alpha_s)$ diagrams are shown, which contribute to the proton structure function.

evidences of the universality of the parton density functions, which are for example presented in [15]. The data used for the fitting of parameters is taken from e^+e^- reactions.

The `SaS` parton distributions [16] are determined using a hadron-like starting contribution which is based on VMD arguments. Two sets of distributions exist: `SaS1` and `SaS2`. The first one assumes a starting scale of $Q_0 = 0.6$ GeV while the latter one takes $Q_0 = 2$ GeV. In this analysis the `SaS2D` set in the DIS scheme is used.

In this thesis photoproduction processes are studied. Based on the factorization theorem, the photoproduction cross section can be decomposed as follows in the presence of a hard scale :

$$\sigma_{\gamma p} \sim f_{i/p}(x_p, \mu_F^2) \otimes \hat{\sigma}_{ij}(\hat{s}, \alpha_s(\mu_R^2), \mu_R, \mu_F) \otimes f_{j/e}(x_e, \mu_F^2) \otimes D(z). \tag{2.14}$$

Here $f_{i/p}$ and $f_{j/e}$ denote the parton distribution functions of the proton and the electron, respectively. They depend on x_p and x_e, which represent the momentum fraction of the parton that participates in the hard interaction. The variable $\hat{\sigma}_{ij}$ stands for the cross section of the hard subprocess. The function $D(z)$ describes the fragmentation and is explained in section 2.7. It depends on z which represents the fraction of the original longitudinal momentum of the hadron carried by the parton.

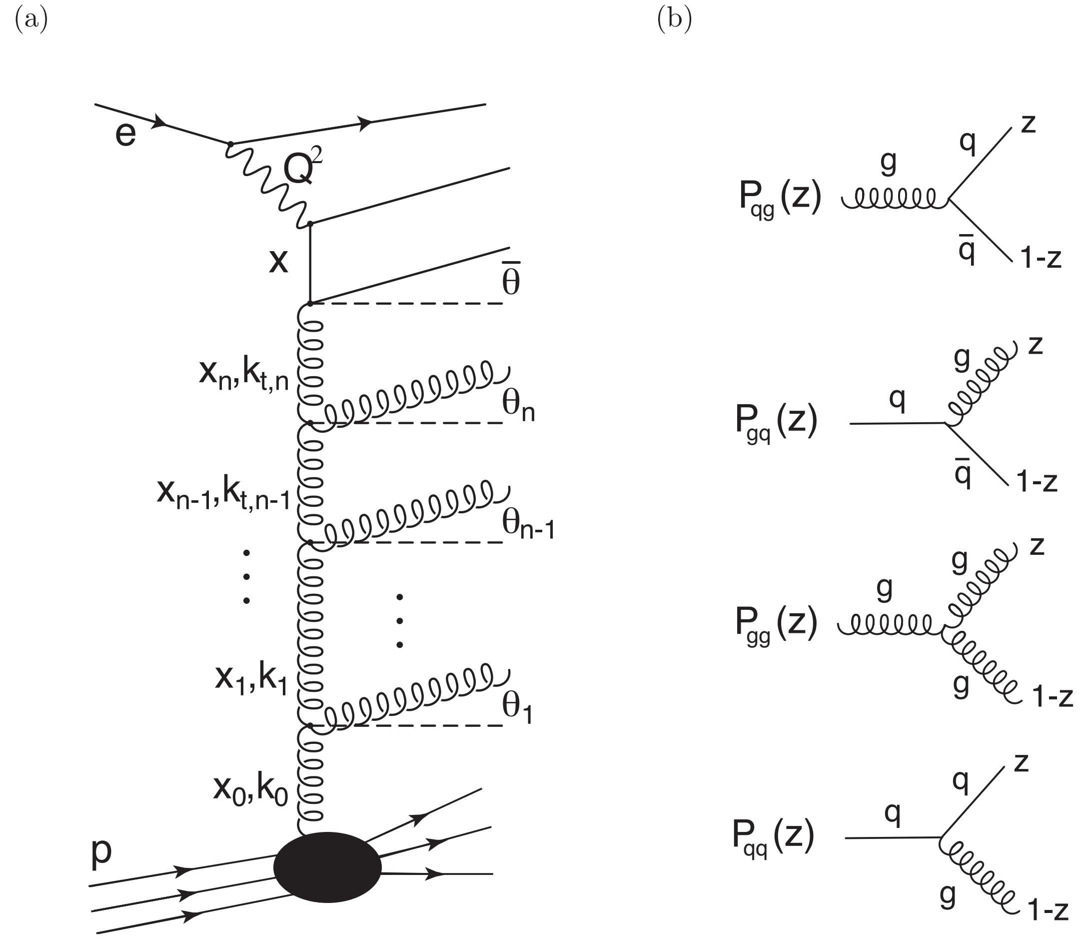

Figure 2.5: A parton evolution diagram is shown on the left (a). Figure (b) illustrates the splitting functions $P_{ab}(z)$.

2.4 Parton Evolution Models

As discussed above, the parton density functions cannot be predicted by pQCD, but their scale dependence can be calculated in this framework. Since the PDFs contain the soft processes up to a certain factorization scale μ_F, it is possible to evolve them to any other scale. For this evolution the knowledge of the PDFs at a certain scale μ_0 is required. The determination at this scale μ_0 is done experimentally.

The evolution itself is performed by considering the parton radiation and splitting processes. Different parton evolution models exist, which cover certain regions of the phase space. The DGLAP, BFKL and CCFM evolution equations are presented in the following.

DGLAP Evolution Model

The DGLAP[1] evolution equation [17], [18], [19], [20] is valid for large Q^2 and moderate x. At the order $O(\alpha_s)$ the processes $\gamma g \to q\bar{q}$ and $\gamma q \to gq$ need to be included. The DGLAP evolution equation for the quark density is in this case of the following form:

$$\frac{\partial q(x,\mu^2)}{\partial \ln \mu^2} = \frac{\alpha_s}{2\pi} \int_x^1 \frac{dy}{y} \Big(f_q(y,\mu^2) P_{qq}\Big(\frac{x}{y}\Big) + f_g(y,\mu^2) P_{qg}\Big(\frac{x}{y}\Big)\Big). \tag{2.15}$$

The function P_{ab} denotes the splitting function for the process $b \to a$. They are depicted in figure 2.5 (b) and describe the probability for parton b to emit parton a with momentum $p_a = zp_b$, with $x = yz$. The evolution equation for the gluon density in the DGLAP approach is given as

$$\frac{\partial g(x,\mu^2)}{\partial \ln \mu^2} = \frac{\alpha_s}{2\pi} \int_x^1 \frac{dy}{y} \Big(f_q(y,\mu^2) P_{gq}\Big(\frac{x}{y}\Big) + f_g(y,\mu^2) P_{gg}\Big(\frac{x}{y}\Big)\Big). \tag{2.16}$$

In leading order, the DGLAP approach is based on resumming the leading $(\alpha_s \ln(Q^2/\mu^2))^n$ contributions. In next-to-leading order evolution the summation of the $\alpha_s(\alpha_s \ln Q^2)^{n-1}$ terms is included. This so-called *Leading Log Approximation* (LLA) requires a strong ordering in the transverse momenta of the emitted partons, as illustrated in figure 2.5 (a):

$$\mu^2 < k_{t,1}^2 < k_{t,2}^2 < \cdots < k_{t,n}^2 < Q^2. \tag{2.17}$$

The DGLAP evolution equation predicts the scaling violations observed at HERA down to the smallest accessible x successfully. It is used to model parton showers for Monte Carlo programs, as described in section 2.8. In this framework all partons entering the hard subprocess are on-shell.

BFKL Evolution Model

The BFKL[2] approach [21], [22], [23] leads to strongly ordered longitudinal momenta $z_i = x_i/x_{i-1}$. The BFKL ansatz can be used for moderate Q^2 and small x. The evolution is performed in x and the leading $\alpha_s \ln(1/x)$ terms are resummed. Here the transverse momenta k_t are free and therefore this approach is also called the k_t-factorization approach. In the kinematical region of HERA the structure function F_2 is not able to discriminate between DGLAP and BFKL. The study of the energy dependence of jets near the proton direction may be sensitive to reveal the BFKL mechanism.

---

[1] Dokshitzer, Gribov, Lipatov, Altarelli, Parisi

[2] Balitsky, Fadin, Kuraev, Lipatov

CCFM Evolution Model

The CCFM[3] evolution model [24], [25], [26], [27] combines the DGLAP and the BFKL approach. It is equivalent to the DGLAP approach for large Q^2 and moderate x and equivalent to BFKL for small x and moderate Q^2. It shows a strong angular ordering of subsequent parton emissions in a certain region of the phase space. This is a property of QCD since in a cascade of gluon and quark emissions the angles of the emitted particles decrease when following down a branch. The unintegrated gluon density $\mathcal{A}(x_g, k_t^2, \mu_F^2)$ stands for the probability to find a parton with longitudinal momentum fraction x_g and transverse momentum fraction k_t at the factorization scale μ_F. In the CCFM model this parton density is more complicated than the one in DGLAP, which depends on x and Q^2 only.

The CCFM approach allows partons to be off-shell when entering the hard matrix element. As a consequence, resolved processes are implicitly included to some extend.

2.5 Heavy Quark Production

The masses of the light quarks u, d and s are below the Λ_{QCD} parameter and therefore not large enough to provide a hard scale. The masses of the heavy quarks c, b, and t are high enough to serve reliable perturbative calculations. Since the mass of top quark production $t\bar{t}$

---

[3] Ciafaloni, Catani, Fiorani, Marchesini

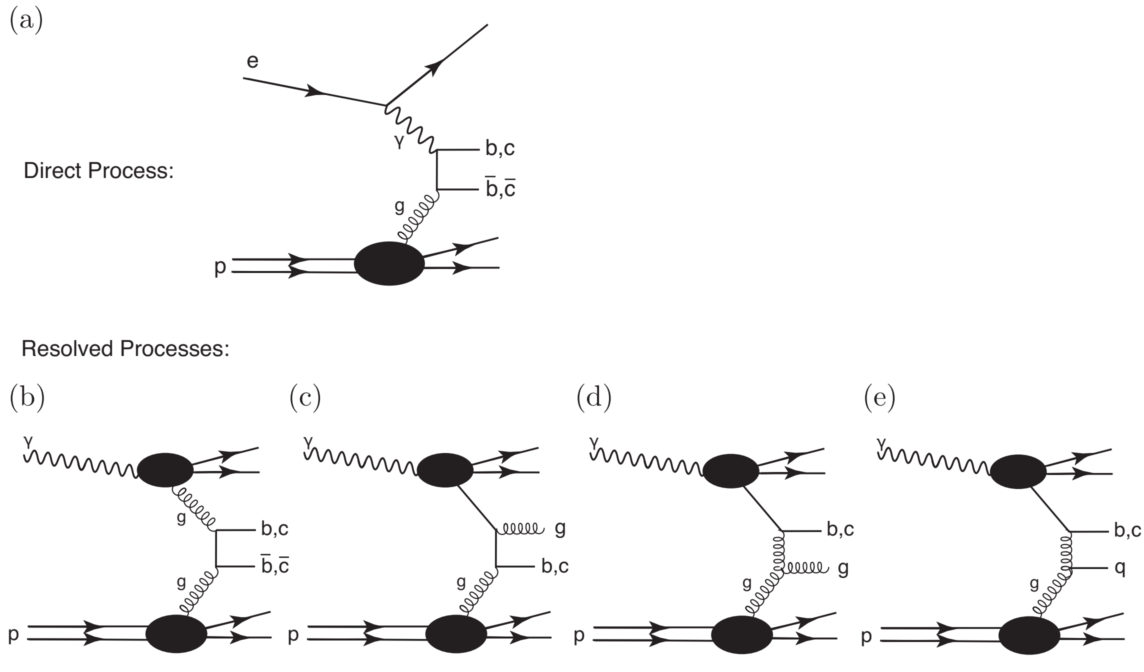

Figure 2.6: Heavy quark production in leading order pQCD. In (a) the direct BGF process is shown while figures (b)-(e) illustrate resolved processes.

is out of reach for the HERA collider, here the heavy quark physics concentrates on c (charm) and b (beauty) quarks. Heavy quark production contributes significantly to the total inclusive cross section at HERA. The dominant contribution to the heavy quark production cross section in leading order $O(\alpha\alpha_s)$ is due to *Boson-Gluon Fusion* (BGF). The ep scattering process can be understood in terms of QCD, where the photon coming from the electron interacts with partons of the proton. At low y virtualities the exchanged photon has a relatively long lifetime and two scattering scenarios must be considered:

- Direct Photoproduction:
  If the photon interacts directly with a parton of the proton, the interaction is called *direct photoproduction*. This process is plotted in figure 2.6 (a). In the final state they form a heavy quark pair $\gamma g \rightarrow q\bar{q}$. Following [28], [29] the cross section for this process can be written as

  $$\hat{\sigma}_{BGF}(\hat{s}, m_q^2) = \frac{\pi e_q^2 \alpha\alpha_s}{\hat{s}} \big[(2 + 2\omega - \omega^2) \ln\big(\frac{1+\chi}{1-\chi}\big) - 2\chi(1+\chi)\big], \tag{2.18}$$

  $$\text{with} \quad \omega = 4m_q^2/\hat{s}, \quad \chi = \sqrt{1-\omega}. \tag{2.19}$$

  Here $\hat{s} = (p_q + p_{\bar{q}})^2$ represents the squared centre-of-mass energy and e_q stands for the electric charge of the heavy quark q. The massive approach is applied which takes the masses of c and b quarks into account. Due to the larger mass and the smaller charge of the b quark in comparison to the c quark, the beauty cross section is suppressed.
  In the massless approach, where $(m_c, m_b) \rightarrow 0$ holds, the charm cross section is expected to be only a factor of four larger than the beauty cross section in the boson-gluon fusion process.

- Resolved Photoproduction:
  If the photon does not interact directly, but fluctuates into a $q\bar{q}$ state before the hard interaction, the process is called *resolved photoproduction*. Resolved processes represent a significant contribution in addition to direct processes. In figure 2.6 (b)-(e) several resolved processes in leading order are shown. In 2.6 (b) a hadron-like process is depicted. Here, a gluon or a light quark coming from the photon interacts with a parton of the proton. In all resolved processes the photon behaves similar to the proton - as a bunch of partons. The photon is therefore treated as a particle with a hadronic structure which can be described by parton density functions. Figures 2.6 (c)-(e) depict *heavy quark excitation processes*. In this case, a heavy quark out of the photon participates in the hard interaction.
  Resolved processes may have two different natures: either the photon fluctuates into an unbound fermion pair or into a $q\bar{q}$ pair forming a vector meson. If quarks are involved, the situation becomes complicated since the spectrum of fluctuations is more rich and QCD corrections have to be taken into account. In the fermion pair production, the photon is also known as a *point-like* or *anomalous* photon. In the second case the vector meson interacts with the proton like a hadron. This process is described by the *Vector Meson Dominance Model* (VDM) and also known as a *hadron-like* resolved process.

A very good agreement between the data and the leading order QCD calculation is achieved, when the resolved processes are taken into account. The distinction between resolved and direct processes is only in the LO calculation unambiguous.

2.6 QCD Calculation Schemes

Physics simulation programs are a fundamental tool for every high energy physics experiment. They are required for designing detectors and help to develop experimental analysis strategies. For this purpose these programs have to provide simulations which model the collision processes as realistic as possible. The input of such programs are calculations performed in pQCD at different orders. In leading order the Monte Carlo event generators are used. They provide an event-by-event prediction based on statistical methods and are described in section 2.8. For the prediction of next to leading contributions cross section Monte Carlo integration programs are used. They are presented in section 2.9. The physics simulation programs are based on different calculation schemes. Therefore these schemes are discussed before the description of the simulation programs.
The hard scale, which is set by the heavy quark mass, complicates the situation since the perturbative expansion series can not be optimized for all scales at once. Different approaches exist to determine next to leading order contributions of heavy quark production. The heavy quark mass is treated in different ways according to the relative magnitudes of the scales p_t and Q^2, which are also present.

Massive Approach

In the massive approach, the heavy quarks are treated as massive partons which are strictly independent of the photon and proton content. Therefore the number of active flavours in the initial state is fixed and restricted to the light quarks. The heavy quarks appear therefore only in the final state and are produced via the BGF mechanism. Since the number of active quark flavours is fixed, this scheme is called the *Fixed Flavour Number Scheme* (FFNS). This model is valid in regions of $p_t \approx m_q$. The quark mass m_q sets the scale for the perturbative calculations and acts as a cutoff. In the calculation of the hard scattering cross section all terms up to $O(\alpha_s^2)$ are taken into account. The leading order and some NLO Feynman diagrams for heavy quark production in the massive scheme are shown in figure 2.7. If $p_t \gg m_q$ collinear gluon emissions and gluon or photon splittings into a heavy quark pair occur, which lead to divergences in the expansion series. To solve this problem, another calculation scheme, the massless approach, is introduced.

Massless Approach

In the massless approach the masses of the heavy quarks are neglected. Here the heavy quarks are part of the photon and proton content. For pQCD calculations, it means, that the heavy quarks are active flavours in the proton and photon structure functions. This ansatz holds for large scales, which means that the p_t of the heavy quark must be much larger than the quark mass itself. In consequence of this restriction, the small p_t regions are not calculable

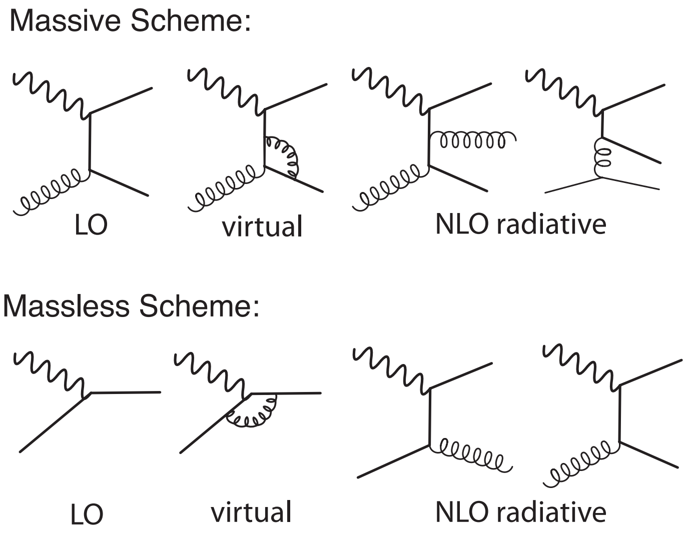

Figure 2.7: Perturbative QCD contributions of the massive and the massless scheme.

in the massless approach since the cross sections are divergent. The massless scheme is also called *Zero Mass Variable Flavour Number Scheme* (ZM-VFNS). The leading order and some NLO Feynman diagrams for heavy quark production in the massless scheme are shown in figure 2.7.

Matched Scheme

The matched scheme combines the massive and the massless approach. It utilizes the best appropriate scheme at a given energy scale Q^2. It is also known as the FONLL scheme [30], which stands for *Fixed Order* (FO) and *Next to Leading Logarithmic* (NLL). It is a full massive NLO calculation which resums additionally the logarithms of p_t^2/m_q^2. The matched scheme certainly would provide very reliable theoretical predictions, but it is presently unavailable for H1 data.

2.7 Fragmentation

Due to the confinement, it is not possible to measure free b and c quarks directly. The strongly interacting particles form in their final state colour neutral states, colourless hadrons. The process of forming hadrons is known as parton *hadronisation* or *fragmentation*. In Monte Carlo generators the two partons, which are produced in the BGF process, undergo a parton shower which can be described by evolution equations (cf. section 2.4). This is possible up to a certain scale μ_F, as discussed before. Afterwards it is not possible anymore to perform pQCD calculations, since the strong coupling constant gets too large and spoils the convergence of the pQCD calculations. Therefore phenomenological models are used to describe the fragmentation process for large distances (soft processes). In this analysis two out of several fragmentation models are used and presented briefly in the following.

- The *string fragmentation* model [31] is used as default in this analysis. In this model $q\bar{q}$ pairs and the colour field between them form 'strings'. At large distances the stored potential energy is proportional to the distance. As a consequence, the string breaks up at larger distances, when the energy got large enough. In this case a new $q\bar{q}$ is produced out of the vacuum. Kinks in these strings are interpreted as gluons in this model. In the final state the produced string fragments form hadrons. According to [31], the *Lund fragmentation function* is defined as

  $$\mathcal{D}_q^h(z) \sim \frac{1}{z}(1-z)^a \exp(-bm_t^2/z), \quad \text{with} \quad m_t = m^2 + p_x^2 + p_y^2. \tag{2.20}$$

  Here m_t denotes the transverse mass of the hadron, while a and b are free parameters. z stands for the longitudinal momentum fraction. In this analysis the Lund-Bowler fragmentation function is used, which is similar to equation (2.20) [32].

- In the *independent fragmentation* model partons form hadrons independently. It is implemented in the Peterson fragmentation model [33]. The probability for a quark q to form the hadron h which carries the longitudinal momentum fraction z is given by

  $$\mathcal{D}_q^h(z) \sim \frac{1}{z\left(1 - \frac{1}{z} - \frac{\epsilon_q}{1-z}\right)^2}. \tag{2.21}$$

  The free parameter ϵ_q has to be determined experimentally and is different for charm and beauty quarks. This value is higher for b quarks, which corresponds to a harder fragmentation for beauty flavoured hadrons. They get a larger longitudinal momentum fraction on average of the initial parton. In this analysis the Peterson fragmentation is used to estimate systematic effects arising from the choice of the fragmentation model.

2.8 Monte Carlo Event Generators

Monte Carlo Generators provide a prediction of the full hadronic final state four vectors for every event. After generating the event, the detector simulation has to be performed. The generating process is divided into three parts: First, the hard process is generated. In the second step, the parton showers and evolution equations (cf. section 2.4) are applied for the initial and final state. In the last step, the hadronic final state is formed by assistance of phenomenological models, such as Lund fragmentation (section 2.7). Additionally hadron decays are modelled, for example semi-leptonic decays of heavy hadrons.

The generated event sample can be fed into detector simulation programs. The simulated event sample can then be compared with data as recorded by experiments. The detector simulation is usually based on the GEANT package [34]. Here, the particle tracking through the different subdetectors is modelled and the detector geometry and (dead) material is simulated. The applied detector simulation is not part of the Monte Carlo generator. In H1 it is implemented in the H1SIM package. At this stage, the simulated Monte Carlo prediction corresponds to the raw data from ep collisions. The final step is to reconstruct both the data and the simulated Monte Carlo events with the H1 reconstruction software H1REC. The simulated and reconstructed Monte Carlo event sample can be used for predictions at hadron and detector level. The determination of corrections such as reconstruction efficiencies is now possible.

To provide the self-consistency of the method to measure the cross sections, detector effects and efficiencies as well as dead material in the detector have to be very well modelled by the simulation. As long as the reconstructed and simulated Monte Carlo describes the data in every aspect, the Monte Carlo predictions for the quark contributions can be used as templates in the fit and for the cross section measurement.

PYTHIA

In this analysis the PYTHIA 6.4 event generator [35] is used. The PYTHIA generator simulates events using the massless calculation scheme. Here a mode is used, which matches direct, excitation and resolved contributions. In excitation processes a heavy quark can originate from the photon or proton. The proton density functions are taken from `CTEQ6L` [13], while the photon distribution functions are used from `SaS2D` [16]. The evolution scheme applied in PYTHIA is DGLAP with on-shell matrix-elements. As fragmentation model the Lund-Bowler function [32] is applied. To study the systematic error arising from this choice of fragmentation model, an additional Monte Carlo set with the Peterson fragmentation is produced. The renormalization scale μ_R is set to $p_t^2 + (P_1^2 + P_2^2 + m_q^2 + m_{\bar{q}}^2)/2$, where P_1^2, P_2^2 represent the virtualities of the two incoming particles, p_t stands for the transverse momentum of the scattering process and m_q, $m_{\bar{q}}$ are the masses of the two outgoing particles. A summary of the parameters and functions used in the LO QCD calculations can be found in table 2.1.

Three different event samples are generated: charm, beauty and inclusive ones. These three samples are generated in the inclusive mode, which is very time consuming. For charm and beauty, the processes $ep \rightarrow eb\bar{b}\mu X$ or rather $ep \rightarrow ec\bar{c}\mu X$ are selected out of all inclusive processes. The luminosity of the charm sample is 2800 pb^{-1}, which corresponds to roughly 16 times the data luminosity. The sample containing beauty events has a luminosity of 3074 pb^{-1}, which is a factor of 18 more than the data. The inclusive sample consists of events containing u, d, s, c, b quarks, dominated by the light quarks. The luminosity of the inclusive sample is roughly 838 pb^{-1} and corresponds to approximately five times the data luminosity. The different run ranges e^+ and e^- are taken into account for the three Monte Carlo samples. The fractions of these three components are predicted by PYTHIA. The sum of the b, c, and uds contributions is compared with the data to ensure that the data is well described by the PYTHIA Monte Carlo simulation. The measured charm and beauty data are compared to the charm and beauty cross sections predicted by PYTHIA.

CASCADE

In CASCADE [36] the process $\gamma g \rightarrow b\bar{b}$ or $\gamma g \rightarrow c\bar{c}$ is modelled. Here the evolution scheme CCFM is applied which uses k_t unintegrated parton distributions in the proton. As discussed in section 2.4, the gluon density depends on the transverse momentum k_t of the parton. The parton distributions are taken from `A0` [37] and are applied with the same mass parameters as

	PYTHIA (LO)	CASCADE (LO)
Version	6.4	2.0
Evolution scheme	DGLAP	CCFM
m_b [GeV]	4.75	4.75
m_c [GeV]	1.5	1.5
Proton PDF	`CTEQ6L`	`A0`
Photon PDF	`SaS2D`	-
Renorm. scale μ_R	$p_t^2 + (P_1^2 + P_2^2 + m_q^2 + m_{\bar{q}}^2)/2$	$\sqrt{\hat{s} + Q_\perp^2}$
Factor. scale μ_F	$p_t^2 + (P_1^2 + P_2^2 + m_q^2 + m_{\bar{q}}^2)/2$	$\sqrt{\hat{s} + Q_\perp^2}$
Lund a	0.437	0.437
Lund b	0.850	0.850
Peterson ϵ_b	0.058	-
Peterson ϵ_c	0.0069	-

Table 2.1: Overview of parameters and functions used in the leading order QCD calculations.

used in PYTHIA. The factorization scale can be written as $\mu_F = \sqrt{\hat{s} + Q_\perp^2}$. Here $\hat{s}$ represents the invariant mass of the $q\bar{q}$ subsystem and $Q_\perp$ stands for its transverse momentum. This choice of μ_F is motivated by the maximum angle allowed for any emission since the CCFM scheme is performed in an angular orderd region. The PYTHIA generator provides the treatment of the final state parton showers, the proton remnant and the fragmentation. In CASCADE the same fragmentation function as used in PYTHIA is applied, the Lund-Bowler function.

The CASCADE Monte Carlo samples are produced to study systematic effects coming from the choice of the underlying physics model. Two different samples are generated: charm and beauty ones. The estimation of the light quark background is done with the PYTHIA inclusive Monte Carlo sample.

2.9 QCD Predictions

Perturbative QCD calculations at next to leading order are available in Monte Carlo integration programs. In this analysis two NLO predictions are compared to the measured cross sections and presented briefly in the following.

FMNR

The FMNR[4] program [38] implements a fixed order calculation in the massive scheme at next to leading order precision. The predictions are therefore expected to be valid in the lower p_t region. FMNR provides weighted parton level events with two or three outgoing partons. This is for example the heavy quark antiquark pair and in the case of three partons a third

---

[4] Frixione, Mangano, Nason, Ridolfi

light quark. A comprehensive overview of the FMNR program is for example given in [39]. The b quark is evaluated into a b flavoured hadron by rescaling the three-momentum of the quark using the Peterson fragmentation function with the parameter $\epsilon_b = 0.0069$. To be able to produce a final state containing a muon as a product of the decay of a beauty flavoured hadron, the program is extended. Both direct and indirect decays of beauty flavoured hadrons into muons are included using the JETSET [40] muon decay spectrum. The k_t jet algorithm is used to reconstruct parton level jets from the outgoing partons.

The hadronisation corrections in the FMNR calculations are determined using the PYTHIA programme in this analysis. The observables related to jets are calculated on the one hand for the events generated with PYTHIA using the final state partons, and on the other hand from the resulting hadrons. On this basis, a migration matrix for each observable is determined, which describes the migration from bins of parton level observables to bins of hadron level observables. To estimate the uncertainties of the hadron level NLO QCD predictions, the mass of the beauty quark $m_b = 4.75$ GeV is varied by ±0.25 GeV. Additionally, the renormalization and factorization scales μ_r and μ_f are varied independently in the range $\mu_0/2 \leq \mu_r, \mu_f \leq 2\mu_f$, using the constraint $1/2 \leq \mu_r/\mu_f \leq 2$. The deviations due to the beauty mass variation and the largest deviation due to the scale variation in both directions are determined in each bin on hadron level. For the total model uncertainty, the deviations are added up in quadrature, as recommended in [41].

For this analysis the proton structure function is taken from `CTEQ5F4` [42] and the photon structure function is calculated by `GRV-G HO` [43]. The heavy quark masses are set to 1.5 GeV and 4.75 GeV for charm and beauty, respectively. A summary of the parameters for the NLO calculations can be found in table 2.2. Due to technical reasons, the FMNR calculation is performed for the beauty measurement only. The calculation is done by Dr. Benno List.

MC@NLO

The MC@NLO program [44] was developed recently and is currently available for HERWIG@NLO only. HERWIG is a Monte Carlo generator [45] which stands for *Hadron Emission Reactions With Interfering Gluons*. HERWIG is able to simulate hard lepton-lepton, lepton-hadron and hadron-hadron scattering as well as soft hadron-hadron collisions. The PYTHIA@NLO program is on the way and will be most probably available for the publication of this analysis.

The MC@NLO program is a Monte Carlo event generator, which determines the matrix elements at next-to-leading order. In such a calculation the situation becomes more complicated than in the leading order picture, since so-called momentum reshuffling occurs. After the parton showering process each parton becomes a jet, which makes a replacement of the parton momenta by jet momenta necessary. This has to be done carefully, since energy momentum must be conserved and double counting has to be avoided. This complication and other issues of the next-to-leading order calculation are taken into account and implemented in the MC@NLO program developed in [44].

In [44] the calculations are done for the case of heavy quarks in photoproduction. The HERWIG@NLO predictions for the charm and beauty measurement are calculated by Tobias Toll for the analysis presented in this thesis and compared to the measured data. The settings

	FMNR (NLO)	MC@NLO
Version Evolution scheme	- angular ordering	HERWIG 6.510 angular ordering
m_b [GeV] m_c [GeV]	4.75 1.5	4.75 1.5
Proton PDF Photon PDF	`CTEQ5F4` `GRV-G HO`	`CTEQ6.6` `GRV-E`
Renorm. scale μ_R Factor. scale μ_F	$\sqrt{m_b^2 + p_t^2}$ μ_R	$\sqrt{m_b^2 + p_t^2}$ μ_R
Fragmentation	Peterson fragmentation $\epsilon_b = 0.0069$	cluster fragmentation -

Table 2.2: Overview of parameters and functions used in the NLO QCD calculations.

for the calculation are listed in table 2.2. The results can be found in chapter 7.

2.10 Properties of Charm and Beauty Hadrons

Charm and beauty flavoured hadrons have a relative large mass and lifetime. The lifetime is of the order $\mathcal{O}(1 \text{ psec})$ and thus measurable with a precision vertex detector. These are remarkable properties in comparison to other hadrons. Their masses, mean lifetimes and branching ratios cannot be calculated theoretically. Therefore, these properties are measured by experiment. The main experimentally determined attributes of some b and c flavoured hadrons are listed in table 2.3.

Decays of ground state hadrons proceed via the weak interaction. Theoretically the Cabbibo-Kobayashi-Maskawa (CKM) matrix describes the change of the different quark flavours. The transition probability for the quarks i, j with $j \rightarrow i$ is given by the squared absolute value of the matrix element $|V_{ij}|^2$. In the dominant weak decays $b \rightarrow cW^-$ and $c \rightarrow sW^+$ the corresponding matrix elements $|V_{cb}|$ and $|V_{cs}|$ are [46]

$$|V_{cb}| = 0.0412 \pm 0.0011, \tag{2.22}$$

$$|V_{cs}| = 1.04 \pm 0.06. \tag{2.23}$$

The smaller measured value for $|V_{cb}|$ indicates that b flavoured hadrons have larger decay lengths and lifetimes than c flavoured hadrons.

In this analysis the semi-leptonic decay $B \rightarrow \mu X$ is studied, which is depicted in figure 2.8. The b quark contained in the B hadron can either decay directly into cW and the W boson decays subsequently into a muon and a neutrino (see figure 2.8 (a)). According to [46], the branching fraction for this decay is roughly 11%. In the case of an indirect decay (figure 2.8 (b)), the beauty quark decays into a charm quark and a W boson. The charm quark decays then into a strange quark and a W boson, which in turn decays into a muon and a neutrino. The branching fraction for the indirect decay is about 8% [46]. Two W bosons are produced

	quark content	mass m_q [GeV]	lifetime τ [psec]	decay length $c\tau$ [μm]
B^0	$d\bar{b}$	5279.53 ± 0.33	1.53 ± 0.009	458.7
B^+	$u\bar{b}$	5279.15 ± 0.31	1.638 ± 0.011	491.1
B_s^0	$s\bar{b}$	5366.3 ± 0.6	1.470 ± 0.027	441
Λ_b^0	udb	5620.2 ± 1.6	1.383 ± 0.049	415
D^0	$c\bar{u}$	1864.84 ± 0.17	0.4101 ± 0.0015	122.9
D^+	$c\bar{d}$	1869.62 ± 0.20	1.040 ± 0.007	311.8
D_s^+	$c\bar{s}$	1968.49 ± 0.34	0.500 ± 0.007	149.9
Λ_c^+	udc	2286.46 ± 0.14	0.200 ± 0.006	59.9

Table 2.3: Properties of heavy hadrons according to the results of the PDG group in 2008 [46].

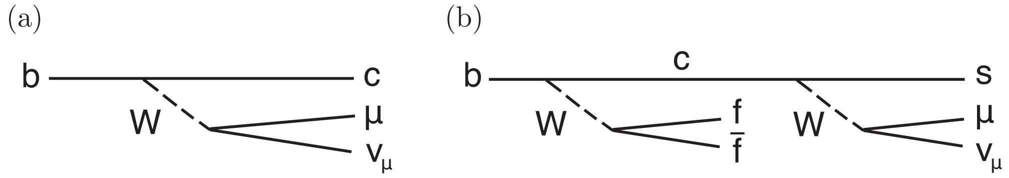

Figure 2.8: Diagrams for semi-leptonic decays of beauty quarks. In (a) the direct process into a charm quark is shown, while in (b) the indirect cascade process into a strange quark via a charm quark is illustrated.

in this cascade decay, which decay into a fermion-antifermion pair. Thus in rare cases two muons can appear in the final state.

2.11 Recent Results of Heavy Quark Production

A comprehensive and nice overview of heavy quark measurements at HERA can be found in [47], [48]. Here, a collection of heavy quark measurements in photoproduction using dijet events is presented. At first, the tagging methods used at HERA for heavy quarks are summarized. Then, some interesting results obtained at HERA are presented briefly for charm and beauty photoproduction separately.

Tagging Methods for Heavy Quark Production

At HERA mainly five basic analysis techniques are used to tag events containing heavy quarks. Usually several of these tagging methods are combined. In the following methods, single tagging is used, which means, that the decay particles of one heavy quark are measured. A double tagging is possible, but not as efficient as the single tagging. The full reconstruction of the decayed hadrons containing heavy quarks is mostly used for charm measurements. Here the D^* meson is used very often, which is reconstructed via the so-called golden decay channel: $D^{*+} \rightarrow D^0\pi_s^+ \rightarrow (K^-\pi^+)\pi_s^+$. Since the branching ratios for decay channels, which can be reconstructed, is too small and the beauty production rates are very low, the full reconstruction method is not used for beauty analyses. A very common tagging method is using leptons, like muons or electrons from semileptonic decays of charm and beauty flavoured hadrons. These leptons have relatively large momenta and can be identified clearly. Another tagging method is the p_t^{rel} method. Here the relative transverse momentum of the lepton to the axis of the associated jet is exploited. Due to the large masses of beauty flavoured hadrons, it is possible to identify events containing beauty quarks with the p_t^{rel} method clearly at statistical level. The single charm fraction cannot be obtained with this method. The fourth tagging method makes use of the large lifetime of heavy flavoured hadrons. Either the full reconstruction of the charged decay tracks at the secondary vertex is performed or the distance of the charged tracks to the primary vertex is used. This method is able to distinguish between events containing charm and beauty quarks. In general at least one jet is required in heavy quark analyses. This is necessary to estimate the direction of the outgoing heavy quark, which is used by the lifetime and p_t^{rel} method. In combination with another heavy quark tagging method a quark jet can be found.

Charm Photoproduction

The charm quark was discovered at two institutes at the same time in November 1974: the Stanford Linear Accelerator (SLAC) [50] and at the Brookhaven National Laboratory (BNL) [51]. Both experiments observed a narrow resonance at 3.1 GeV, which was interpreted as a $c\bar{c}$ bound state. This meson got the name J/Ψ to take both suggestions for its name into

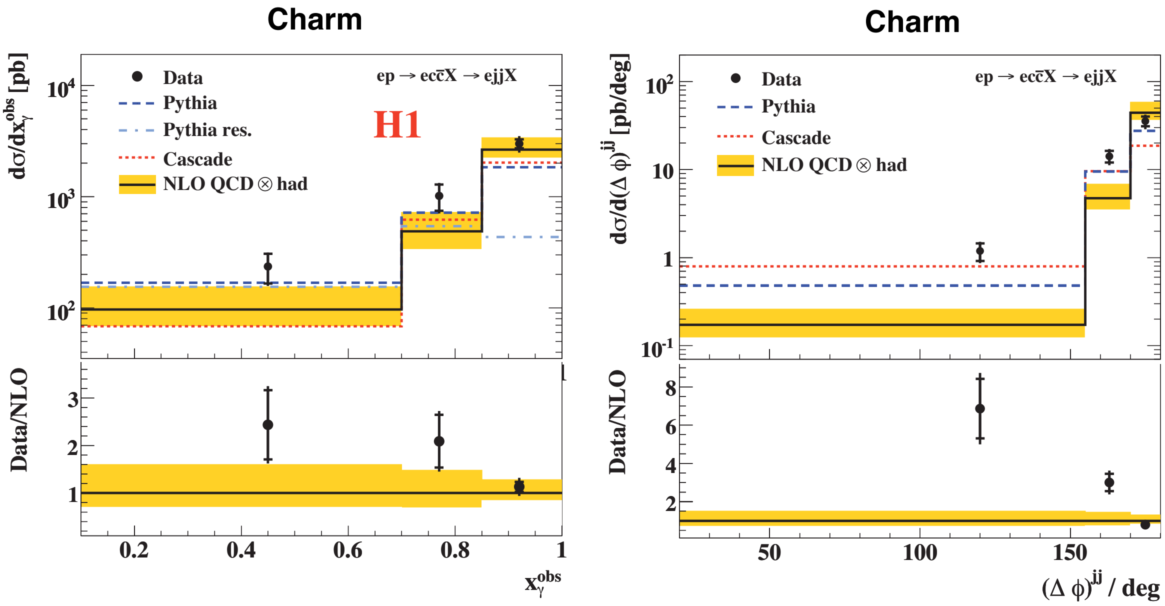

Figure 2.9: Cross sections for the process $ep \rightarrow ec\bar{c}X \rightarrow ejjX$ as a function of the observable x_γ^{obs} and the angular separation of the two jets $\delta\phi^{jets}$ in the transverse plane measured in [49].

account.
Since then, charm production was studied at many different colliders in various interactions, e.g. at the Tevatron in $p\bar{p}$ interactions. An overview of open charm and beauty results from the D0 and CDF experiments can for example be found in [52]. In the following, the discussion is focussed on recent HERA results.
In [49] charm and beauty dijet cross sections in photoproduction at high p_t are presented. Here the impact parameter of all tracks with respect to the primary vertex is used to determine the fractions of events containing charm and beauty events. The agreement of the charm cross sections in comparison to the next-to-leading order pQCD calculations is in general reasonably good. In contrast to beauty in photoproduction, the charm cross sections as a function of the transverse momentum is in good agreement with NLO calculations. Only in the region of low x_γ^{obs} and low values of the azimuthal angular separation of the two jets $\delta\phi^{jets}$, the NLO prediction underestimates the data, as depicted in figure 2.9. The observables $\delta\phi^{jets}$ and x_γ^{obs} are explained in detail in section 5.4. Here, processes involving resolved photons or higher order contributions are expected to contribute significantly. This observation is also reported in other analyses on independent data sets from H1 [53] and ZEUS [54]. Therefore, it is interesting to perform further studies in the region of resolved processes ($x_\gamma^{obs} < 0.75$), which is done in this thesis.

Beauty Photoproduction

The beauty quark was discovered in 1977 at the Fermi National Accelerator Laboratory (FERMILAB) [55]. The Υ resonance at 9.5 GeV was observed, a $b\bar{b}$ meson. The production

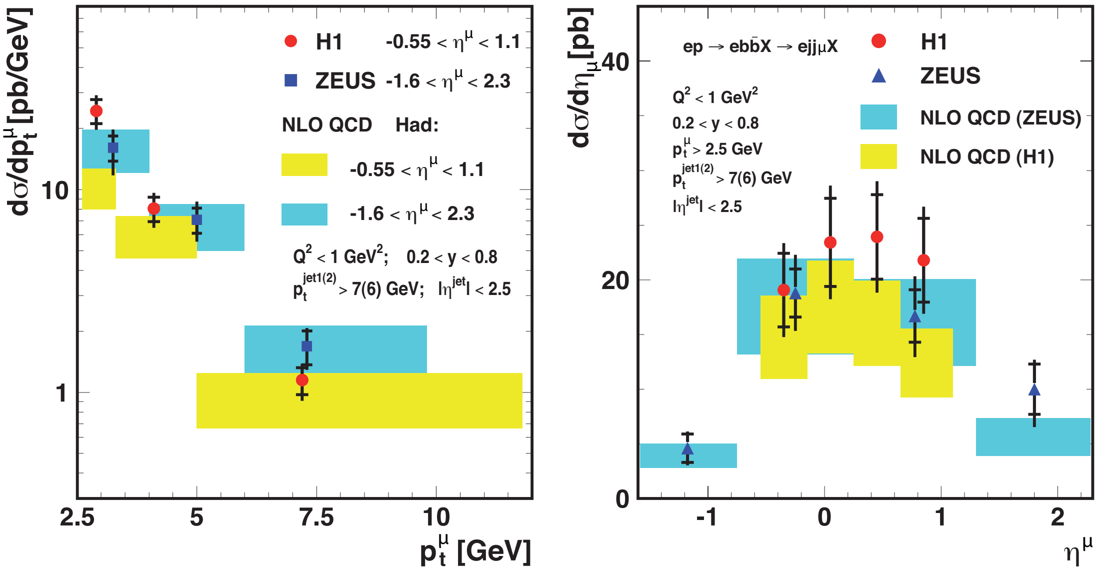

Figure 2.10: Comparison of the H1 and ZEUS analysis for $ep \to eb\bar{b}X \to ejj\mu X$ with HERA I data as a function of the transverse momentum of the muon and its pseudorapidity.

of beauty quarks was studied at different colliders, for example in $p\bar{p}$ collisions at the $Sp\bar{p}S$, in $\gamma\gamma$ interactions at LEP, in $p\bar{p}$ collisions at the TEVATRON and in ep collisions at HERA. The large mass of the beauty quark provides a hard scale and thus pQCD calculations are expected to give reliable results. Therefore it was a surprise, that early measurements performed at LEP and the TEVATRON show large discrepancies between the measured data and the NLO predictions (see e.g. [56]). In the meantime, both the measurements and the NLO calculations were improved, which lead to a much better agreement. This can be seen for example in a recent measurement from the CDF experiment [57]. Here, the fixed order and the next to leading log (FONLL) calculation scheme is used.

In the first publication [58] on beauty photoproduction at HERA the meanwhile well established method of using semileptonic decays of a beauty hadron inside jets from the hadronisation of the beauty quark was presented. To enrich the beauty sample, a muon with a high transverse momentum was required. In this measurement, the NLO prediction underestimates the data, which was also seen at other experiments.

Several analyses for beauty in photoproduction at HERA were performed in the last years.

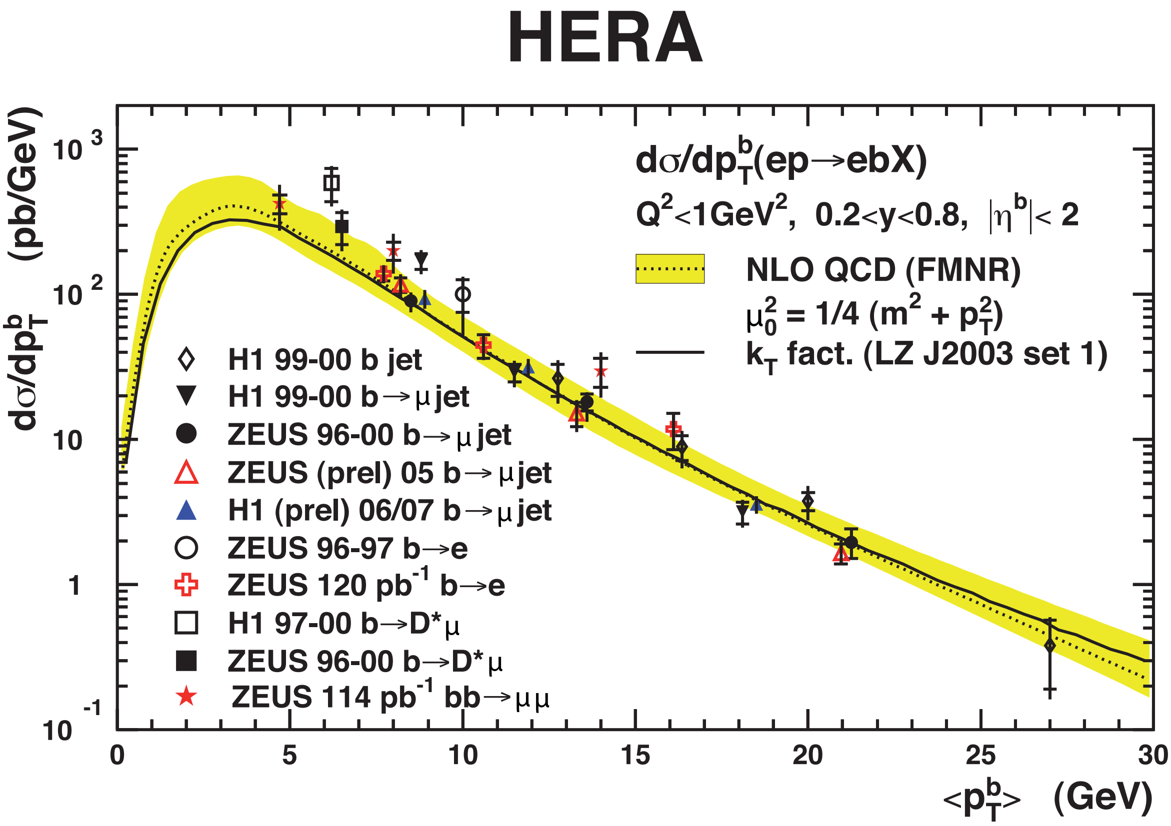

Figure 2.11: Several analyses for beauty in photoproduction performed at HERA from the H1 and the ZEUS experiment.

A collection of these results is summarised in figure 2.11.
In a recent H1 measurement with HERA I data [59] at least two jets accompanied by a muon associated to one of these jets are required. The extraction of the beauty fraction is done using a combination of the p_t^{rel} and the lifetime method. A similar analysis in a slightly different phase space was performed by ZEUS [60]. Here, only the p_t^{rel} method is used to obtain the fraction of beauty events. Both results of H1 and ZEUS agree reasonably in the overlapping region. The cross sections of both measurements as a function of the transverse momentum p_t^{μ} and the pseudorapidity of the muon η^{μ} are shown in figure 2.10. For both results the NLO calculation is also plotted. In general a good agreement for the data and the NLO prediction [61] is observed except for the first p_t^{μ} bin in the range 2.5 GeV to 3.3 GeV of the H1 analysis. This discrepancy is also seen in the first bin of the cross section as a function of the transverse momentum of the highest p_t jet. Also a tendency of a too low NLO prediction in the very forward region for the muon is observed in both the H1 and ZEUS analyses.
To clarify these discrepancies and to obtain a deeper understanding of beauty in photoproduction, it is interesting to repeat the above described measurement with a higher statistical precision as it is done in this thesis. It is thus possible to measure also double differential cross sections. In this analysis, the regions of direct and resolved processes are investigated further.

Chapter 3

The Experiment

This chapter gives an overview of the HERA accelerator and a description of the most relevant components of the H1 experiment for the presented analysis. Further details about the H1 detector can be found in [62].

3.1 The HERA Accelerator

From 1992 to 2007, the *Hadron Electron Ring Accelerator* (HERA) at the *Deutsches Elektronen Synchrotron* laboratory (DESY) in Hamburg, Germany, provided high energy electron and proton beams. The beam collisions occurred at two interaction points, namely at the experiments H1 and ZEUS. The two fixed target experiments HERA-B and HERMES respectively used one of the two beams.

HERA has a circumference of 6.3 km with four experiment halls as pictured in figure 3.1. The proton ring is equipped with superconducting magnets while the electron ring consists of normal conducting magnets.

In the first running period from 1992 to 2000, named HERA I, an integrated luminosity of 130 pb^{-1} was collected with the H1 experiment. The accumulation of luminosity as a function of time is illustrated on the right-hand side in figure 3.1. During the years 2000 to 2003 a luminosity upgrade was performed. New focussing magnets were installed close to the interaction regions. This made a modification of the H1 detector necessary. The HERA II running period from 2004 to summer 2007 provided an integrated luminosity of almost 400 pb^{-1} for each H1 and ZEUS.

In this period protons at energies of 920 GeV collided with electrons or positrons at energies of 27.6 GeV yielding a centre-of-mass energy of $\sqrt{s} \approx 319$ GeV.

3.2 The H1 Detector

The H1 experiment is an asymmetric, multi-purpose detector, which covers a solid angle of almost 4π. The detector's weight is approximately 2800 t and its dimensions are 12 m × 15 m × 10 m. Due to the higher energy of the protons and their hadronic properties, the detector is more instrumented to proton direction.

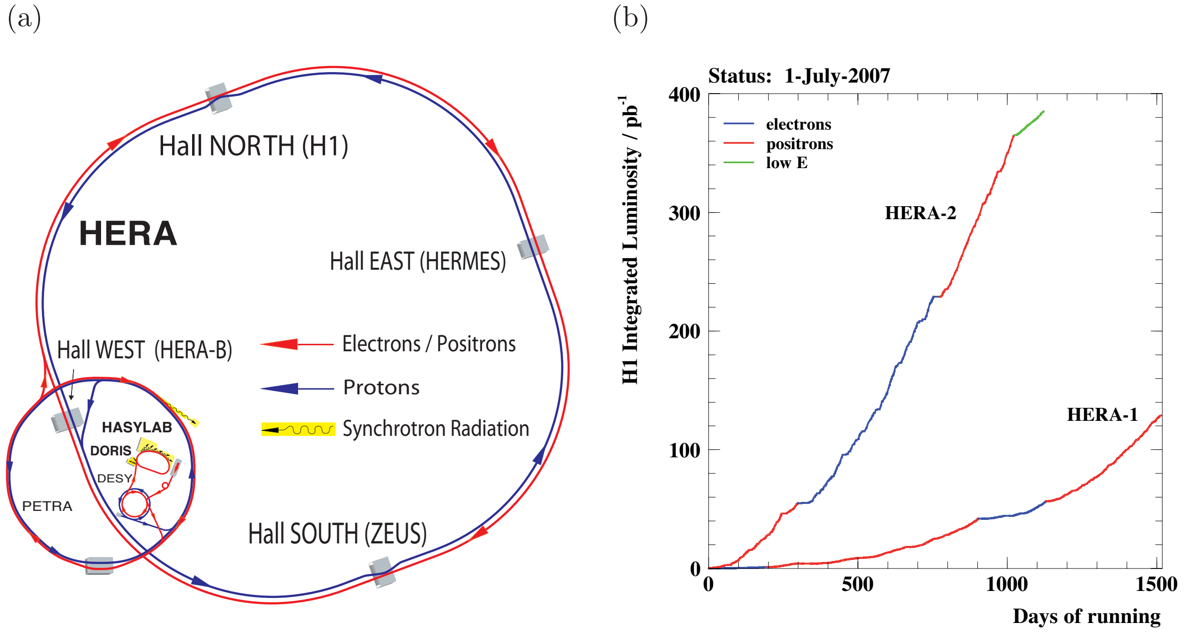

Figure 3.1: On the left a schematic illustration of the HERA ring, its preaccelerators and its four experiment halls can be seen. The right-hand side shows the integrated luminosity for the HERA I and HERA II phase collected with the H1 experiment.

In figure 3.2 a cross section of the H1 detector is depicted. The interaction point of the electrons coming from the left and the protons entering the detector from the right, is defined as the origin of the right handed coordinate system of H1. The z-axis corresponds with the flight direction of the protons. The region with positive z values is called the 'forward' region, the one with negative values is termed the 'backward' region. The x-axis points at the centre of the HERA ring and the y-axis points upwards perpendicular at the x and z-axis. In spite of the cylindrical shape of the H1 detector, a spherical coordinate system with the coordinates (r, θ, ϕ) is often used. r stands for the radial length, θ denotes the polar angle measured with respect to the positive z-axis and ϕ is the azimuthal angle relative to the positive x-axis. Instead of θ the so-called pseudorapidity $\eta = -\ln(\tan(\theta/2))$ is often used. Sometimes the $x - y$ or $r - \phi$ plane is also labelled as the transverse plane.

For taking the different characteristics of decay particles into account, H1 consists of several subdetectors which are built cylindrically around the beam pipe. The first component, the decay particles have to go through, is the tracking system, which is explained in section 3.2.1. Afterwards, they pass the calorimeter which is described briefly in section 3.2.2. The trackers and the calorimetry are surrounded by the superconducting coil and the iron return yoke. Instrumented with limited streamer tubes the latter one operates as the central muon detector which is presented in section 3.2.3. A toroid magnet was installed, to cover the forward region as well.

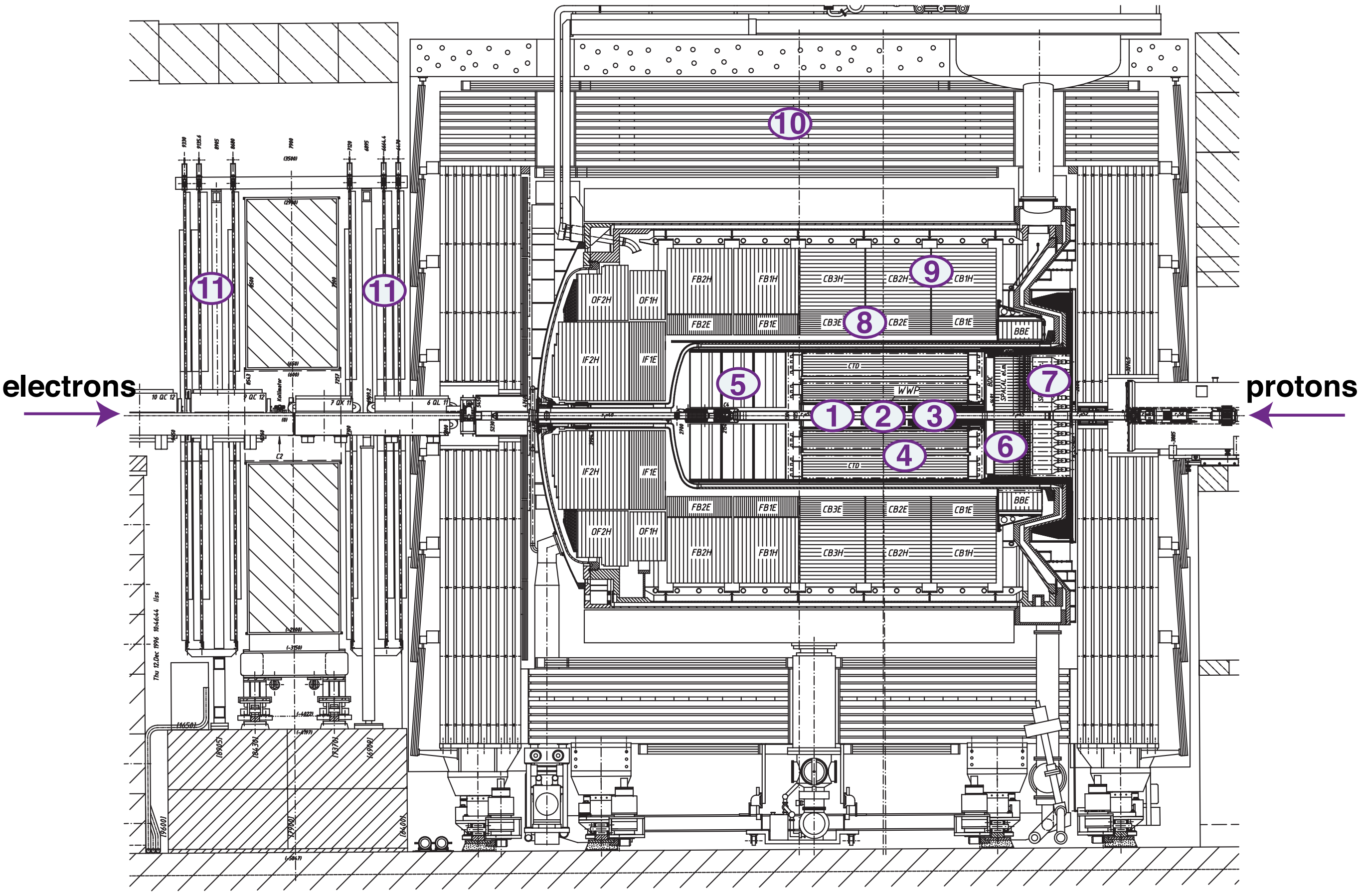

Figure 3.2: Technical view of the H1 detector. Legend can be found in table 3.1.

3.2.1 Tracking Detectors

The *Central Tracking Detector* (CTD) delivers track and vertex information of charged particles in the range $10^\circ < \theta < 170^\circ$, the central region of the detector. It consists of five radial components (see figure 3.3) within a solenoidal magnetic field of 1.16 T which causes curved tracks, depending on the transverse momentum of the particle. The components of the CTD are described briefly in the next sections, as they play an important role for this thesis.

The very forward region is equipped with the *Forward Tracking Detector* (FTD), which is designed to measure tracks in the region smaller than 20°.

Central Silicon Tracker (CST)

In 1995 the H1 experiment was equipped with a vertex detector, the *Central Silicon Tracker* (CST). It provides precise tracking and vertex information in the central region, which is very important for this analysis. In 2001 a luminosity upgrade of HERA necessitated a redesign of the CST owing to a modified shape of the beampipe. Details concerning the redesign can

No.	Subdetector	Abbreviation
	Tracking Detectors	
1	Forward Silicon Tracker	FST
2	Central Silicon Tracker	CST
3	Backward Silicon Tracker	BST
4	Central Tracking Detector	CTD
5	Forward Tracking Detector	FTD
	Calorimetry	
6	Electromagnetic Spaghetti Calorimeter	em. SpaCal
7	Hadronic Spaghetti Calorimeter	hadr. SpaCal
8	Electromagnetic Liquid Argon Calorimeter	em. LAr
9	Hadronic Liquid Argon Calorimeter	hard. LAr
	Muon System	
10	Central Muon Detector (Instrumented Iron)	CMD
11	Forward Muon Detector	FMD

Table 3.1: List of subdetectors of the H1 experiment. A sketch of the central tracking detector is given in figure 3.3.

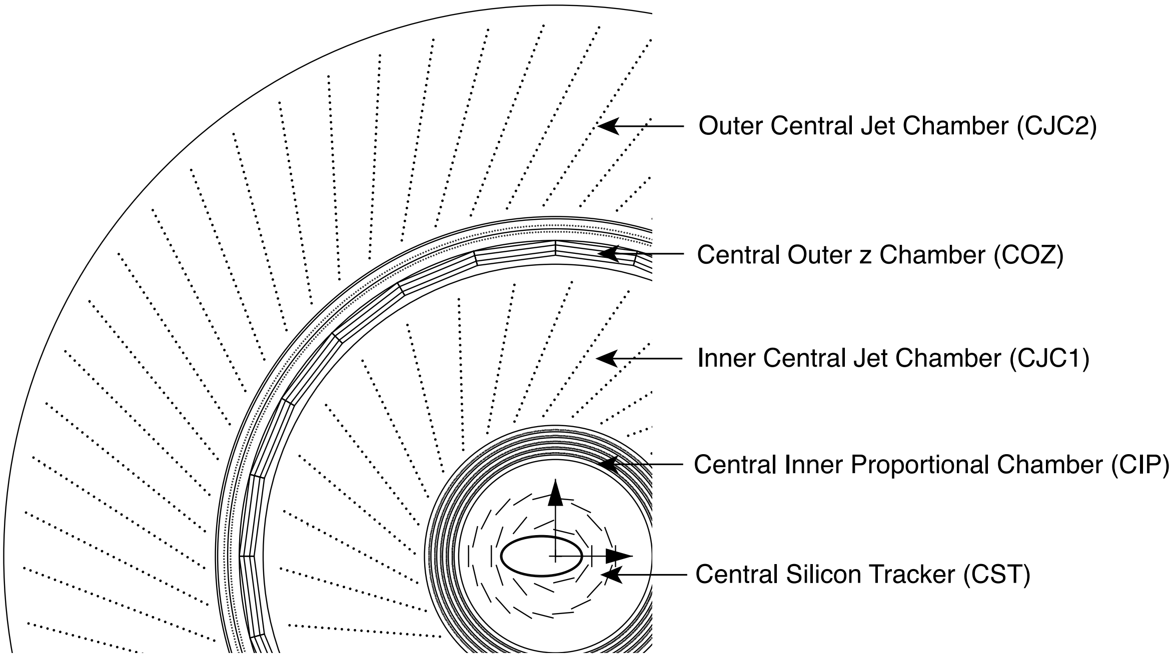

Figure 3.3: Radial view of the central tracking detectors for the HERA II period.

be found in [63].
The CST itself was built in a collaboration of PSI, ETH and the University of Zürich [64] and consists of two layers with double-sided silicon strip sensors, which are described in [65]. The strip sensors are oriented in such a way, that the p side allows a precise measurement of track points in the coordinates $r\phi$. The strips on this side are parallel to the beam axis. The strip pitch on the p side amounts to 50μm. The n side allows a measurement of the z coordinate. Here the strips are oriented perpendicular to the beam axis with a pitch of 88 μm. The single hit resolution in $r\phi$ amounts to 11 μm [66].
The inner layer has 12 ladders and the outer layer has 20 ladders, as illustrated in figure 3.3. Each ladder consists of 6 sensors, altogether the CST is equipped with 192 silicon sensors on 32 ladders. Every ladder consists of 2 half ladders (see figure 3.4) with 1280 strips per half ladder. These 64 half ladders and 81920 strips can be read out individually. The readout is performed by the APC 128 readout chip which was developed at PSI [67], [68]. The analog data are then digitized and processed.
The CST is sensitive to charged particles, which produce pairs of positive and negative charge carriers when crossing a half ladder. A difference of electrical potential between both sides of the sensors leads to a drift of the charge carriers, which are then read out. The signals are classified in the hit finding algorithm [69] and a cluster candidate is defined, if one or several neighbouring strips with signals at least one sigma above the noise level are found. For each cluster candidate, the sum of the strip significances is calculated, defined as ratio between the signal and the respective noise RMS value. A cluster is accepted as hit if the summed significance is at least five. The hit position is approximated by the center of gravity of the strip signals belonging to the cluster. The center of gravity is calculated separately for the p and n side. For the next step, in the algorithm three dimensional space points have to be found by combining the clusters of both sides.
There are two kind of hits: hits which are linked to a good track are called signal hits and those which could not be linked are called background or noise hits. The signal hits are linked to a reconstructed track provided by the central jet chamber, which is described briefly in section 3.2.1.

Central Inner Proportional Chamber (CIP)

The *Central Inner Proportional Chamber* (CIP) is a multiwire proportional chamber with wires parallel to the beam, arranged in five layers. The CIP surrounds the CST and covers the range -112.7 cm $< z <$ 104.3 cm and the angular region $11^\circ < \theta < 169^\circ$. The readout is performed by 9600 readout pads arranged in a projective geometry. The spatial resolution of the CIP in z amounts to 1.5 cm. The polar acceptance of the CIP allows a rejection of proton induced background with a true or apparent vertex position outside the H1 detector at -150 cm to -200 cm. Information on the event timing t_0, the track multiplicity and the significance of the event vertex are delivered to the central trigger logic.

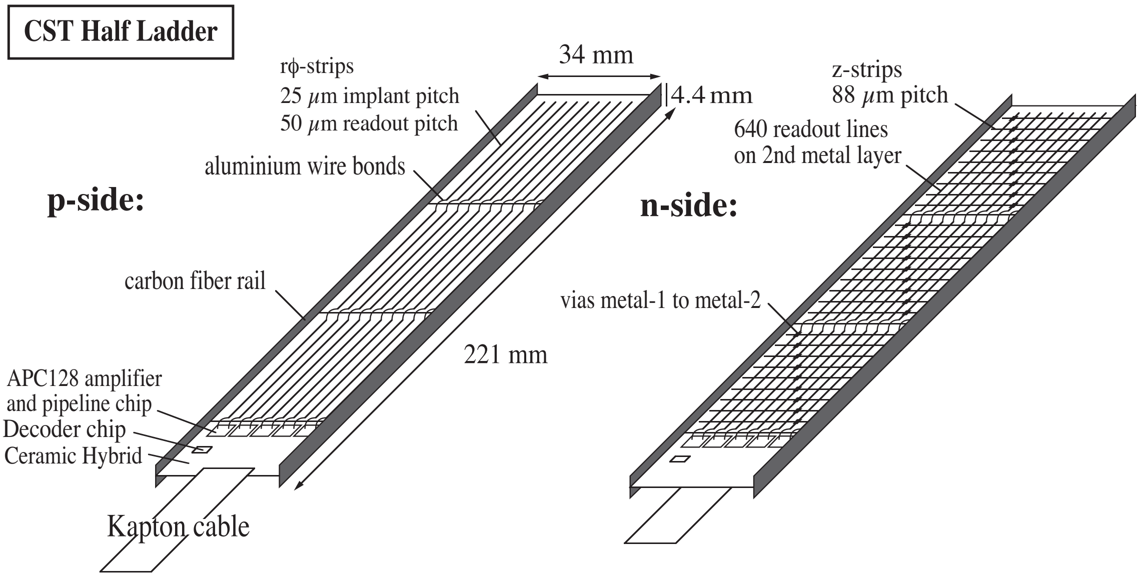

Figure 3.4: The p and n side of a CST half ladder.

Central Jet Chamber (CJC)

The *Central Jet Chamber* (CJC) is the main tracking device of the H1 detector, since the basic charged track identification and trajectory measurement relies on this detector. The CJC is divided into two parts: the inner (CJC1) and the outer jet chamber (CJC2). The inner chamber is located between the CIP and the COZ while the outer one is installed around the COZ. They cover an polar angle range of $10° < \theta < 170°$ between a radius of 20 cm and 85 cm. The CJC1 consists of 30 drift cells containing 24 sense wires, while the CJC2 has 60 drift cells with 32 sense wires. To be able to measure the curved tracks, the sense wires strung parallel to the beam axis are tilted by 30° in the radial direction. This makes sure that particles from the interaction vertex traverse more than one drift cell, which avoids drift ambiguities due to mirror track segments. In the $r\phi$ plane, a resolution of 130 μm is achieved. The resolution in z amounts to 22 mm and is larger than in $r\phi$, since the z position is determined by charge division.

Central Outer z Chamber (COZ)

The *Central Outer z Chamber* (COZ) complements the CJC info by providing a precise measurement of the z position. It has a resolution of 350 μm and covers the polar angle range $24° < \theta < 157°$. The COZ is located between the CJC1 and CJC2 as shown in figure 3.3 and has a cylindrical shape. It consists of 24 identical rings with a length of 9 cm in z direction ($L_{COZ} = 2.16$ m). Each of these rings is divided into 24 drift cells in ϕ and contains four sense wires and three pairs of potential wires strung perpendicular to the beam line.

3.2.2 Calorimetry

The H1 detector is equipped with two main calorimeters: the liquid argon calorimeter in the forward and central region and the spaghetti calorimeter, which covers the backward domain. Due to the fact that in photoproduction the incoming electron is scattered under a small angle escaping detection the calorimeters are used to detect the absence. Both calorimeters are used for the reconstruction of the hadronic final state. In addition, the liquid argon calorimeter is used for the identification of muons and electrons e.g. from semileptonic decays of heavy quarks. The following sections give a brief overview of the two calorimeters.

Liquid Argon Calorimeter (LAr)

The *Liquid Argon Calorimeter* (LAr) covers the forward and the central region between $4^\circ < \theta < 153^\circ$ of the H1 detector and is described in detail in [70]. The inner electromagnetic part (ECAL) uses lead absorbers while the outer hadronic section (HCAL) consists of steel absorbers. Both detector components use liquid argon as active material. Therefore the calorimeter is enclosed by a cryostat.

The LAr is divided into eight wheels along the z-axis and each of them is segmented into eight octants in ϕ, as illustrated in figure 3.5. To avoid long travel distances through a layer, the absorber and detector layers are oriented in such a way, that the impact angle of particles coming from the interaction point is larger than 45°. Therefore the detector and absorber layers are installed perpendicular to the beam axis in the forward region while the layers in the central region are parallel to the beam axis.

The response for hadronic showers is roughly 30% smaller than for electromagnetic ones. The LAr is a calorimeter of non compensating type. The compensation is obtained during the reconstruction, using software algorithms. Following [71] the energy resolution of the LAr calorimeter is

$$\frac{\sigma(E_e)}{E_e} \approx \frac{0.1}{\sqrt{E_e[\text{GeV}]}} \oplus 1\% \quad \text{for the ECAL and} \tag{3.1}$$

$$\frac{\sigma(E_\pi)}{E_\pi} \approx \frac{0.55}{\sqrt{E_\pi[\text{GeV}]}} \oplus 2\% \quad \text{for the HCAL.} \tag{3.2}$$

Spaghetti Calorimeter (SpaCal)

The *Spaghetti Calorimeter* (SpaCal) covers the backward region of the H1 detector between $153^\circ < \theta < 174.5^\circ$ and is described in detail in [72]. It is divided into an electromagnetic section and a hadronic part, while both use lead as absorber and scintillating fibres as detector material.

The electromagnetic part consists of 1150 quadratic lead absorber cells which have an active volume of $4 \times 4 \times 25$ cm^3 corresponding to approximately 27.5 radiation lengths X_0. These cells contain scintillating fibres which are pairwise arranged in submodules, where eight of them build a module. The fibres have a diameter of 0.5 mm and direct the light through

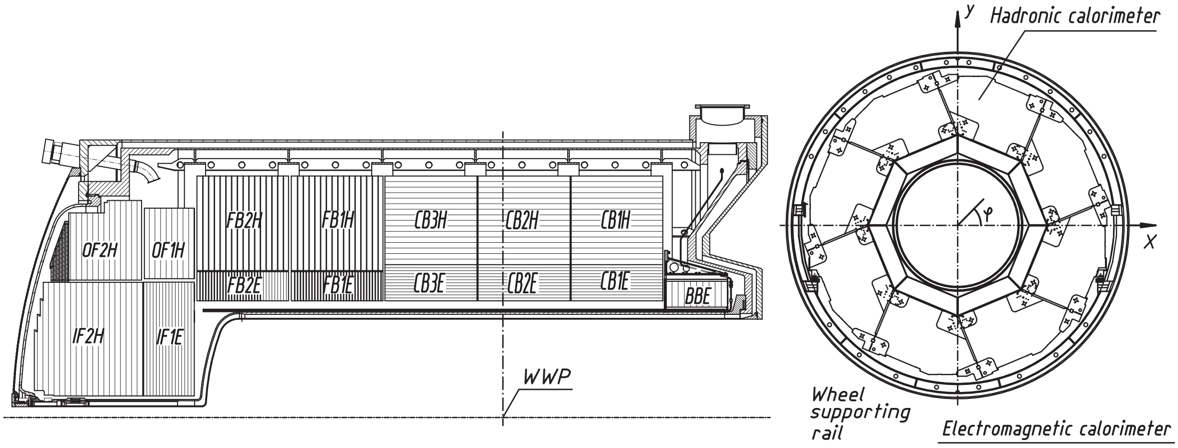

Figure 3.5: The left-hand side shows a lateral view of the upper half of the Liquid Argon calorimeter while on the right the cross section of a wheel in the barrel is illustrated.

light mixers to *Photomultiplier Tubes* (PMT).
The hadronic section is build similar to the electromagnetic part, but has nearly three times larger edge lengths. The cell depth corresponds to one interaction length and therefore almost all electrons are stopped in the electromagnetic part of the SpaCal. The hadronic part is mainly used as a veto against hadrons, which fake a scattered electron.

3.2.3 Muon System

The muon system of the H1 detector is divided into two parts, the *Central Muon Detector* (CMD) and the *Forward Muon Detector* (FMD). The FMD covers the polar angle range $3^\circ < \theta < 17^\circ$ and is not used in this analysis.
The CMD is embedded in the iron return yoke of the superconducting coil and is divided into 64 modules which are illustrated in figure 3.6. It consists of four subdetectors (see figure 3.6), the *Forward EndCap* (FEC), which covers the range $5^\circ < \theta < 35^\circ$, the forward and backward *Barrel* (BAR, $35^\circ < \theta < 130^\circ$), and the *Backward EndCap* (BEC), which is designed to detect muons in the range $130^\circ < \theta < 175^\circ$. The endcaps consist of an inner (modules 6-11) and outer part (modules 54-59). The modules are composed of ten iron layers, each with a thickness of 7 cm. There are nine gaps in between them, which are instrumented with limited streamer tubes, which are filled with a mixture of Argon and Isobutane (< 10%). They have a cross section of 9×9 mm^2 and their insides are coated by graphite to act as a cathode.
A double layer of streamer tubes is installed in the gap between the fourth and the fifth iron layer only. Additionally, three layers of streamer tubes are placed on both sides of the iron return yoke, the so-called 'muon boxes'. In total, the CMD has 16 layers.
Spatial resolution along the wire-axis is achieved through the outer two layers of the muon boxes and the double layer in the middle. They are read out via strip electrodes, installed perpendicular to the sense wires. The resolution of these layers is $\sigma_\perp \approx 4$ mm perpendicular

and $\sigma_{\|} \approx 12$ mm parallel to the sense wires. The measurement of the momentum is rather poor with only the CMD information and gains values of $dP/P \gg 30\%$ [73].

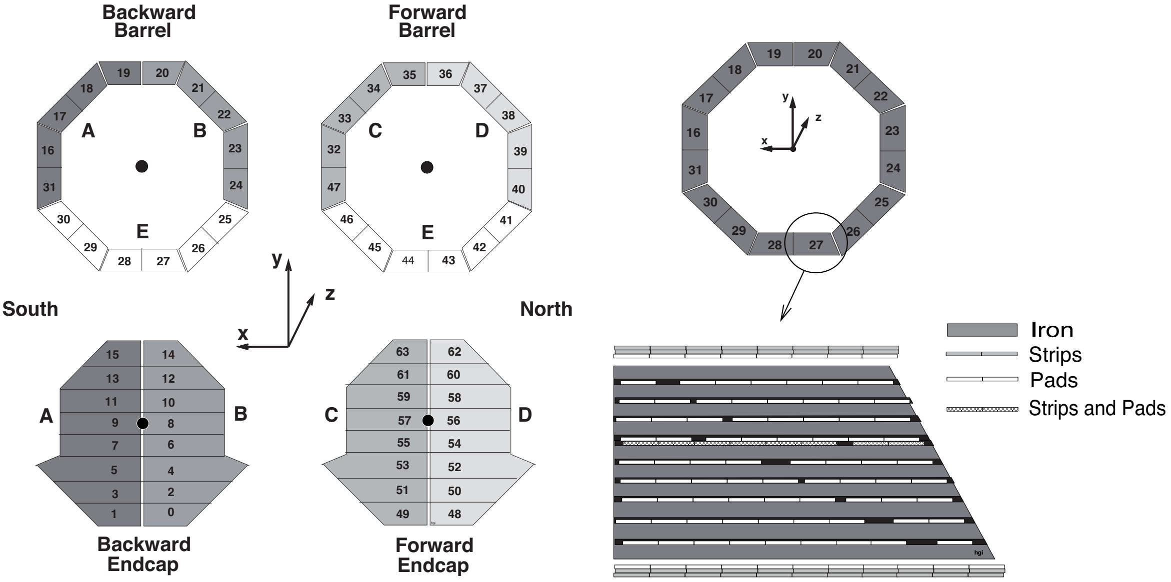

Figure 3.6: On the left an overview of the 64 modules of the central muon detector is illustrated. The right-hand side shows a module and its layers in more detail.

3.2.4 Triggering at H1

The H1 trigger system selects interesting physics events and rejects background events aiming for the smallest dead time possible. At a collision rate of 10.4 MHz, a recording of all events would be impossible as the detector can only be read out at a rate of 50 Hz. The rejected background events arise mainly from interactions of the proton beam with the beam pipe (beam wall) or residual gas as well as from beam halo and cosmic muons.

The four level trigger system was optimized to suppress background events efficiently with minimal dead time. Only the second and third trigger level produce dead time. The first trigger level does not induce dead time itself. The fourth trigger level operates as a filter, reducing the amount of data written to tape for the offline analyses.

In the following section, the four levels of the H1 trigger system are described briefly. Further information can be found for instance in [74]. The trigger elements of the required subtriggers used in this analysis are presented.

Level 1

The decision of the first trigger level (L1) is based on the information of several subdetectors of H1 and takes 2.3 μsec, which corresponds to 24 bunch crossings. The data coming from the subdetectors is written to pipelines and the data taking continues during the determination of the trigger decision. At this level no dead time is introduced. Upon a positive trigger decision, a signal is sent to stop the pipeline and to read out the current event. The readout of the data takes about 1 msec, leading to 5% dead time at 50 Hz.

The subdetectors provide 256 *Trigger Elements* (TEs) in total, which are combined to up to 192 *SubTriggers* (STs) in the *Central Trigger Logic* (CTL). The TEs are based on signals coming from the muon system as well as from the central tracker and energy depositions in the calorimeters.

To be able to control the accept rate of L1 and to optimize the usage of the available bandwidth some of the subtriggers are prescaled. A prescale factor of n means, that only every n-th positive decision is taken into account. Therefore, the prescaled subtriggers collect only a fraction of the luminosity. The presented analysis requires subtriggers which are prescaled with average prescale factors unequal, but close to one.

Level 2

The second trigger level (L2) analyses the information from the different subdetectors in more detail and its decision is available after 20 μsec. L2 is used to tighten the output rates of the L1 subtriggers from 1 kHz down to 50 Hz. Three trigger systems are implemented, namely the *Topological Trigger* (L2TT), the *Neural Network trigger* (L2NN), and the *Fast Track Trigger* (FTT). L2TT and the L2NN combine information coming from the trackers, calorimeters, and the muon system.

Level 3

The third trigger level (L3) started its operation at the beginning of 2006. It was planned from the early stages of H1 and before its activation, the information of L2 was directly delivered to L4. The third trigger level provides a partial event reconstruction based on the track information from level 2, the muon system and the calorimeter. The level 3 trigger provides 48 trigger elements to the central trigger logic, which verifies the TE conditions and rejects the event, if the condition is not fulfilled. It is kept though, if a subtrigger does not have any level 3 condition.

This trigger level must ensure a maximum output rate of 50 Hz.

Level 4

The fourth trigger level (L4) provides a full reconstruction of the triggered event after confirming the decisions of the former levels. For reducing the amount of written data to tape, background finders reject unwanted events like cosmic muons or residual gas or beam pipe events. 10% of these events are kept and used for monitoring the background finders. The events that remain, which are of physics interest, are categorized into classification bits, based on the presence of a hard scale, such as a high Q^2, high p_t track, high p_t jet or missing E_t. If the event fulfills one of the latter requirements or passes one of the final state finders, it is accepted without prescale. If this is not applicable, it is downscaled and receives a L4 event weight. The class of interest for this thesis is number 16, which stands for heavy flavour physics.

After full reconstruction on L4, the events are written to so-called *Physics Output Tapes* (POT) with a rate of roughly 20 Hz, which contain the full event information (150 kB/event). A fraction of information most relevant for analysis is written to *Data Summary Tapes* (DST), which is usually sufficient for physics analyses (20 kB/event).

Chapter 4

Event Reconstruction

The signal extraction of heavy quarks used in this thesis exploits the long lifetime and the large mass of hadrons containing heavy quarks. The lifetime is derived from the reconstructed impact parameter, while the mass is exploited using the relative transverse momentum of the selected muon candidate to the axis of the associated jet. This chapter presents the main aspects of the event reconstruction, which are applied to the objects entering these distributions.

In section 4.1, the reconstruction of muon candidates is described briefly. Sections 4.2 and 4.3 contain relevant aspects of the track reconstruction. The tracks are basically measured with the CJC and the measurement is improved using the CST information. In section 4.4, the tuning of the CST simulation is presented. This section also contains a discussion of the CST efficiency and contributions to the track resolution. The following sections concentrate on the reconstruction and calibration of hadronic final state objects and jets. In the last section of this chapter, the used trigger elements and their efficiencies are discussed.

4.1 Muon Identification and Reconstruction

Muons are identified in the H1 experiment by three subsystems: the tracking system, the LAr and the muon detectors. The main identification uses reconstructed tracks in the CMD. Muon tracks are classified by their quality $Q_\mu = Q_{iron} + Q_{cal}$, which is the sum of the quality determined in the CMD Q_{iron} and the quality of the track in the LAr calorimeter Q_{cal}. The determination of the single qualities is explained in the following.

In this analysis, the information of the instrumented iron is used to identify muon candidates. The information of the LAr is not used, but described here for completeness.

Only a few hadrons are able to reach the CMD and are wrongly identified as muons. Therefore, the purity of the muon identification in the muon detector is very high.

Muons in the Instrumented Iron

The energy losses of muons in the detector originate mainly from ionisation at here considered energies. The energy loss due to Bremsstrahlung is negligible, since the cross section for

H1 Iron Tracks
$\rho_0 < 100$ cm
$z_0 < 100$ cm
number of hit layers $\geqslant 3$
number of first hit layer $\leqslant 5$
number of last hit layer $\geqslant 2$
link probability $> 10^{-4}$

Table 4.1: Selection criteria for H1 Iron Tracks.

Bremsstrahlung is proportional to the inverse of the squared particle mass. Based on the fact, that the muon mass is roughly 200 times larger than the electron mass, Bremsstrahlung is heavily suppressed for muons with respect to electrons. According to the Bethe-Bloch equation, muons are minimal ionising at energies of about 300 MeV. To be able to reach the central muon system, the momentum of the muon has to be greater than 1.5 GeV. In the instrumented iron, muons lose roughly 90 MeV per iron plate. To allow the reconstruction of a track, the muon has to traverse several iron plates. Therefore, the energy of a muon has to be larger than 2 GeV to be detected in the instrumented iron with an efficiency larger than 50% [75].

The H1 reconstruction software `H1REC` performs a track fit over all hits in the CMD to identify muons in the instrumented iron. These tracks are also called outer tracks. They are required to link to an inner track, since the momentum and angle resolution of tracks reconstructed in the instrumented iron is not sufficient for this analysis. Inner tracks are reconstructed using the central and forward tracking system. The linking between inner and outer tracks is performed by `H1REC`. Here, only outer tracks are used, which fulfil certain quality criteria listed in table 4.1. The outer tracks are required to have hits in at least three out of 16 layers of the muon system. The first hit should appear within the first five layers, while the last hit is required to be at least in the second layer. The distance of closest approach *dca* of the outer track to the event vertex has to be smaller than one meter in cylindrical coordinates (ρ_0, z_0). Inner tracks, which match outer tracks in the polar and azimuthal angle are selected. These selected inner tracks are extrapolated into the muon system. Multiple scattering and energy losses due to ionisation are taken into account assuming that the inner track is a muon. After the linking procedure is done, the compatibility of each track pair is performed. For this purpose a χ^2 value is calculated, which depends on the track momenta, their polar and azimuthal angles and the derivatives of both angles. The integral of χ^2 gives the linking probability $P^{\mu}_{link}(\chi^2)$, which needs to be larger than $P^{\mu}_{link}(\chi^2) > 0.1$ for iron muon candidates in this analysis.

A quality of $Q_{iron} = 10$ is assigned to a muon candidate in the CMD, if it fulfils all cuts listed in table 4.1.

Muons in the LAr

Electrons generate electromagnetic showers and are absorbed in the first layers of the liquid argon calorimeter. Hadrons produce showers containing an electromagnetic and a hadronic

component and are stopped as well in the LAr. Whereas muons are *Minimal Ionising Particles* (MIPs), which have an average energy loss of about $dE/dx \approx 10$ MeV/cm in lead. They can be identified in the LAr via their uniform energy deposition within a narrow cone, since they do not produce showers. The high granularity of the LAr with roughly 45.000 cells makes it possible to use this signature for muon identification. To be able to reach the LAr, the muon tracks need a minimal transverse momentum of 800 MeV.
The algorithm `KALEP` [76], [77], which is performed in the H1 event reconstruction, searches for the above described signature of MIPs in the LAr calorimeter. Four discriminators are determined, which are based on the summed energy of the calorimeter cells and on the topology of the responding cells. These four discriminators are used to define the quality of each muon track.

Muon Reconstruction Efficiency

Extensive studies of the efficiency to reconstruct muons in the LAr and in the instrumented iron were performed in [78] and in [75]. The investigations in [78] are for low p_t measurements and [75] investigates higher p_t regions. In this analysis, a muon candidate in the instrumented iron with a transverse momentum of at least $p_t^\mu > 2.5$ GeV is required, which corresponds to the higher p_t region. Therefore, the results of [75] are used. It is found, that the reconstruction efficiency of muon candidates in the instrumented iron are well described by the Monte Carlo simulation (solid line) above $p_t^\mu > 2.5$ GeV as depicted in figure 4.1. On the left hand side the efficiency to find a muon in the instrumented iron with a transverse momentum larger than $p_t^\mu > 2.5$ GeV as a function of the polar angle θ is shown. The efficiency gains values around roughly 80%. In figure 4.1 (b) the ratio of the data efficiency over the simulation efficiency is plotted. Both figures are taken from [75]. Based on these studies, no correction factors for the simulation in this thesis are applied.

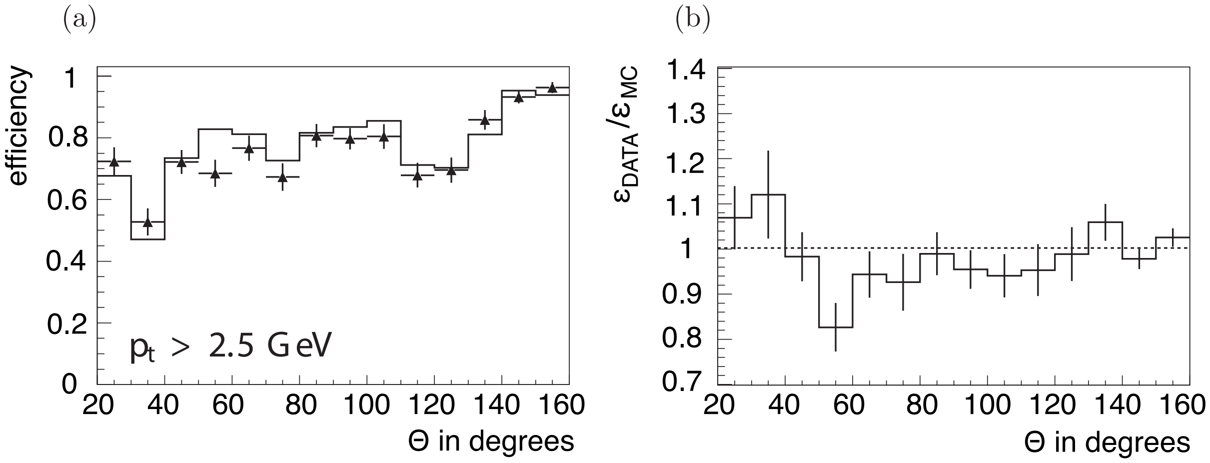

Figure 4.1: Efficiency to identify muon candidates in the instrumented iron for $p_t^\mu > 2.5$ GeV as a function of the polar angle θ. Both figures are taken from [75].

4.2 Impact Parameter

Events containing heavy quarks show an experimental signature, which can be used to distinguish them from events containing only light quarks. As described in section 2.10, beauty and charm flavoured hadrons have lifetimes of the order $\mathcal{O}(1 \text{ psec})$, which lead to a resolvable distance between tracks originating from the decay and the primary vertex. The decay process and the corresponding variables are shown in figure 4.3 in the $r\phi$-plane. A heavy hadron is produced at the primary vertex which lies inside the beam spot. The long lifetime entails a travel of usually a few hundred micrometers in the lab frame for the hadron (cf. table 2.3). The decay of the hadron into charged particles produces a decay vertex, which is also called the secondary vertex. The travelling distance between the primary and the secondary vertex is referred to as the decay length. In the $r\phi$-plane, the displacement of the track can be quantified via the so-called *impact parameter* δ, which denotes the closest distance between the particle's trajectory and the primary vertex. To approximate the flight direction of the hadron, a jet-based reference axis is used. A sign for the impact parameter is introduced, which takes the jet containing the muon as a reference. If the angle β between the axis of the associated jet and the line, joining the primary vertex to the point of closest approach of the track, is less than 90°, then the sign is positive. If β is larger than 90°, it is negative. A schematic illustration of the sign convention is shown in figure 4.2.
The width of the impact parameter distribution reflects the finite track and vertex reconstruction resolutions. Events without lifetime information have a reconstructed spectrum of δ which is symmetric around zero, while events with decays of long-lived particles are expected to have an asymmetric distribution with an excess at positive impact parameters. The region of large positive impact parameters is expected to be dominated by muons from decays of beauty flavoured hadrons.

4.3 Track Reconstruction

The track reconstruction is based on information from the central tracking detectors. The goal is the reconstruction of the trajectory and the determination of five track parameters κ, ϕ_0, θ, dca, z_0 at the vertex. This is achieved by performing a fit to the measured hits

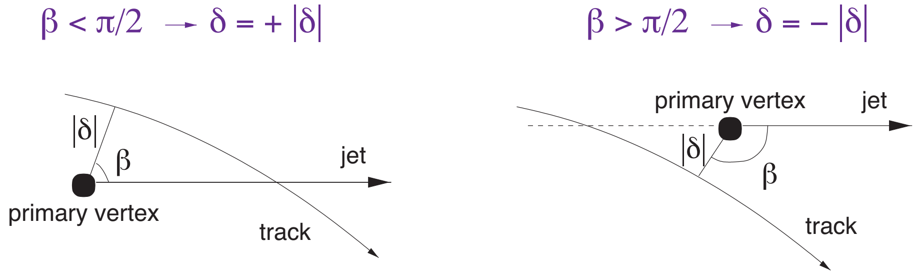

Figure 4.2: Sign convention of the impact parameter δ with respect to the angle β.

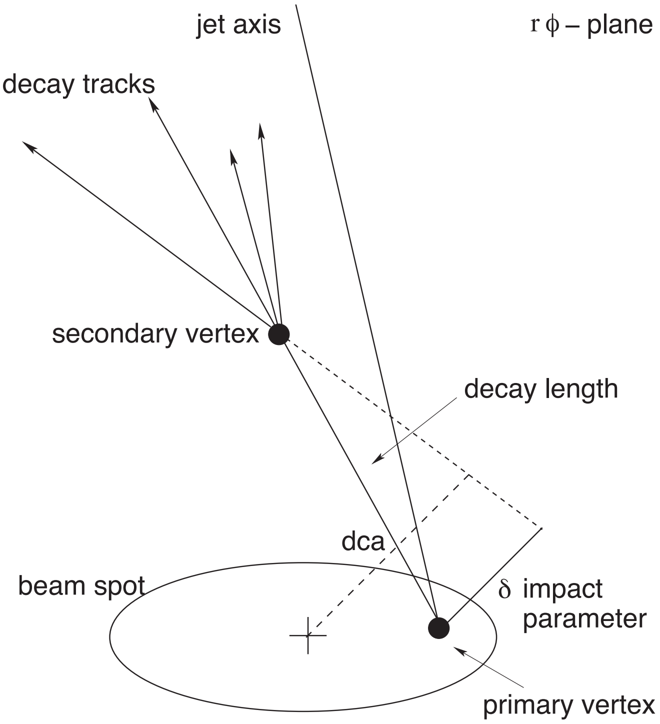

Figure 4.3: Schematic view of the impact parameter in the $r\phi$ plane.

in the CJC. The uniform magnetic field parallel to the z-axis bends the tracks of charged particles in the $r\phi$-plane. Due to the Lorentz force the bending radius is proportional to the strength of the magnetic field and inverse proportional to the transverse momentum of the charged particle. The flight trajectory can be described by a helix. It can be parameterized in H1 coordinates as a function of the arclength s:

$$x(s) = dca - \frac{1}{\kappa}\sin(\phi_0) + \frac{1}{\kappa}\sin(\phi_0 + \kappa s), \tag{4.1}$$

$$y(s) = -(dca - \frac{1}{\kappa}\cos(\phi_0) - \frac{1}{\kappa}\cos(\phi_0 + \kappa s)), \quad s \geq 0 \tag{4.2}$$

$$z(s) = z_0 + s\cot(\theta). \tag{4.3}$$

The azimuthal angle ϕ_0 describes the flight direction of the particle in the transverse plane with respect to the positive x-axis as depicted in figure 4.4. It is measured at the point of closest approach to the z-axis, which is defined as starting point of the helix ($s = 0$). In the zs plane the track trajectory is a straight line which crosses the z-axis at the point z_0. The angle θ between the trajectory and the z-axis describes the flight direction with respect to the positive z-axis. The curvature κ is the inverse of the bending radius r and has a positive sign for negative charged particles and vice versa. The distance of closest approach *dca* stands for the minimal radial distance of the track to the origin $(0, 0)$ in the $r\phi$-plane. If the origin lies

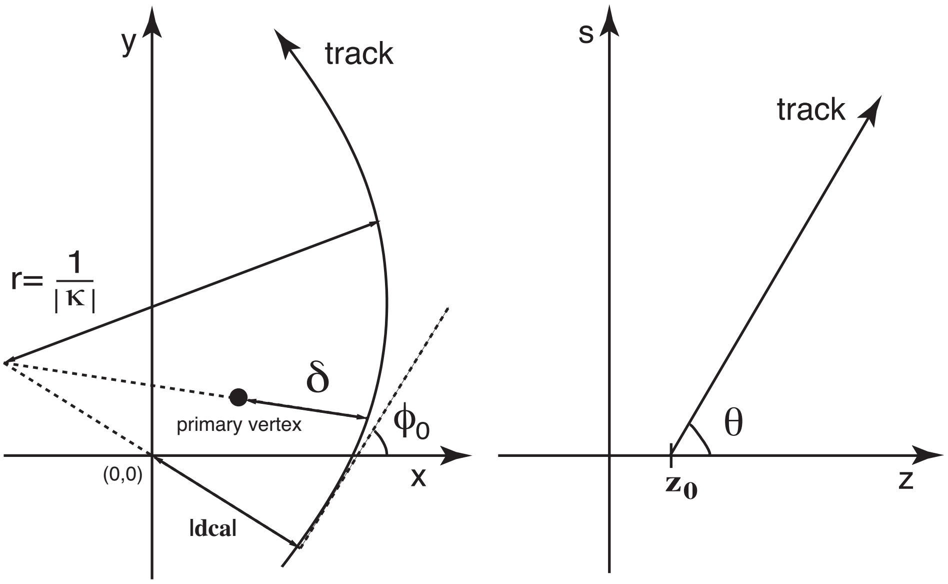

Figure 4.4: The track parameters κ, ϕ_0, θ, *dca* and z_0 in the $r\phi$- and zs-plane.

inside the circle, which describes the track, the signs of *dca* and κ are equal. If the origin lies outside, the sign of *dca* is chosen opposite to the one of κ.

4.3.1 CST improved Tracks

The momentum resolution and the precision of the track trajectories measured by the CJC is improved by adding the CST information. The CJC tracks are associated (linking) to CST hits and the determination of the improved track parameters is done via a CJC-CST combined track fit. This renders possible to resolve primary and secondary vertices of long lived heavy hadrons, which is crucial for this analysis.
The selection of the tracks required in this analysis is discussed in chapter 5.

The Track Fit

The linking of CST hits and non-vertex fitted CJC tracks is done in the $r\phi$- and zs-plane separately using the H1 software `CSTLIN` [79]. This permits to use p-side ($r\phi$) information only to obtain improved $r\phi$ track parameters of the CST improved tracks.
The track fit is divided into two steps: first, a circle fit in the $r\phi$-plane is performed which determines κ, *dca* and ϕ_0. Second, a straight line fit is done in the zs-plane to determine θ and z_0. The input for the circle fit are the track parameters of the non-vertex fitted CJC tracks, which are stored in the BOS bank `DTNV`. Further input are selected CST hits. For each CJC track and all possible suitable combinations of p-side hits from both CST layers, the circle track fit is applied. This circle fit minimizes a χ^2 function [79] depending on the $r\phi$ track

parameters obtained by the CJC and their covariance matrix. Furthermore, the distance of the track circle and the CST hits in the inner and outer layer as well as the corresponding error of the distance are included. The CST hit combination and corresponding track fit is chosen, which gives the smallest χ^2 of the track fit. Solutions with a maximum number of CST hits are preferred as long as they have a reasonable χ^2.

4.3.2 Primary Vertex Reconstruction

The usage of the impact parameter requires a precise knowledge of the *Primary Vertex* (PV) position in the plane transverse to the beam axis. For each run, the average coordinates x_{beam} and y_{beam} of the ep interaction point (*beam spot*) are defined by using the information of many events contained in the run. The *Run Vertex* (RV) is obtained by a least-squares fit. This fit minimizes the overall distance of closest approach of tracks to the run vertex. It uses only well-measured non-vertex fitted CST improved tracks with high transverse momenta. This run vertex is used as starting point for an event-wise primary vertex fit to selected tracks. The primary event vertex fit is performed by the H1 software `CSPRIM` [80] within two steps. At first, the determination of the vertex position in the xy plane is done. As second step, the z coordinate is reconstructed from selected tracks which are matched to the xy vertex position.

In this analysis, the fit of the primary event vertex is performed after excluding the selected muon track candidate, which comes from the secondary vertex. This fit is based on CST improved non-vertex fitted tracks. Only tracks are used, which are compatible with the run vertex with two standard deviations.

4.4 Tuning of the CST Simulation

In this section, the tuning of the CST Monte Carlo simulation is described [81]. The CST itself is presented in section 3.2.1. The Monte Carlo simulation of the CST should provide a description of all relevant aspects of the data, such as efficiency, resolution, multiplicity and distribution of dead channels. The simulation should also provide a reasonable description of the noise present in data. For this task, the occupancy and the noise amplitude in the simulation are adjusted to the data.

Tuning of the Signal to Noise Ratio

There are two kind of hits: hits which are linked to a good track get named signal hits, and those which could not be linked are called background or noise hits. The significance or signal to noise ratio for signal and noise hits before the tuning shows a discrepancy between data and Monte Carlo simulation as can be seen in figure 4.5 (a). The data used here, was collected at the beginning of 2006 by the H1 detector. For getting a better agreement of data and Monte Carlo simulation the significance distribution is fitted for both hit types. For the background, a sum of two exponentials is used. For the signal hits, a Landau distribution is added to the background function. After fitting the data, the parameters of these fits are used to convert the significances of the simulation. This is done separately for each of the

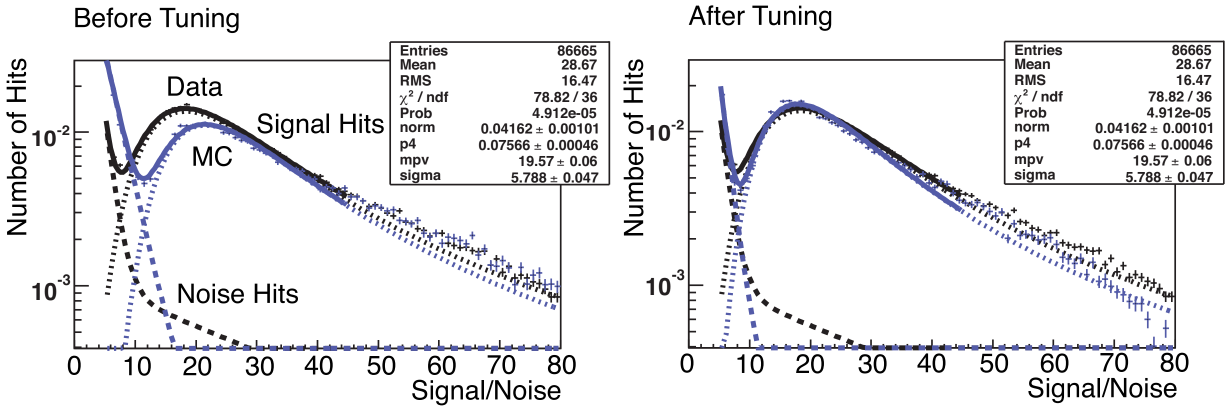
(a) (b)

Figure 4.5: Signal to noise ratio of both hit types on one half ladder side for 2006 data (dotted black line) and Monte Carlo simulation (dotted blue line) in comparison. Figure (a) shows the Monte Carlo simulation before the tuning and in (b) the tuning result is illustrated. The solid lines represent the used fit functions. The same tuning procedure was performed for all 64 half ladders separately.

64 half ladders, because their distributions are significantly different. After this adjustment, the Monte Carlo simulation describes the data much better than before as shown in figure 4.5 (b).

Description of Dead Channels

Each of the 64 half ladders has an individual number of dead channels. To check which of the 640 channels of each half ladder do not work properly or are dead, the so-called center of

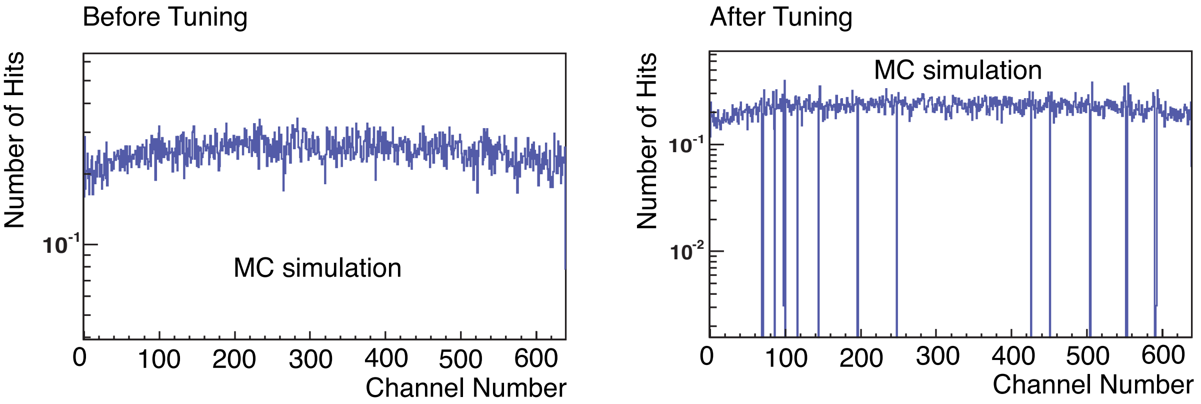
(a) (b)

Figure 4.6: Distribution of the center of gravity of hits in units of strip numbers of one half ladder side in the Monte Carlo simulation. Figure (a) shows the center of gravity for one half ladder before the tuning. No dead channels can be seen in that plot while (b) depicts the result of adding dead channels.

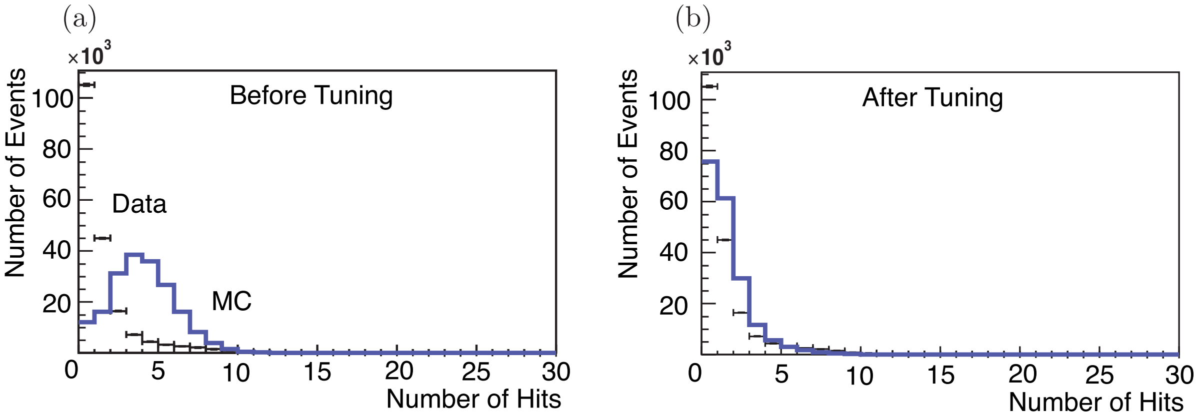

Figure 4.7: Occupancy of one half ladder side for 2006 data (points) and Monte Carlo simulation (solid line) in comparison. Figure (a) shows a very high occupancy for the untuned simulation while in (b) a good description of the data can be seen. Again, this plot is done for one of the 64 half ladders.

gravity of a cluster for the signal hits is studied. Before tuning, the simulation did not have any dead channels at all. Strips with more than 50% deviation of signal hits, compared to the average occupancy of the respective half ladder, are marked as dead in the Monte Carlo simulation. The result is exemplarily shown for one of the 64 half ladders in figure 4.6 for the Monte Carlo simulation. The data is not shown here.

Adjustment of the Occupancy

For a better description of the electronic background, an adjustment of the occupancy is necessary. The occupancy is defined as the number of noise hits per half ladder per event. In the simulation, the occupancy is too high before tuning, which can be seen in figure 4.7. The noise amplitude is rescaled using the parameters stored in the bank `CSNP`, which stands for *CST Noise Parameter*. In this bank, all parameters contributing to the noise amplitude are stored. This rescaling in the significance distribution leads to a very good agreement with the data.

CST Efficiency

After the tuning procedure, a satisfactory description of the efficiency is obtained. The total CST track finding efficiency includes the CST hit efficiency, the CJC-CST linking efficiency and losses due to inactive parts of the CST. The total CST efficiency is defined as the fraction of tracks measured by the CST with $P_{link}^{CST} > 0.1$ and $N_{CST}^{hits} \geqslant 1$ over all CJC tracks. The linking probability and the number of CST hits are plotted in figure 4.12. Both variables plotted with the data (points) are reasonably described by the simulation (solid line).
These efficiency studies are done using the final selection cuts as listed in table 5.3. The average CST track finding efficiency amounts to roughly 70%. The total CST efficiency is plotted as a function of the transverse momentum of the muon track in figure 4.8 (a) and

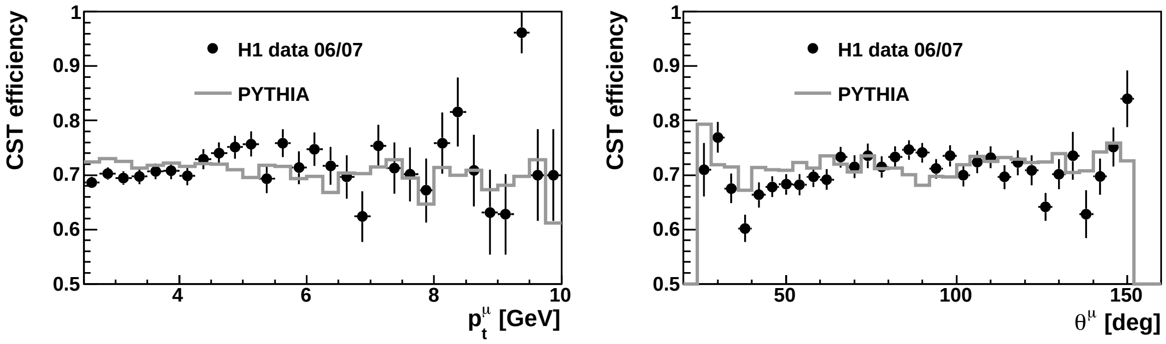
(a) (b)

Figure 4.8: The total CST track finding efficiency as a function of p_t^μ (a) and θ^μ (b). The selected muon tracks are required to have at least 1 CST hit and a CJC-CST linking probability of at least 10%.

in its polar angle in figure 4.8 (b). The Monte Carlo simulation (solid line) describes the data (points) reasonably well in both cases. To take the remaining uncertainty of the Monte Carlo description into account, an systematic error of 3% is estimated for the total track finding efficiency. Before tuning, the efficiency of the Monte Carlo simulation was about 10% higher than in the data. The improvement is mainly due to the above described corrections of the signal to noise ratio in the simulation. The efficiency is almost independent of the two variables shown here and the distributions are almost flat.

The CST efficiency per half ladder is illustrated in figure 4.9 for data (a) and the simulation (b). The data is modelled reasonably well by the simulation, since the above described tuning is done for each half ladder separately. Both distributions are almost flat and show an efficiency of roughly 70%. The Monte Carlo simulation tend to be slightly higher than the data.

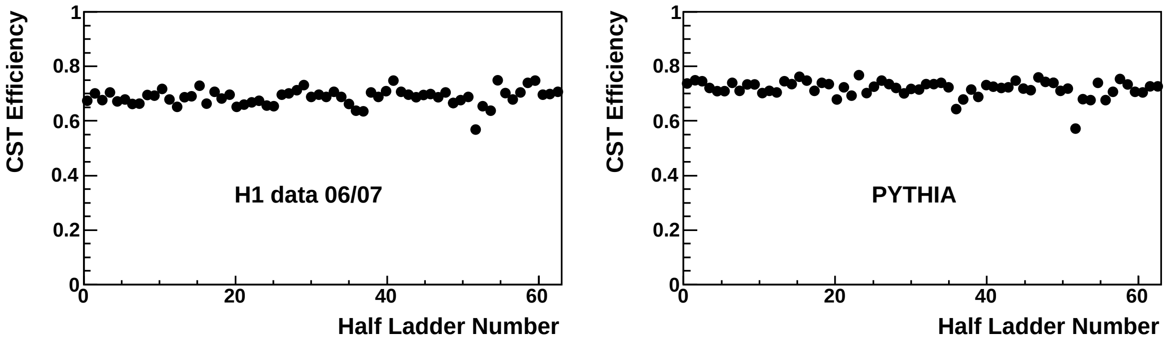
(a) (b)

Figure 4.9: The total CST track finding efficiency as a function of the half ladder number for data (a) and Monte Carlo simulation (b). The selected muon tracks are required to have at least 1 CST hit and a CJC-CST linking probability of at least 10%.

4.4.1 Resolutions

In this analysis, the resolution of the impact parameter plays an important role. It has to be small enough, to be able to distinguish between tracks coming from long lived hadrons and tracks of the zero lifetime combinatorial background. In addition, a small systematic error is desirable, which is only possible if the impact parameter resolution is well described.
In figure 4.10, the various contributions to the impact parameter are illustrated schematically. The intrinsic resolution of the CST for tracks with two hits amounts to 20 μm. This resolution is due to uncertainties on the internal alignment of the CST with respect to other detector components. Multiple scattering effects depend on the transverse momentum of the track and originate from the beam pipe and the first layer of the CST. The contribution is measured to be $\approx 70\ \mu\text{m}/p_t[\text{GeV}]$. Requiring one hit in the CST leads to a slightly worse resolution. If the hit is in the outer layer, the resolution becomes a factor of two worse [83], [84].

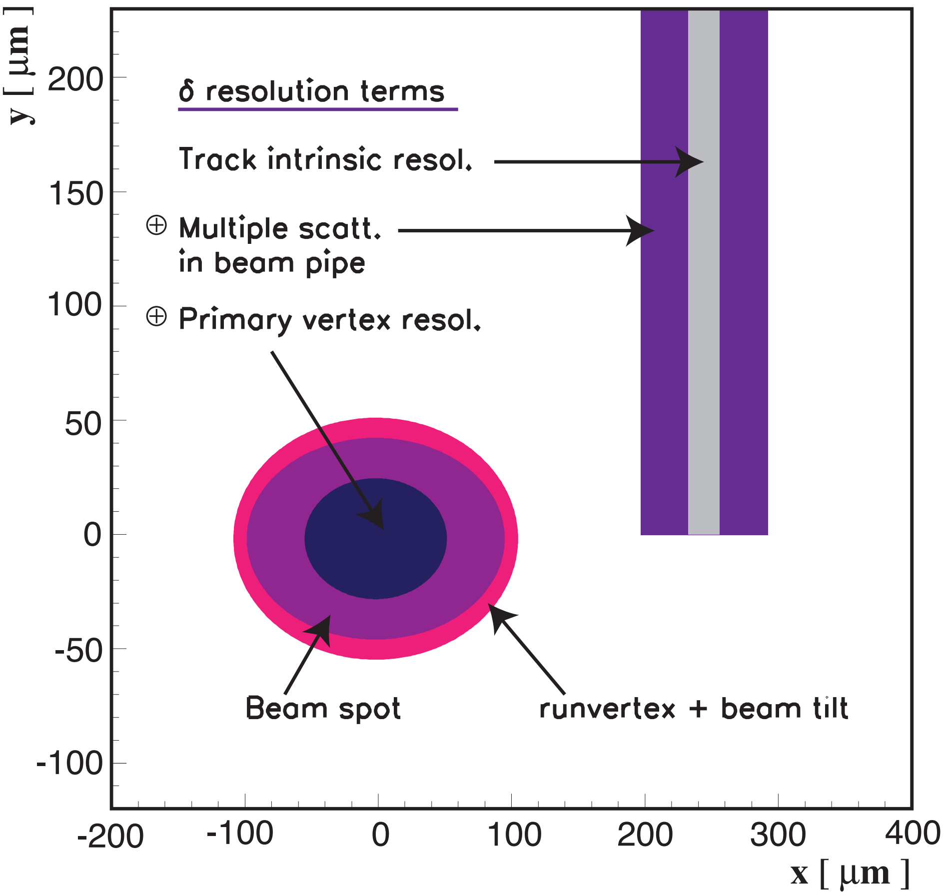

Figure 4.10: Schematic view of the contributions to the impact parameter resolution. Made by PD Dr. Olaf Behnke [82] and slightly modified to illustrate the HERA II conditions.

Contributions from the primary vertex fit depend on the reference point of the impact parameter measurement. To disentangle these contributions, the resolution is studied separately for the run vertex and the primary event vertex as reference for the impact parameter.

Primary Vertex Resolution

The beam position is precisely known [83] and amounts to

$$\begin{aligned} 2006\ e^{-}: &\quad \sigma_x = 80\ \mu\text{m} \quad \text{and} \quad \sigma_y = 20\ \mu\text{m} \\ 2006/2007\ e^{+}: &\quad \sigma_x = 92\ \mu\text{m} \quad \text{and} \quad \sigma_y = 23\ \mu\text{m} \end{aligned} \tag{4.4}$$

in x and y for the two different run periods, respectively. The maximal size of the primary event vertex errors is given by the size of the elliptical beam spot. In figure 4.11 (a) and (b) the calculated errors on the radial position of the primary event vertex are depicted. The uncertainties on x_{PV} and y_{PV} are dominated by the beam extensions due to small errors on the run vertex parameters, which were obtained with high statistics when averaging over many events. A comprehensive overview of the vertex determination and event reconstruction with the CST is for example given in [69]. The distribution of $\sigma(x_{PV})$ gains values up to

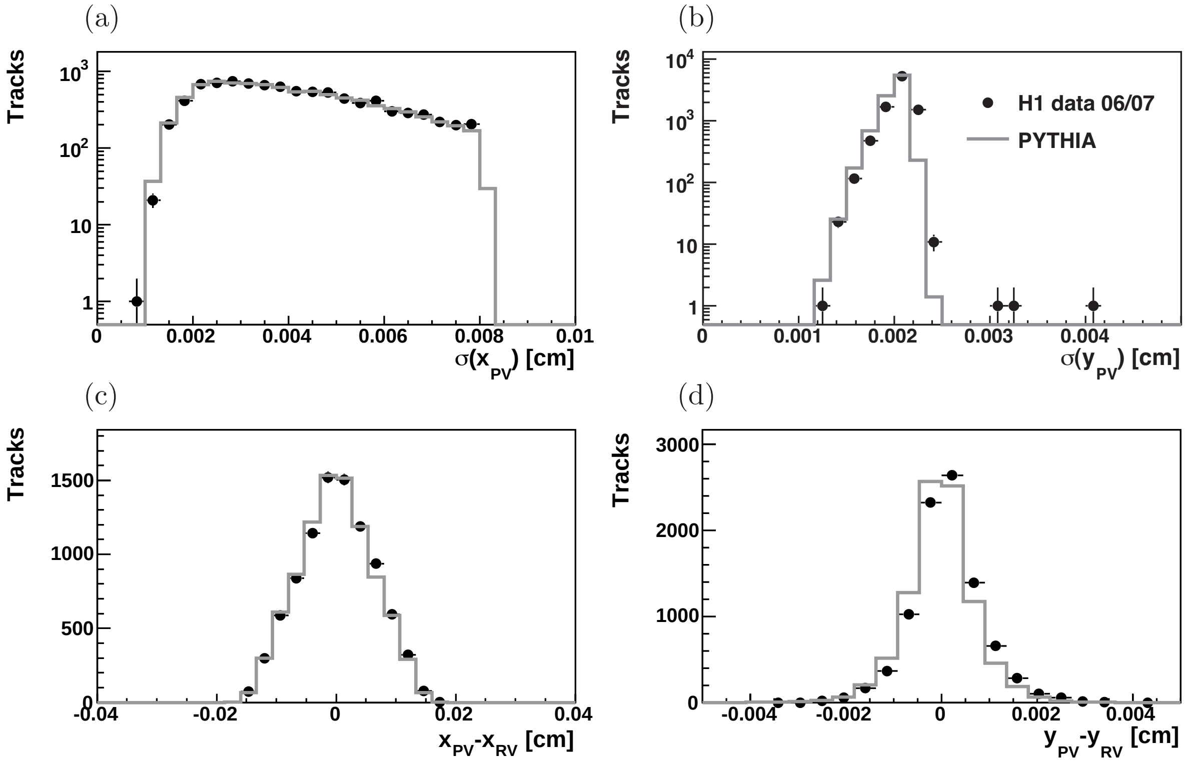

Figure 4.11: Calculated errors on the primary vertex position in x (a) and y (b), respectively. In figure (c) and (d) the difference of the reconstructed primary vertex and the run vertex are plotted. Shown are the data (points) and the PYTHIA prediction (solid line) in comparison.

~ 80 μm, which reflects approximately the width of the beam spot in x. The primary event vertex error in x of the data (points) is well modelled by the PYTHIA prediction (line). Figure 4.11 (b) shows the event vertex error in y. The small beam spot size in y can hardly be resolved. The agreement between data and the PYTHIA simulation is reasonable.
In figure 4.11 (c) and (d), the difference of the reconstructed primary vertex and the run vertex is depicted. While the projection in x shows a well agreement between data and the Monte Carlo simulation, it is described reasonably in y. The distributions have a RMS of 61 μm in x and of 7 μm in y. These values have to be compared to the beam spot size.
Both distributions of the data in y, figures 4.11 (b) and (d), are not described perfectly, yet still reasonably, by the Monte Carlo simulation. This ows to a non perfect simulation of the beam tilt in the Monte Carlo. The beam tilt contributes to the error of the run vertex and is therefore also migrated to the calculation of the primary event vertex error. The beam tilt in y is larger than in x and has therefore a higher impact on the calculated errors in y. The beam spot size in y is already very small and the same holds for the calculated primary event vertex error. Thus the non perfect description of the data in y by the simulation has a negligible effect.

Track Resolution

The track resolution can be investigated using the linking probability P_{link}^{CST} of CJC tracks and CST hits. This quantity measures the accuracy of the covariance matrix of the track parameters directly. The linking probability is defined as

$$P_{link}^{CST}(\chi^2, N) = \frac{1}{\sqrt{2^N}\Gamma(N/2)} \int_{\chi^2}^{\infty} e^{-0.5t} t^{-0.5N-1} dt. \tag{4.5}$$

Here χ^2 is taken from the combined fit of CJC tracks and CST hits in the $r\phi$ plane. The variable N is the number of degrees of freedom, which stands for the number of linked CST hits. The linking probability P_{link}^{CST} is the probability of having a larger χ^2 value as obtained by the minimization algorithm. The distribution of P_{link}^{CST} should be flat between 0 and 1 if a good description of the track resolution is given.
Extensive investigations concerning the understanding of the track linking probability were performed in [82]. The covariance matrix of the CST track parameters consists of two parts: the intrinsic part and contributions from multiple scattering. Both parts are corrected to achieve a good agreement between data and Monte Carlo simulation. For the intrinsic part correction factors of $f_{r\phi} = 1.35$ and $f_{rz} = 1.0$ are obtained from the data for the $r\phi$ plane and the rz plane, respectively. The Monte Carlo is then smeared by help of these parameters, since the track resolution in the Monte Carlo was too optimistic before tuning.
Additionally a correction factor $f_{MS} = 1.22$ for the multiple scattering is determined in [82] for tracks with a transverse momentum of $p_t > 0.3$ GeV. Following [49], this factor is chosen to be $f_{MS} = 1.09$ to avoid an overestimation. Since the transverse momentum of the muon track in this analysis is $p_t > 2.5$ GeV, multiple scattering effects are negligible for the track resolution. The choice of these three parameters is proper, as the linking probability is well modelled by the PYTHIA prediction as depicted in figure 4.12 (b). Here, all analysis

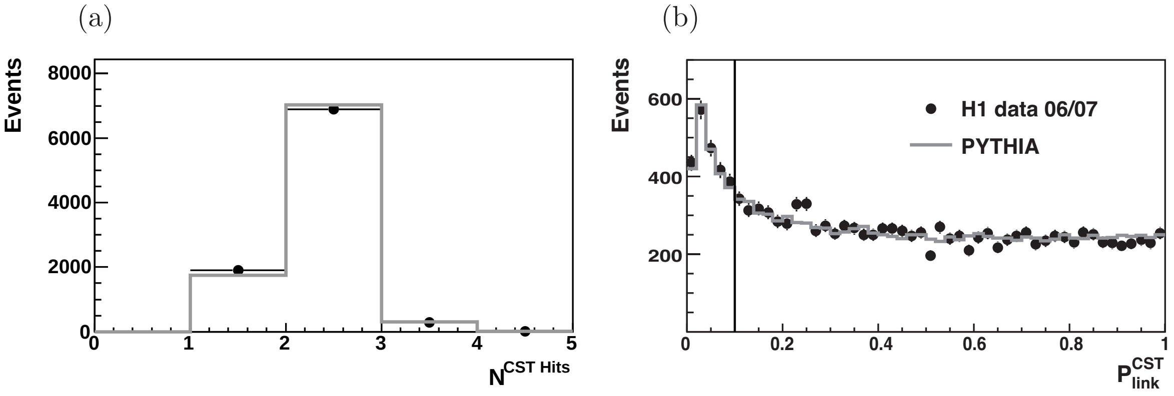

Figure 4.12: The number of CST hits (a) in the analysed sample and the CJC-CST linking probability (b) in the $r\phi$ plane. The vertical line in (b) represents the cut at 10%. Data (points) and the PYTHIA prediction (line) in comparison.

cuts are applied (table 5.3), besides the cut on the linking probability itself to show the full distribution. The analysis cut is located at $P_{link}^{CST} > 0.1$ and represented by the vertical line in figure (b). The number of CST hits in figure 4.12 (a) shows a good agreement for the data and the PYTHIA prediction. For this distribution, all analysis cuts are applied (table 5.3) including the cut on the linking probability.

Impact Parameter Resolution

The resolution of the impact parameter consists of contributions from the track resolution, the beam spot and the primary vertex resolution. In order to separate contributions from the primary vertex fit, the run vertex and the primary event vertex are used as reference in the impact parameter definition separately. Due to technical reasons, the analysed data and Monte Carlo samples for these studies contain identified muons.

The impact parameter with respect to the run vertex is studied first. For tracks with a transverse momentum of minimum 2.5 GeV and at least one CST hit, the Gaussian width of the impact parameter distribution dca_{RV} as a function of the azimuthal angle ϕ of the track is plotted in figure 4.13 (a). The distribution represents the measured impact parameter resolution of the data (full points) in comparison to the Monte Carlo simulation (open points). The resolution values are between $\approx 90 - 120$ μm, depending on the track direction in ϕ.

Replacing the run vertex with the primary event vertex in the impact parameter definition, the ϕ dependence is decreased. This is illustrated in figure 4.13 (b). Here, the gaussian widths of the impact parameter, with respect to the primary event vertex as a function of the azimuthal angle ϕ, is shown. The distribution is almost flat and dominated by the track resolution, which is also flat. A mean resolution of ≈ 80 μm is achieved in both, data and Monte Carlo simulation.

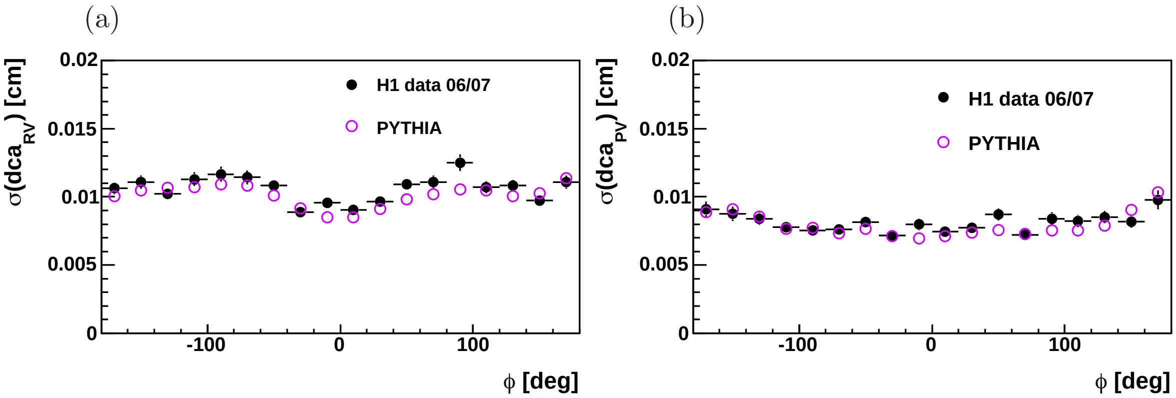

Figure 4.13: The gaussian width of the impact parameter with respect to the run vertex dca_{RV} in (a) and with respect to the primary event vertex dca_{PV} in (b) as a function of the azimuthal angle ϕ of the track. The Data (full points) and the Monte Carlo simulation (open points) are shown in comparison.

4.5 Reconstruction of the Hadronic Final State

In this section, the reconstruction of the *Hadronic Final State* (HFS) is described briefly. The reconstruction is performed by the Hadroo2 [85] algorithm. The information of the track measurement and the calorimeter is used as the input of the algorithm to reconstruct the kinematics of the particles forming the hadronic final state.

The Hadroo2 algorithm creates HFS particles, combining the information coming from the tracks and clusters. Both information are matched and a double counting of energies is avoided. Their relative resolutions are compared to decide, whether tracks or clusters are taken for the construction of HFS objects, for keeping the best measurement. The exact precision of the calorimeter is unknown due to possible contributions of neutral particles. Thus the average relative error $\sigma_{E\ LAr}^{expectation}$ expected for the calorimeter measurement is estimated as

$$\left(\frac{\sigma_E}{E}\right)_{LAr}^{expectation} = \frac{\sigma_{E\ LAr}^{expectation}}{E_{track}} = \frac{0.5}{\sqrt{E_{track}}}. \tag{4.6}$$

The track measurement is favoured for the creation of the HFS particle if the comparison

$$\left(\frac{\sigma_E}{E}\right)_{track} < \left(\frac{\sigma_E}{E}\right)_{LAr}^{expectation} \tag{4.7}$$

is true or if the track energy is below the cluster energy

$$E_{track} < E_{cylinder} - 1.96 \cdot \sigma_E^{cylinder}. \tag{4.8}$$

Here $E_{cylinder}$ and $\sigma_E^{cylinder} = 0.5\sqrt{E_{track}}$ denote the electromagnetic (hadronic) energy of the clusters and its error within a cylinder of 25 cm (50 cm) around the extrapolated track. The energy within this cylinder is removed up to the track energy to avoid double counting. Possible fluctuations of both measurements are taken into account and potentially remaining cluster energy due to neutral particles or from another track is extrapolated in the same region of the calorimeter [85].
If (4.7) turns out to be false and the track energy E_{track} is within 2σ of $E_{cylinder}$, both track and cluster measurement are considered to be compatible. In that case, the calorimetric measurement is used to reconstruct the HFS particle candidate.
After treatment of all tracks, the remaining clusters are considered to be massless. They originate from neutral hadrons with no corresponding track, or from charged particles with a badly measured track.
The track measurement gives better results up to 12 GeV for forward tracks, 25 GeV for central tracks and about 13 GeV for combined ones. If the energy deposited in the central region is above 25 GeV, the calorimetric measurement is better.

4.6 Jet Reconstruction

Measuring directly the final state quarks and gluons coming out of the hard interaction would be the best way to analyse photoproduction events. But, due to the fact that these partons carry colour, it is not possible, since they produce parton showers and finally recombine to colour singlet states - the colourless hadrons. They are the measurable final state particles, collimated around the direction of the originating parton. These groups of hadrons are called jets. Jets are measured by the detector and reconstructed with the objective of achieving direction and energy of the original partons.

Jet Finding Algorithm

Clustering algorithms define jets by merging particles together to so-called 'pseudoparticles' in an iterative procedure. These pseudoparticles are the constituents of the final jet and are assigned to the jet in an unambiguous way. Clustering algorithms are mainly used for e^+e^- experiments. They are both collinear and infrared safe.

Recombination Schemes

Recombination schemes are procedures to determine the momentum four vector of the jet on basis of the momentum four vectors of merged jet particles. The Snowmass Convention [86] provides the basic recombination schemes. These are the p_t-weighted and the covariant E scheme. The first one results in massless jets while the second one leads to massive jets.
In this analysis, jets are reconstructed using the inclusive k_t-clustering algorithm [87] in the laboratory frame. This scheme makes use of the p_t-weighted recombination scheme and provides therefore massless jets. The p_t-weighted scheme is defined as follows:

$$p_t^{jet} = \sum_i p_{t,i} \tag{4.9}$$

$$\eta^{jet} = \sum_i \frac{1}{p_{t,i}}(p_{t,i}\eta_i) \tag{4.10}$$

$$\phi^{jet} = \sum_i \frac{1}{p_{t,i}}(p_{t,i}\phi_i). \tag{4.11}$$

4.7 Calibration of the Hadronic Final State

In sections 4.5 and 4.6, the reconstruction algorithms were presented. An additional calibration of jets and the complete hadronic final state is applied to improve the reconstructed quantities of the jet and the hadronic final state. In this section, the calibration is described briefly and a cross-check, using a DIS neutral current dijet sample, is performed. The consequences for the systematic error on the hadronic energy scale is discussed at the end of this section. The energy of a hadronic shower is not fully measurable and leads to a systematic deviation from the true value. Therefore, the measured energy is significantly smaller than the energy carried by the hadron, which initiated the hadronic shower. In order to correct this effect, a calibration is performed. In H1, different calibration methods for different purposes exist. The *Iterative method* [88], [89] includes all calorimeter clusters in the event and gives thus a global calibration of hadronic energy measurements. The *High Pt Jet Calibration* [85], [90] considers only clusters, which belong to the reconstructed jet. It is developed for high Q^2 events ($Q^2 > 100$ GeV^2) and for jets with transverse momenta above 10 GeV. The *Low Pt HFS Calibration* [91] is useful for events where the total transverse momentum of the hadronic system is lower than 10 GeV. This method is based on an iterative method for hadronic systems with low transverse momenta, and on a *Low Pt Jet Calibration* method which is developed for jets with transverse momenta below 10 GeV. In this analysis, a combined calibration method is applied. Here, the particles belonging to the reconstructed jets are calibrated with the Low and High Pt Jet Calibration, while the remaining particles are calibrated with the iterative method.

The total transverse momentum of the initial state at HERA is zero, since the electron and proton beams are colliding head-on. Considering momentum conservation, the total trans-

NC DIS Dijet Sample
$E_e > 14$ GeV
$Q_e^2 > 100$ GeV^2
$y_e > 0.15$
40 GeV $< E - P_z <$ 70 GeV
$\lvert z_{vtx} \rvert < 35$ cm
Number of jets > 1

Table 4.2: The selection cuts for the neutral current DIS dijet event sample.

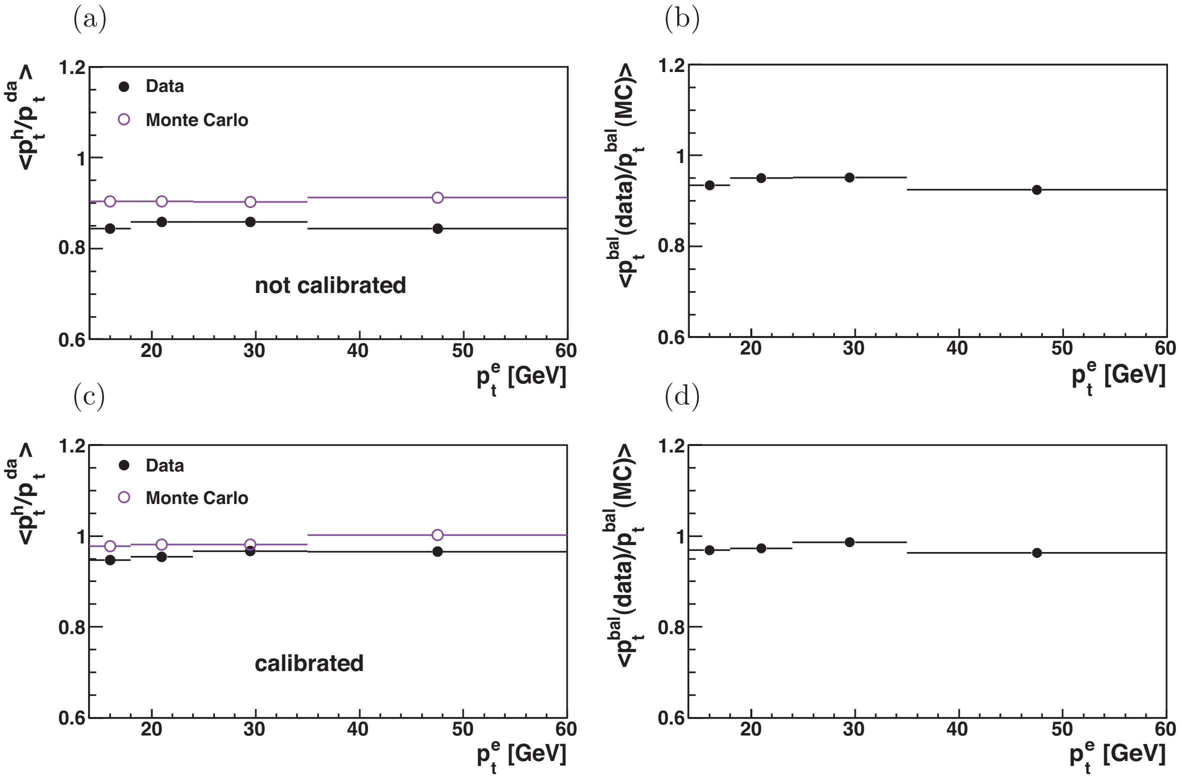

Figure 4.14: The mean balanced transverse momentum between the hadron and the electron as a function of the electron's transverse momentum before (top) and after (bottom) calibration.

verse momentum of the final state has to be zero as well. Therefore, the transverse momentum of the scattered electron needs to be balanced by the transverse momentum of the hadronic final state in the laboratory system. This balanced transverse momentum p_t^{bal} is defined as

$$p_t^{bal} = \frac{p_t^{had}}{p_t^{da}}, \tag{4.12}$$

with p_t^{had} being the total transverse momentum of the hadronic system. The observable p_t^{da} stands for the transverse momentum of the outgoing lepton, obtained by the double angle method. This method exploits the scattering angle of the outgoing lepton and the effective angle of the hadronic system. The double angle method is ideal to test the calibration of the calorimeter, because it is almost independent of the energy scale itself. The agreement of data and simulation is checked with a neutral current DIS dijet sample. The applied selection cuts are summarized in table 4.2. The data was taken in the years 2006/2007 and is compared to the DJANGO Monte Carlo simulation. The distribution of the balanced transverse momentum is plotted before calibration and afterwards.

The balanced transverse momentum as a function of the electron's transverse momentum p_t^e is depicted in figure 4.14, before and after the calibration is applied to data and simulation.

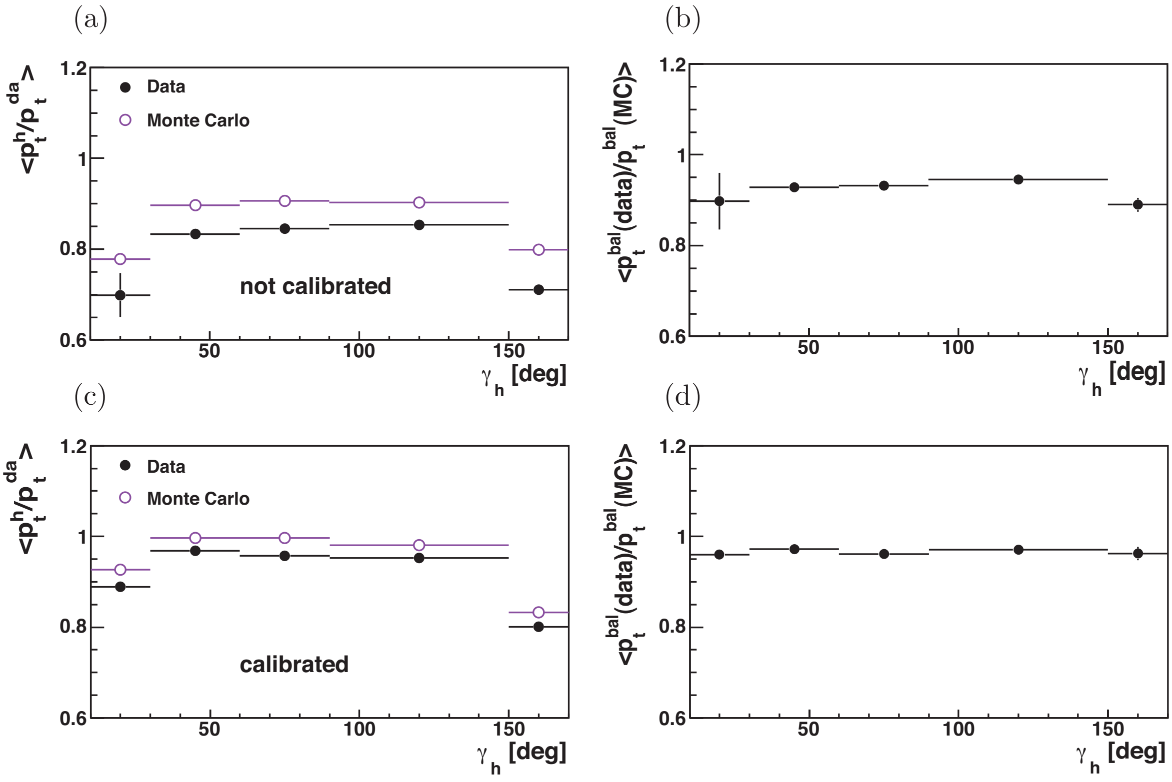

Figure 4.15: The mean balanced transverse momentum between the hadron and the electron as a function of the hadronic angle before (top) and after (bottom) calibration.

Additionally, the ratio $p_t^{bal}(data)/p_t^{bal}(MC)$ is plotted. After the calibration, the distribution of p_t^{bal} becomes more flat and is shifted from 90% to higher values close to one for the data. The distribution for the DJANGO Monte Carlo lies slightly above the data. The agreement between data and simulation is improved as well after the calibration is performed.
Figure 4.15 illustrates the same quantities as a function of the hadronic angle γ_h. In the forward and backward region the response for hadrons is low. After the calibration, the agreement between data and simulation is improved.
The applied calibration improves the agreement between data and the simulation. In all regions of p_t^e and γ_h the disagreement is smaller than 2%. Therefore, an uncertainty of the hadronic energy scale of ±2% is used for estimation of the systematic error of the hadronic energy scale.

4.8 Trigger Elements and their Efficiencies

In this analysis, the photoproduction triggers `s19` or `s23` are required. These triggers are sensitive to signals coming from the CMD and the CTD (cf. 3.2.3 and 3.2.1). Their conditions on the first trigger level differ in that `s19` triggers events detected in the barrel of the muon system and `s23` triggers signals in the endcap of the CMD:

$$\begin{aligned}&\texttt{L1(s19)} : \texttt{Mu\_Bar} \wedge \texttt{FTT\_mul\_Tc} > 1 \wedge \texttt{FTT\_mul\_Td} > 0 \wedge \texttt{CIP\_Sig} > 1\\&\texttt{L1(s23)} : \texttt{Mu\_ECQ} \wedge \texttt{FTT\_mul\_Tc} > 2 \wedge \texttt{CIP\_Sig} > 1.\end{aligned}$$

The L2 and L3 conditions for `s19` and `s23` are the same:

$$\begin{aligned}&\texttt{L2} : \texttt{FTT\_Tc\_gt\_0} && \text{(since 16.11.2006)}\\&\texttt{L3} : \texttt{L3\_V17[3]} && \text{(since 08.12.2006).}\end{aligned}$$

Both trigger photoproduction events. In the following, the trigger elements of `s19` and `s23` are described briefly and their efficiencies are investigated.

Muon Trigger Elements

The trigger element `Mu_Bar` demands hits in two out of the four trigger layers of the muon barrel. The requirement of the muon endcap trigger element `Mu_ECQ` consists of several conditions:

$$\texttt{Mu\_ECQ} = \texttt{Mu\_BOEC} \vee \texttt{Mu\_2\_BIoOEC} \vee \texttt{Mu\_FOEC}. \tag{4.13}$$

The backward inner endcap `Mu_BIEC` and the backward outer endcap `Mu_BOEC` as well as the forward outer endcap `Mu_FOEC` demand hits in three out of the five trigger layers. In the forward inner endcap `Mu_FIEC` four out of five layers are required to avoid the identification of high energetic hadrons from the proton remnant, as muons. If two trigger signals in the forward or backward endcap occur the elements `Mu_2_BIoOEC` or `Mu_2_FIoOEC` return a positive decision.

FTT Trigger Elements

The FTT trigger elements are based on information coming from the CJC. Three out of the four FTT layers are located in the CJC1, while the fourth layer is situated in the CJC2. The FTT provides online trigger decisions on the first three trigger levels.

On level 1 the track curvature $\kappa \propto 1/p_t^{track}$ and the azimuthal angle ϕ^{track} at a track radius of 20 cm are determined. As the trigger decision has to be made within 2.3 μsec, a fast calculation is performed which compares the measured hit patterns of the FTT with precalculated patterns. The trigger decision is based on the counted FTT tracks above a certain p_t threshold (cf. table 4.3).

On level 2 a similar, but more precise pattern identification than on level 1 is performed. This decision delivers angular and momentum resolutions, which are close to those of the final reconstruction. The second trigger level of the FTT is available since November 2006.

The decision on L3 is based on the FTT L2 tracks and on information from other subsystems, e.g. the CMD. For the subtriggers, used in this analysis, the L3 FTT element requires at least one track which points to one of the triggering modules in the CMD. Thus a matching of muon tracks is performed, which is active since December 2006.

FTT Element	Definition
`FTT_mul_Tc>`n	n L1 FTT tracks above 400 MeV
`FTT_mul_Td>`n	n L1 FTT tracks above 900 MeV
`FTT_Tc_gt_0`	A L2 FTT track above 417 GeV
`L3_V17[3]`	muon matching on L3

Table 4.3: List of used FTT trigger elements and their definition.

z Vertex Trigger Elements

The z vertex trigger element `CIP_Sig` constrains the z position of the vertex in order to reject background events, which are far away from the nominal interaction point (cf. section 5.3). The information of the CIP is used to build the trigger decision. Reconstructed tracks are extrapolated to the z axis and then plotted as a z vertex distribution. The significance S of this distribution

$$S = \frac{N^{trk}_{cen}}{N^{trk}_{bwd} + N^{trk}_{fwd}}, \tag{4.14}$$

which is determined using the number of tracks in the forward (N^{trk}_{fwd}), central (N^{trk}_{cen}) and backward (N^{trk}_{bwd}) region of the z axis, is used as well for the trigger decision. The requirement of `CIP_Sig>1` indicates more tracks coming from the central region than from the backward and forward region.

Trigger Efficiencies

In this section, the efficiencies of the required subtriggers `s19` and `s23` are determined. For the cross section measurement the trigger efficiency as calculated from the data is used. To determine the efficiency of a subtrigger, monitor triggers are used that do not contain any

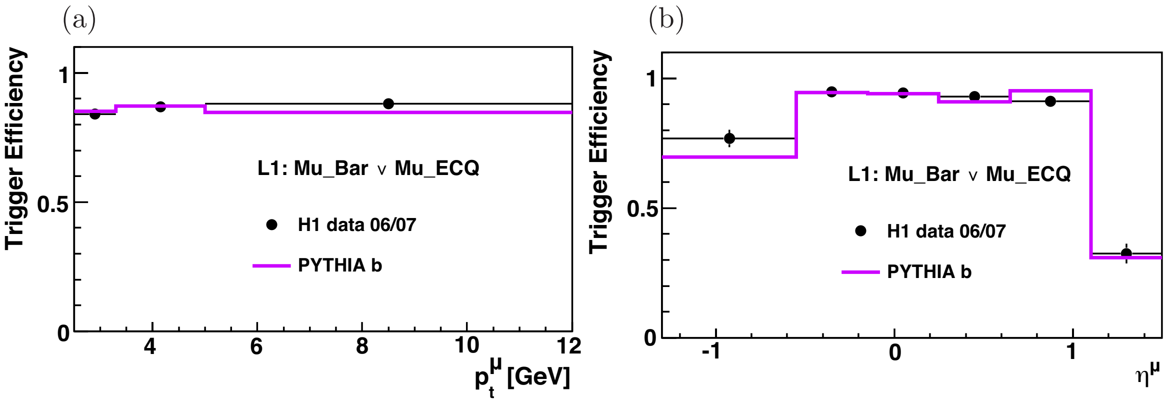

Figure 4.16: Efficiencies of the L1 muon trigger elements `Mu_Bar` $\vee$ `Mu_ECQ` as a function of p_t^μ (a) and η^μ (b). The PYTHIA simulation (solid line) in comparison to the data (points).

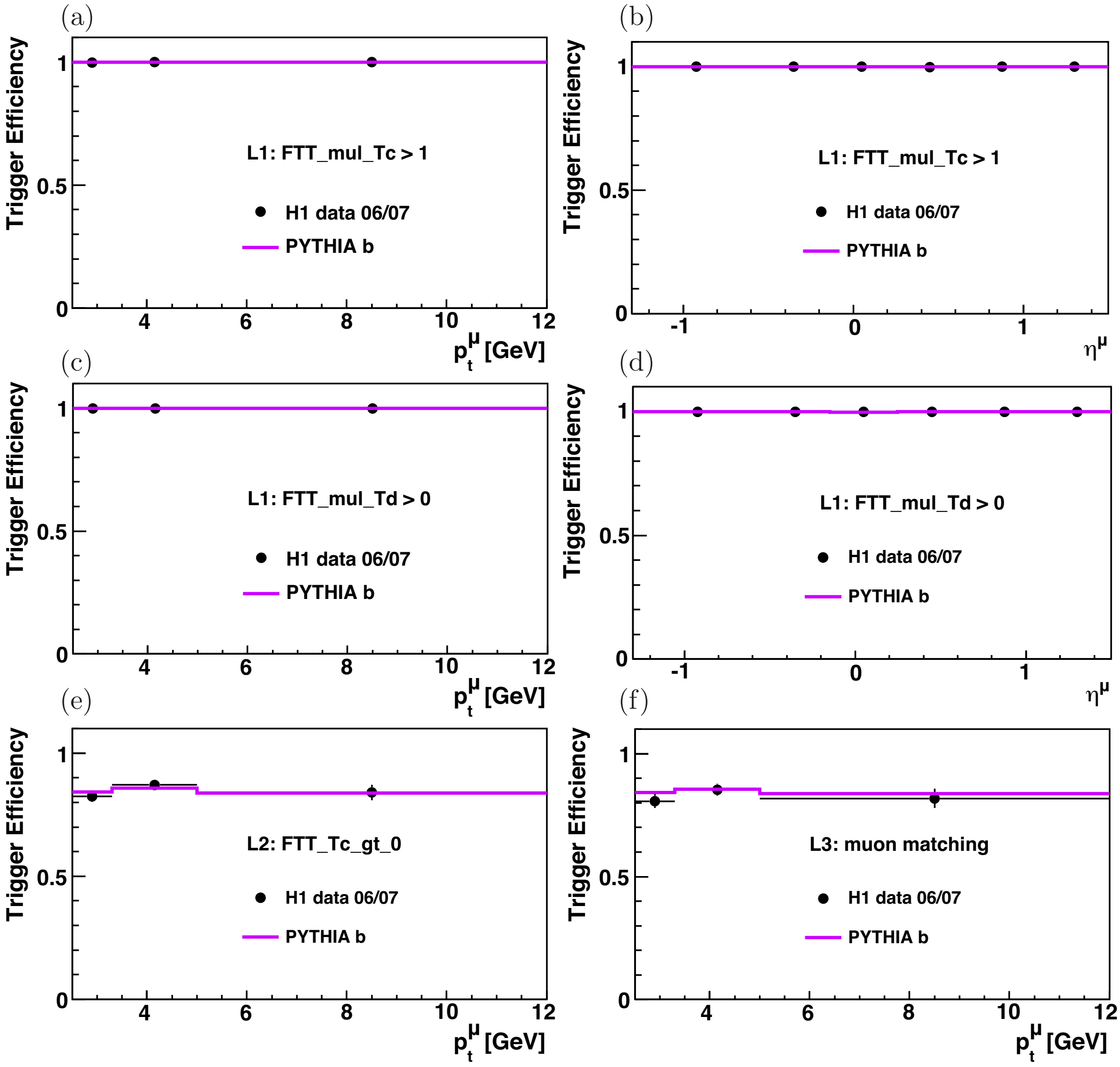

Figure 4.17: Trigger efficiencies of the FTT trigger elements as a function of p_t^μ [(a),(c),(e),(f)] and η^μ [(b),(d)]. The PYTHIA simulation (solid line) in comparison to the data (points).

of the trigger elements from the analysed trigger. The trigger efficiency is determined for data and Monte Carlo separately at the trigger element level to be able to compare it. Each trigger element is investigated separately.

The Monte Carlo simulation provides the first three trigger levels and the FTT elements are simulated. The trigger efficiency $\epsilon_{trigger}$ is calculated by the fraction of events that are triggered by both, the monitor and the analysis trigger $N_{signal \wedge monitor}$, relative to all events triggered by the monitor trigger $N_{monitor}$:

$$\epsilon_{trigger} = \frac{N_{signal \wedge monitor}}{N_{monitor}}. \tag{4.15}$$

The subtriggers `s19` and `s23` are sensitive to signals coming from the CMD and the CTD (cf. section 3.2.3 and 3.2.1). The subtrigger `s19` is sensitive to events with muons in the CMD barrel and `s23` to events with muons in the CMD endcaps. Both triggers select events that contain central tracks above a certain momentum threshold (table 4.3) and a reconstructed CIP-vertex. No independent photoproduction triggers are available and thus the investigation of the trigger efficiency is carried out using events that were independently triggered by the SpaCal. These DIS events have a similar hadronic final state and a scattered electron in addition. Accordingly, the cuts are removed, which restrict the sample to the photoproduction regime.

The trigger efficiencies for `Mu_Bar` $\vee$ `Mu_ECQ` are shown in figure 4.16 as a function of the transverse momentum of the muon and its pseudorapidity. The points correspond to the data, while the solid line represents the PYTHIA Monte Carlo simulation. The simulated efficiency underestimates that of the data, especially in the backward region and at high p_t.

The trigger efficiencies of the FTT elements are shown in figure 4.17 as a function of p_t^μ and η^μ. The points correspond to the data while the solid line illustrates the PYTHIA prediction. On level 1 the data efficiency is very close to 100% and nicely described by the Monte Carlo simulation. On level 2 and 3, the data has an efficiency of more than 80% and is again in very good agreement with the simulated efficiencies.

In figure 4.18 the trigger efficiency of `CIP_Sig` is shown. The efficiency in the data (points) reaches nearly 100% and is well described by the PYTHIA simulation (solid line) in all variables.

Trigger Efficiency of `s19` and `s23`

The total trigger efficiency for the subtriggers `s19` $\vee$ `s23` is shown in figure 4.19. The muon trigger elements `Mu_Bar` $\vee$ `Mu_ECQ` dominate the efficiencies of the subtriggers `s19` and

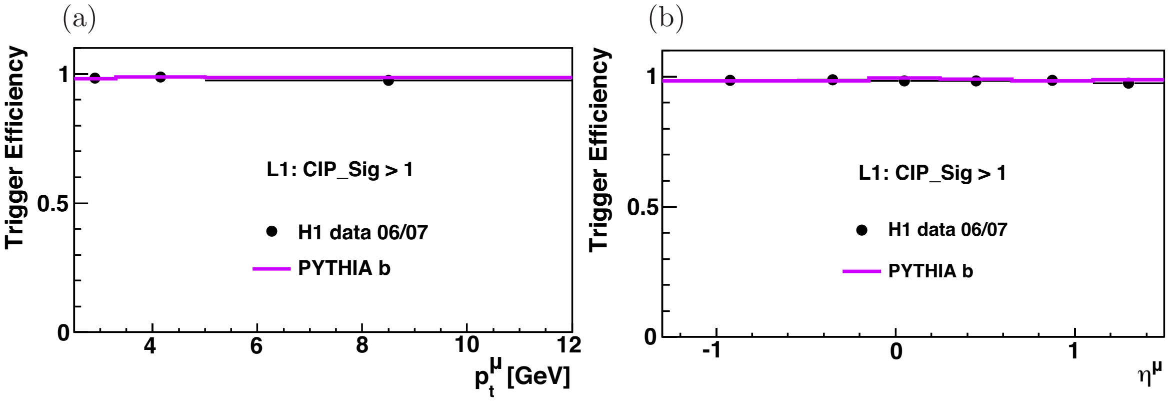

Figure 4.18: Efficiency of the z vertex trigger element `CIP_Sig` on L1. The data (points) shows an efficiency of nearly 100% and is compared to PYTHIA (solid line). In (a) the efficiency is plotted as a function of p_t^μ and in (b) as a function of η^μ.

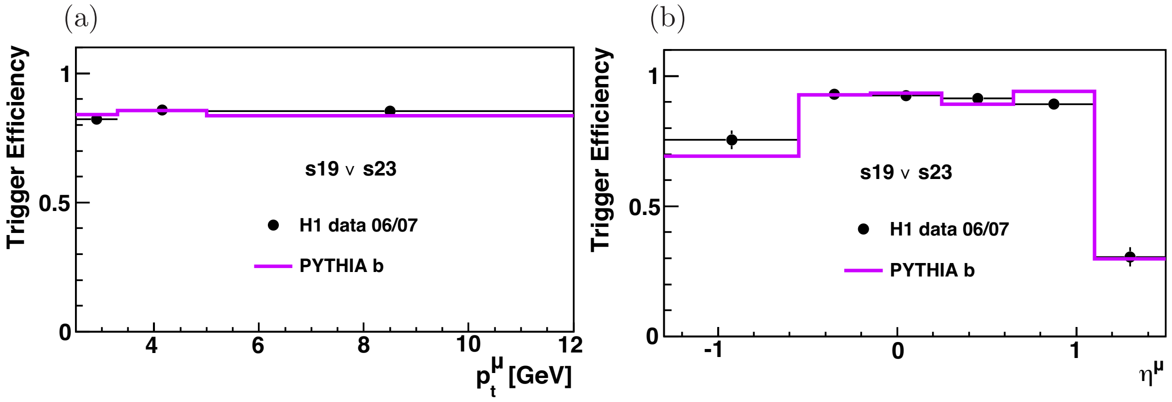

Figure 4.19: Trigger efficiency for the subtriggers `s19` ∨ `s23` as a function of p_t^μ (a) and η^μ (b). The data (points) in comparison to the PYTHIA simulation (solid line).

`s23`. The data (points) and the simulated Monte Carlo are in good agreement. The trigger efficiencies are checked for both, the beauty and the charm Monte Carlo simulation and only the simulated efficiencies for events containing beauty are shown here. The charm simulation gives very similar results.

Chapter 5

Event Selection

In this chapter, the procedure to select the photoproduction dijet sample is presented. It starts with a selection of periods with stable detector conditions and continues with the selection of photoproduction heavy quark events. Afterwards, background events from cosmic rays and other sources are discussed. Finally, the correlation between reconstructed and generated variables is studied.
The distributions presented in this chapter contain a comparison of the data and the PYTHIA simulation. The distributions of beauty, charm and light quarks are scaled with their fractions and normalised to the data. The fractions are obtained by the 2-dimensional fit as explained in chapter 6. The sum of these three quark contributions is then compared to the data.

5.1 Data Sample

The data sample analysed in this thesis, was recorded with the H1 detector in the years 2006 and 2007 and corresponds to an integrated luminosity of 179.8 pb^{-1}. Before autumn 2006 protons of 920 GeV energy were collided with electrons and afterwards with positrons of 27.6 GeV energy. The different lepton charges are not expected to have an impact on this analysis and the two run periods are analysed together. The integrated luminosities for the different run ranges are listed in table 5.1.

Run Selection

In order to select events for the analysed physics process, several selection steps are performed. At first, runs with *good* and *medium* quality are selected. Each run is required to have an integrated luminosity of at least 0.1 nb^{-1}. The relevant detector components listed in table

Run Period	Run Range	Luminosity [pb^{-1}]
2006 e^-	445592-466997	49.7
2006/2007 e^+	468531-500611	130.1

Table 5.1: Run ranges analysed in this thesis and the corresponding integrated luminosities.

Subdetector	HV symbol
Inner Central Jet Chamber	`CJC1`
Outer Central Jet Chamber	`CJC2`
Liquid Argon Calorimeter	`LAR`
Time-of-flight System	`TOF`
Luminosity System	`LUMI`
Central Inner Proportional Chamber	`CIP`
Spaghetti Calorimeter	`SPAC`
Central Muon Detector	`IronClusters`
Central Silicon Tracker	`CST`
Fast Track Trigger	`FTT`

Table 5.2: List of relevant subdetectors with switched on high voltage.

5.2 must be fully operational and their *High Voltage* (HV) is required to be on. They have to be in the read out as well.

Some run ranges are known as problematic. In some cases, the FTT software on L1 or L2 was wrongly loaded or a power glitch of L2 occurred. The year 2004 is completely excluded, since no CST information is available, which is crucial for this analysis. 2005 is excluded as well due to a very problematic period of the CST. Only 2/3 of the half ladders were operational. A bug concerning the wires which connect neighbouring strips, reduced the hit efficiency and degraded the resolution. The wires were crossed, which caused an interchange of the signals coming from neighbouring strips. This bug is not fully fixed for the recorded data of 2005, but the crossed wires were corrected in 2005 to be fully operational for the last 1.5 years of data taking. In 2005 another problem occurred: the beampipe touched the CST, which caused a movement in every lumi fill when the magnets were ramped up. Even during a fill, the position of the CST was not completely stable. Therefore, only the data taking periods 2006 and 2007 are analysed since the CST had its best operational period. Only a small number of runs in these years is excluded due to failures of some CST half ladders.

5.2 Heavy Quark Selection in Photoproduction

In this section, the selection of event candidates with heavy quarks in photoproduction is discussed. The selection contains kinematic cuts, a requirement of a muon candidate and a dijet selection. In table 5.3 an overview of the selection cuts is given.

5.2.1 Kinematic Selection

In photoproduction, the virtuality of the exchanged photon is small and the electron is scattered under very small angles, escaping detection in the main H1 calorimeters. Photoproduction events are selected requiring that there is no electron candidate found in the calorimeters with an energy of more than 8 GeV. The SpaCal acceptance restricts the virtuality of the photon to $Q^2 \lesssim 2.5$ GeV^2.

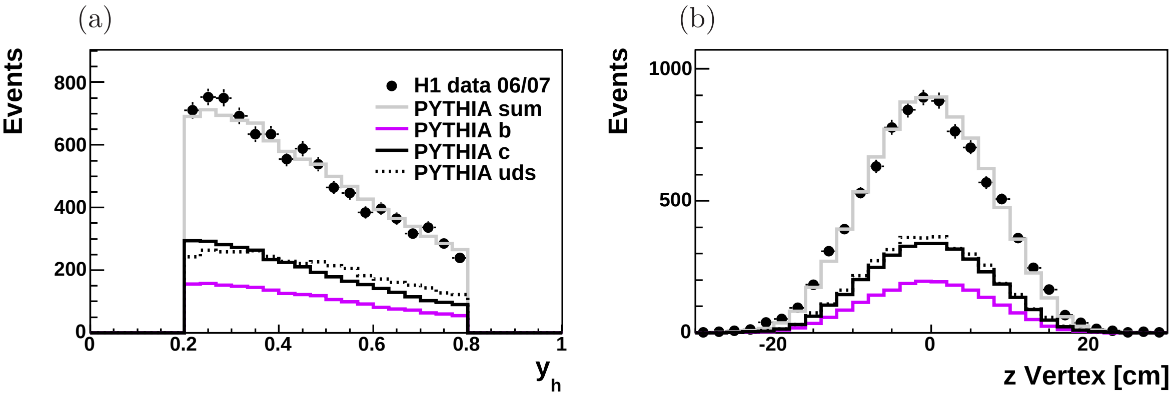

Figure 5.1: The inelasticity in (a) and the z vertex distribution in (b) for data (points) and PYTHIA (lines) in comparison.

As the kinematic quantities of the scattered electron are not accessible, one has to use the hadrons to determine the kinematic variables with the *Jacquet-Blondel method* (JB) [92]. The cut on the inelasticity y_{JB} helps to reject *Deep Inelastic Scattering* (DIS) background events, which might still be in the sample due to inefficiencies of the electron finder. The inelasticity is defined as

$$y_{JB} = \frac{\sum(E - p_z)}{2E_e}. \tag{5.1}$$

Here, E and p_z are the energies and the z-components of the momenta of the hadronic final state particles, while E_e denotes the lepton beam energy. The definition (5.1) shows that DIS events can be found at high inelasticties since the $\sum(E - p_z)$ conservation leads typically to values of twice the beam energy $\sum(E - p_z) = 2E_e = 55.2$ GeV. Therefore, the upper limit of y_{JB} is restricted to $y_{JB} < 0.8$, taking also the acceptance of the muons into account.
To ensure a complete reconstruction of the final state, events in the very forward region have to be discarded leading to an inelasticity of $0.2 < y_{JB} < 0.8$. Figure 5.1 (a) shows the inelasticity for the data (points) and the PYTHIA Monte Carlo simulation (see legend) after applying all selection cuts. The simulated inelasticity shows a good agreement with the data.

5.2.2 Muon Selection

The muon identification and reconstruction is presented in section 4.1. In the following, the applied selection cuts are discussed. In this analysis, a muon candidate identified in the instrumented iron is required. To ensure a reconstruction efficiency larger than 60%, a transverse momentum of at least 2.5 GeV is demanded [75]. This cut also removes events with large multiple scattering. Multiple scattering effects are proportional to $1/p_t$, as explained in section 5.5.1. The transverse momentum of the muon candidate is depicted in figure 5.2

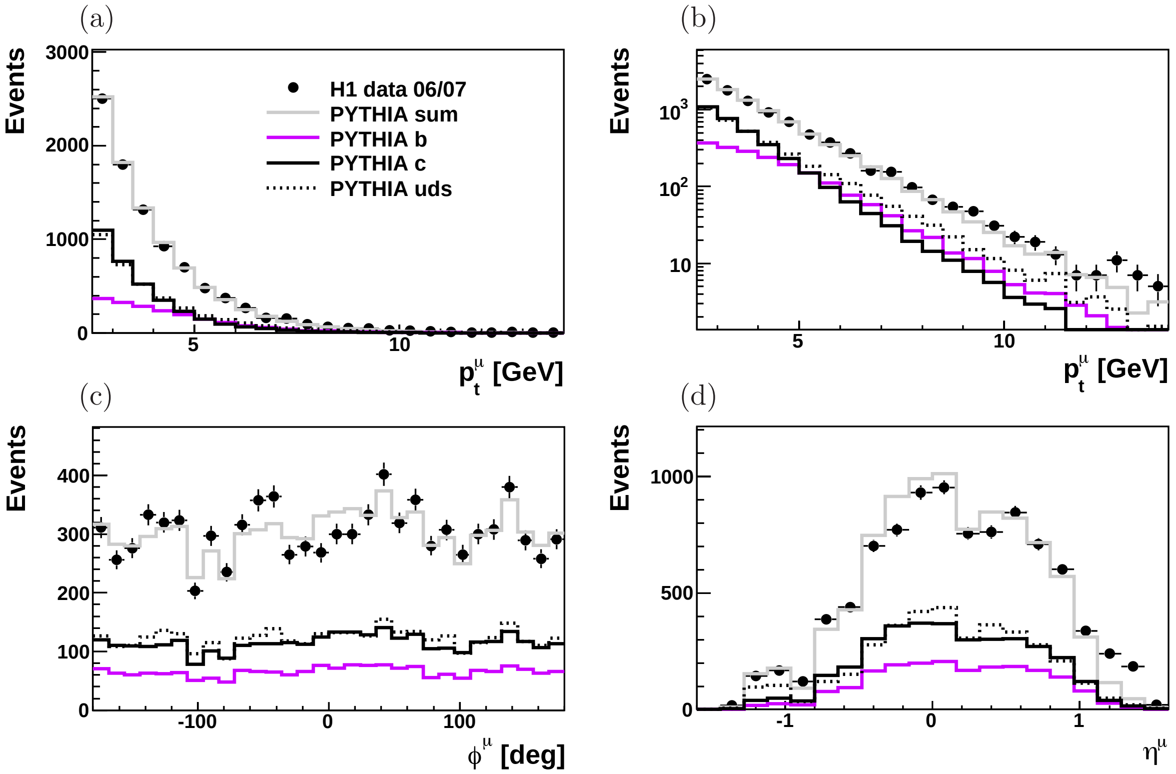

Figure 5.2: The transverse momentum p_t^μ in (a) and (b), the azimuthal angle ϕ^μ in (c) and the pseudorapidity η^μ in (d) of the selected muon candidate for data (points) and PYTHIA (lines) in comparison. All cuts discussed in this section are applied.

(a) and (b) with linear and logarithmic scale. The data is well modelled by the PYTHIA simulation.

The analysed range is $-1.3 < \eta^\mu < 1.5$, corresponding to an angular range $25° < \theta^\mu < 150°$, which is an extension of the forward and backward region compared to the previous measurement [59]. The θ^μ cuts are motivated by the angular acceptance of the CST. In figure 5.2 (c) and (d), the distribution of the pseudorapidity and the azimuthal angle of the muon are presented. The PYTHIA simulation underestimates the data in the very forward region $\eta^\mu > 1.2$ and overestimates it in the region $-0.4 < \eta^\mu < 0.2$. The underestimation in the very forward region can be explained by an increase of the light quark contribution in the data. In general, the angular distributions of the data (points) are modelled reasonably by the simulation.

If more than one muon candidate is found, the one with the highest p_t is taken. This happens very rarely: more than one muon candidate is found in less than 1% of the selected events.

To provide a high purity of the muon sample, further selection cuts are applied. The track measured with the CMD is therefore required to have hits in at least four out of the 16 layers of the muon detector. The number of hit layers in the instrumented iron is depicted in figure 5.3 (a). The PYTHIA simulation is shifted to the left. To reduce the number of fake muons coming from misidentified hadrons, the distance between the last and the first hit layer is required to be larger than three, as plotted in figure 5.3 (b). Again, the simulation overestimates the data at low values and underestimates it at high values of the layer distance. In the backward region ($130^\circ < \theta^\mu < 150^\circ$), the distance between the hits in the last and first layer is required to be at least 8 layers, since the calorimeter (BBE) is instrumented with less than two hadronic interaction lengths. This causes an increase of background coming from hadrons, which are misidentified as muons. In figure 5.3 (d) a comparison of hadrons misidentified as muons with (dotted line) and releasing (solid line) the above described cuts on the layer of the muon system is shown. The increase of hadrons in the backward region without the cuts is clearly visible. Both distributions are obtained from a PYTHIA Monte Carlo sample containing only misidentified hadrons, which survive all other applied analysis cuts listed in table 5.3.

The distributions shown in figures 5.3 (a) and (b) are not perfectly modelled by the simulation. This is most probably due to a not perfect description of the detector and its performance in the CMD Monte Carlo simulation. In the scope of this analysis it is crucial, that the reconstruction efficiency in the instrumented iron is well modelled by the simulation. This is the case, as was shown in [75]. Because the shown distributions do not effect the detector corrections in the measurement and the shown quantities are only used to reject misidentified hadrons, no further steps are taken.

The linking probability of the outer to the inner muon track is required to be at least 10% and is shown in figure 5.3 (c). Here, the simulation provides a good description of the data.

5.2.3 Jet Selection

Jets are reconstructed in the laboratory frame using the inclusive k_t clustering algorithm as described in section 4.6. In this analysis, events containing at least two jets with transverse momenta of $p_t^{jet1(2)} > 7(6)$ GeV within the pseudorapidity range $|\eta^{jet}| < 2.5$ are selected, taking the angular acceptance of the detector into account. In the leading order QCD picture, these two jets result from the hadronization of two heavy quarks. The methods, used to extract the heavy quark fraction (see chapter 6), demand a sufficient precision of the reconstructed direction of the jets. This is only provided for jets with a sufficiently high transverse momentum, which motivates the selection criteria of $p_t^{jet1(2)} > 7(6)$ GeV.

If several jets are found, the two highest p_t jets are taken. The selected muon candidate is required to be associated to one of these two jets and the association is provided by the jet algorithm. In the following, the jet, which contains the muon candidate, is called 'muonjet' while the other one is called 'other jet'. The indices '1' and '2' denote the ordering in transverse momenta and give no hint if the jet contains the muon candidate or not.

Figure 5.4 shows the transverse momenta of the two highest p_t jets. A good agreement between the data (points) and the PYTHIA prediction is achieved. In figure 5.5 (a) and (b) the number of HFS particles per jet of the highest and second highest p_t jet are shown. Figure 5.5 (c) and (d) present the azimuthal angular distributions for jet1 and jet2, respectively. The histograms (e)-(h) illustrate the pseudorapidities for jet1, jet2, muonjet and the other jet. In all cases, the simulation describes the data reasonably well. The Monte Carlo simulation is normalised to the number of entries and scaled with the quark contributions obtained by the

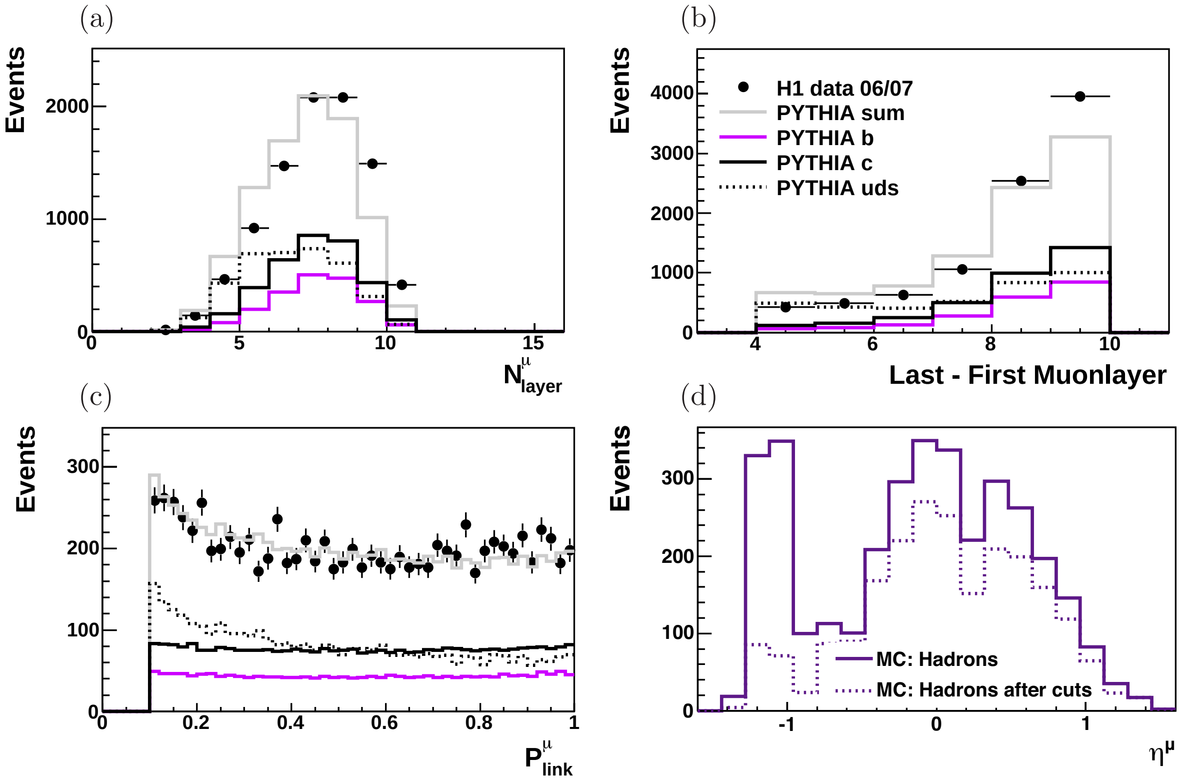

Figure 5.3: Number of hit layers in the muon detector in (a), distance of last and first hit layer in (b), linking probability of the outer to the inner muon track in (c) and hadrons misidentified as muons (d). The Data (points) are shown in comparison to the PYTHIA simulation.

2-dimensional fit as explained in chapter 6. All selection cuts discussed in this section are applied and listed in table 5.3.

Jet Profiles

A useful tool for getting insights to the character of the selected dijet events is the transverse energy flow around the jet axis. The energy flow is visualized by so-called jet profiles which illustrate the distance in η and ϕ between the objects of the hadronic final state and the jet axis. This distance is weighted by the transverse energy of each object. In other words, the jet profile shows the angular energy distribution around the jet axis.
Figure 5.6 (a) presents the jet profile in the region $|\Delta\eta| < 1$, where $\Delta\eta = \eta^{obj} - \eta^{jet1}$. The points correspond to the data and the solid line illustrates the sum of the different quark contributions in PYTHIA, which describes the data very well. The peak around zero originates from particles of the jet itself, while the increase of the energy flow to $\pm\pi$ is caused by the particles of the second jet.
Figure 5.6 (b) illustrates the jet profile in the region $|\Delta\phi| < 1$, with $\Delta\phi = \phi^{obj} - \phi^{jet1}$. Again the agreement between data and PYTHIA is very good. The shape of the distribution shows

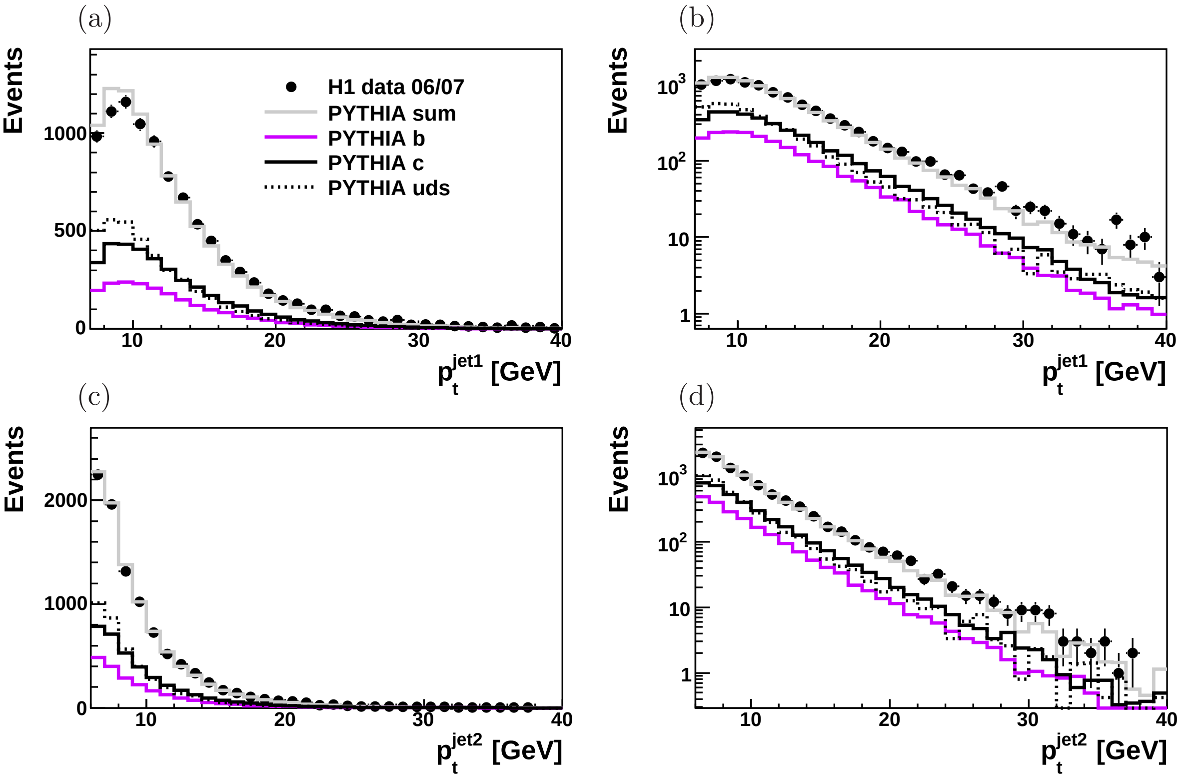

Figure 5.4: The transverse momenta of the highest [(a),(b)] and second highest [(c),(d)] p_t jets for the data (points) and PYTHIA prediction in comparison after all cuts.

an asymmetry to higher values of $\Delta\eta$, which indicates a higher energy flow in the direction of the proton remnant.
In figures 5.7 and 5.8, the jet energy flow is illustrated in bins of p_t^{jet1} and x_γ^{obs} as a function of $\Delta\phi$ and $\Delta\eta$. In all cases, the PYTHIA simulation models the data very well.

5.3 Background Studies

After applying the cuts discussed in the last section, the event sample consists of candidates for heavy quarks in dijet events containing a muon. The sample contains also background events like cosmic or fake muons, which are explained in the next two sections, including selection cuts to reduce their contribution. Background, coming from non *ep* events, is eliminated constraining the position of the reconstructed primary vertex within a certain range of the z position of the nominal vertex. This rejects events coming from collisions of satellite bunches with nominal bunches. Thus, the primary vertex is required to be reconstructed close to the nominal interaction point $|z_{vtx}| < 35$ cm. Figure 5.1 (b) presents the z vertex distribution. Since the variable z_{vtx} is generated too broad (not shown) in the PYTHIA simulation, it is reweighted in terms of the generated z vertex. The data (points) is well described by the reweighted simulation.

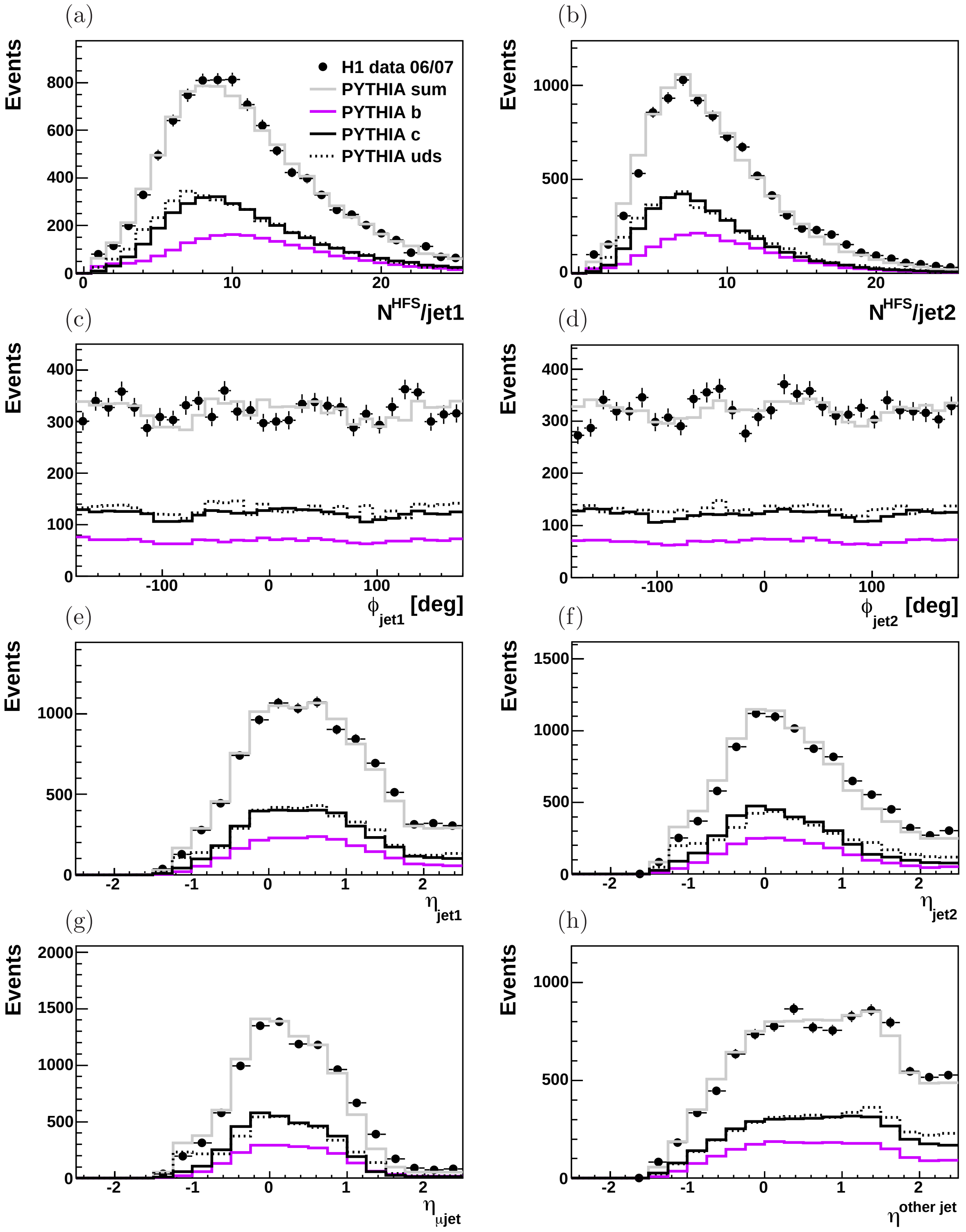

Figure 5.5: Control distributions of jet quantities for data (points) and PYTHIA (lines) in comparison. For jet1, the number of HFS particles (a), azimuthal angle (c) and the pseudorapidity (e) are shown. The same quantities are plotted for jet2 in (b), (d) and (f), respectively. The η distributions for the muonjet and the other jet are presented in (g) and (h). All cuts discussed in this section are applied.

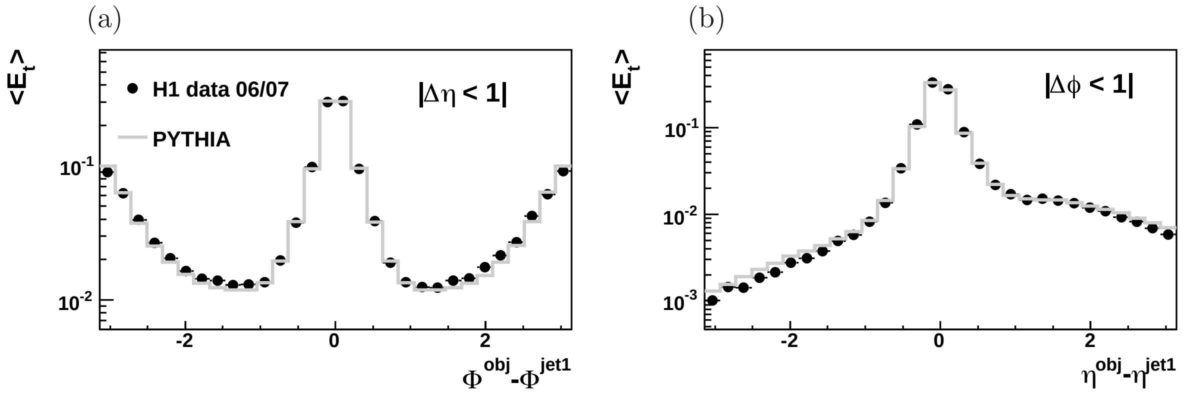

Figure 5.6: The transverse energy flow around the jet axis as a function of the distance between the angles of the object and the jet axis. (a) shows the distance in azimuthal angles $\phi^{obj} - \phi^{jet1}$ and in (b) the distance in pseudorapidities $\eta^{obj} - \eta^{jet1}$ is illustrated. The referring jet is the one with the highest p_t, namely $jet1$.

Cosmics

Muons from cosmic rays are a natural source of background events as nearly 10000 of them reach every square meter of the earth's surface per minute. Thus, they are equally distributed in time and in the detector, which is a convenient property to remove them. The timing information of the CJC track must be consistent with the average event time to make sure that the detected signal does not come from a cosmic muon. As a cosmic muon flies straight through the detector, it pretends to be two muons with a back to back topology. This feature is used as well to reject them performing a matching between two muon tracks. Since a pure cosmic event has only two tracks the number of central tracks is restricted to at least three tracks $N_{cen}^{tracks} \geq 3$. A last step to reject cosmic events is to constrain the signed impact parameter δ (cf. section 4.2) to a certain range as the cosmic muons are distributed equally in the detector. The following cuts are applied in this analysis to reduce background from cosmics:

- The timing information of the CJC tracks must be consistent with the average event time within 3 σ, which corresponds to 2.8 nsec.

- Events are rejected if a second muon is found, which fits the other muon candidate in the opposite hemisphere in ϕ and p_t.

- The signed impact parameter must lie in the range $-0.1 < \delta < 0.1$ cm.

These cuts reject 3% of the selected events.

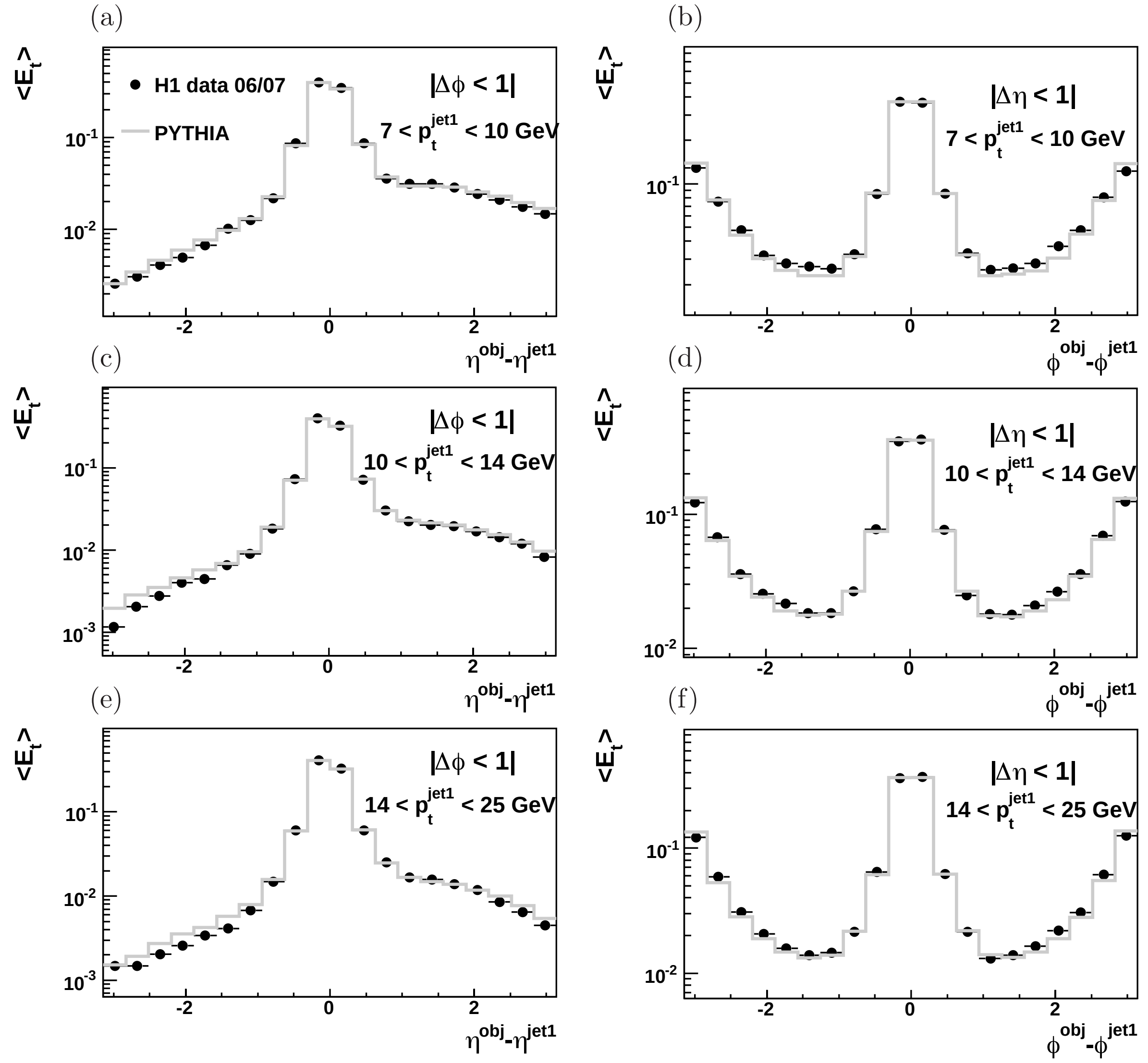

Figure 5.7: The transverse energy flow around the jet axis as a function of $\Delta\eta$ (left column) and $\Delta\phi$ (right column) for different regions of p_t^{jet1}. The data (points) in comparison to the PYTHIA simulation (solid line).

Fake Muons

Another important source for background events in this analysis are the so-called fake muons. Hadrons or their decay products, which reach the muon system, can be wrongly identified as muons from heavy quark decays for three reasons:

- *sail through*: A hadron, which reaches the muon detector in case it suffers no hadronic interaction with the calorimeter is not strong is a so-called 'sail through' hadron. Here, the hadron acts like a minimum ionising particle. According to [76], the maximum

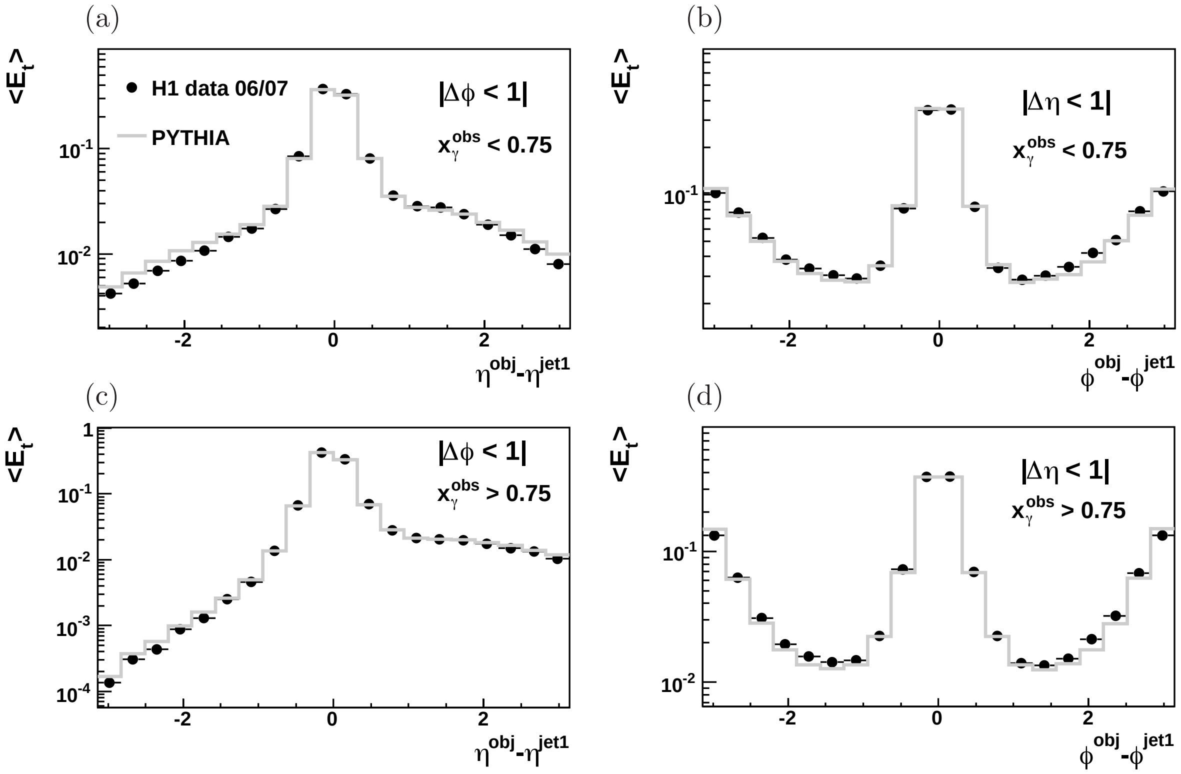

Figure 5.8: The transverse energy flow around the jet axis as a function of $\Delta\eta$ (left column) and $\Delta\phi$ (right column) for different regions of x_γ^{obs}. The data (points) compared to the PYTHIA (solid line).

probability for this reaches 0.6% as a function of the polar angle. The probability depends on the hadronic interaction length and the travel distance.

- *punch through*: A 'punch through' hadron interacts with the calorimeter, but does not deposit its entire energy since the radiation length of the calorimeter is too small. The energy leaking, passing some of the iron layers, could cause the misidentification of this hadron as a muon.

- *inflight decay*: Some light hadrons, like pions or kaons, have decay channels with muons in the final state. Pions have a branching fraction of almost 100% to decay into a muon and a neutrino, while the kaons show a fraction of roughly 65% [46]. If one of these hadrons decays inside the detector, the resulting muon could reach the muon detector. Here, it might be misidentified as a muon, which originates from a heavy quark decay.

The backward part of the LAr calorimeter (BBE) in the region $140° < \theta < 160°$ is instrumented with less than two hadronic interactions lengths in front of the muon detector. This causes an increase of wrongly identified hadrons as depicted in figure 5.3 (d). To reduce the number of misidentified hadrons, the cut on the distance between the first and the last hit layers is tightened in the backward region. Here the distance is required to be at least eight

Photon Virtuality $\mathbf{Q^2}$ [GeV^2]	< 2.5
Inelasticity y	$0.2 \ldots 0.8$
Trigger	`s19` $\vee$ `s23`
Muon Selection	associated to one Jet
Transverse Momentum $\mathbf{p_t^{\mu}}$ [GeV]	> 2.5
Pseudorapidity η^{μ}	$-1.3 \ldots 1.5$
# Muon Layer N^{μ}_{layer} (BEC)	≥ 4 (≥ 8)
Iron Link Probability P^{μ}_{link}	> 0.1
# CST Hits N^{hits}_{CST}	≥ 1
CST Link Probability P^{CST}_{link}	> 0.1
Jet Selection	
Pseudorapidity $\eta^{\mathbf{jet}}$	$-2.5 \ldots 2.5$
Transverse Momentum $\mathbf{p_t^{jet1}}$ [GeV]	> 7
Transverse Momentum $\mathbf{p_t^{jet2}}$ [GeV]	> 6

Table 5.3: Summary of the applied cuts. The cuts defining the kinematic range are in bold letters.

layers, which rejects 35% of the events according to a PYTHIA Monte Carlo sample, which contains only misidentified hadrons. Requiring a larger distance between the first and last hit layers increases the purity and keeps the single iron layer efficiency constant. If the number of layers itself would be increased, these conditions would not be fulfilled [78].

The contributions of sail through and punch through hadrons are taken together in the following. According to the inclusive Monte Carlo simulation the contribution of hadrons, which reach the muon detector, is 24%. The contribution of inflight decays to the fake muon background is found to be 3.7%.

Event Yield

Figure 5.9 shows the event yield of the data sample. All analysis cuts presented in section 5.2 are applied. The number of events per pb^{-1} increases at approximately run number 477000 slightly. This step is observed by several independent analyses and the source is not clarified at present. The average number of events per pb^{-1} is approximately 50 before the step and 60 afterwards.

Selection Summary

The data sample analysed in this thesis contains 9093 events after applying all cuts discussed above (cf. table 5.3). In figure 5.10, a typical dijet event containing a muon is depicted, which is one of the analysed events in this thesis. Figure 5.10 illustrates a schematical view of the H1 detector in the rz and xy plane and is plotted using the program H1Red [93]. The LAr energy of the two selected jets is also shown.

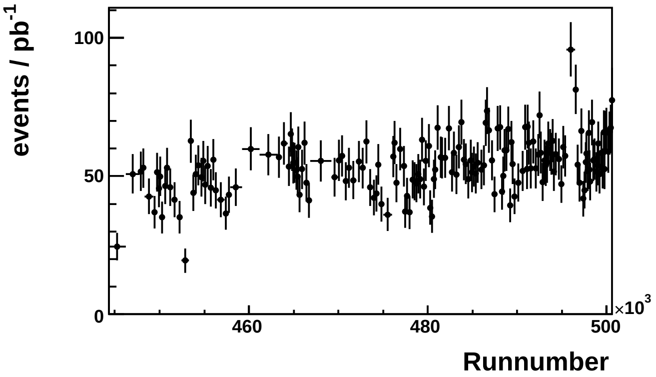

Figure 5.9: Event yield for the photoproduction dijet sample containing a muon (`s19` $\vee$ `s23`). The number of events per pb^{-1} are shown as a function of the runnumber.

5.4 Dijet Event Observables

As explained in section 2.5, processes in the kinematic region of photoproduction can be direct or resolved in the LO QCD picture. The relative fraction depends on the energy of the photon, which comes from the electron and interacts with partons of the proton. The measurement of dijet events enables to investigate several quantities, which are related to the heavy quark production mechanism. The following considerations are based on the assumption, that the two highest p_t jets describe the kinematics of the outgoing partons. In the case of a direct process, the outgoing partons are a heavy quark pair. If it is a resolved process, the two outgoing partons can be a heavy quark and another parton, like for example a light quark or a gluon.

The observable x_γ^{obs} represents the fraction of the photon energy, which enters the hard interaction. It is thus feasible to distinguish between direct and resolved processes. Based on the above mentioned assumption, it is estimated using

$$x_\gamma^{obs} = \frac{\sum_{jet1}(E - p_z) + \sum_{jet2}(E - p_z)}{\sum_{had}(E - p_z)}, \tag{5.2}$$

where E stands for the energies and p_z for the z-components of the particles contained in the two jets in the numerator and in the denominator the sum runs over all detected hadronic final state particles. With this definition the range of x_γ^{obs} is restricted to $0 < x_\gamma^{obs} \leq 1$. In the direct process the photon enters the hard interaction completely and thus a x_γ^{obs} of roughly one is expected. In that case, the hadronic final state consists of only the two hard jets and the proton remnant in the forward region, which makes an insignificantly small contribution to the denominator in (5.2). In resolved processes x_γ^{obs} becomes smaller due to the contribution of the photon remnant to the hadronic final state, which increases $\sum_{had}(E - p_z)$. Contributions from next-to-leading order processes can also lead to smaller values of x_γ^{obs}, since a third jet, initiated by the additional hard outgoing parton, is produced. To summarize, the observable x_γ^{obs} is sensitive to the resolved photon structure and contributions from higher

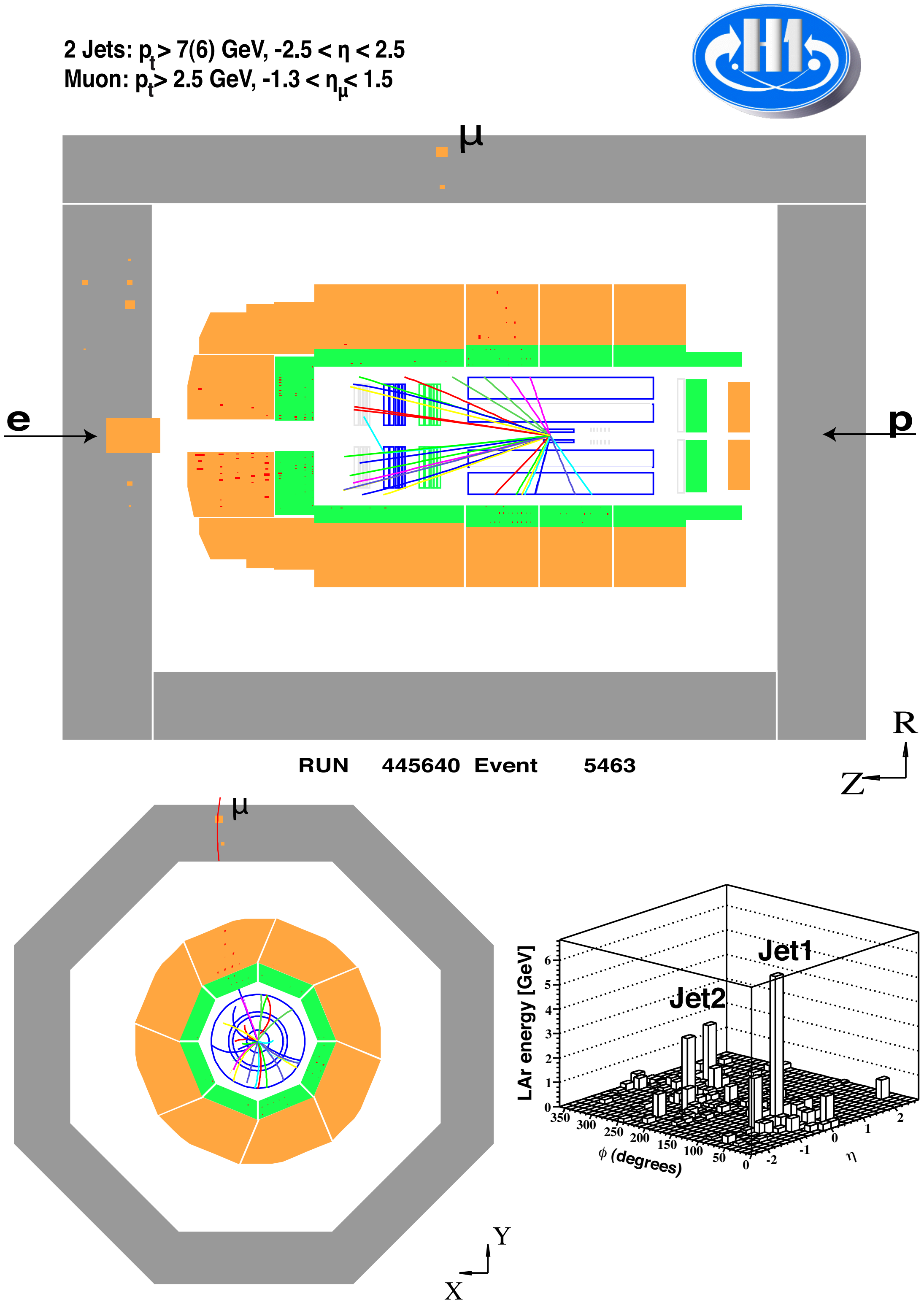

Figure 5.10: Schematical rz and xy view of the H1 detector showing a typical event out of this analysis. The LAr energy of the two selected jets is also illustrated.

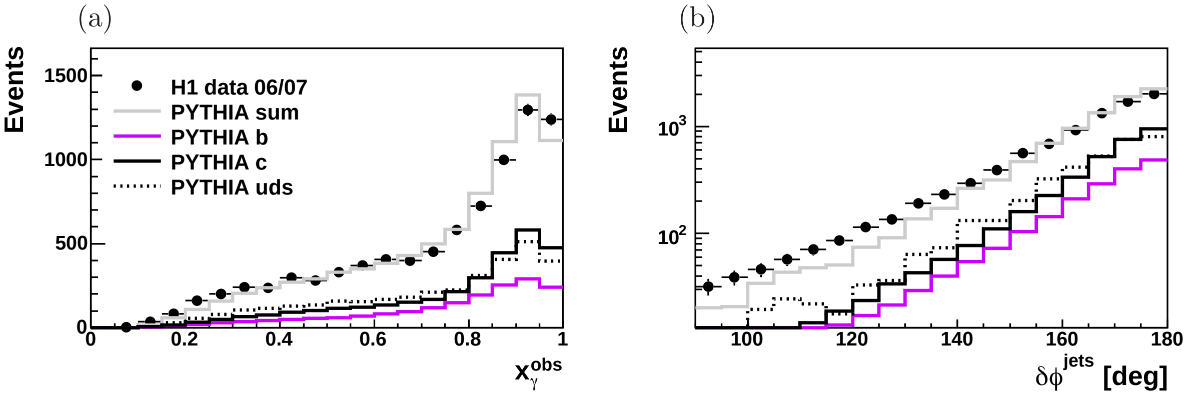

Figure 5.11: The observable x_γ^{obs} in (a) and $\delta\phi^{jets}$ in (b) for data (points) and PYTHIA (lines) in comparison after all cuts.

order processes. The reconstructed x_γ^{obs} for the selected events (cf. table 5.3) is shown in figure 5.11 (a). The PYTHIA Monte Carlo simulation is normalized to the data and the three contributions coming from events containing beauty, charm and light quarks are scaled with the fractions obtained by the 2-dimensional fit (cf. chapter 6). The observable x_γ^{obs} shows a peak at values close to one which indicates the presence of more direct than resolved processes. The sum of the different quark contributions, simulated with PYTHIA, models the data (points) reasonably well. At very high x_γ^{obs} the simulation overestimates the data somewhat, at low values of x_γ^{obs} the simulation underestimates the data slightly.
In leading order QCD, the distribution of the azimuthal angle between the two jets is expected to peak at 180° since the two heavy quarks should be back to back in the photon-gluon rest frame. The distribution is smeared out due to detector resolution effects and shows a tail to smaller angles as depicted in figure 5.11 (b). The tail originates from hard gluon radiation and fragmentation. Figure 5.11 (b) shows, that the PYTHIA simulation is not fully able to reproduce the data at lower values of $\delta\phi^{jets}$, as the higher order contributions are apparently somewhat underestimated in the Monte Carlo simulation.

5.5 Reconstructed and Generated Variables

In this section the correlations between generated and reconstructed variables are evaluated. These studies are done with the simulated PYTHIA Monte Carlo prediction and a correction factor is determined, which takes the limited acceptance, efficiency and resolution of the detector into account. The following sections present the resolutions and correlations (section 5.5.1), the amount of migrations (section 5.5.2) and the reconstruction efficiencies (section 5.5.3).

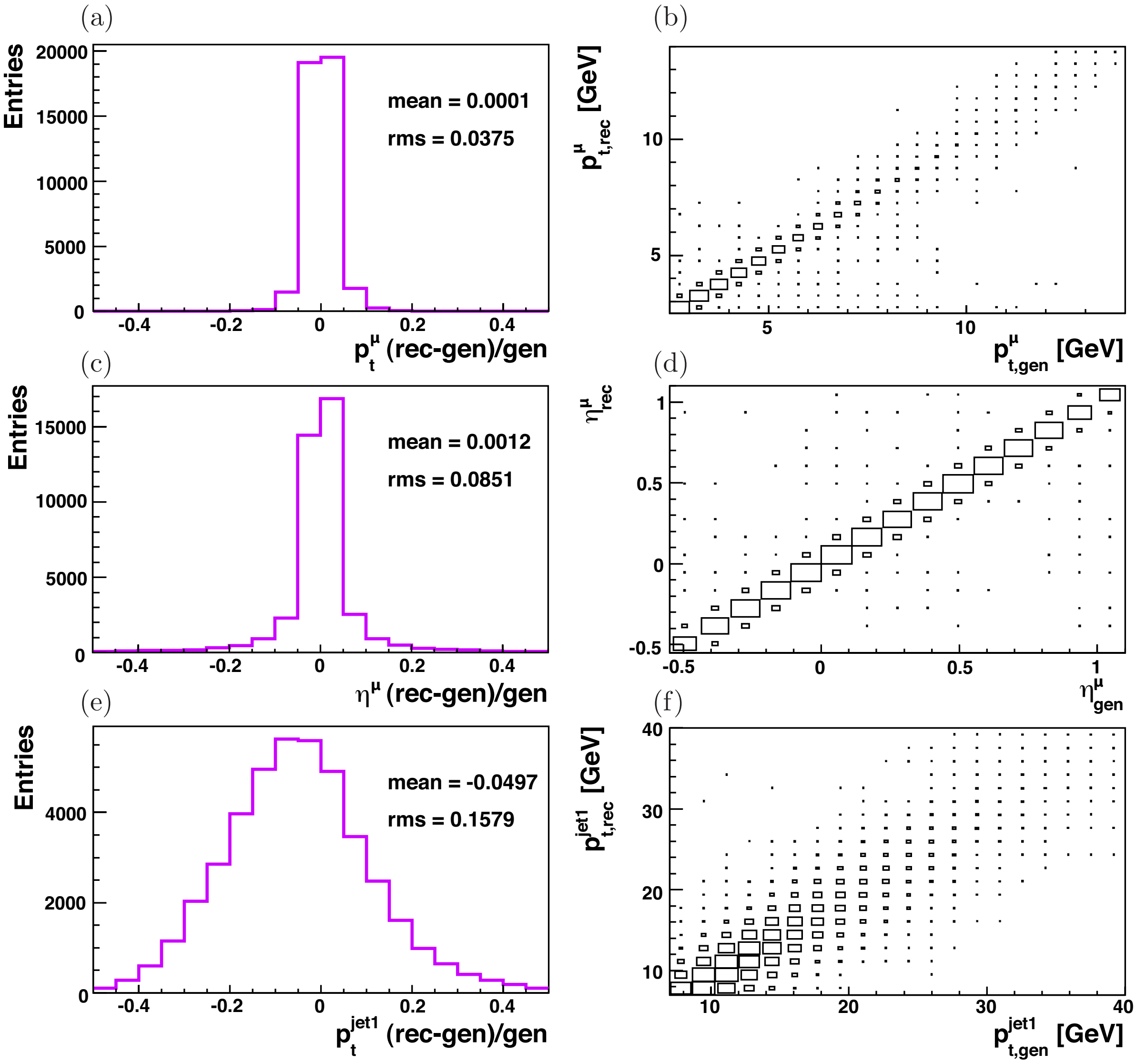

Figure 5.12: Resolutions (left column) and correlations (right column) for the PYTHIA beauty Monte Carlo simulation as a function of p_t^μ, η^μ and p_t^{jet1}.

5.5.1 Resolutions and Correlations

The resolutions and correlations, as calculated with the PYTHIA simulation for events with beauty quarks, are shown in figure 5.12 and 5.13 for the variables p_t^μ, η^μ, p_t^{jet1}, $\delta\phi^{jets}$ and x_γ^{obs}. The plots show the correlation between reconstructed and generated variables for events, which fulfill all cuts on detector and on hadron level. The PYTHIA charm simulation has a very similar behaviour.

The resolution illustrates the relative deviation of the reconstructed variable from the generated one. Figure 5.12 (a) shows, that according to the simulation, the variable p_t^μ has a

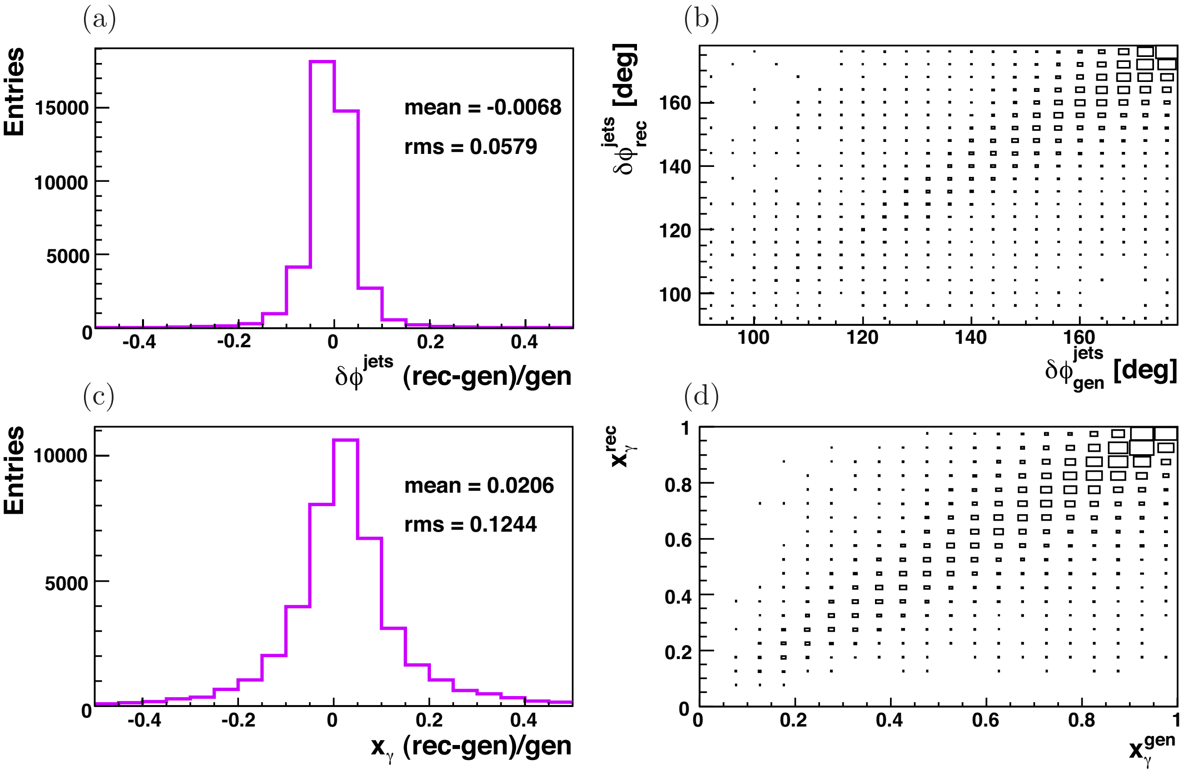

Figure 5.13: Resolutions (left column) and correlations (right column) for the PYTHIA beauty Monte Carlo simulation as a function of $\delta\phi^{jets}$ and x_γ^{obs}.

resolution of $\sim$ 4% and is reconstructed on average only $\sim$ 0.01% too high, which is a very good result. Figure (c) illustrates that the pseudorapidity of the muon is reconstructed on average 0.1% too high and its resolution is roughly 9%. The transverse momentum of the leading jet p_t^{jet1} is reconstructed on average $\sim$ 5% too low and has a resolution of $\sim$ 16% as can be seen in figure 5.12 (e). The explanation is, that the jet energy is reconstructed lower than the generated one due to the neutrino energy, which is not detectable, but contained in the generated jet.

Figure 5.13 (a) shows that the difference in azimuthal angle between the two jets is reconstructed on average about 0.1% too low and its resolution is roughly 6%. This is a very good result. Figure (c) illustrates an average resolution of x_γ^{obs} of roughly 12%, which could be caused by the complex event structure of the resolved processes that are included. On average, this variable is reconstructed about 2% too high.

In the right column of figures 5.12 and 5.13 the correlation between detector and hadron level are shown for the PYTHIA Monte Carlo simulation containing beauty quarks. The charm Monte Carlo gives very similar results and is not shown here. The matching between detector and hadron level is very good for η^μ and p_t^μ. For the other three variables, the correlation is reasonable. The histograms illustrate that jets and their quantities, found on detector level, are not necessarily the same as on hadron level. This is most probably due to events with more than two jets, which differ on detector and hadron level.

5.5.2 Purity and Stability

The purity is the fraction of the number of events which are reconstructed and generated $N_{rec\&gen}(i)$ in a certain bin i, divided by the number of events that are reconstructed in the same bin $N_{rec}(i)$. The stability is calculated by the number of reconstructed and generated events in a bin, divided by the number of generated events $N_{gen}(i)$ in this bin. The purity and stability of the PYTHIA Monte Carlo simulation is determined by using equations (5.3) and (5.4):

$$\text{Purity}(i) = \frac{N_{rec\&gen}(i)}{N_{rec}(i)} \tag{5.3}$$

$$\text{Stability}(i) = \frac{N_{rec\&gen}(i)}{N_{gen}(i)}. \tag{5.4}$$

Thus $(1 - \text{Purity}(i))$ gives the fraction of events which migrate into a certain bin while $(1-\text{Stability}(i))$ yields the migration out of a bin. In an ideal detector both quantities would be equal to one, which would indicate a perfect resolution.

The purity (left column) and the stability (right column) as a function of p_t^μ, η^μ, p_t^{jet1}, $\delta\phi^{jets}$ and x_γ^{obs} are shown in figure 5.14 for the PYTHIA beauty (solid line) and charm (dashed line) Monte Carlo simulation. The purities are always well above 40%. As illustrated in figure 5.12 (e) and explained above, p_t^{jet1} is reconstructed on average too low due to the missing neutrino energy. This leads to migrations into lower bins, which are illustrated by the low purity and the high stability at low p_t^{jet1}.

The purity and stability of the muon quantities p_t^μ and η^μ are found to be very high. This indicates very low migrations and this is expected as their resolutions are very good as shown in figure 5.12 [(a), (b)].

Figure 5.15 depicts the purity and the stability in the region $x_\gamma^{obs} > 0.75$ as a function of p_t^μ, η^μ, p_t^{jet1} and $\delta\phi^{jets}$. The results are very similar to the full sample. The beauty and charm Monte Carlo simulation show a very similar behaviour.

5.5.3 Reconstruction Efficiency

As shown in the last sections, the PYTHIA Monte Carlo simulation models the data reasonably well and it can thus be used for the determination of the reconstruction efficiency. The reconstruction efficiency ϵ_{rec} is the fraction of the number of events reconstructed N_{rec} divided by the number of events generated, N_{gen}, in the visible range:

$$\epsilon_{rec} = \left.\frac{N_{rec}}{N_{gen}}\right|_{vis}. \tag{5.5}$$

It is studied for the PYTHIA Monte Carlo simulation and the visible selection cuts presented in the last sections including the reconstruction itself are applied, except for the trigger

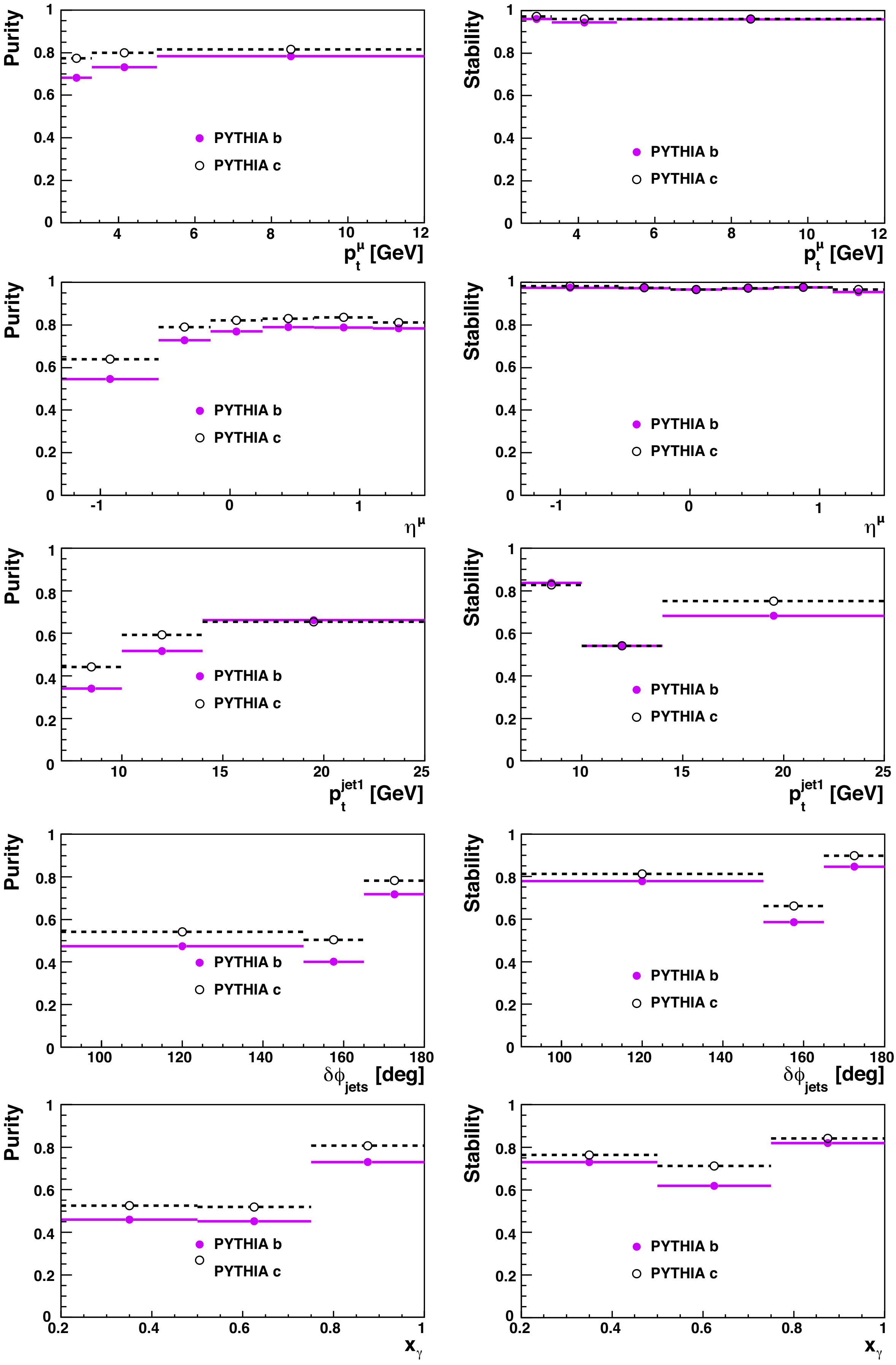

Figure 5.14: Purity (left column) and stability (right column) for the PYTHIA Monte Carlo simulation. The beauty (solid pink line) is shown in comparison to the charm (dashed black line) simulation as a function of p_t^{μ}, η^{μ}, p_t^{jet1}, $\delta\phi^{jets}$ and x_{γ}^{obs}.

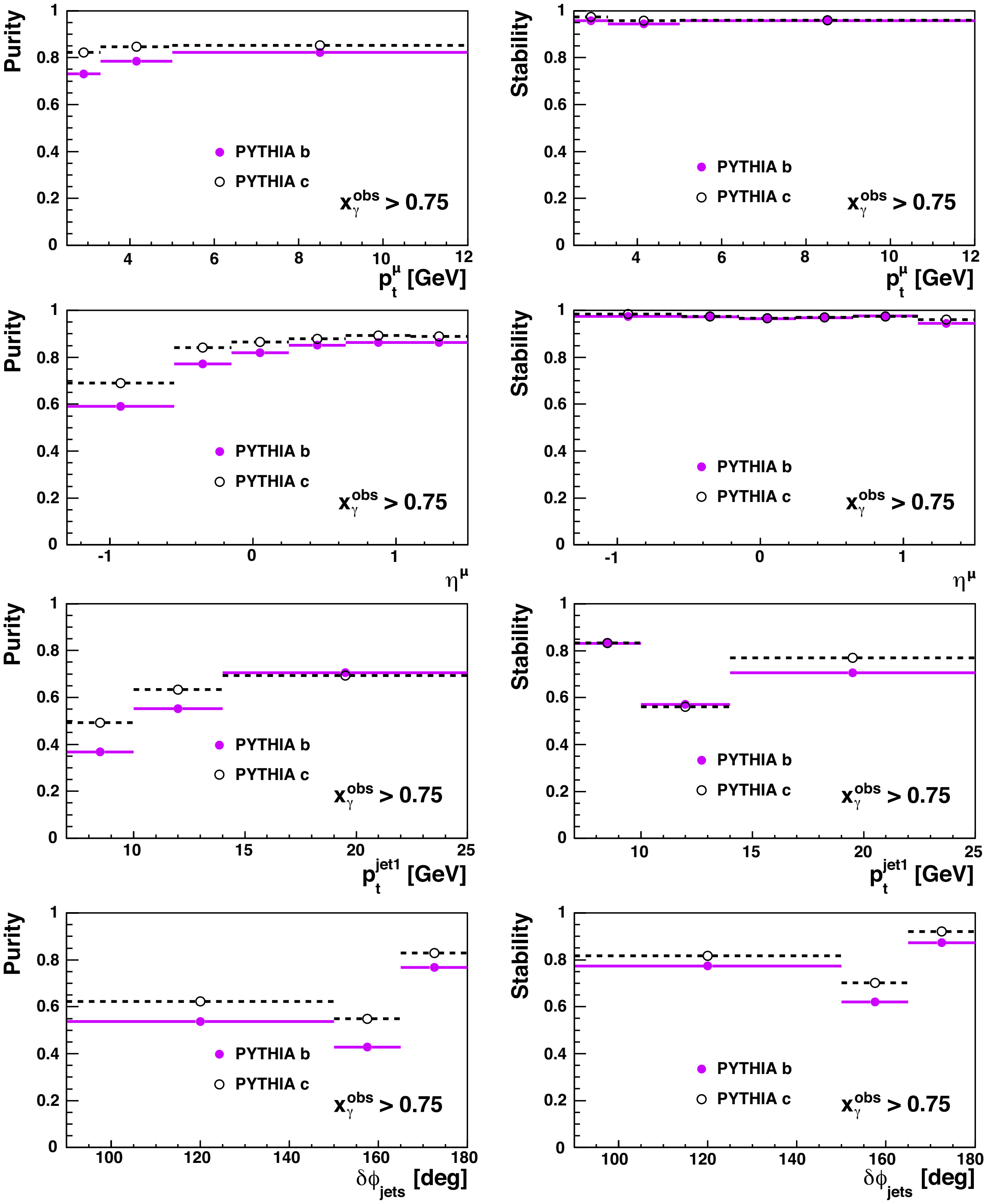

Figure 5.15: Purity (left column) and stability (right column) for the PYTHIA Monte Carlo simulation. The beauty (solid pink line) is shown in comparison to the charm (dashed black line) simulation as a function of p_t^μ, η^μ, p_t^{jet1} and $\delta\phi^{jets}$ for the region $x_\gamma^{obs} > 0.75$.

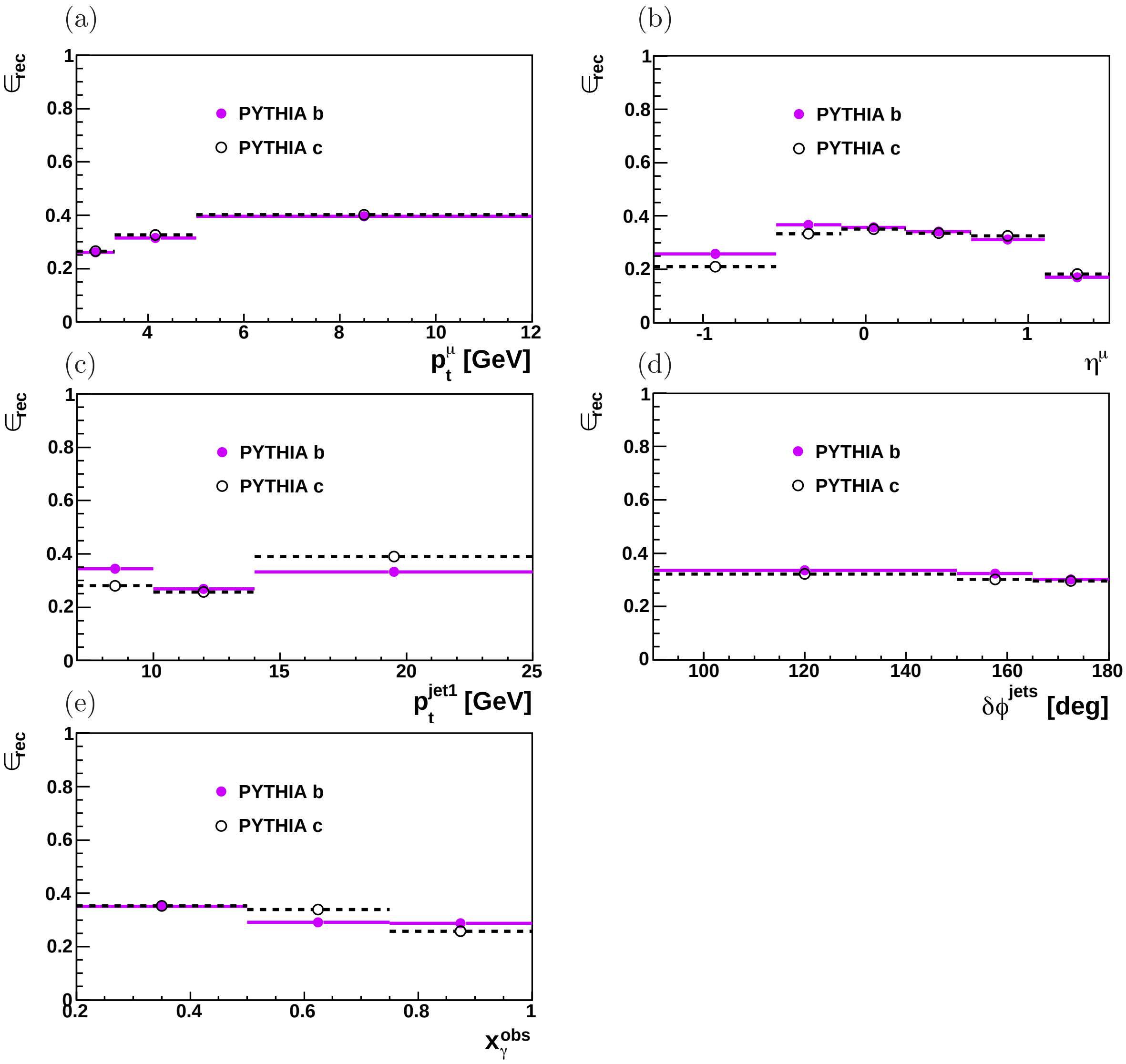

Figure 5.16: Reconstruction efficiency calculated with the beauty (solid line) and charm (dashed line) PYTHIA Monte Carlo simulation as a function of p_t^μ (a), η^μ (b), p_t^{jet1} (c), $\delta\phi^{jets}$ (d) and x_γ^{obs} (e).

requirements. Figure 5.16 shows the reconstruction efficiencies as a function of p_t^μ (a), η^μ (b), p_t^{jet1} (c), $\delta\phi^{jets}$ (d) and x_γ^{obs} (e). The efficiencies are calculated using the PYTHIA beauty (solid line) and the charm (dashed line) simulation. In both cases, the efficiencies have a similar behaviour. The reconstruction efficiency of the full sample is 31% according to the PYTHIA simulation. The values of the reconstruction efficiencies according to the PYTHIA simulation for the charm and beauty measurement can be found in appendix A. The reconstruction efficiency as a function of p_t^μ (a) shows an increase towards higher values of the transverse momentum of the muon as expected for both beauty and charm simulations. Figure 5.16 (b) shows a decreasing reconstruction efficiency in the first and the last bins, which correspond to the backward and forward region, respectively. This can be explained as, due to the fact that tracks measured in the barrel and the end caps are not linked, causing a step in the efficiency for the transition regions. The histogram in (c) depicts ϵ_{rec} as a function of p_t^{jet1}. The reconstruction efficiency is almost flat for both the Monte Carlo simulations containing beauty and charm events. In the first bin of p_t^{jet1}, the reconstruction efficiency for the beauty simulation is higher than the one for charm. This effect is more prominent in the region $x_\gamma^{obs} > 0.75$, as depicted in figure 5.17 (c). Figure 5.16 (d) shows an almost flat distribution at a level of roughly 30% of the reconstruction efficiency as a function of the azimuthal angle between the two jets for the beauty and the charm simulation. Figure (e) depicts the reconstruction efficiency as a function of x_γ^{obs}. The beauty and the charm simulation show a similar behaviour. In both cases, the distribution is nearly flat and the reconstruction efficiency is almost independent of x_γ^{obs}. In figure 5.17 the reconstruction efficiency is studied for direct processes only. Here, the region $x_\gamma^{obs} > 0.75$ is investigated, which shows a similar dependence of the variables as the whole sample. Since 5.16 (d) depicts a flat distribution, this similar result is expected.

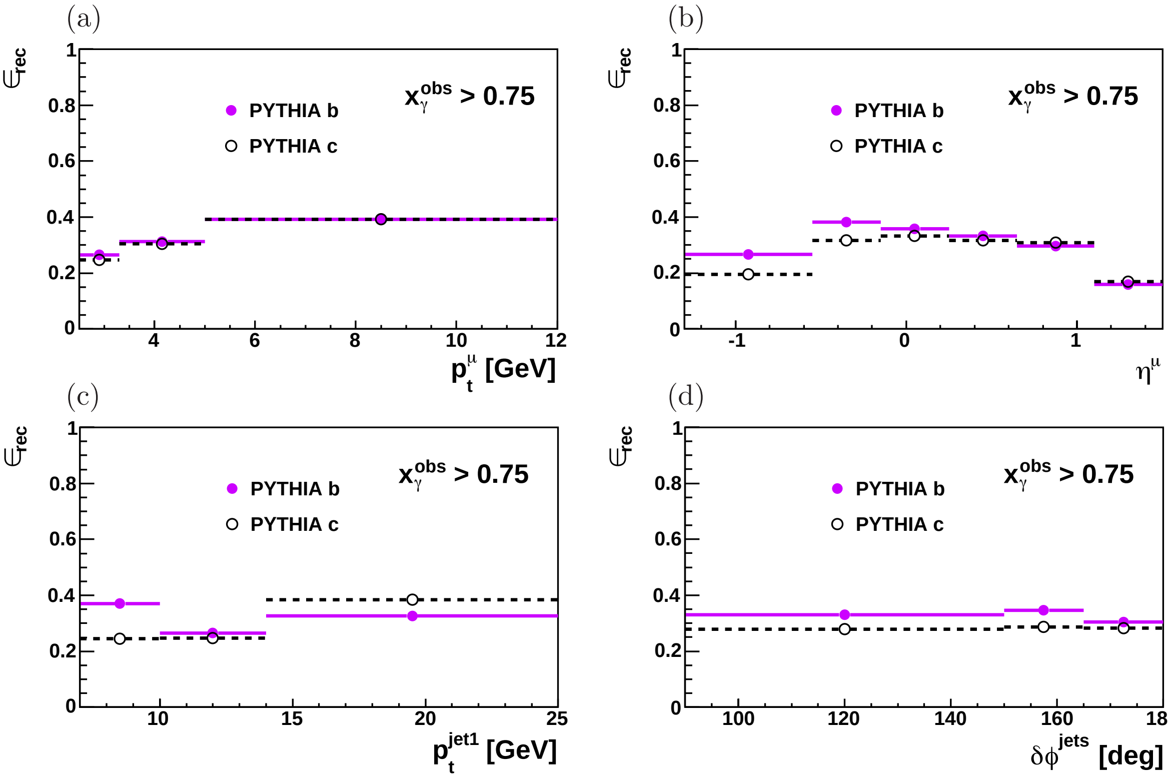

Figure 5.17: Reconstruction efficiency calculated with the beauty (solid line) and charm (dashed line) PYTHIA Monte Carlo simulation as a function of p_t^μ (a), η^μ (b), p_t^{jet1} (c) and $\delta\phi^{jets}$ (d) for the region $x_\gamma^{obs} > 0.75$.

Chapter 6

Quark Flavour Separation

In this chapter, the method to distinguish events containing different quark flavours is explained. As the goal is to measure charm and beauty cross sections, it is crucial to find quantities, which are sensitive to these flavours. The two variables providing this feature are the transverse momentum of the muon relative to the jet axis, p_t^{rel}, and the distance of the muon track to the event vertex, δ. The first one makes use of the large mass of b hadrons, while the second variable profits from the large lifetime of charm and beauty flavoured hadrons. The two variables are almost independent and thus a cross check is possible. For the measurement of the beauty contribution, one can either use the two variables separately or combine them and perform a 2-dimensional fit. These methods are well established and were already used in former theses and publications [58], [59].
The chapter is structured as follows: at first, the separation methods are discussed, followed by an explanation of the fitting procedure. Then, the stability and consistency of the fits are investigated and finally the results of the combined fits are presented and discussed.

6.1 Separation Methods

6.1.1 The Mass Method

The transverse momentum of the muon relative to the jet axis p_t^{rel} is determined as follows:

$$p_t^{rel} = \frac{|\vec{p}_\mu \times (\vec{p}_{jet} - \vec{p}_\mu)|}{|\vec{p}_{jet} - \vec{p}_\mu|}, \tag{6.1}$$

here $\vec{p}_\mu$ and $\vec{p}_{jet}$ are the momentum vectors of the muon and the associated jet, respectively. Following the convention in [59], the muon momentum is subtracted from the jet momentum. Figure 6.1 shows the p_t^{rel} distribution for the selected events after the corrections described in the following. The PYTHIA Monte Carlo is normalized to the data (points) and weighted according to the 2-dimensional fit result. The sum of the charm, beauty and light quark contributions describes the data reasonably well. The shapes of the simulated quark contributions differ as the beauty distribution is shifted to higher p_t^{rel}. The shapes of the charm and light quarks distributions look very similar, which demonstrates that the 1-dimensional

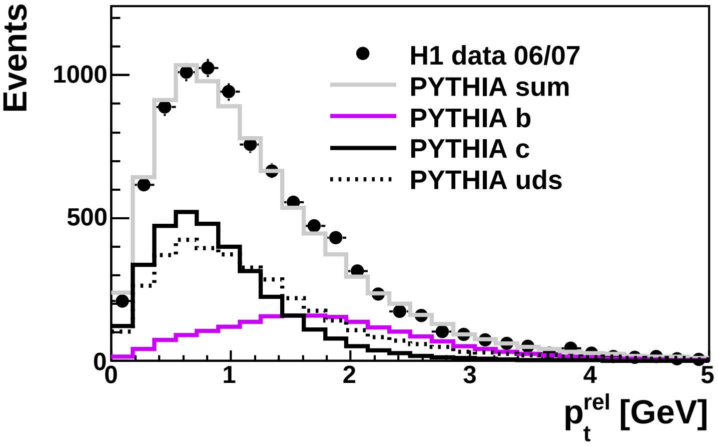

Figure 6.1: The p_t^{rel} distribution after all corrections for the selected events. The data (points) in comparison to the PYTHIA Monte Carlo simulation.

fit of p_t^{rel} can only distinguish between two components: beauty and the sum of charm and light quarks. In the following, the fraction of events containing light quarks in the p_t^{rel} fit is fixed to the value obtained in the δ fit. Therefore, the 1-dimensional fit of p_t^{rel} is used as a cross-check for beauty only. The advantage of the mass method is the usage of higher statistics as no CST requirements are needed.
In order to obtain reliable fit results with the mass method, a good description of the background shapes in the Monte Carlo simulation is crucial. This is investigated by comparing background distributions of the data and the simulation. A data sample containing mainly background is produced by applying the event selection (cf. table 5.3) without muon identification. Instead of the muon requirements, a single track selection is performed in the same kinematic region. The association of the track to one of the two highest p_t jets is done by applying a ΔR cut:

$$\Delta R = \sqrt{\Delta\eta^2 + \Delta\phi^2}. \tag{6.2}$$

The variable p_t^{rel} is calculated again using formula (6.1) with $\vec{p}_{track}$ instead of $\vec{p}_\mu$. This data sample is compared to a simulated light quark Monte Carlo sample, where the same track requirements are applied. The comparison is shown in figure 6.2 (a). The PYTHIA simulation (dotted line) overestimates the data (points) at low p_t^{rel} and underestimates it at high values of p_t^{rel}. This is corrected by a smearing of the polar and azimuthal angle resolution of the jet. A Gaussian function with a width of 2° is added randomly to the polar and azimuthal angle of the jet in every simulated event in the light quark Monte Carlo. As depicted in figure 6.2 (a) (solid line), a much better description of the data is achieved. A further motivation of this smearing parameter is the 1-dimensional fit of the p_t^{rel} distribution. The quality of the fit can be checked by the help of χ^2, which should be very small. Therefore, several background

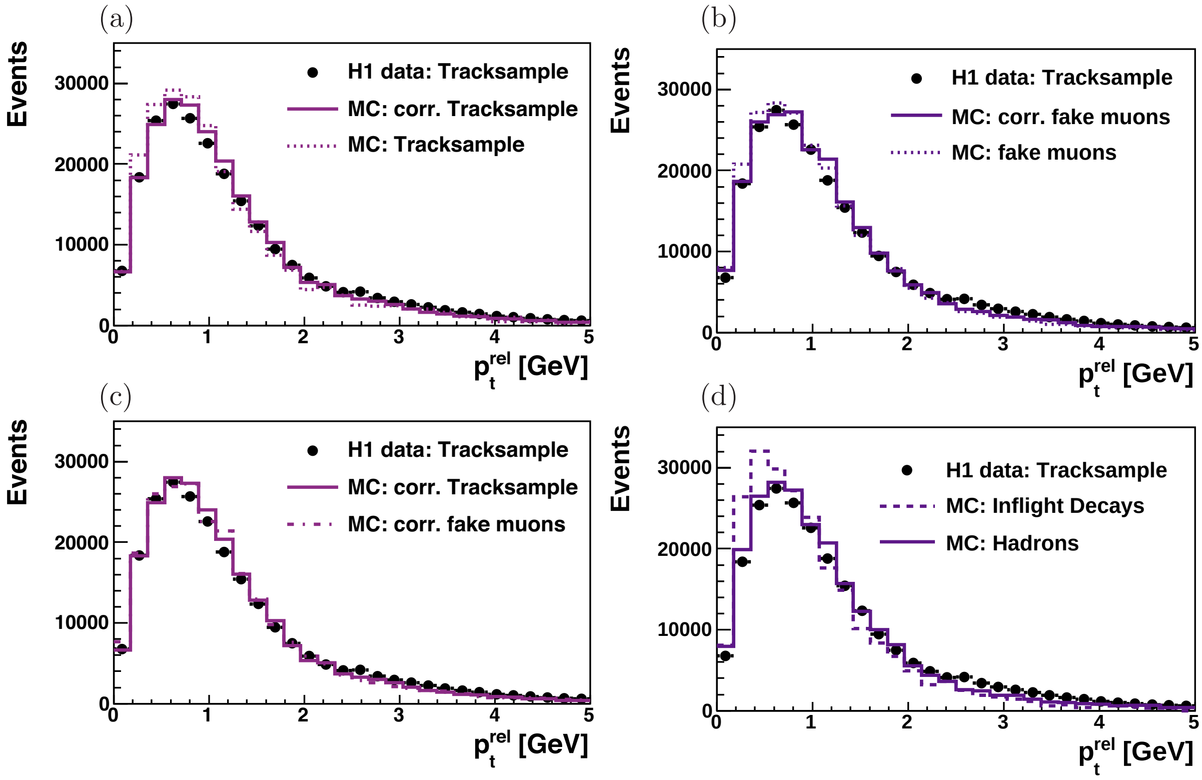

Figure 6.2: Distribution of p_t^{rel} for a data tracksample (points) in comparison to the Monte Carlo simulation. In (a), the data is compared to an inclusive Monte Carlo tracksample with (solid line) and without (dotted line) the corrections. In (b), the fake muon sample before (dotted line) and after (solid line) the correction are shown. In (c), the corrected tracksample (solid line) and fake muon sample (dashed dotted line) are compared. In (d), the data tracksample is compared to inflight decays (dashed line) and misidentified hadrons (solid line). Both fake muon contributions are normalised to the data, to be able to compare the shapes.

samples were produced with different values for the jet direction smearing from 0° up to 4°. The 1-dimensional fits are performed with every background sample and the χ^2 values of the total fit of p_t^{rel} are checked. It is found, that a value of 2° leads to a reasonable χ^2/ndf of ≈ 2.

The fake muon background can be divided into two parts as discussed in section 5.3: inflight decays and misidentified hadrons. The contribution of inflight decays is controlled - amongst others - by the PYTHIA parameter `PARJ(2)`. This parameter stands for the ratio $\mathcal{P}(s)/\mathcal{P}(u)$, which controls the suppression of strange quark pair production compared to up quark pair production. According to the results obtained in [94], this parameter should be set to 0.22. In the Monte Carlo samples used in this thesis, `PARJ(2)` is set to 0.28, which could cause an overestimation of inflight decays contributing to the fake muon background. In figure 6.2 (d), the light quark Monte Carlo sample is divided into inflight decays (dashed line) and hadrons (solid line), which are misidentified as muons. All analysis cuts are applied, including the muon identification. The p_t^{rel} distribution of a data tracksample, which fulfils all analysis

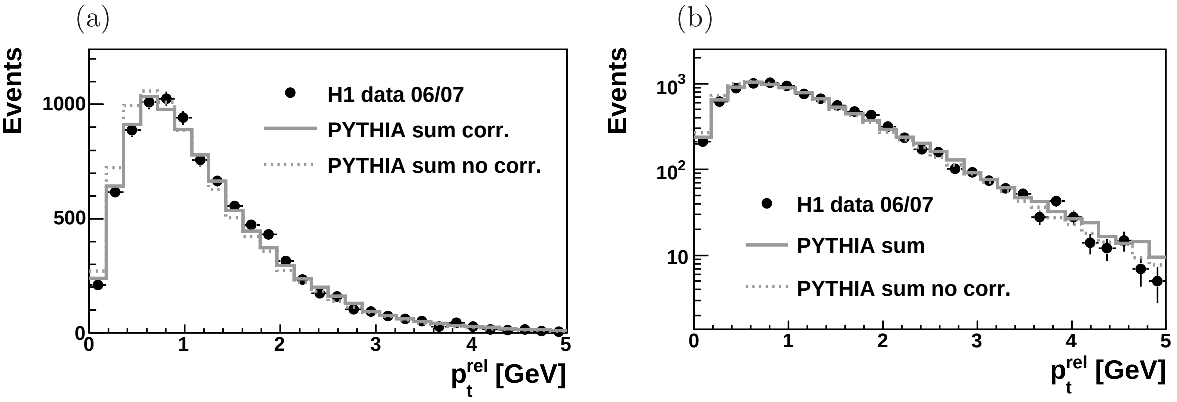

Figure 6.3: Distribution of p_t^{rel} for data (points) in comparison to the corrected (solid line) and not corrected (dotted line) Monte Carlo simulation.

cuts besides the muon identification, is compared to these two contributions of the fake muon background. For a comparison of their shapes, the Monte Carlo distributions are normalised to match the data. The p_t^{rel} distribution of inflight decays is shifted to smaller values of p_t^{rel}, while hadrons show a harder p_t^{rel} spectrum, which is very similar to the data. The softer p_t^{rel} spectrum of inflight decays can be explained by the neutrino, which is also produced in kaon and pion decays. It escapes undetected and therefore lower values of the transverse momenta of the final state particles are observed in comparison to undecayed, misidentifed hadrons, which are also mainly kaons and pions. Applying all corrections, the p_t^{rel} distribution of the fake muon sample also describes the data distribution better than before. This is shown in figure 6.2 (b). Here, the dotted line represents the fake muon sample without and the solid line with the corrections.

In order to cross check, if the above described adjustment of the Monte Carlo tracksample to the data tracksample is usable, the simulated tracksample (solid line) including the corrections is compared to the simulated fake muon sample (dashed dotted line) with corrections in figure 6.2 (c). Since the Monte Carlo tracksample contains mainly background, the two samples should be very similar. As expected, both distributions are in good agreement.

After the jet direction smearing and the change of the inflight decay contribution, the p_t^{rel} distribution of the analysed data is much better described. The comparison of the corrected (solid line), not corrected simulation (dotted line) and the data is shown in figure 6.3 in linear and logarithmic scale. The Monte Carlo distribution is the sum of the quark contributions scaled with their fractions obtained in the combined fit and normalised to the data.

6.1.2 The Lifetime Method

The lifetime method is able to distinguish between three components of the quark contributions: charm, beauty and light quarks. This is caused by long lifetimes of charm and beauty flavoured hadrons, which leads to distinguishable distributions. The signed impact parameter is calculated with respect to the primary event vertex as explained in section 4.2. The axis of the jet, which is associated to the selected muon candidate, is the direction of its

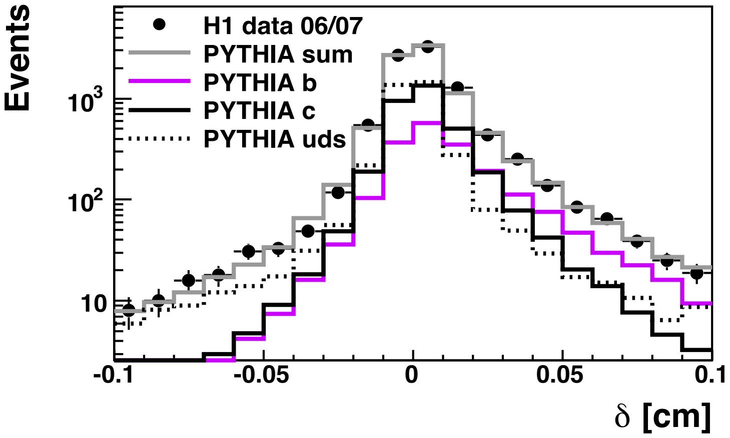

Figure 6.4: The δ distribution for the selected events. The data (points) in comparison to the PYTHIA Monte Carlo simulation.

three momentum vector $\vec{p}_{muonjet}$ provided by the jet algorithm. To be consistent with the definition of p_t^{rel}, the three momentum vector of the muon $\vec{p}_\mu$ has to be subtracted from the one of the muonjet:

$$\vec{p}_{jet} = \vec{p}_{muonjet} - \vec{p}_\mu. \tag{6.3}$$

The impact parameter δ is depicted in figure 6.4. The sum of the simulated quark contributions is in excellent agreement with the data (points). The results of the 2-dimensional fit are applied to the three different quark flavours. Due to the long lifetimes, the shape of the distributions is asymmetric. Since the lifetimes for charm, beauty and light flavoured hadrons are different, the asymmetries differ as well. While the b component shows a very marked asymmetry, the c distribution is moderately asymmetric. The light quark component is nearly symmetric at low δ. The asymmetry at $|\delta| > 0.1$ cm is mainly due to decays of long lived strange particles such as K_s^0. To reduce the effects of the strange contribution, the signed impact parameter is restricted to $|\delta| < 0.1$ cm. The region of negative δ reflects the finite resolution of the impact parameter reconstruction.

The error of the signed impact parameter σ_δ contains contributions from the uncertainty of the event vertex position and the error of the muon track. It is reasonably well described by the simulation.

The significance S_i is shown in figure 6.5 (b). The data is very well modelled by the PYTHIA simulation. It is defined by the ratio of the signed impact parameter to its error for all selected tracks i:

$$S_i = \frac{\delta_i}{\sigma_{\delta_i}}. \tag{6.4}$$

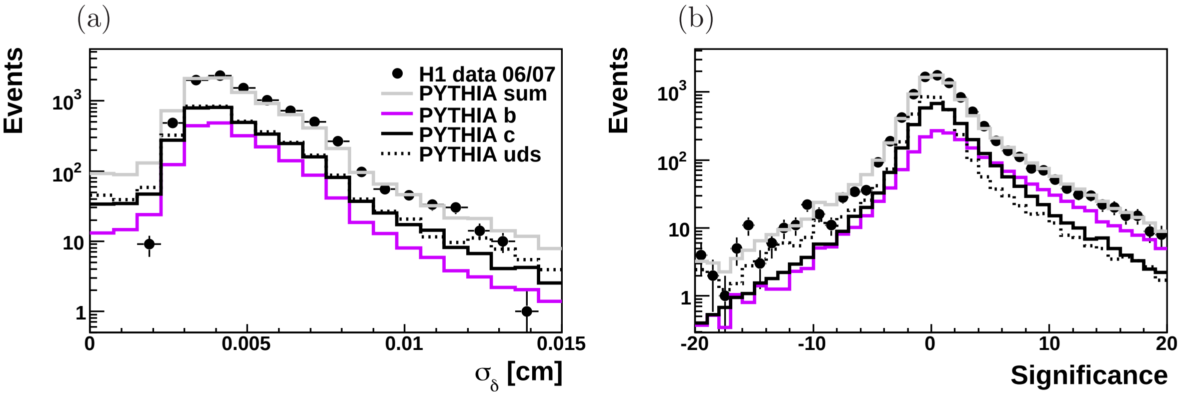

Figure 6.5: The error of the signed impact parameter σ_δ (a) and the significance (b), which is defined as the ratio of the signed impact parameter to its error. The data (points) in comparison to the PYTHIA simulation.

The advantage of the 1-dimensional fit of the signed impact parameter is the ability to distinguish between three quark contributions. Therefore, this method is the basis of extracting the charm contribution. For the beauty contribution, this method is used to cross check the results obtained by the mass method. The disadvantage of the lifetime method is the usage of lower statistics than for fitting the p_t^{rel} distribution, since CST requirements are necessary. The mass method has a higher separation power to differentiate between the beauty and the sum of the charm and light quark contribution.
The above described correction for p_t^{rel} concerning the PYTHIA parameter `PARJ(2)` also has an impact on the lifetime method. Since particles containing strange quarks can be found mainly at high positive δ, the downscaling of the strange contribution leads to a higher fitted contribution of events containing beauty quarks. In the combined fit of the two variables, the effects of a lower beauty contribution in the p_t^{rel} fit and a higher one in the δ fit cancel almost. The aim of these corrections is an improved description of the single variables and a better agreement of their 1-dimensional fit results.

6.2 Fitting Procedure

To measure the charm and beauty fractions, a statistical method is used, which is based on a fit of template distributions derived from the Monte Carlo simulations to the data. The Monte Carlo templates can be used, since the lifetimes and masses of the heavy flavoured hadrons are well known, as well as the track resolutions are well determined. In the lifetime method charm, beauty and light quark Monte Carlo templates are used as input. For the p_t^{rel} method the fraction of events containing light quarks is fixed to the value obtained in the δ fit. The shapes of the distributions are not smooth but binned and a *binned likelihood fit* [95] is performed. The content of each bin is assumed to be Poisson distributed for both the data and the simulated templates. In this analysis, an extended fitting method is used [95], which takes fluctuations of the simulated events into account. Additionally, it is possible to use weighted Monte Carlo templates and single empty bins are treated adequately. The Root analysis package [96] provides the implementation of the fitting package and is applied in this analysis. The MINUIT minimisation library is used in Root to perform the fit [97]. In the following, a brief description of the fit method is presented, further details can be found in [95].

The predicted number of data events in each bin i is described by the function $f_i(P_1, \ldots, P_m)$, which depends on the strengths P_j for each source j. The P_j sum to unity, since they are the actual proportions of the Monte Carlo samples. It is convenient to introduce strength factors $p_j = N_D P_j / N_j$, which are calculated using the total number of data events N_D and the total number of Monte Carlo events N_j. Taking statistical fluctuations of the input templates into account, the (unknown) expected number of Monte Carlo events is described by A_{ji}. With this variable the prediction for the number of data events is given by

$$f_i = \sum_{j=1}^{m} p_j A_{ji}. \tag{6.5}$$

The estimation of the strength factors p_j is done by maximising the total likelihood. For convenience, the maximisation is done for the logarithm of the total likelihood:

$$\ln \mathcal{L} = \sum_{i=1}^{n} d_i \ln f_i - f_i + \sum_{i=1}^{n} \sum_{j=1}^{m} a_{ji} \ln A_{ji} - A_{ji}. \tag{6.6}$$

Here, d_i are the number of data events in each bin i and a_{ji} stands for the number of Monte Carlo events from source j in bin i. The parameter of interest is the strength factor p_j. The expected number of Monte Carlo events A_{ji} is a tool and the result is not of importance. To maximise the total likelihood, equation (6.6) is differentiated and set to zero afterwards. This gives a set of $m \times (n+1)$ equations, which are nonlinear and coupled. After a simplification a solution is found using an iterative method.

To be able to use this fitting method, the data has to be described very well by the Monte Carlo templates. As shown before, this is the case for the presented analysis. The method is only able to separate different Monte Carlo simulation contributions, if their shapes of the fitted distributions deviate. As described above, the two variables p_t^{rel} and the impact parameter provide this.

6.2.1 Stability and Consistency of the Fit

The results of the fit should not depend significantly on arbitrarily chosen circumstances, like the binning or the Monte Carlo or data statistics. The dependence on the binning is checked by repeating the analysis for different numbers of bins for the input distributions. The fit results seem to be very stable and the very small deviations are within the statistical errors of the fits. Changing the binning from equidistant to non-equidistant gives consistent results. The same is tested for the combined fit. Reasonable variations of the number of bins and non-equidistant binnings lead again to results, which are consistent.

Both, the mass and the lifetime method, are able to extract the contribution of events containing beauty quarks. Their 1-dimensional fit results are compared to check their consistency. As described above, the two methods are extensively independent. Since the mass method is not able to extract the charm fraction, the cross check is done for beauty only. Fitting the p_t^{rel} (cf. figure 6.1) and the δ (cf. figure 6.4) distribution separately using the complete event sample leads to beauty fractions of

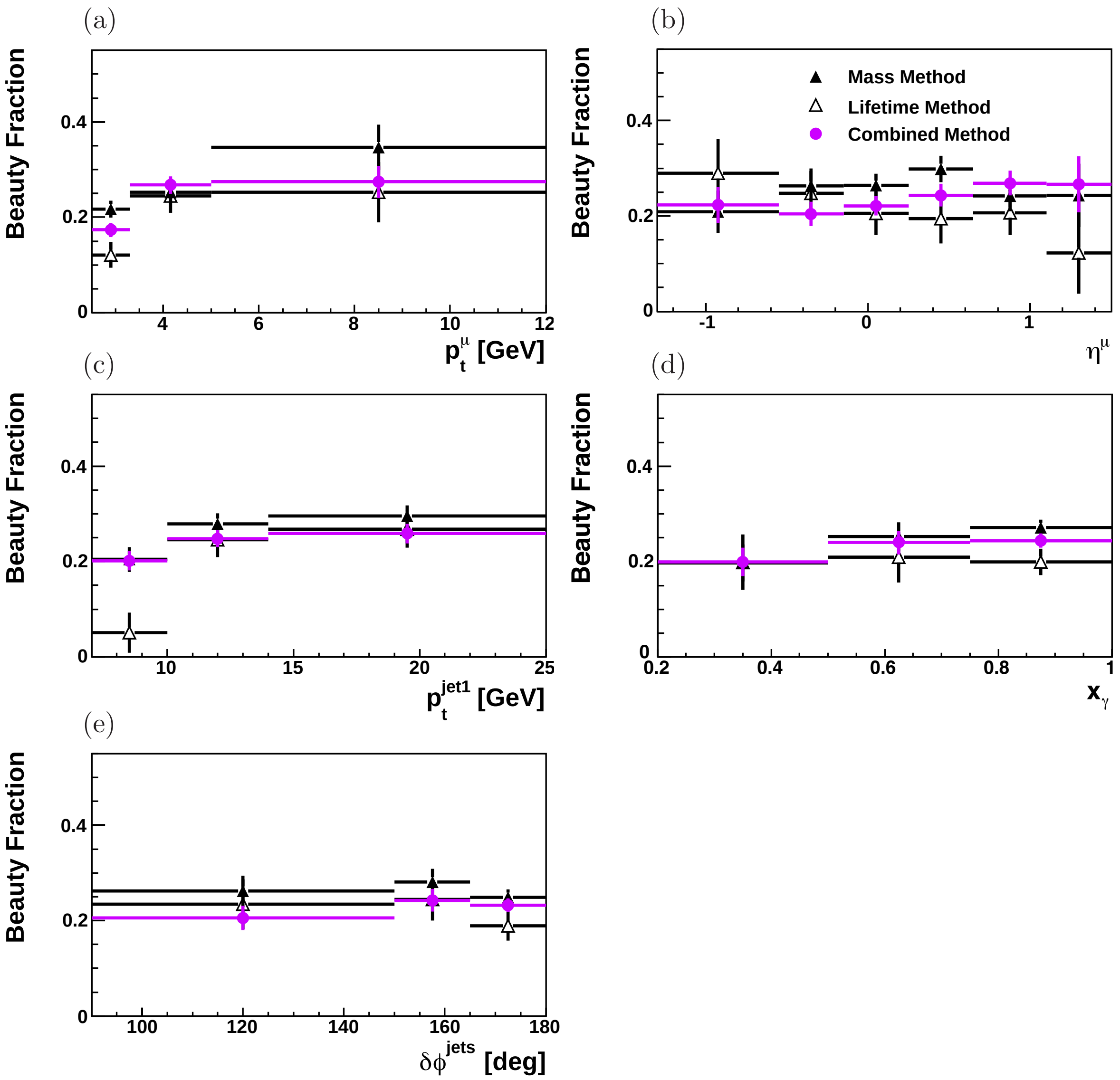

Figure 6.6: Beauty quark fractions determined with the mass (full triangle), the lifetime method (open triangle) and combined method (full circle) in comparison. The fractions are plotted as a function of p_t^μ (a), η^μ (b), p_t^{jet1} (c), $\delta\phi^{jets}$ (d) and x_γ^{obs} (e).

$$f_b^{mass} = 0.26 \pm 0.01 \quad \text{with} \quad \chi^2/ndf = 1.8 \tag{6.7}$$

$$f_b^{lifetime} = 0.21 \pm 0.02 \quad \text{with} \quad \chi^2/ndf = 1.9 \tag{6.8}$$

The results are close together within their statistical errors. The number of degrees of freedom ndf of the fit is the number of bins of the 1-dimensional histogram plus one to take the total number of events into account and minus the free parameters of the fit. For the mass method, the number of free parameters is two: f_b and f_c, since f_{uds} is fixed to the value obtained with the lifetime method. For the lifetime method it is three, since the charm component can be fitted separately. The comparisons of the beauty fractions obtained with the mass and lifetime method as a function of p_t^μ, η^μ, p_t^{jet1}, x_γ^{obs} and $\delta\phi^{jets}$ are shown in figure 6.6. The obtained fractions can be found in the appendix A. The χ^2/ndf are in most cases close to one, which underlines that the fits give reliable results.

Figure 6.6 shows the fractions of beauty events obtained by the mass (full triangle), lifetime (open triangle) and combined (full circle) methods in comparison. The beauty fraction increases towards higher values of p_t^μ, as depicted in (a). This is expected, since the light quark cross section is suppressed towards higher transverse momenta of the jet, whereas the increase of the cross section is slower for heavy quarks due to their masses. The p_t^{rel} results are observed to be higher than the ones obtained by the lifetime method. The combined result is in between.

In figure 6.6 (b), the fit results are depicted differentially in η^μ. In the very backward region the lifetime result is higher than the mass result, in the other regions it is vice versa. The fit results obtained with p_t^{rel} are rather constant, while the lifetime results tend to decrease towards the forward region. The fit results differentially in the variables p_t^{jet1}, x_γ^{obs} and $\delta\phi^{jets}$ are depicted in figures 6.6 (c), (d) and (e), respectively. The dependence on these variables is not very strong. Again, the results obtained by the mass method are higher than the ones fitted with the impact parameter. In most cases, the combined result lies in between.

In general, a good agreement between the two methods is found. But, in the first bin of p_t^μ and p_t^{jet1} a large discrepancy between the two methods is observed. These two bins are correlated. The discrepancy is not understood yet and needs further investigations.

In order to establish the consistency of the two variables further, the beauty cross section as a function of p_t^{rel} and δ is investigated separately. The contribution of the beauty component is enriched by restricting the range of either p_t^{rel} or δ. The beauty cross section is then measured by performing the fit to the other, not restricted variable. The p_t^{rel} spectrum is restricted from > 0 GeV up to > 2.7 GeV in steps of 0.3 GeV, which leads to 10 measurements. The δ distribution is restricted from > -0.1 cm up to > 0.08 cm in steps of 0.02 cm, which also leads to 10 measurements. The contribution of events containing beauty increases as a function of the cut to the restricted variable. The reconstruction efficiency decreases as a function of the cut, since the number of reconstructed events is reduced by the cut. The increase of the beauty fraction and the decrease of the reconstruction efficiency should cancel each other due to the definition of the cross section. This should result in a constant cross section as a function of the cut to the restricted variable. In figure 6.7 (a) and (b), the beauty cross section obtained with the cut, divided by the total beauty cross section as a function of the p_t^{rel} and δ cut is shown. This ratio is expected to be one, which is approximately the case for both measurements.

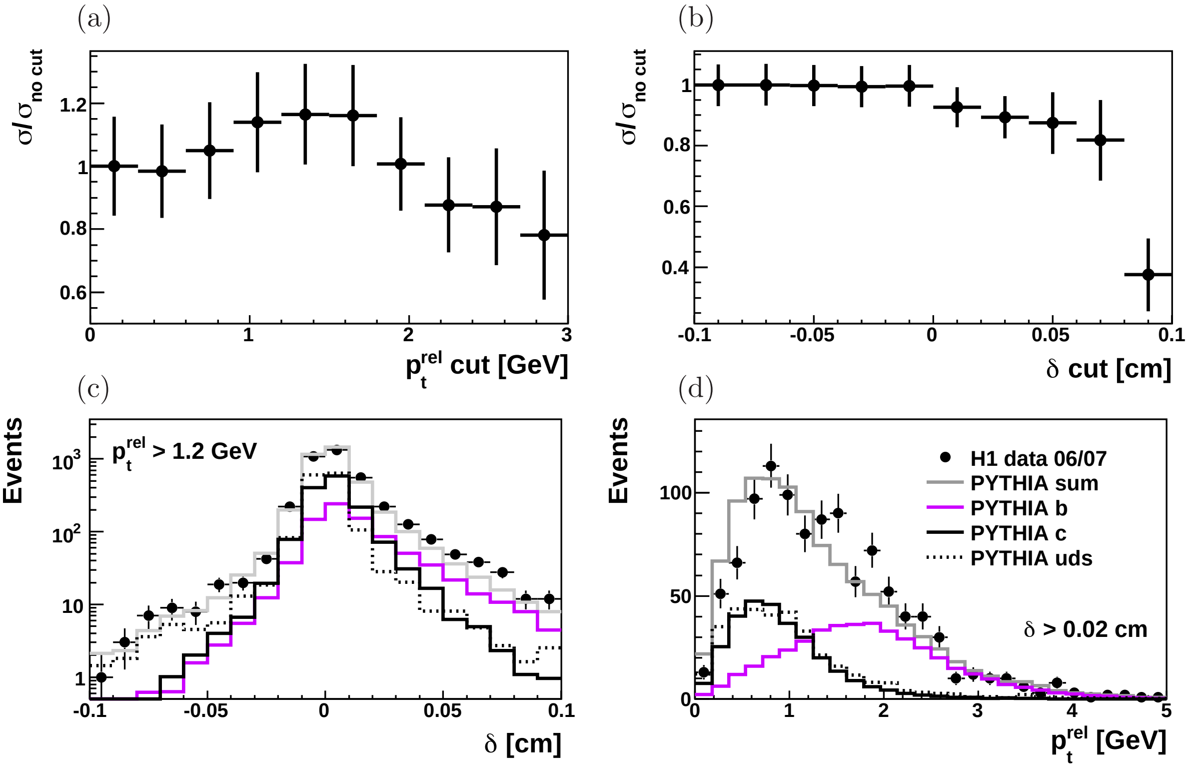

Figure 6.7: The beauty cross section obtained with the cut, divided by the total beauty cross section of the full sample as a function of the p_t^{rel} cut (a) and the δ cut (b). The impact parameter distribution for the region $p_t^{rel} > 1.2$ GeV is shown in (c), while in (d) the p_t^{rel} distribution for $\delta > 0.02$ cm is depicted. The predictions for the quark contributions to the restricted sample are taken from the combined fit.

In figure 6.7 (c), the impact parameter distribution is shown for $p_t^{rel} > 1.2$ GeV. Figure (d) depicts the p_t^{rel} distribution in the region $\delta > 0.02$ cm. The three PYTHIA Monte Carlo distributions are normalised to the data and scaled with the fractions obtained by the 2-dimensional fit. Both figures demonstrate the expected enhancement of the beauty contribution. The quality of the data description by the Monte Carlo simulation illustrates the consistency between the results obtained using the two variables independently.
In the comparison of the 1-dimensional fit results in the first bins of p_t^{jet1} and p_t^{μ} large discrepancies between the obtained beauty fractions are found (figures 6.6 (a) and (c)). For a further investigation of these differences the beauty cross section as a function of p_t^{rel} and δ is determined in the two problematic bins and depicted in figure 6.8. In figures (a) and (b), the cross section ratio is plotted as a function of p_t^{rel} and an almost flat distribution within the errors is observed. In the last two bins in figure (a), the ratio is zero due to low statistics. Figures (c) and (d) depict the cross section ratio as a function of the δ cut. A decrease of the ratio for $\delta > 0$ cm is observed, which may give a hint to a not understood aspect of the lifetime observable. On the other hand, the lifetime distribution decreases exponentially in its tails, which may lead to difficulties in the fits - especially for such low data statistics as

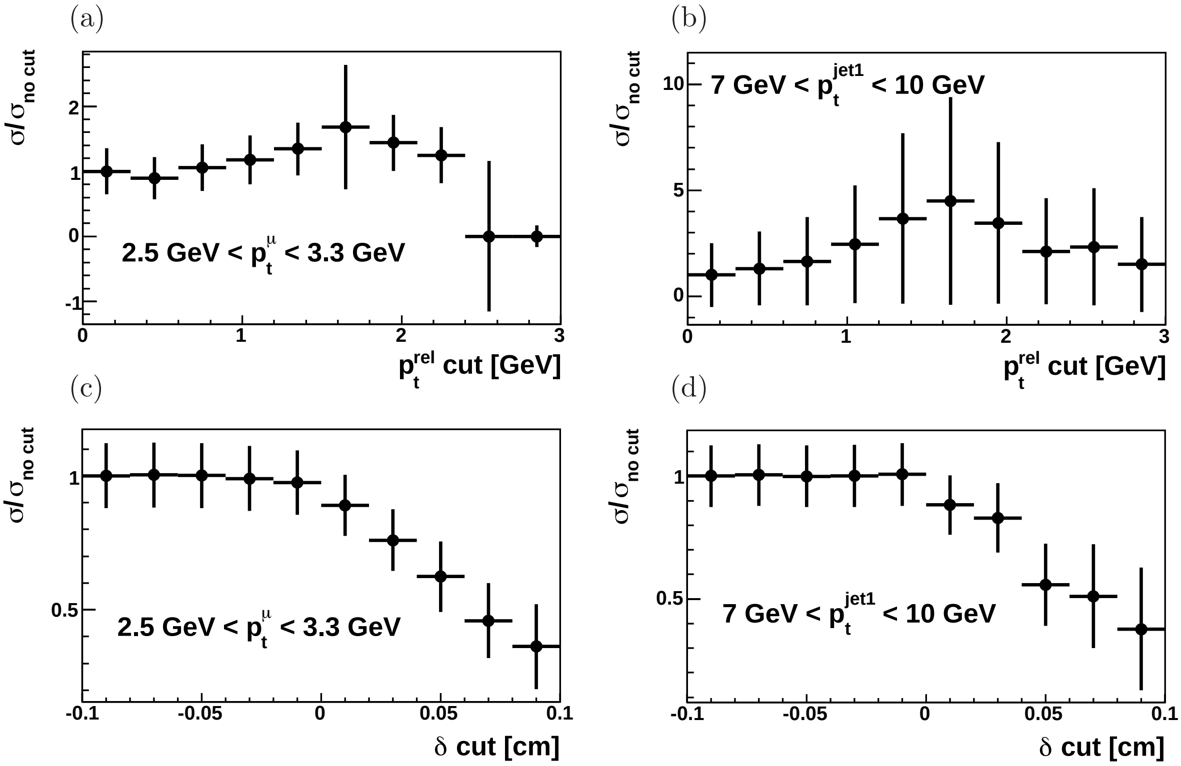

Figure 6.8: The beauty cross section obtained with the cut, divided by the total beauty cross section of the full sample as a function of the p_t^{rel} cut (top) and the δ cut (bottom) in the first p_t^{μ} bin (left) and the first p_t^{jet1} bin (right).

used here in figures 6.8 (c) and (d). To summarize, the fits of the two variables separately give in general consistent and reliable results as shown above. Only in the first bins of p_t^{μ} and p_t^{jet1}, a large discrepancy is observed, which points most likely to the same problem, since these bins are correlated.

6.2.2 Combined Fit Results

Using the two variables separately leads to a consistent description of the signal content in the data, as shown in the last sections. Therefore, the two observables are combined to profit from their individual advantages. The input distributions for the combined fit of the total event sample is depicted in figure 6.9. In (a), the data distribution is shown, while in (b) beauty, in (c) charm and in (d) the light quark distributions are depicted. The combined fit of p_t^{rel} and δ to the complete data sample using the simulated PYTHIA predictions gives the following quark contributions:

$$f_b = 0.24 \pm 0.01 \tag{6.9}$$

$$f_c = 0.32 \pm 0.02 \tag{6.10}$$

$$f_{uds} = 0.45 \pm 0.03. \tag{6.11}$$

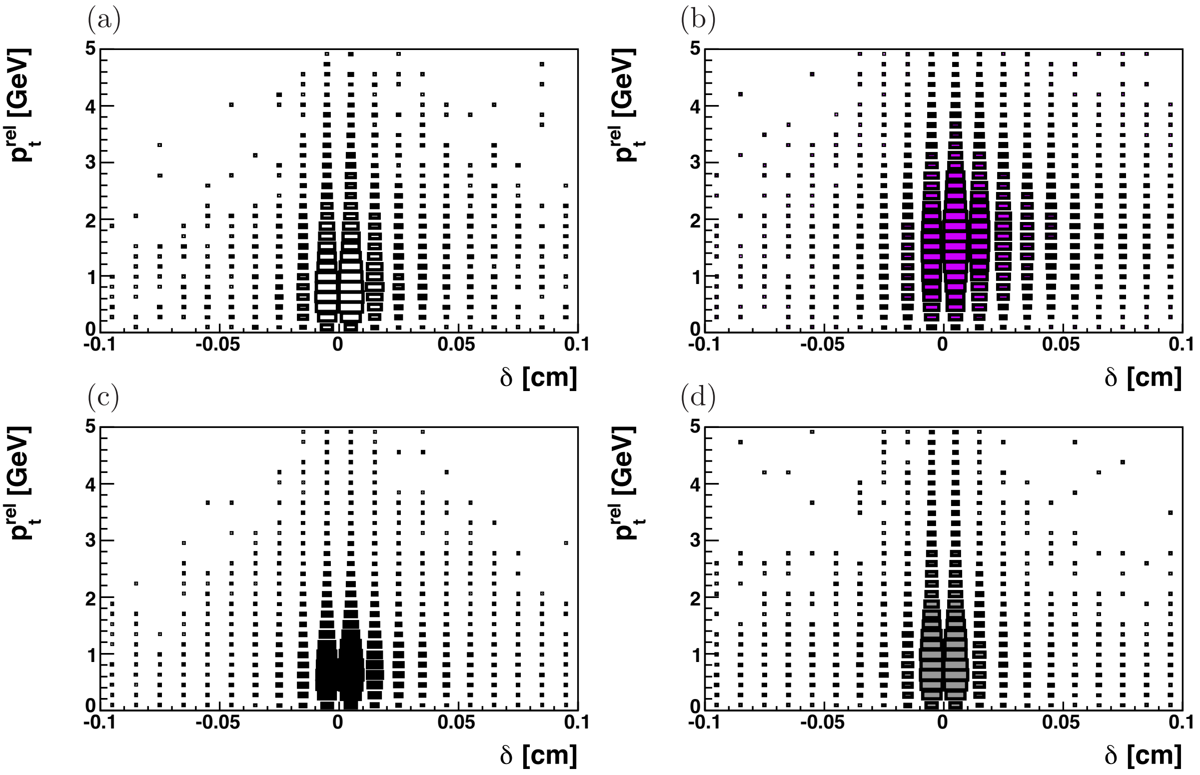

Figure 6.9: The 2-dimensional distribution of p_t^{rel} versus δ for data (a), beauty (b), charm (c) and light quarks (d).

The χ^2/ndf of this fit is calculated to be 1.2. The number of degrees of freedom ndf of the fit is the number of bins of the 2-dimensional histogram plus one to take the total number of events into account and minus three for the free parameters of the fit f_b, f_c and f_{uds}. The correlation coefficients are found to be $\rho_{b,c} = 0.18$, $\rho_{b,uds} = -0.49$ and $\rho_{c,uds} = -0.85$. The quality of the fit is illustrated by a 2-dimensional pull distribution, shown in figure 6.10. Here, the size of an entry in a bin corresponds to the difference between the fit result and the data, divided by the statistical error for this bin. Cells with negative contents are drawn with an X on top of it, while positive regions are open squares. In figure 6.10, no structure is visible, neither in the size nor in the sign of the pull distribution. This leads to the conclusion, that a good description of the data is found in the fit result.

The combined fit is performed in every analysis bin of the transverse momentum p_t^{μ} of the muon, the pseudorapidity η^{μ} of the muon, the transverse momentum p_t^{jet1} of the leading jet, the angular separation $\delta\phi^{jets}$ of the two selected jets and the observable x_{γ}^{obs}. To demonstrate the quality of the combined fit, the contributions of charm, beauty and light quarks are applied to the respective PYTHIA Monte Carlo sample and the sum of them is compared to the data. This comparison is done for the p_t^{rel} and δ distributions separately in all analysis bins. A

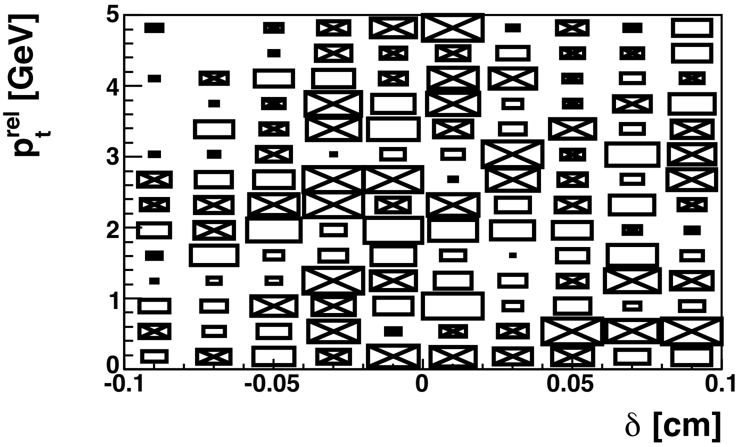

Figure 6.10: Pull distribution for the combined fit of p_t^{rel} and δ.

reasonably well description of the data is achieved, as shown in appendix B.
The results for the fraction of events containing beauty (full circle) and charm (open circle) in the analysis bins are depicted in figure 6.11. Figure 6.11 shows, that in almost all cases the fraction of charm events is greater than the fraction of beauty events. The fraction of events containing beauty quarks in general is around 20% and the fraction of charm events is in most cases between 20% and 40%.

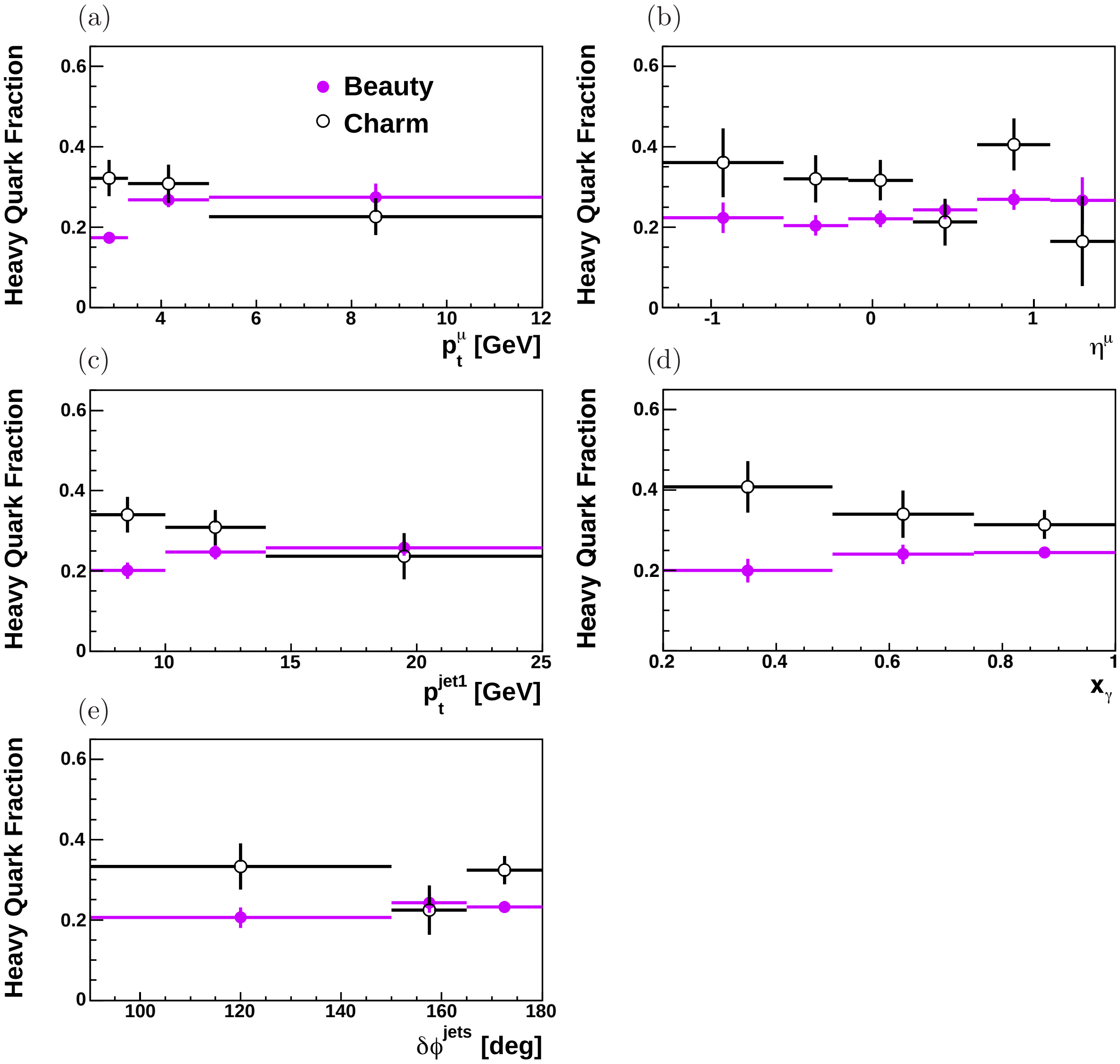

Figure 6.11: Beauty (full circle) and charm (open circle) fractions obtained by the combined fit as a function of p_t^μ (a), η^μ (b), p_t^{jet1} (c), x_γ^{obs} (d) and $\delta\phi^{jets}$ (e).

Chapter 7

Cross Section Measurement

This chapter presents the measurement of beauty and charm dijet photoproduction in the reaction $ep \rightarrow eq\bar{q}X \rightarrow ejj\mu X'$, where $q\bar{q}$ is $b\bar{b}$ or $c\bar{c}$. The phase space region is defined in equation (7.6). The measured cross sections are compared to several QCD models and to former measurements.
Section 7.1 describes sources for systematic uncertainties relevant for this analysis and their contributions to the beauty and the charm measurement, respectively.
In section 7.2, the analysed phase space and the cross section definition are presented. Afterwards, the measured beauty and charm cross sections are shown. Both are determined as a function of the transverse momentum of the muon p_t^μ, the pseudorapidity of the muon η^μ, the transverse momentum of the leading jet p_t^{jet1}, the observable x_γ^{obs} and the azimuthal separation $\delta\phi^{jets}$ of the two jets. To get further insights into the nature of direct and resolved processes the same differential cross sections are also measured separately in the region $x_\gamma^{obs} > 0.75$ and $x_\gamma^{obs} \leq 0.75$.

7.1 Systematic Uncertainties

Systematic uncertainties of the beauty and charm cross section measurement are determined by dedicated studies or appropriate variations of the Monte Carlo simulations. The resulting systematic uncertainties are listed in table 7.1. For all systematic studies presented here, the deviation of the differential cross sections are checked separately in each bin of the measurement. These deviations are input for the estimation of the respective systematic uncertainty.

Impact Parameter Resolution

As shown in section 6.1.2, the PYTHIA simulation models the impact parameter of the data very well. To estimate an uncertainty arising from the knowledge of the impact parameter resolution of the tracks, the resolution of the impact parameter in the Monte Carlo simulation is varied. The variation of the resolution is chosen such, that it encompasses the differences between the data and simulation (cf. figure 7.1). It amounts to roughly 10% of the resolution. The variation is done by applying a Gaussian smearing of 200 μm to 5% of randomly selected

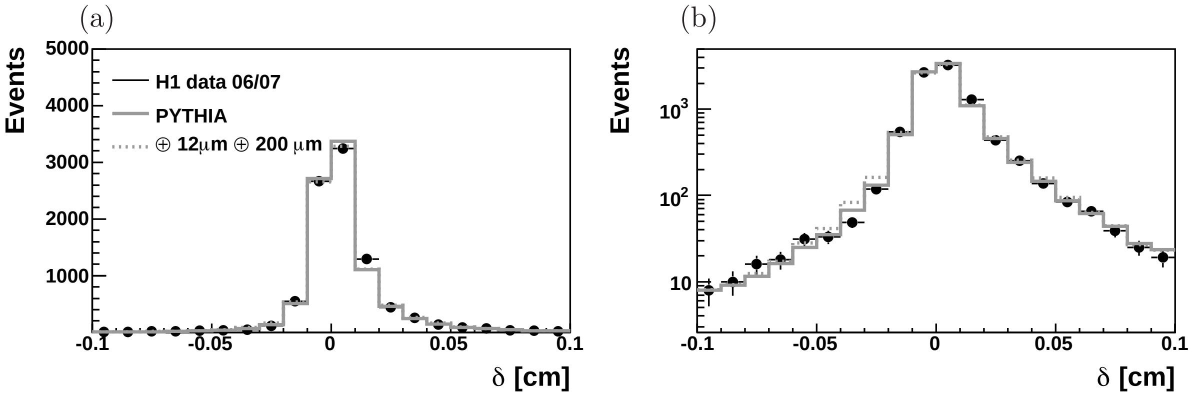

Figure 7.1: Impact parameter δ in linear (a) and logarithmic scale (b) for data (points), default PYTHIA simulation (solid line) and smeared PYTHIA simulation (dotted line) in comparison.

tracks and of 12 μm to the rest. The large smearing is applied to account for non-Gaussian tails in the impact parameter distribution. The complete analysis is repeated using these modified PYTHIA samples. For both the charm and the beauty measurement the increase of the assumed resolution leads to a decrease of the fit results. The measurement of the charm cross section shows a deviation of 4%. In the case of the beauty measurement the modified PYTHIA samples lead to a difference of 3%.

Hadronic Energy Scale

The systematic uncertainty on the hadronic energy scale is known to an accuracy of 2% [91]. The influence of this uncertainty is studied by varying the jet energy by a factor of ±2% for the charm, beauty and light quark Monte Carlo simulation. This is done by varying the energy of the hadronic final state particles. In the case of +2% variation of the jet energy, the charm cross section is 6% lower, while the beauty cross section is 4.5% higher. If the jet energy is scaled down by 2%, the charm cross section is 8% higher, while the beauty cross section is 2% lower. The highest deviations are taken to estimate the systematic uncertainty resulting from the hadronic energy scale. This leads to a systematic uncertainty of 8% for the charm and 5% for the beauty measurement.

Jet Axis

The influence of the jet axis reconstruction on the cross section measurement is studied by a variation of the polar and azimuthal angle resolution in the Monte Carlo simulation. The polar angle resolution of the jet is found to be 2.1° on average, according to the PYTHIA simulation. The azimuthal resolution is found to be 2.6° on average. This is depicted in figure 7.2 (a) and (b). The resolutions are obtained by fitting a Gaussian function to the shown distributions.

As explained in section 6.1.1, a smearing of the jet direction in polar and azimuthal angles is applied to correct the background sample containing light quarks. Both angles are therefore

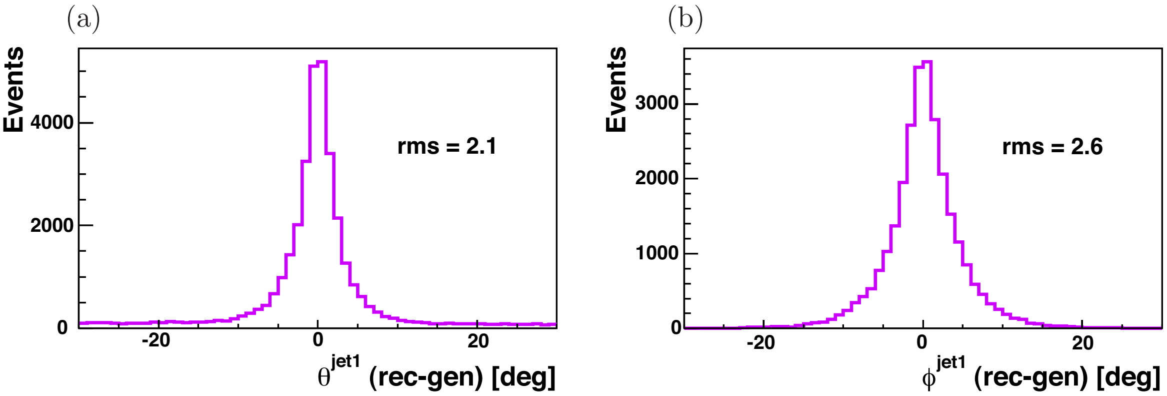

Figure 7.2: Polar angle resolution of the jet in (a) and azimuthal angle resolution in (b) as found in the PYTHIA Monte Carlo simulation.

modified in each simulated event in the light quark sample by applying a Gaussian smearing with a width of 2°. In recent analyses, the systematic error of the jet axis reconstruction is estimated by varying the angular resolution by 10% (cf. [98]). This is well within the applied correction and therefore the deviation of the cross sections as a consequence of the jet axis smearing is used to estimate the systematic uncertainty arising from the jet axis reconstruction. The whole analysis chain is repeated and the cross sections obtained with and without the correction are compared. For the beauty measurement, a deviation of $+4\%$ is observed, while for the charm measurement the difference is -8%. The uncertainty in the charm measurement is larger, since the charm and light quark components in the combined fit are stronger anticorrelated than the beauty and the light quarks components (cf. section 6.2.2).

Heavy Quark Production Model

To investigate the dependence on the physics model used in the Monte Carlo simulation, the complete analysis is repeated using CASCADE Monte Carlo samples for charm and beauty instead of PYTHIA. The heavy quark production model used in the simulation influences the efficiency corrections of the data determined with the Monte Carlo simulation and it changes the p_t^{rel} and δ templates used in the combined fits.

As an example, in figure 7.3 a comparison of data (points), PYTHIA (solid line) and the CASCADE prediction (dotted line) are shown. Both Monte Carlo predictions are the sum of the three quark contributions, which are scaled with their individual fractions obtained in the combined fit. For the CASCADE simulation, the PYTHIA light quark sample is used to estimate the fake muon background. In figure 7.3 (a) the observable x_γ^{obs} is shown. Here, the PYTHIA simulation agrees better with the data than the CASCADE prediction. In figure (b) the distribution of $\delta\phi^{jets}$ is depicted. The CASCADE Monte Carlo models the data nicely, while PYTHIA overestimates it at high values of $\delta\phi^{jets}$ and underestimates it at low values. To study the influence of the heavy quark production model on the cross sections, the efficiency corrections and the fit results are checked separately for the two different models.

It is found, that the reconstruction efficiency of the CASCADE simulation is very similar to the one of PYTHIA. Due to changes in the p_t^{rel} and δ templates, the fit results differ slightly. This leads to a deviation of the cross section. The deviations of the differential and double-differential cross sections show a very similar behaviour for the beauty and charm measurement: in all cases the results obtained with the CASCADE model are below the results containing the PYTHIA prediction. The discrepancies observed for the two Monte Carlo generators are larger for the beauty measurement. According to the deviations of the total cross sections the systematic error of the beauty measurement is estimated to 4% and for the charm measurement the uncertainty is estimated to 2%.

Fragmentation Model

The systematic uncertainties of the fragmentation model are estimated by repeating the complete analysis chain with a PYTHIA simulation generated using the Peterson fragmentation function instead of the default Lund-Bowler function. The used parameters are listed in section 2.8. The reconstruction efficiencies are found to be very similar for both fragmentation models for the charm and beauty Monte Carlo samples. Differences in the p_t^{rel} and δ templates result in discrepancies of the fit results for both models. The fit results, obtained with the Monte Carlo templates using the Peterson fragmentation function, are somewhat lower than the ones obtained with the default Lund-Bowler function. The relative deviations of the final cross sections for the two fragmentation models are of up to 3% for both the charm and beauty measurement.

Kaon and Pion Decays

The inclusive Monte Carlo sample is split into two samples. One containing inflight decays and the other one misidentified hadrons, as explained in detail in section 6.1.1. To estimate a systematic uncertainty arising from kaon and pion decays, the sample containing inflight

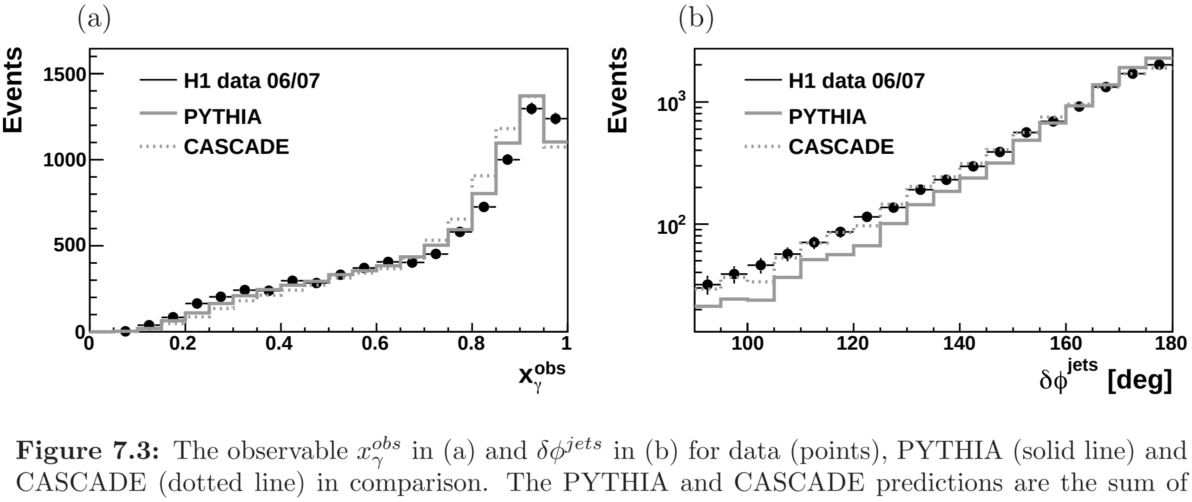

Figure 7.3: The observable x_γ^{obs} in (a) and $\delta\phi^{jets}$ in (b) for data (points), PYTHIA (solid line) and CASCADE (dotted line) in comparison. The PYTHIA and CASCADE predictions are the sum of the three different quark contributions scaled with their fractions obtained by the combined fit. For CASCADE the PYTHIA light quark sample is used to predict the fake muon background.

decays with the parameter `PARJ(2)=0.22` is varied by ±25%. The variation is motivated by the applied correction of the strangeness suppression factor, as explained in section 6.1.1. The complete analysis chain including the fits is repeated. In the beauty measurement this leads to a difference of less than 1% in the total cross section. For the charm measurement the deviation is slightly higher at 1.5%, as a result of the higher correlation of charm and the light quark component in the combined fit (cf. section 6.2.2).

Trigger Efficiency

The trigger efficiency studies are presented in section 4.8. Since no independent photoproduction trigger exists, DIS event samples with SpaCal trigger requirements are used to determine the trigger efficiency. In a similar H1 analysis using HERA II data [98] in the DIS regime, the trigger efficiency is known to an uncertainty of 1%. Considering the different kinematic ranges and the small differences of the data and simulated trigger efficiencies, the systematic uncertainty of the trigger efficiency in this analysis is conservatively estimated to 3% for both, the charm and beauty measurement.

Muon Identification

The muon identification is described in section 4.1. The results for the efficiency to reconstruct muon candidates in the instrumented iron are adopted from [75] and a detailed overview can be found there. According to [75], the reconstruction efficiency for the kinematic region analysed in this thesis is known with an uncertainty of 4%. This holds for both, the beauty and charm measurement, since semi-muonic decays are used in both analyses.

Track Finding Efficiency

The reconstruction efficiency of tracks in the CJC with high transverse momenta is known with an uncertainty of about 1%. In section 4.4 the CST efficiency to find tracks with at least one CST hit is discussed. Because small deviations in the Monte Carlo description of the data are found, the systematic error is estimated to 3% as depicted in figure 4.8.

Luminosity

In analyses of HERA I data the uncertainty of the luminosity measurement amounted to 1.5%. It was dominated by the geometric acceptance of the photon detector and the estimation of the non *ep* background on the basis of proton pilot bunches [99]. At the end of the year 2006 a significant increase of the luminosity corrected event yield was observed by several independent analyses, see for example [100]. In this analysis the increase at approximately run number 477000 is also visible, as depicted in figure 5.9. At present, the source of this increase is not clarified yet. The H1 collaboration decided to estimate the uncertainty of the luminosity measurement to 2.5% before and to 5% after the step occurred. Therefore, the uncertainty of the luminosity measurement is estimated to 4% for this analysis. Here, the errors are weighted before and after the step according to the corresponding luminosities.

Systematic Error	Beauty $\Delta\sigma/\sigma[\%]$	Charm $\Delta\sigma/\sigma[\%]$
Trigger Efficiency	3	3
Muon identification	4	4
Track finding efficiency	3	3
Luminosity	4	4
δ Resolution	3	4
Jet axis	4	8
Hadr. Energy Scale	5	8
Pythia vs. Cascade	4	2
Fragmentation	3	3
K, π decays	1	1.5
Total	11	15

Table 7.1: Summary of the systematic uncertainties.

Total Systematic Uncertainties

For the charm and beauty measurements, total systematic uncertainties of 15% and 11% are obtained respectively by adding up the single contributions in quadrature. Both measurements are complex and thus have a large number of sources for systematic uncertainties, which were investigated separately. For both analyses, the dominant contribution comes from the variation of the hadronic energy scale. Also the systematic error obtained by the jet axis smearing is found to be large. For the charm measurement, this systematic uncertainty is much higher than for the beauty measurement, as the jet axis smearing, which is applied to the light quark Monte Carlo sample only, has a larger impact on the fitted charm contribution than on the fitted beauty contribution. The quark contributions of the charm and the light quark component are strongly anticorrelated, which explains this behaviour.

7.2 Cross Section Definition

The cross section definition presented in the following is valid for both the charm and the beauty measurement. The index q is used synonymously for either beauty or charm quark events. The dijet muon cross section $\sigma_{q,vis}^{data}$ is measured by counting the number of events in the visible region N^{data} normalized to the corresponding integrated luminosity $\mathscr{L}^{data}$. The fraction of beauty or charm events contained in N^{data} is represented by the factor f_q. This factor is obtained by the combined method explained in chapter 6. The cross section $\sigma_{q,vis}^{data}$ is determined using the following formula:

$$\sigma_{q,vis}^{data}(ep \rightarrow eq\bar{q}X \rightarrow ejj\mu X') = \frac{f_q N^{data}}{\mathscr{L}^{data}\epsilon A}. \tag{7.1}$$

The factor ϵA takes the limited acceptance, efficiency and resolution of the detector into account, and amounts to about 30%. It is determined using the Monte Carlo simulation as (for details see section 5.5)

$$\epsilon A = \frac{N^{MC}_{q,rec}}{N^{MC}_{q,gen}}. \tag{7.2}$$

Here $N^{MC}_{q,rec}$ ($N^{MC}_{q,gen}$) denotes the number of charm or beauty events reconstructed (generated) in the visible region. To determine these numbers, the charm and beauty Monte Carlo samples are used, respectively. For the visible cross section of the Monte Carlo simulation the number of generated events $N^{MC}_{q,gen}$ is normalized to the corresponding generated luminosity $\mathscr{L}^{MC}$ of the simulation:

$$\sigma^{MC}_{q,vis}(ep \rightarrow eq\bar{q}X \rightarrow ejj\mu X') = \frac{N^{MC}_{q,gen}}{\mathscr{L}^{MC}}. \tag{7.3}$$

Using equations (7.2) and (7.3) to modify equation (7.1) this leads to

$$\sigma^{data}_{q,vis}(ep \rightarrow eq\bar{q}X \rightarrow ejj\mu X') = \frac{f_q N^{data} \mathscr{L}^{MC}}{\mathscr{L}^{data} N^{MC}_{q,rec}} \cdot \sigma^{MC}_{q,vis}. \tag{7.4}$$

Bin averaged cross sections are defined as

$$\left.\frac{d\sigma^{data}_{q,vis}}{dx}\right|_{\text{bin i}} = \frac{f_q N^{data}|_{\text{bin i}}}{dx_i} \cdot \frac{\mathscr{L}^{MC}}{\mathscr{L}^{data} N^{MC}_{q,rec}|_{\text{bin i}}} \cdot \sigma^{MC}_{q,vis}|_{\text{bin i}}. \tag{7.5}$$

Here, dx_i stands for the width of bin i of the respective variable x.
To summarize, the cross section is determined with equation (7.4) and the differential cross sections by using formula (7.5). The results for the beauty and charm measurements are presented in the following.

7.3 Charm and Beauty Dijet Muon Cross Sections

The charm and beauty cross sections are measured in the region

$$\begin{aligned} Q^2 &\approx 0 \text{ GeV}^2 & 0.2 &< y < 0.8 \\ p_t^{\mu} &> 2.5 \text{ GeV} & -1.3 &< \eta^{\mu} < 1.5 \\ p_t^{jet1(2)} &> 7(6) \text{ GeV} & -2.5 &< \eta^{jet} < 2.5. \end{aligned} \tag{7.6}$$

The scaling factors f_b and f_c are determined from the 2-dimensional fits of p_t^{rel} and the impact parameter δ as explained in chapter 6. The total charm cross section for dijet events containing a muon is measured to be

$$\sigma_c(ep \rightarrow ec\bar{c}X \rightarrow ejj\mu X') = 57.5 \pm 4.9(stat.) \pm 8.6(sys.)\text{pb}. \tag{7.7}$$

	Charm [pb]	Beauty [pb]
Data	$57.5 \pm 4.9(stat.) \pm 8.9(sys.)$	$41.8 \pm 2.0(stat.) \pm 4.6(sys.)$
MC@NLO	76.8	27.9
FMNR	-	$42.4^{+11.3}_{-7.8}$
FMNR × Had	-	$34.2^{+9.1}_{-6.3}$
PYTHIA	65.9	41.9
CASCADE	83.2	30.1

Table 7.2: Theoretical predictions in comparison to the measured charm and beauty dijet muon cross sections.

The total beauty cross section in photoproduction for dijet events containing a muon is measured to be

$$\sigma_b(ep \to eb\bar{b}X \to ejj\mu X') = 41.8 \pm 2.0(stat.) \pm 4.6(sys.)\text{pb}. \tag{7.8}$$

The results from the theoretical predictions are listed in table 7.2. For the charm measurement, the MC@NLO calculation is shown. This NLO prediction is found to be higher than the measured charm cross section. The measured beauty cross section is in very good agreement with the FMNR NLO prediction within the errors. After applying the hadronization corrections, the FMNR NLO prediction is found to be somewhat lower than the prediction on parton level, but still in reasonable agreement within the errors. The MC@NLO prediction is found to be below the measured beauty data.

7.3.1 Differential Cross Sections

The differential cross sections for charm and beauty are measured as a function of the transverse momentum p_t^μ of the muon, the pseudorapidity η^μ of the muon, the transverse momentum p_t^{jet1} of the leading jet, the observable x_γ^{obs} and the azimuthal separation $\delta\phi^{jets}$ of the two selected jets. The fits are performed in each analysis bin as described in chapter 6. The respective fractions for the heavy quarks are taken from the combined fits. The bin averaged cross sections for the data are determined with detector corrections calculated with the PYTHIA Monte Carlo simulation. The inner error bars of the data points in the following figures represent the statistical errors while the outer error bars stand for the statistical and systematic uncertainties added in quadrature. The measured cross sections can be found in tables A.1 and A.3.

The data points of the charm and beauty measurement are compared to the PYTHIA (dotted-dashed line) and CASCADE (dotted line) predictions obtained with equation (7.3), which represent LO QCD calculations. Parton showers are implemented to account for higher order effects. The used settings of the PYTHIA and CASCADE simulation can be found in section 2.8. The beauty cross sections are compared to NLO QCD predictions obtained with the MC@NLO program [44] on hadron level (dashed line), NLO QCD predictions calculated with the FMNR program [38] on parton and on hadron level. The central value of the FMNR

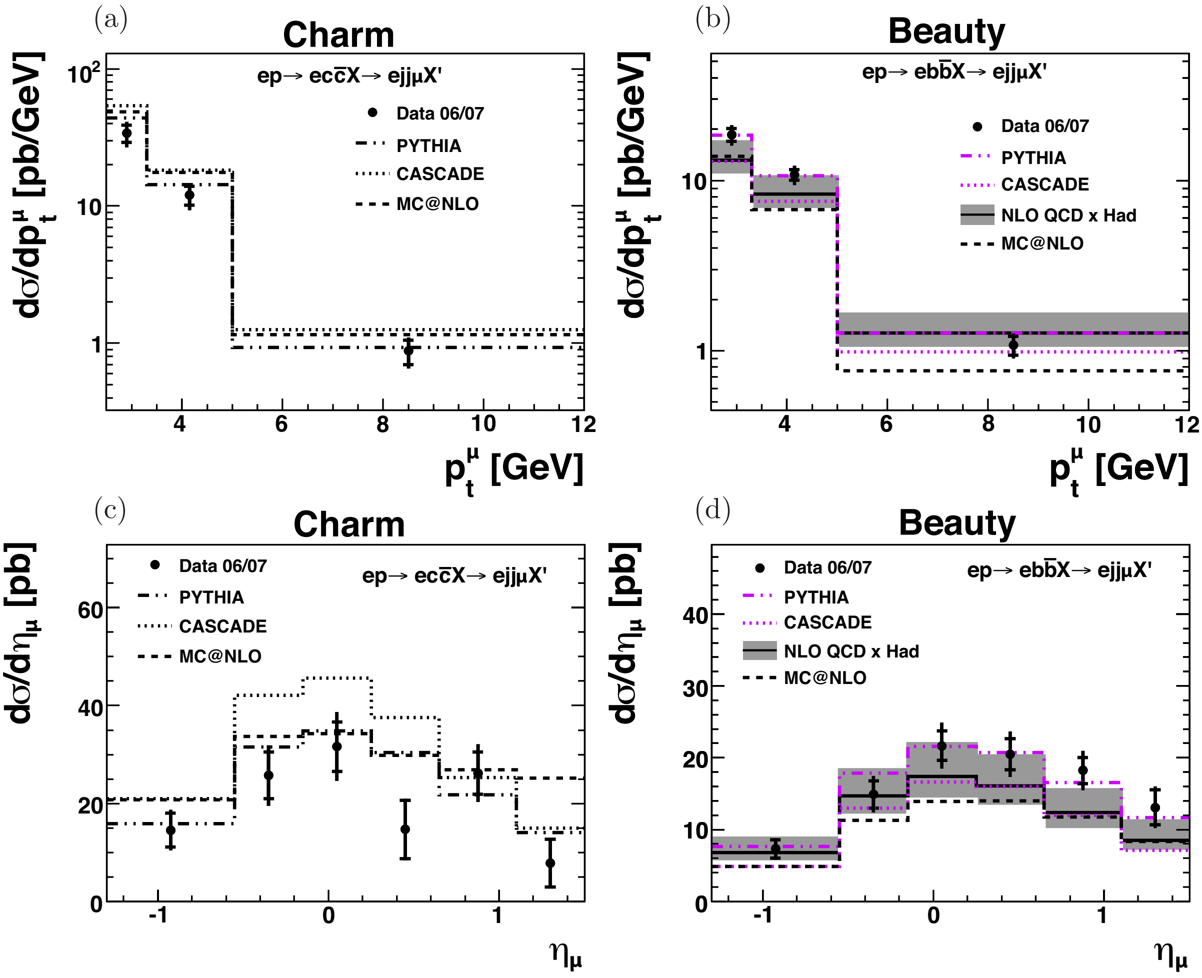

Figure 7.4: Differential charm and beauty cross sections as a function of p_t^μ [(a), (b)] and η^μ [(c), (d)]. The results are compared to the PYTHIA (dotted-dashed line) and CASCADE (dotted line) simulations representing LO QCD. The solid line indicates the central value of the FMNR NLO prediction on hadron level, while the grey shaded band represents its error. The MC@NLO prediction on hadron level is shown as dashed line.

NLO QCD predictions on hadron level is illustrated by the solid line and the error is shown as grey shaded band. The hadronisation corrections in the FMNR program are calculated using the PYTHIA program. Details of the hadronisation corrections and the used settings are discussed in section 2.9. The predicted cross sections by the FMNR and MC@NLO program can be found in tables A.4 and A.2.

Figure 7.4 depicts the differential charm (a) and beauty (b) photoproduction dijet muon cross sections as a function of p_t^μ. The measured $d\sigma/dp_t^\mu$ for charm and beauty decreases with in-

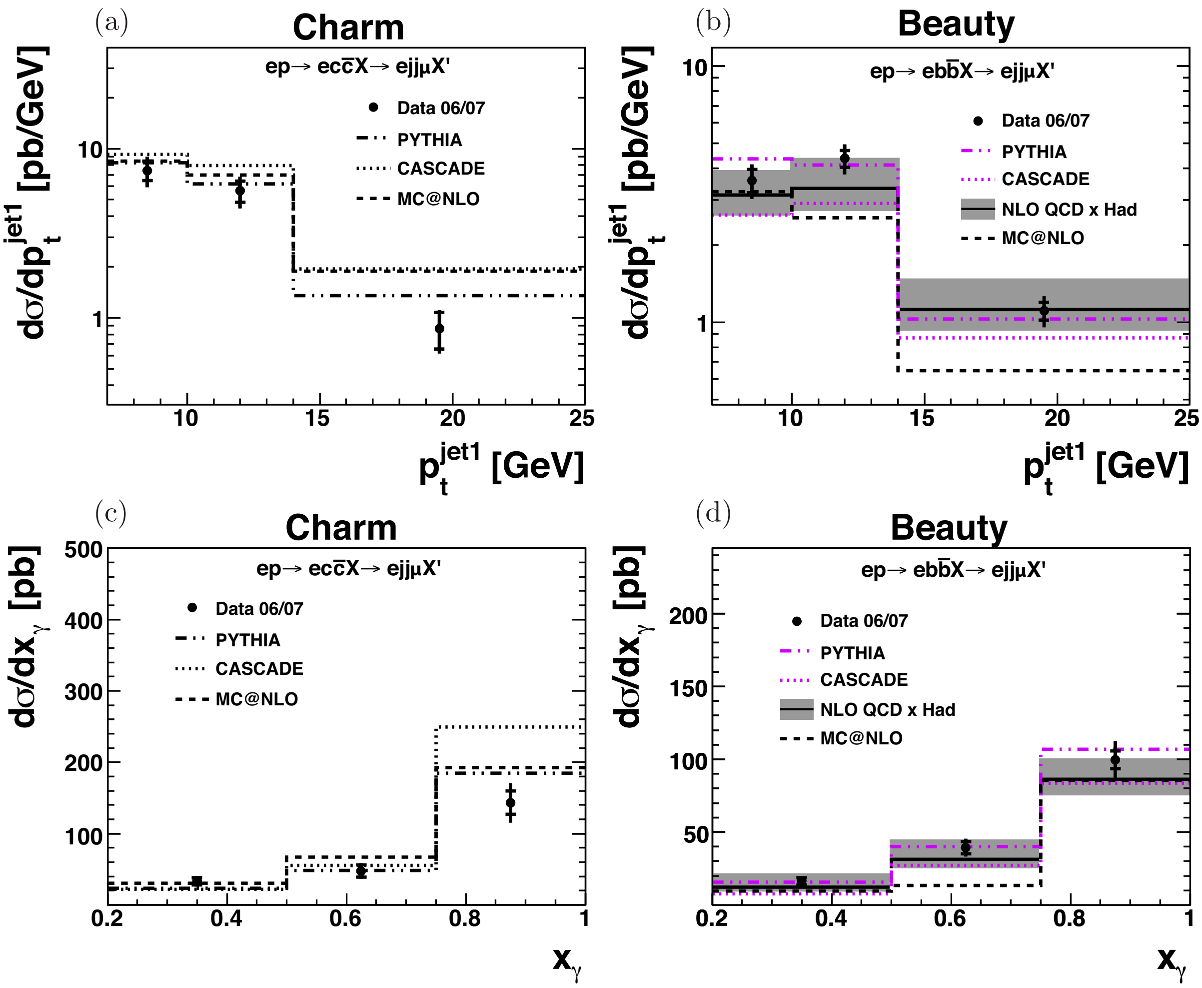

Figure 7.5: Differential charm and beauty cross sections as a function of p_t^{jet1} [(a), (b)] and x_γ^{obs} [(c), (d)]. The results are compared to the PYTHIA (dotted-dashed line) and CASCADE (dotted line) simulations representing LO QCD. The solid line indicates the central value of the FMNR NLO prediction on hadron level, while the grey shaded band represents its error. The MC@NLO prediction on hadron level is shown as dashed line.

creasing values of p_t^μ. The shape is well described by PYTHIA and CASCADE and shows a similar behaviour for charm and beauty. For charm, the MC@NLO calculation models the measured data reasonably well. The MC@NLO prediction for the beauty cross section as a function of p_t^μ describes the shape of the data. The FMNR NLO predictions agree well with the beauty data in all measured bins.
Figure 7.4 shows the charm (c) and beauty (d) cross sections as a function of η^μ. The measured charm cross sections agree reasonably with the PYTHIA and CASCADE predictions.

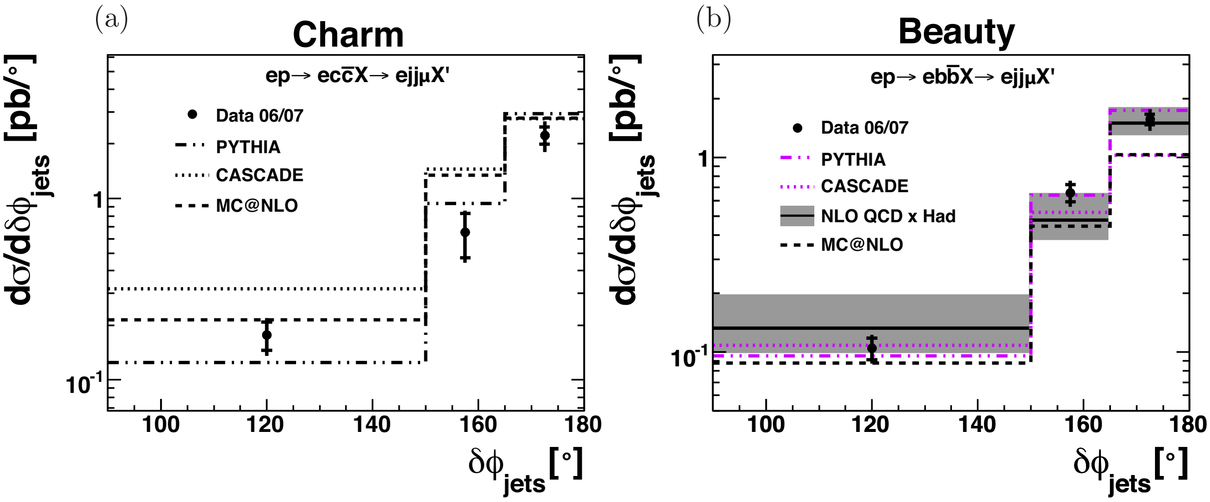

Figure 7.6: Differential charm (a) and beauty (b) cross sections as a function of $\delta\phi^{jets}$. The results are compared to the PYTHIA (dotted-dashed line) and CASCADE (dotted line) simulations representing LO QCD. The solid line indicates the central value of the FMNR NLO prediction on hadron level, while the grey shaded band represents its error. The MC@NLO prediction on hadron level is shown as dashed line.

The MC@NLO calculation describes the measured charm data reasonably well in shape. In the beauty measurement of $d\sigma/d\eta^{\mu}$ the PYTHIA and CASCADE predictions are in good agreement with the data. The MC@NLO prediction describes the shape of the measured beauty data. The FMNR NLO QCD prediction on hadron level models the data well within the errors. Here, a tendency of an underestimation is visible in the very forward region, where resolved processes are expected to be enhanced.

Figure 7.5 (a) and (b) show the differential cross sections $d\sigma/dp_t^{jet1}$ for charm and beauty, respectively. The measured charm and beauty data decrease towards higher values of p_t^{jet1}. The shape of the charm and beauty data is described reasonably by both LO Monte Carlo simulations. The MC@NLO prediction models the measured charm cross section as a function of p_t^{jet1} reasonably well in shape. In the measurement of the beauty cross section, the CASCADE simulation predicts for the first bin a smaller value than for the second bin. The same holds for the FMNR NLO prediction, but not for the MC@NLO and the PYTHIA prediction. The beauty data shows this predicted behaviour and is nicely described by the FMNR NLO prediction within the errors.

In figures (c) and (d) the cross sections are plotted as a function of x_γ^{obs} for charm and beauty. The measured $d\sigma/dx_\gamma^{obs}$ rises towards higher values of x_γ^{obs}. In the charm measurement the predicted cross sections increase more steeply than the measured data, which is especially reflected in an overestimation by LO and NLO predictions of the data in the last bin. The shape is reasonably well described by the PYTHIA, CASCADE and MC@NLO prediction. For the beauty measurement, a slightly better agreement between the PYTHIA prediction and the data is observed. The MC@NLO calculation describes the beauty data very well in the highest x_γ^{obs} bin and underestimates it somewhat in the first two bins. The FMNR NLO calculations are in good agreement with the measured beauty cross sections within the estimated errors.

The measured differential cross section as a function of $\delta\phi^{jets}$ is presented in figure 7.6. The cross sections for charm (a) and beauty (b) increase towards 180° where both jets show a back-to-back topology in $r\phi$ in the LO picture. This cross section is sensitive to higher-order QCD topologies, since additional soft radiation lead to small azimuthal decorrelations, while additional hard radiation is visible at low values of $\delta\phi^{jets}$. The shape of the measured charm data is described reasonably by both LO predictions and the MC@NLO calculation. The PYTHIA and CASCADE simulations describe the shape of the beauty data reasonably well. The FMNR NLO and the MC@NLO predictions describe the beauty data. The normalisation of the FMNR and MC@NLO predictions are similar.

To summarize, for both the charm and beauty measurement a better agreement with the PYTHIA than with the CASCADE prediction is observed in general, since CASCADE tends to be higher for the measured charm and lower for the measured beauty data. The MC@NLO calculation describes the measured charm data in general reasonably well and tends to overestimate it. Both NLO calculations are able to describe the shape of the measured beauty cross sections. While the MC@NLO calculation shows a tendency to underestimate the beauty data, the FMNR calculation describes it very well within the errors. Only in the very forward region of $d\sigma/d\eta^\mu$ the FMNR calculation tends to underestimate the data, but is still in reasonable agreement.

7.3.2 Differential Cross Sections in two x_γ^{obs} regions

The measurements are performed separately in the regions $x_\gamma^{obs} \leq 0.75$ and $x_\gamma^{obs} > 0.75$ as well. In the former region resolved like processes are expected to be enhanced and in the latter region direct like processes. The cross sections are measured as a function of the transverse momentum p_t^μ of the muon, the pseudorapidity η^μ of the muon, the transverse momentum p_t^{jet1} of the leading jet and the azimuthal separation $\delta\phi^{jets}$ of the two selected jets. The measured results for the region $x_\gamma^{obs} > 0.75$ are listed in tables A.5 and A.7. The FMNR and MC@NLO predictions for $x_\gamma^{obs} > 0.75$ can be found in tables A.6 and A.8. The measured results for $x_\gamma^{obs} \leq 0.75$ can be found in tables A.9 and A.11, while the predicted NLO results are listed in tables A.10 and A.12.

Figure 7.7 shows $d\sigma/dp_t^\mu$ and $d\sigma/d\eta^\mu$ for the charm measurement in the region of $x_\gamma^{obs} \leq 0.75$ and $x_\gamma^{obs} > 0.75$. The PYTHIA, CASCADE and MC@NLO predictions model the shape of the measured charm data reasonably well. In figure 7.7 (c) $d\sigma/d\eta^\mu$ for $x_\gamma^{obs} \leq 0.75$ is depicted. Here, the MC@NLO prediction shows an increase towards the forward region of η^μ. In the data, this effect is not as prominent and due to statistical fluctuations it is hard to draw a clear conclusion.

Figure 7.8 shows $d\sigma/dp_t^\mu$ and $d\sigma/d\eta^\mu$ for the beauty measurement in the region of $x_\gamma^{obs} \leq 0.75$ and $x_\gamma^{obs} > 0.75$. The shape of the data is described reasonably by the two LO Monte Carlo predictions. Both NLO calculations are able to describe the beauty data well. The agreement between the beauty data and the LO and NLO predictions for $x_\gamma^{obs} > 0.75$ is very similar

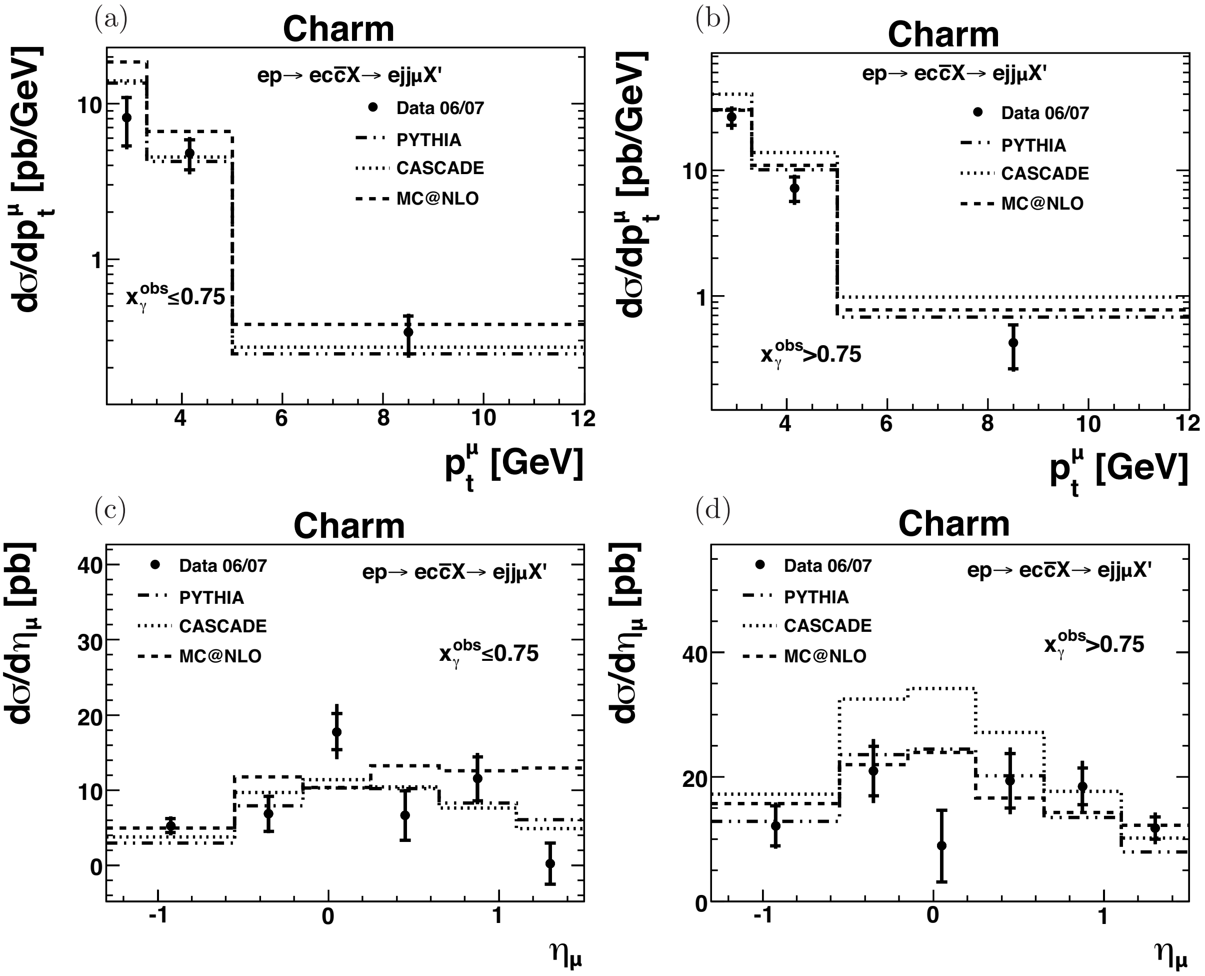

Figure 7.7: Differential charm cross sections as a function of p_t^μ [(a), (b)] and η^μ [(c), (d)] for both x_γ^{obs} regions. The results are compared to the PYTHIA (dotted-dashed line) and CASCADE (dotted line) simulations representing LO QCD. The solid line indicates the central value of the FMNR NLO QCD prediction on hadron level and its estimated uncertainty is shown as shaded band. The MC@NLO prediction on hadron level is shown as dashed line.

to the one observed in the full sample. This is expected, since direct processes are expected to dominate the event sample. The underestimation of the NLO predictions in the forward region of η^μ is more prominent for $x_\gamma^{obs} > 0.75$ than in the full sample, a depicted in figure 7.8 (d). The deviations might be caused by higher order effects. Resolved processes are expected to contribute more in the forward than in the backward region, as illustrated in figure 7.8 (c). For $x_\gamma^{obs} \leq 0.75$ the agreement between data and the FMNR NLO prediction is well within the errors.

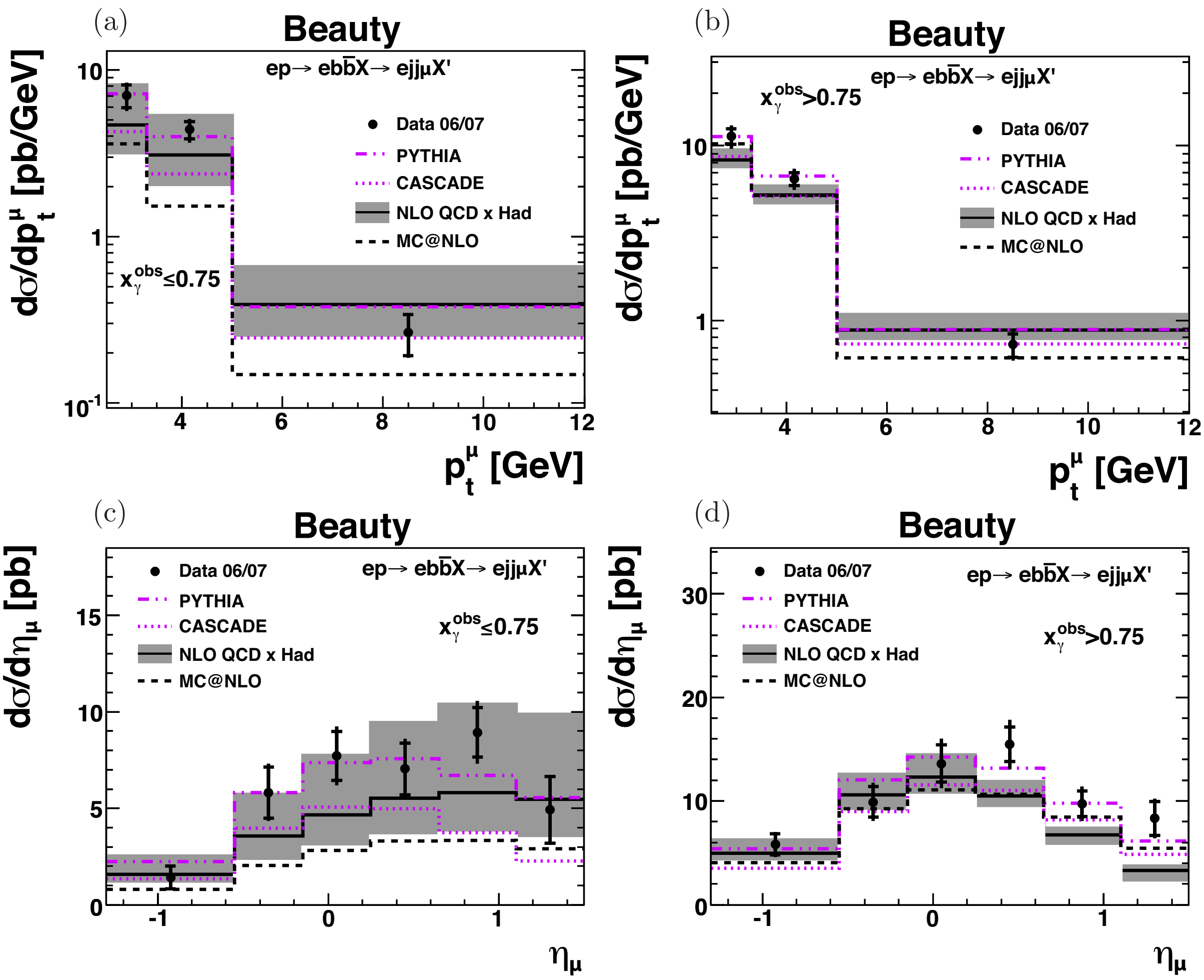

Figure 7.8: Differential beauty cross sections as a function of p_t^{μ} [(a), (b)] and η^{μ} [(c), (d)] for both x_{γ}^{obs} regions. The results are compared to the PYTHIA (dashed-dotted line) and CASCADE (dotted line) simulations representing LO QCD. The solid line indicates the central value of the FMNR NLO QCD prediction on hadron level and its estimated uncertainty is shown as shaded band. The MC@NLO prediction on hadron level is shown as dashed line.

In figure 7.9, the charm cross sections are measured as a function of p_t^{jet1} and $\delta\phi^{jets}$ in the region $x_{\gamma}^{obs} \leq 0.75$ and $x_{\gamma}^{obs} > 0.75$. The measured charm data is reasonably well described by the CASCADE and PYTHIA predictions. Also the MC@NLO calculation is able to reproduce the shape of the measured charm data reasonably.
In figure 7.10 the beauty cross sections as a function of p_t^{jet1} and $\delta\phi^{jets}$ are shown for the two x_{γ}^{obs} regions. In figure 7.10 (b) $d\sigma/dp_t^{jet1}$ for $x_{\gamma}^{obs} > 0.75$ is illustrated. In general, a good agreement between the measured data and the predictions is observed. For the region

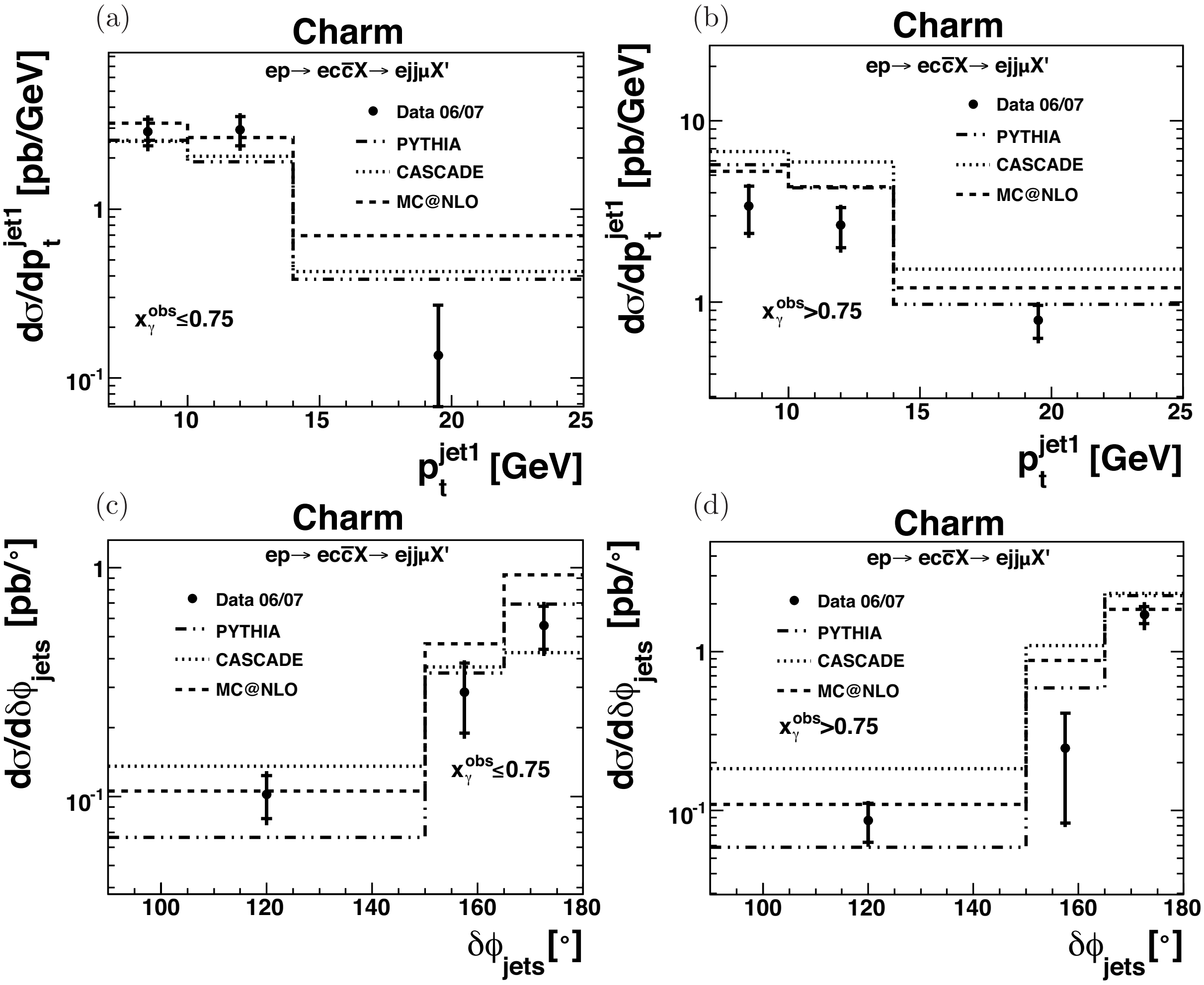

Figure 7.9: Differential cross sections as a function of p_t^{jet1} and $\delta\phi^{jets}$ for the charm measurement in both regions of x_γ^{obs}. The results are compared to the PYTHIA (dotted-dashed line) and the CASCADE (dotted line) simulation. The FMNR NLO QCD prediction on hadron level are depicted as solid line and the uncertainties as shaded band. The MC@NLO prediction on hadron level is depicted as dashed line.

$x_\gamma^{obs} \leq 0.75$ the underestimation of the MC@NLO prediction is more prominent, but the shapes are reasonably well described. The value of the first bin of p_t^{jet1} is predicted to be clearly below the value of the second bin by the FMNR calculation and the CASCADE prediction. This behaviour is observed in the beauty data and described very well by these two predictions. The PYTHIA prediction and the MC@NLO calculation predict higher values. The full sample shows also a lower measured cross section in the first bin than in the second bin, but the effect is more visible in the region $x_\gamma^{obs} > 0.75$. In contrast to this, the data point

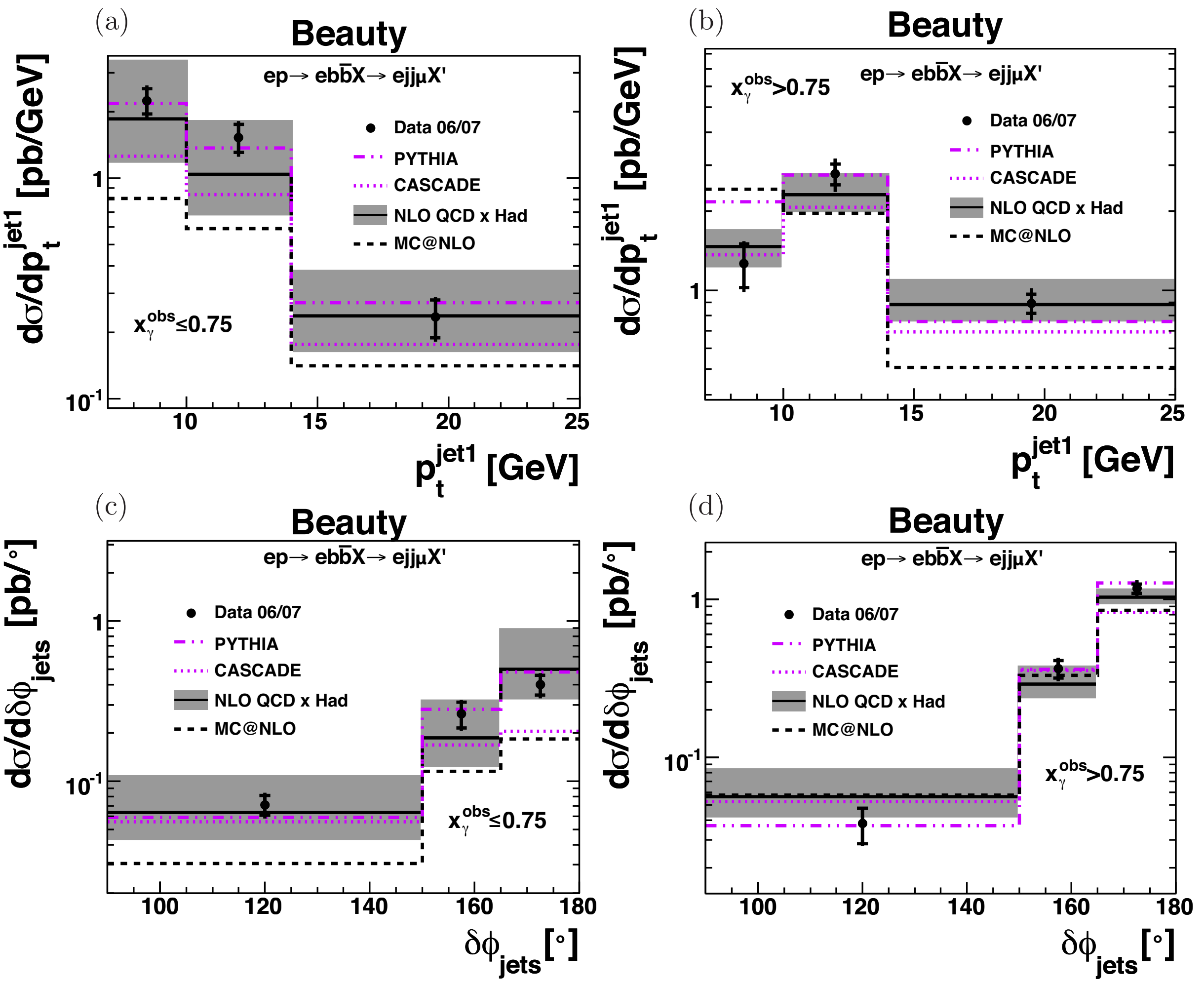

Figure 7.10: Differential cross sections as a function of p_t^{jet1} and $\delta\phi^{jets}$ for the beauty measurement in both regions of x_γ^{obs}. The results are compared to the PYTHIA (dotted-dashed line) and the CASCADE (dotted line) simulation. The FMNR NLO QCD prediction on hadron level are depicted as solid line and the uncertainties as shaded band. The MC@NLO prediction on hadron level is depicted as dashed line.

in the first bin of p_t^{jet1} in the region $x_\gamma^{obs} \leq 0.75$ is higher than the second one as depicted in figure 7.10 (a). In all bins the data points are in good agreement with the FMNR NLO calculation for both x_γ^{obs} regions.

7.4 Discussion

In a previous H1 HERA I measurement [59], beauty cross sections in dijet events containing a muon were measured as a function of the transverse momentum p_t^μ of the muon, the pseudorapidity η^μ of the muon, the transverse momentum p_t^{jet1} of the leading jet and the observable x_γ^{obs}. The same beauty cross sections in the same phase space were measured in a preliminary result [101] using HERA II data. In addition, the beauty cross section as a function of the angular correlation between the two leading jets ($\delta\phi^{jets}$) was measured to investigate higher order effects. The analysis presented in this thesis is measured in an extended phase space compared to the previous results and for the first time also for charm simultaneously.

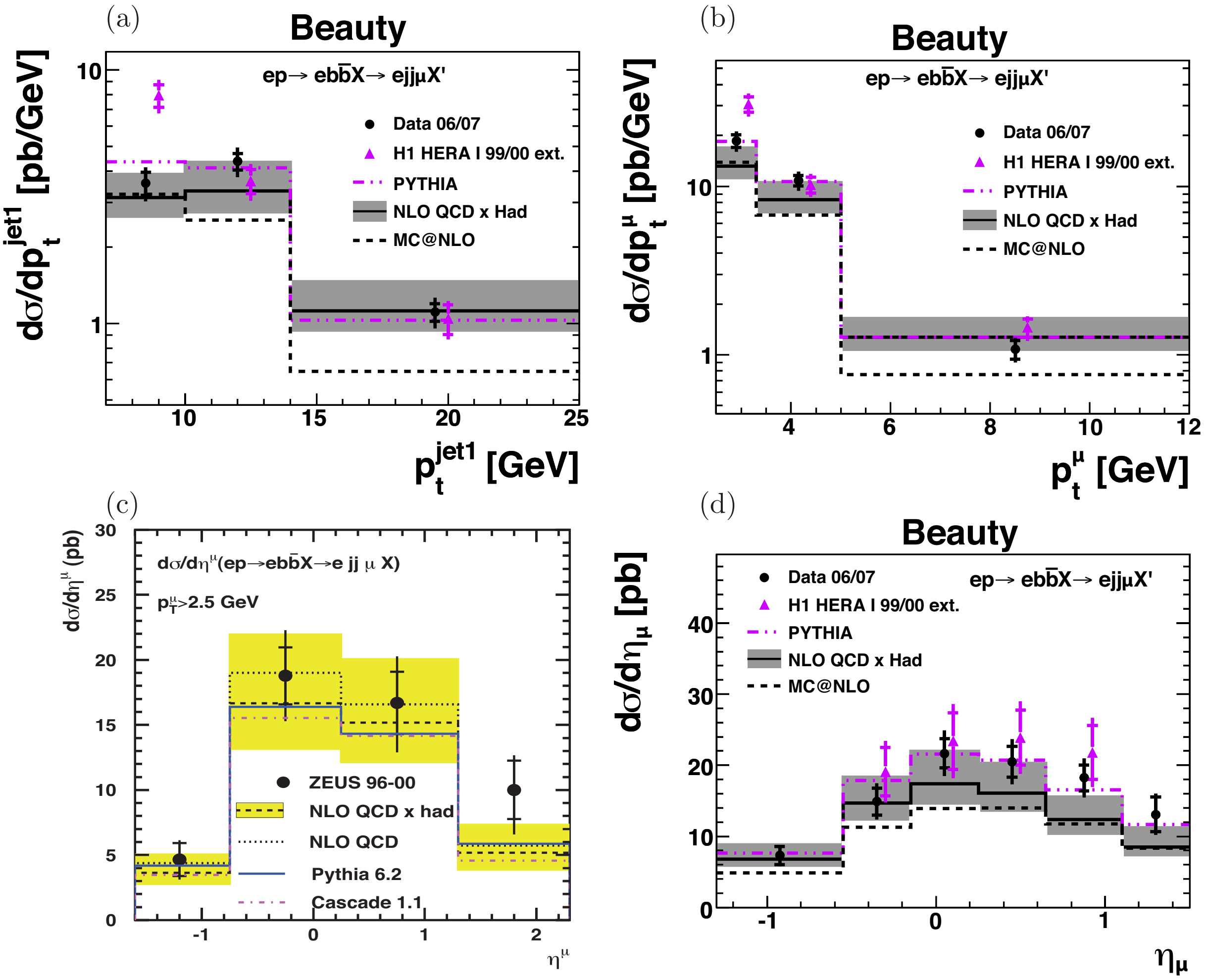

Figure 7.11: Differential beauty dijet muon cross sections as a function of p_t^{jet1} (a), p_t^μ (b) and η^μ in (c) and (d). The ZEUS result in (c) is taken from [60]. The H1 HERA I data points are taken from [59] and extrapolated to the extended phase space analysed in this thesis.

The beauty measurement in this thesis confirms the measured cross sections presented in the preliminary result [101]. The increase in the amount of data collected by a factor of 3.5 compared to the HERA I analysis, provides significant improvements of the statistical precision. It is thus possible to measure the charm and beauty dijet muon cross sections in two regions of x_γ^{obs}. The region $x_\gamma^{obs} \leq 0.75$ is enriched in resolved photon processes, while in the region $x_\gamma^{obs} > 0.75$ an enrichment of direct processes is expected. The beauty cross sections measured in this thesis are in general well described by NLO QCD predictions. In earlier measurements, an underestimation of the beauty data by NLO calculations was observed. Latest results do not show these differences generally, which could be explained due to an improved precision of the measurements.

The measured beauty cross sections as a function of p_t^{jet1} and p_t^{μ} are well described by the NLO calculations in this analysis. This holds for the full sample as well as for the two x_γ^{obs} regions. The results in this thesis agree with measurements performed at ZEUS using HERA I [60] and HERA II [102] data. The results obtained with the H1 HERA I data in [59] and the HERA II data in this analysis agree as well in general. Only in the first bin of $d\sigma/dp_t^{jet1}$ and $d\sigma/dp_t^{\mu}$ the measured H1 HERA II data are a factor of two lower than the H1 HERA I data, as depicted in figure 7.11 (a) and (b), where the H1 HERA I data points are extrapolated. The measurements of $d\sigma/dp_t^{\mu}$ and $d\sigma/dp_t^{jet1}$ are correlated, which explains the similar behaviour. Both similar ZEUS analyses using HERA I [60] and HERA II [102] data do not observe this excess. Since the new H1 HERA II data is based on a much larger data set and has a better precision, it is most likely, that the measurement of very high cross section of the previous publication was due to a statistical fluctuation or unaccounted systematic effects. Nevertheless, as shown in chapter 6, these two bins appear to be somewhat problematic.

A tendency of an underestimation is still visible in the very forward region of the pseudorapidity of the muon, where resolved processes are expected to be enhanced. This is also observed in the previous H1 HERA I data [59], as depicted in figure 7.11 (d), where the H1 HERA I data points are extrapolated to the extended phase space in this thesis. In a comparable analysis of ZEUS using HERA I data [60] (figure 7.11 (c)), the same excess in the forward region is observed. The presented analysis is the first at HERA, where the beauty cross section as a function of η^{μ} is measured separately for the regions $x_\gamma^{obs} > 0.75$ and $x_\gamma^{obs} \leq 0.75$ using the combination of p_t^{rel} and δ to extract the beauty fractions. As shown in figure 7.8 and 7.7, the excess of the data in the forward region is visible for $x_\gamma^{obs} > 0.75$, but for $x_\gamma^{obs} \leq 0.75$ the data is well described. For $x_\gamma^{obs} > 0.75$, the MC@NLO prediction is higher than the FMNR NLO prediction and thus describes the data better. The cut in x_γ^{obs} leads to an enrichment of resolved processes at $x_\gamma^{obs} \leq 0.75$ and of direct processes for $x_\gamma^{obs} > 0.75$. Since MC@NLO underestimates the data generally for $x_\gamma^{obs} \leq 0.75$, it is most likely, that for example higher order effects could cause the increase of the data in the forward region of η^{μ}. To clearly identify the underestimated processes, pure Monte Carlo samples should be used, which contain on the one hand resolved and on the other hand direct processes, since resolved processes are distributed over the whole x_γ^{obs} range.

The measured beauty cross section as a function of x_γ^{obs} is well described by the FMNR NLO calculation in this thesis. In a comparable analysis at ZEUS using HERA II data [102], a tendency of an underestimation is visible at small values of x_γ^{obs}, which is illustrated in figure

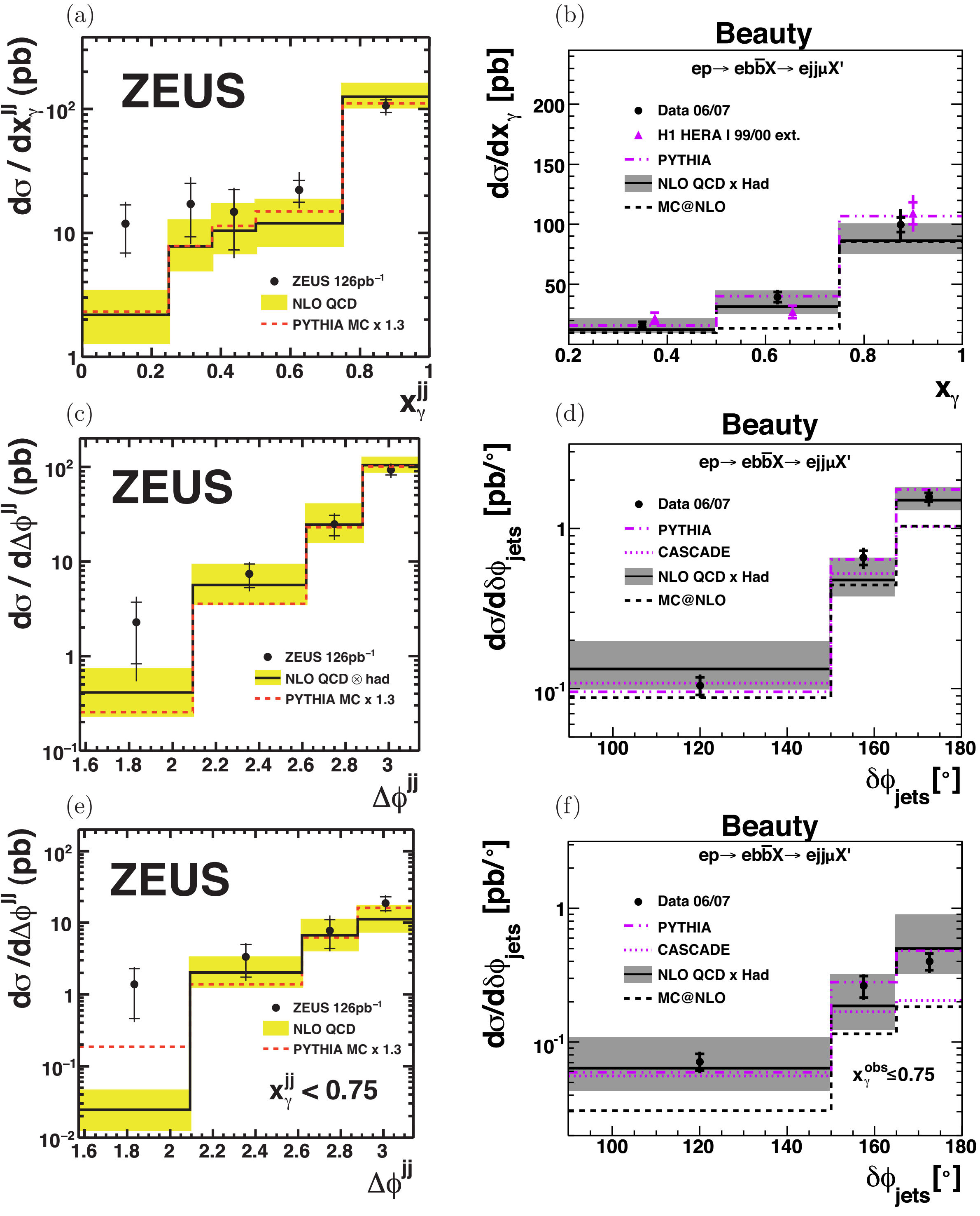

Figure 7.12: Differential beauty dijet muon cross sections as a function of x_γ^{obs} and $\delta\phi^{jets}$ for the ZEUS analysis using HERA II data [102], the H1 HERA I analysis [59], where the data points are extrapolated, and the analysis presented in this thesis. Figures (c) and (d) show $d\sigma/d\delta\phi^{jets}$ for the full sample, while (e) and (f) depict the same for the region $x_\gamma^{obs} \leq 0.75$.

7.12 (a). This bin is not covered in the analysis presented in this thesis (see figure 7.12 (b)). The MC@NLO calculation underestimates the measured beauty data at low values of x_γ^{obs}. This difference in the cross sections is consequently visible in all differential beauty cross sections in the region $x_\gamma^{obs} \leq 0.75$. The region at low x_γ^{obs} is sensitive to higher order effects and it indicates, that MC@NLO using the HERWIG generator could be improved in that aspect.

The beauty cross section as a function of $\delta\phi^{jets}$ is measured using the full event sample and in the regions $x_\gamma^{obs} > 0.75$ and $x_\gamma^{obs} \leq 0.75$. In all samples a reasonable description by the NLO calculations is achieved. In a similar ZEUS analysis using HERA II data [102], the region of low $\delta\phi^{jets}$ is divided into two bins and the first bin shows an underestimation of the beauty data, as depicted in figure 7.12 (c)-(f). The region of low values of $\delta\phi^{jets}$ is sensitive to higher order effects, giving a hint, that the modelling of higher order effects might need further investigations.

The measured charm cross sections in this thesis are in general reasonably well described by the MC@NLO predictions. Since this measurement is the first, where charm and beauty cross sections are measured simultaneously in semi-muonic decays using dijet events with a combination of p_t^{rel} and the impact parameter δ in the photoproduction regime, it is not possible to compare the obtained results directly with other measurements. In [49], a similar H1 HERA I measurement using high p_t dijet events, but no semi-muonic decays, is performed in the photoproduction regime. Here, the measured charm cross sections are in general found to be consistent in shape and normalisation with the NLO QCD calculations. Only in the region of small $\delta\phi^{jets}$, significant differences between the charm data and the NLO prediction are found as depicted in figure 7.13.

A measurement of inclusive $D^{*\pm}$ in photoproduction performed by ZEUS using HERA I data [103] is comparable in precision to the charm analysis presented in this thesis. The presented analysis is another test of charm production in the photoproduction regime. The full reconstruction of the decayed hadrons containing charm quarks provides a higher precision than analysing semi-muonic decays in dijet events. Nevertheless, in this analysis it is shown, that the usage of the combination of p_t^{rel} and the impact parameter δ is sufficiently precise to extract the charm contribution and to measure charm cross sections in photoproduction.

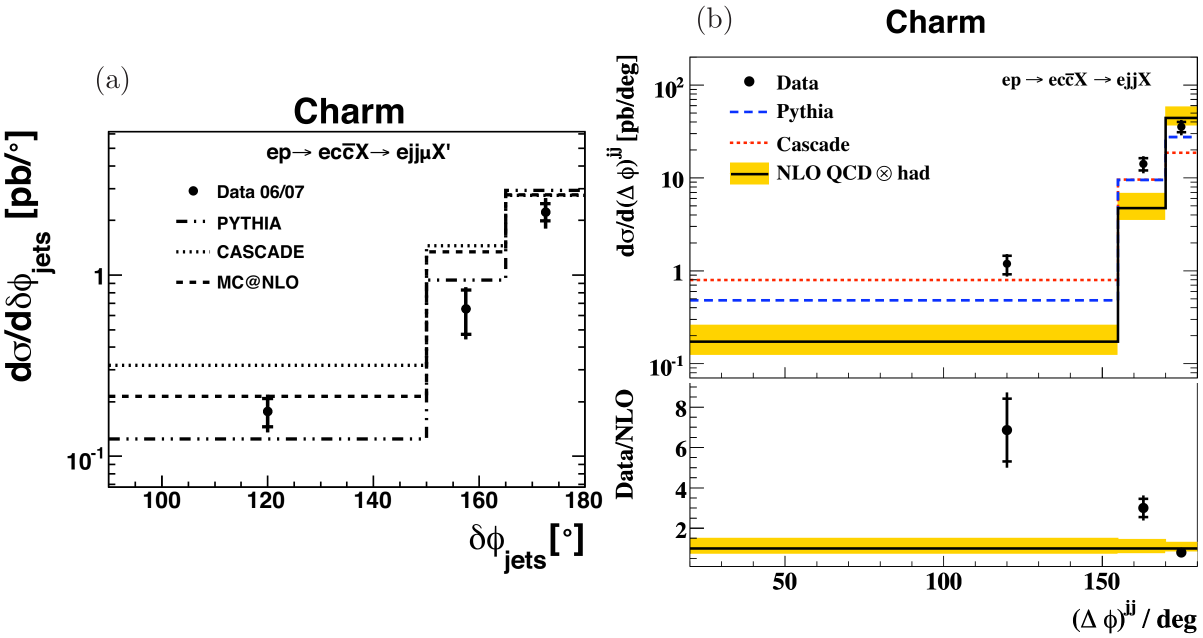

Figure 7.13: Charm cross sections as a function of the angular separation of the two selected jets $\delta\phi^{jets}$ for the presented analysis in (a) and for the process $ep \rightarrow ec\bar{c}X \rightarrow ejjX$ for high p_t dijet events in (b) as measured in [49].

Chapter 8

Conclusions

For the first time, simultaneous measurements of open charm and beauty dijet muon cross sections in photoproduction in *ep* scattering at a centre-of-mass energy of 319 GeV are presented. The analysed data corresponds to an integrated luminosity of $\mathcal{L} \approx 179$ pb^{-1} and was recorded with the H1 detector at the HERA collider in 2006 and 2007. The presented beauty analysis provides the highest statistical precision which was ever achieved in this kind of measurement at HERA. Events containing charm and beauty flavoured hadrons are identified through their semi-muonic decay in dijet events. Their contributions are extracted using the muon impact parameter δ and the transverse momentum p_t^{rel} of the muon relative to the direction of an associated jet. The large mass of the beauty quark leads in particular to a good separation of beauty from charm and light quark events using the p_t^{rel} observable. Due to the smaller mass of the charm quark, the p_t^{rel} observable cannot be used for the separation of charm and light quark events. The combination of p_t^{rel} and the impact parameter δ allows to extract the contributions from events containing charm, beauty and light quarks separately. The anticorrelation of charm and the light quark component leads to a higher systematic uncertainty for the charm measurement.

The H1 vertex detector provides precise tracking information, which is necessary to resolve decay vertices of charm or beauty flavoured hadrons. Since the quark flavour separation is based on the impact parameter, the vertex detector simulation should model the data well. In the context of this work, a detailed tuning of the vertex detector simulation was performed, as described in this thesis. The occupancy and the noise amplitude in the simulation are adjusted to the data to provide a description of the efficiency, resolution, multiplicity and distribution of dead channels. This led to a good agreement of the data and the simulation.

The cross sections are measured as functions of the transverse momentum p_t^{μ} of the muon, of the pseudorapidity η^{μ} of the muon, of the transverse momentum p_t^{jet1} of the leading jet, of the observable x_γ^{obs} and of the azimuthal angular correlation $\delta\phi^{jets}$ between the two selected jets. For the first time, these cross sections are also measured in the region of enriched resolved processes ($x_\gamma^{obs} \leq 0.75$) and of direct processes ($x_\gamma^{obs} > 0.75$).

The measured beauty cross sections in this thesis are found to be consistent with a previously published H1 HERA I analysis. Only in the first bin of the measured $d\sigma/dp_t^{jet1}$ and $d\sigma/dp_t^{\mu}$, the measured beauty data in this analysis is a factor of two lower than in the previous publication. Since the new measurement is based on a much larger data set and has a better precision, it is most likely that the measurement of a very high cross section in the first bin of $d\sigma/dp_t^{jet1}$ and $d\sigma/dp_t^{\mu}$ of the previous publication, which excessed the NLO prediction, was caused by a statistical fluctuation or unaccounted systematic effects.

The results are compared to several QCD models, such as the leading order plus parton shower Monte Carlo simulations PYTHIA and CASCADE as well as NLO QCD predictions obtained with the FMNR and the MC@NLO program. In the FMNR program, theoretical uncertainties arising from contributions beyond NLO are estimated by scale variations. The hadronization corrections are applied using the PYTHIA Monte Carlo generator. The MC@NLO program is currently implemented for the HERWIG Monte Carlo generator only, which is used for the hadronization corrections.

The leading order plus parton shower Monte Carlo simulations PYTHIA and CASCADE describe the shape of both the charm and the beauty measurement. The normalisation is found to be in good agreement with the data. The CASCADE model is based on k_t unintegrated parton distributions in the proton and the gluon density depends on the transverse momentum k_t of the parton. This leads to processes with similar final state configurations as the mode used in PYTHIA, which matches direct, excitation and resolved contributions.

The measured charm cross sections are described reasonably in shape by the MC@NLO prediction. The normalisation of the MC@NLO calculation is found to be somewhat higher than the measured charm data. The beauty cross sections are in general well modelled by the NLO QCD calculations both in shape and normalisation as obtained by FMNR. Only in the very forward region of the pseudorapidity of the muon, the data tends to be somewhat underestimated by the FMNR NLO calculation. Here, resolved processes are expected to be enhanced. The measured beauty cross section as a function of η^{μ} in the region $x_{\gamma}^{obs} > 0.75$ could point to the origin of the differences. Here, the FMNR values are clearly below the beauty data in the forward region, while the measurement for $x_{\gamma}^{obs} \leq 0.75$ shows a good agreement between the beauty data and the NLO calculation. The MC@NLO prediction describes the shape of the beauty cross sections and the central value of it tends to be somewhat lower than the data.

It is shown, that the first measurement of charm in photoproduction in semi-muonic decays with dijet events using the combination of p_t^{rel} and the impact parameter δ to extract the quark fractions provides a sufficient precision. The presented charm and beauty cross sections are in general well described by several LO and NLO theoretical predictions.

Appendix A

Data Tables

		Charm				
p_t^μ range [GeV]		$d\sigma/dp_t^\mu$ [pb/GeV]	stat.	sys.	f_c [%]	ϵ_{rec}
2.5	3.3	33.9	4.8	5.1	32.2 ± 4.5	26.4
3.3	5.0	12.0	1.9	1.8	30.8 ± 4.8	32.6
5.0	12.0	0.9	0.2	0.1	22.6 ± 4.6	40.1
η^μ range		$d\sigma/d\eta^\mu$ [pb]	stat.	sys.	f_c [%]	ϵ_{rec}
-1.30	-0.55	14.6	3.5	2.2	36.0 ± 8.6	20.9
-0.55	-0.15	25.7	4.8	3.9	32.0 ± 5.8	33.3
-0.15	0.25	31.6	5.1	4.7	31.6 ± 5.0	35.1
0.25	0.65	14.7	5.9	2.2	17.0 ± 6.8	33.5
0.65	1.10	26.2	4.3	4.0	40.6 ± 6.5	32.5
1.10	1.50	7.8	4.9	1.2	19.2 ± 11.0	18.2
p_t^{jet1} range [GeV]		$d\sigma/dp_t^{jet1}$ [pb/GeV]	stat.	sys.	f_c [%]	ϵ_{rec}
7	10	7.4	1.0	1.2	34.0 ± 4.4	28.0
10	14	5.6	0.8	0.9	30.8 ± 4.4	25.7
14	25	0.9	0.2	0.1	23.7 ± 5.7	39.1
x_γ^{obs} range		$d\sigma/dx_\gamma^{obs}$ [pb]	stat.	sys.	f_c [%]	ϵ_{rec}
0.20	0.50	33.2	5.3	5.0	40.8 ± 6.4	35.3
0.50	0.75	47.6	8.3	7.1	34.0 ± 5.9	34.0
0.75	1.00	143.2	16.4	21.5	31.4 ± 3.6	25.8
$\delta\phi^{jets}$ range [deg]		$d\sigma/d\delta\phi^{jets}$ [pb/deg]	stat.	sys.	f_c [%]	ϵ_{rec}
90	150	0.17	0.03	0.03	33.3 ± 5.8	32.1
150	165	0.65	0.18	0.10	22.4 ± 6.1	30.2
165	180	2.23	0.25	0.35	32.4 ± 3.5	29.5

Table A.1: Measured differential charm dijet muon cross sections in photoproduction as a function of p_t^μ, η^μ, p_t^{jet1}, x_γ^{obs} and $\delta\phi^{jets}$ with statistical and systematic errors. Also listed are the fractions of events containing beauty quarks, f_b, and the reconstruction efficiency ϵ_{rec} as obtained from the PYTHIA Monte Carlo simulation.

		Charm
		MC@NLO NLO x Had
p_t^μ range [GeV]		$d\sigma/dp_t^\mu$ [pb/GeV]
2.5	3.3	48.6
3.3	5.0	17.5
5.0	12.0	1.2
η^μ range		$d\sigma/d\eta^\mu$ [pb]
-1.30	-0.55	20.7
-0.55	-0.15	33.7
-0.15	0.25	34.2
0.25	0.65	29.8
0.65	1.10	26.9
1.10	1.50	25.2
p_t^{jet1} range [GeV]		$d\sigma/dp_t^{jet1}$ [pb/GeV]
7	10	8.5
10	14	7.0
14	25	1.9
x_γ^{obs} range		$d\sigma/dx_\gamma^{obs}$ [pb]
0.20	0.50	30.5
0.50	0.75	67.1
0.75	1.00	192.4
$\delta\phi^{jets}$ range [deg]		$d\sigma/d\delta\phi^{jets}$ [pb/deg]
90	150	0.2
150	165	1.3
165	180	2.8

Table A.2: Predicted differential beauty dijet muon cross sections in photoproduction at next-to-leading order as a function of p_t^μ, η^μ, p_t^{jet1}, x_γ^{obs} and $\delta\phi^{jets}$ on hadron (Had) and level calculated with MC@NLO.

		Beauty				
p_t^μ range [GeV]		$d\sigma/dp_t^\mu$ [pb/GeV]	stat.	sys.	f_b [%]	ϵ_{rec}
2.5	3.3	18.6	1.6	2.1	17.3 ± 1.5	26.0
3.3	5.0	10.8	0.7	1.2	26.8 ± 1.8	31.4
5.0	12.0	1.1	0.1	0.1	27.4 ± 3.3	39.6
η^μ range		$d\sigma/d\eta^\mu$ [pb]	stat.	sys.	f_b [%]	ϵ_{rec}
-1.30	-0.55	7.3	1.2	0.8	22.3 ± 3.7	25.8
-0.55	-0.15	14.9	1.9	1.7	20.4 ± 2.5	36.6
-0.15	0.25	21.7	2.1	2.4	22.1 ± 2.1	35.8
0.25	0.65	20.5	2.2	2.3	24.1 ± 2.4	34.1
0.65	1.10	18.2	1.8	2.0	26.9 ± 2.6	31.0
1.10	1.50	13.1	2.5	1.5	29.8 ± 5.4	17.0
p_t^{jet1} range [GeV]		$d\sigma/dp_t^{jet1}$ [pb/GeV]	stat.	sys.	f_b [%]	ϵ_{rec}
7	10	3.6	0.4	0.4	20.1 ± 2.0	34.4
10	14	4.4	0.3	0.5	24.8 ± 1.8	26.8
14	25	1.1	0.1	0.1	25.8 ± 2.0	33.3
x_γ^{obs} range		$d\sigma/dx_\gamma^{obs}$ [pb]	stat.	sys.	f_b [%]	ϵ_{rec}
0.20	0.50	16.3	2.5	1.8	20.0 ± 3.0	35.2
0.50	0.75	39.2	4.1	4.4	24.0 ± 2.5	29.1
0.75	1.00	99.7	6.2	11.2	24.4 ± 1.5	28.7
$\delta\phi^{jets}$ range [deg]		$d\sigma/d\delta\phi^{jets}$ [pb/deg]	stat.	sys.	f_b [%]	ϵ_{rec}
90	150	0.10	0.01	0.01	20.1 ± 2.6	33.5
150	165	0.66	0.07	0.07	24.3 ± 2.4	32.4
165	180	1.57	0.09	0.18	23.3 ± 1.4	30.1

Table A.3: Measured differential beauty dijet muon cross sections in photoproduction as a function of p_t^μ, η^μ, p_t^{jet1}, x_γ^{obs} and $\delta\phi^{jets}$ with statistical and systematic errors. Also listed are the fractions of events containing beauty quarks, f_b, and the reconstruction efficiency ϵ_{rec} as obtained from the PYTHIA Monte Carlo simulation.

		Beauty		
		FMNR		MC@NLO
		NLO x Had	NLO x Part	NLO x Had
p_t^μ range [GeV]		$d\sigma/dp_t^\mu$ [pb/GeV]		
2.5	3.3	$13.1^{3.7}_{-2.4}$	$18.3^{5.2}_{-3.3}$	13.9
3.3	5.0	$8.3^{2.2}_{-1.6}$	$10.1^{2.7}_{-1.9}$	6.7
5.0	12.0	$1.27^{0.36}_{-0.24}$	$1.34^{0.38}_{-0.25}$	0.8
η^μ range		$d\sigma/d\eta^\mu$ [pb]		
-1.30	-0.55	$6.8^{2.0}_{-1.3}$	$9.2^{2.7}_{-1.7}$	4.8
-0.55	-0.15	$14.7^{3.6}_{-2.7}$	$18.7^{4.6}_{-3.4}$	11.3
-0.15	0.25	$17.4^{4.6}_{-3.2}$	$21.4^{5.6}_{-4.0}$	13.9
0.25	0.65	$16.1^{4.1}_{-2.9}$	$19.5^{5.0}_{-3.5}$	14.0
0.65	1.10	$12.3^{3.2}_{-2.4}$	$14.7^{3.8}_{-2.9}$	11.8
1.10	1.50	$8.5^{2.7}_{-1.6}$	$10.2^{3.3}_{-1.9}$	8.4
p_t^{jet1} range [GeV]		$d\sigma/dp_t^{jet1}$ [pb/GeV]		
7	10	$3.15^{0.73}_{-0.57}$	$5.47^{1.21}_{-0.98}$	3.2
10	14	$3.33^{0.99}_{-0.66}$	$3.66^{1.18}_{-0.75}$	2.6
14	25	$1.12^{0.34}_{-0.21}$	$0.83^{0.25}_{-0.15}$	0.6
x_γ^{obs} range		$d\sigma/dx_\gamma^{obs}$ [pb]		
0.2	0.5	$12.4^{8.3}_{-4.3}$	$13.9^{9.9}_{-5.0}$	9.5
0.5	0.75	$31.4^{12.6}_{-7.5}$	$24.1^{16.8}_{-8.6}$	13.4
0.75	1.0	$86.3^{13.5}_{-12.1}$	$122.5^{17.8}_{-16.2}$	85.7
$\delta\phi^{jets}$ range [deg]		$d\sigma/d\delta\phi^{jets}$ [pb/deg]		
90	150	$0.133^{0.061}_{-0.036}$	$0.061^{0.037}_{-0.019}$	0.1
150	165	$0.476^{0.167}_{-0.108}$	$0.55^{0.31}_{-0.18}$	0.4
165	180	$1.50^{0.29}_{-0.23}$	$1.96^{0.31}_{-0.27}$	1.0

Table A.4: Predicted differential beauty dijet muon cross sections in photoproduction at next-to-leading order as a function of p_t^μ, η^μ, p_t^{jet1}, x_γ^{obs} and $\delta\phi^{jets}$ on hadron (Had) and on parton (Part) level calculated with FMNR and MC@NLO.

$x_\gamma^{obs} > 0.75$		**Charm**				
p_t^μ range [GeV]		$d\sigma/dp_t^\mu$ [pb/GeV]	stat.	sys.	f_c [%]	ϵ_{rec}
2.5	3.3	26.5	3.9	4.0	40.4 ± 5.9	24.6
3.3	5.0	7.2	1.6	1.1	28.6 ± 6.2	30.5
5.0	12.0	0.4	0.2	0.1	15.5 ± 5.9	39.2
η^μ range		$d\sigma/d\eta^\mu$ [pb]	stat.	sys.	f_c [%]	ϵ_{rec}
-1.30	-0.55	12.1	3.2	1.8	37.2 ± 9.7	19.6
-0.55	-0.15	20.9	4.0	3.1	35.7 ± 6.7	31.6
-0.15	0.25	8.9	5.8	1.3	13.3 ± 8.7	33.3
0.25	0.65	19.4	4.4	2.9	35.7 ± 8.0	31.6
0.65	1.10	18.5	3.0	2.8	55.5 ± 8.6	30.9
1.10	1.50	11.7	1.8	1.8	59.5 ± 7.9	17.0
p_t^{jet1} range [GeV]		$d\sigma/dp_t^{jet1}$ [pb/GeV]	stat.	sys.	f_c [%]	ϵ_{rec}
7	10	3.4	1.0	0.5	25.7 ± 7.4	24.4
10	14	2.7	0.7	0.4	22.5 ± 5.6	24.6
14	25	0.8	0.2	0.1	31.0 ± 6.4	38.2
$\delta\phi^{jets}$ range [deg]		$d\sigma/d\delta\phi^{jets}$ [pb/deg]	stat.	sys.	f_c [%]	ϵ_{rec}
90	150	0.09	0.02	0.01	33.5 ± 9.2	27.9
150	165	0.25	0.16	0.04	14.2 ± 9.3	28.6
165	180	1.70	0.21	0.26	33.3 ± 4.1	28.3

Table A.5: Measured differential charm dijet muon cross sections in photoproduction as a function of p_t^μ, η^μ, p_t^{jet1}, x_γ^{obs} and $\delta\phi^{jets}$ with statistical and systematic errors for direct processes ($x_\gamma^{obs} > 0.75$). Also listed are the fractions of events containing beauty quarks, f_b, and the reconstruction efficiency ϵ_{rec} as obtained from the PYTHIA Monte Carlo simulation.

$x_\gamma^{obs} > 0.75$		**Charm**
		MC@NLO NLO x Had
p_t^μ range [GeV]		$d\sigma/dp_t^\mu$ [pb/GeV]
2.5	3.3	30.0
3.3	5.0	10.9
5.0	12.0	0.8
η^μ range		$d\sigma/d\eta^\mu$ [pb]
-1.30	-0.55	15.7
-0.55	-0.15	21.9
-0.15	0.25	23.9
0.25	0.65	16.6
0.65	1.10	14.3
1.10	1.50	12.2
p_t^{jet1} range [GeV]		$d\sigma/dp_t^{jet1}$ [pb/GeV]
7	10	5.3
10	14	4.3
14	25	1.2
$\delta\phi^{jets}$ range [deg]		$d\sigma/d\delta\phi^{jets}$ [pb/deg]
90	150	0.1
150	165	0.9
165	180	1.8

Table A.6: Predicted differential beauty dijet muon cross sections in photoproduction at next-to-leading order as a function of p_t^μ, η^μ, p_t^{jet1} and $\delta\phi^{jets}$ on hadron (Had) level calculated with MC@NLO in the region $x_\gamma^{obs} > 0.75$.

$x_\gamma^{obs} > 0.75$		**Beauty**				
p_t^μ range [GeV]		$d\sigma/dp_t^\mu$ [pb/GeV]	stat.	sys.	f_b [%]	ϵ_{rec}
2.5	3.3	11.3	1.1	1.3	18.5 ± 1.8	26.4
3.3	5.0	6.5	0.5	0.7	26.2 ± 2.1	31.3
5.0	12.0	0.7	0.1	0.08	26.4 ± 4.0	39.2
η^μ range		$d\sigma/d\eta^\mu$ [pb]	stat.	sys.	f_b [%]	ϵ_{rec}
-1.30	-0.55	5.8	1.0	0.7	24.4 ± 4.0	26.6
-0.55	-0.15	9.9	1.5	1.1	20.5 ± 2.8	38.3
-0.15	0.25	13.6	1.8	1.5	22.1 ± 2.9	35.8
0.25	0.65	15.5	1.7	1.7	30.0 ± 3.1	33.3
0.65	1.10	9.8	1.2	1.1	28.2 ± 3.4	29.6
1.10	1.50	8.3	1.6	0.9	39.5 ± 7.3	15.9
p_t^{jet1} range [GeV]		$d\sigma/dp_t^{jet1}$ [pb/GeV]	stat.	sys.	f_b [%]	ϵ_{rec}
7	10	1.3	0.2	0.1	14.6 ± 2.7	37.1
10	14	2.8	0.3	0.3	25.4 ± 2.2	26.6
14	25	0.9	0.07	0.1	29.6 ± 2.4	32.6
$\delta\phi^{jets}$ range [deg]		$d\sigma/d\delta\phi^{jets}$ [pb/deg]	stat.	sys.	f_b [%]	ϵ_{rec}
90	150	0.04	0.01	0.004	17.3 ± 4.3	33.0
150	165	0.36	0.05	0.04	25.2 ± 3.2	34.6
165	180	1.17	0.08	0.13	24.5 ± 1.7	30.5

Table A.7: Measured differential beauty dijet muon cross sections in photoproduction as a function of p_t^μ, η^μ, p_t^{jet1}, x_γ^{obs} and $\delta\phi^{jets}$ with statistical and systematic errors for direct processes ($x_\gamma^{obs} > 0.75$). Also listed are the fractions of events containing beauty quarks, f_b, and the reconstruction efficiency ϵ_{rec} as obtained from the PYTHIA Monte Carlo simulation.

$x_\gamma^{obs} > 0.75$		**Beauty**		
		FMNR		MC@NLO
		NLO x Had	NLO x Part	NLO x Had
p_t^μ range [GeV]		$d\sigma/dp_t^\mu$ [pb/GeV]		
2.5	3.3	$8.31^{1.15}_{-1.04}$	$13.44^{1.86}_{-1.68}$	10.3
3.3	5.0	$5.24^{0.64}_{-0.74}$	$7.44^{0.91}_{-1.05}$	5.2
5.0	12.0	$0.88^{0.20}_{-0.13}$	$1.00^{0.22}_{-0.14}$	0.6
η^μ range		$d\sigma/d\eta^\mu$ [pb]		
−1.30	−0.55	$4.98^{1.27}_{-0.86}$	$8.1^{2.1}_{-1.4}$	4.0
−0.55	−0.15	$10.6^{2.0}_{-1.6}$	$15.8^{3.0}_{-2.4}$	9.2
−0.15	0.25	$12.3^{2.2}_{-1.8}$	$17.2^{3.0}_{-2.5}$	11.1
0.25	0.65	$10.49^{1.40}_{-1.24}$	$14.19^{1.90}_{-1.68}$	10.7
0.65	1.10	$6.72^{0.63}_{-1.11}$	$8.84^{0.83}_{-1.46}$	8.4
1.10	1.50	$3.29^{0.44}_{-1.20}$	$4.32^{0.58}_{-1.58}$	5.5
p_t^{jet1} range [GeV]		$d\sigma/dp_t^{jet1}$ [pb/GeV]		
7	10	$1.47^{0.22}_{-0.26}$	$3.66^{0.59}_{-0.78}$	2.4
10	14	$2.31^{0.45}_{-0.36}$	$2.82^{0.67}_{-0.47}$	2.0
14	25	$0.88^{0.21}_{-0.13}$	$0.670^{0.163}_{-0.098}$	0.5
$\delta\phi^{jets}$ range [deg]		$d\sigma/d\delta\phi^{jets}$ [pb/deg]		
90	150	$0.056^{0.027}_{-0.016}$	$0.039^{0.024}_{-0.012}$	0.1
150	165	$0.290^{0.082}_{-0.060}$	$0.43^{0.24}_{-0.14}$	0.3
165	180	$1.026^{0.119}_{-0.122}$	$1.45^{0.18}_{-0.23}$	0.8

Table A.8: Predicted differential beauty dijet muon cross sections in photoproduction at next-to-leading order as a function of p_t^μ, η^μ, p_t^{jet1}, x_γ^{obs} and $\delta\phi^{jets}$ on hadron (Had) and on parton (Part) level calculated with FMNR and MC@NLO.

$x_\gamma^{obs} \le 0.75$		**Charm**				
p_t^μ range [GeV]		$d\sigma/dp_t^\mu$ [pb/GeV]	stat.	sys.	f_c [%]	ϵ_{rec}
2.5	3.3	8.1	2.8	1.2	21.2 ± 7.2	30.5
3.3	5.0	4.8	1.1	0.7	36.4 ± 7.8	37.6
5.0	12.0	0.3	0.1	0.1	30.2 ± 8.0	42.5
η^μ range		$d\sigma/d\eta^\mu$ [pb]	stat.	sys.	f_c [%]	ϵ_{rec}
-1.30	-0.55	5.3	1.0	0.8	68.1 ± 11.3	26.4
-0.55	-0.15	6.9	2.3	1.0	32.0 ± 10.8	38.1
-0.15	0.25	17.8	2.4	2.7	53.9 ± 7.0	39.4
0.25	0.65	6.7	3.3	1.0	21.0 ± 10.3	37.4
0.65	1.10	11.5	2.9	1.7	37.7 ± 9.3	35.2
1.10	1.50	0.2	2.7	0.1	1.0 ± 13.2	19.8
p_t^{jet1} range [GeV]		$d\sigma/dp_t^{jet1}$ [pb/GeV]	stat.	sys.	f_c [%]	ϵ_{rec}
7	10	2.9	0.5	0.4	35.6 ± 6.4	35.8
10	14	3.0	0.6	0.5	46.1 ± 9.0	28.3
14	25	0.1	0.1	0.02	12.4 ± 12.3	41.0
$\delta\phi^{jets}$ range [deg]		$d\sigma/d\delta\phi^{jets}$ [pb/deg]	stat.	sys.	f_c [%]	ϵ_{rec}
90	150	0.10	0.02	0.02	37.1 ± 9.1	35.9
150	165	0.29	0.10	0.04	24.9 ± 8.4	33.0
165	180	0.56	0.12	0.09	32.1 ± 6.8	33.5

Table A.9: Measured differential charm dijet muon cross sections in photoproduction as a function of p_t^μ, η^μ, p_t^{jet1}, x_γ^{obs} and $\delta\phi^{jets}$ with statistical and systematic errors for resolved processes ($x_\gamma^{obs} \le 0.75$). Also listed are the fractions of events containing beauty quarks, f_b, and the reconstruction efficiency ϵ_{rec} as obtained from the PYTHIA Monte Carlo simulation.

$x_\gamma^{obs} \leq 0.75$		**Charm**
		MC@NLO NLO x Had
p_t^μ range [GeV]		$d\sigma/dp_t^\mu$ [pb/GeV]
2.5	3.3	18.6
3.3	5.0	6.6
5.0	12.0	0.4
η^μ range		$d\sigma/d\eta^\mu$ [pb]
-1.30	-0.55	5.0
-0.55	-0.15	11.8
-0.15	0.25	10.3
0.25	0.65	13.2
0.65	1.10	12.6
1.10	1.50	13.0
p_t^{jet1} range [GeV]		$d\sigma/dp_t^{jet1}$ [pb/GeV]
7	10	3.2
10	14	3.7
14	25	0.7
$\delta\phi^{jets}$ range [deg]		$d\sigma/d\delta\phi^{jets}$ [pb/deg]
90	150	0.1
150	165	0.4
165	180	1.0

Table A.10: Predicted differential beauty dijet muon cross sections in photoproduction at next-to-leading order as a function of p_t^μ, η^μ, p_t^{jet1}, x_γ^{obs} and $\delta\phi^{jets}$ on hadron (Had) level calculated with MC@NLO.

$x_\gamma^{obs} \leq 0.75$		**Beauty**				
p_t^μ range [GeV]		$d\sigma/dp_t^\mu$ [pb/GeV]	stat.	sys.	f_b [%]	ϵ_{rec}
2.5	3.3	7.1	1.1	0.8	15.3 ± 2.2	25.5
3.3	5.0	4.4	0.5	0.5	27.9 ± 3.2	31.2
5.0	12.0	0.3	0.07	0.03	22.8 ± 6.2	40.6
η^μ range		$d\sigma/d\eta^\mu$ [pb]	stat.	sys.	f_b [%]	ϵ_{rec}
-1.30	-0.55	1.4	0.6	0.2	16.6 ± 6.8	23.9
-0.55	-0.15	5.8	1.3	0.7	23.6 ± 5.3	33.1
-0.15	0.25	7.7	1.3	0.9	21.2 ± 3.4	35.7
0.25	0.65	7.1	1.4	0.8	21.1 ± 4.0	35.6
0.65	1.10	8.9	1.3	1.0	27.4 ± 3.8	33.1
1.10	1.50	4.9	1.7	0.6	21.8 ± 7.5	18.2
p_t^{jet1} range [GeV]		$d\sigma/dp_t^{jet1}$ [pb/GeV]	stat.	sys.	f_b [%]	ϵ_{rec}
7	10	2.2	0.3	0.3	24.6 ± 3.2	31.2
10	14	1.5	0.2	0.2	22.9 ± 3.3	27.2
14	25	0.2	0.05	0.03	18.5 ± 3.4	35.2
$\delta\phi^{jets}$ range [deg]		$d\sigma/d\delta\phi^{jets}$ [pb/deg]	stat.	sys.	f_b [%]	ϵ_{rec}
90	150	0.07	0.01	0.01	24.5 ± 3.4	33.9
150	165	0.26	0.05	0.03	20.5 ± 3.7	29.6
165	180	0.40	0.06	0.04	20.1 ± 2.8	29.3

Table A.11: Measured differential beauty dijet muon cross sections in photoproduction as a function of p_t^μ, η^μ, p_t^{jet1}, x_γ^{obs} and $\delta\phi^{jets}$ with statistical and systematic errors for resolved processes ($x_\gamma^{obs} \leq 0.75$). Also listed are the fractions of events containing beauty quarks, f_b, and the reconstruction efficiency ϵ_{rec} as obtained from the PYTHIA Monte Carlo simulation.

$x_\gamma^{obs} \leq 0.75$		**Beauty**		
		FMNR		MC@NLO
		NLO x Had	NLO x Part	NLO x Had
p_t^μ range [GeV]		$d\sigma/dp_t^\mu$ [pb/GeV]		
2.5	3.3	$4.7^{3.5}_{-1.6}$	$4.8^{3.6}_{-1.7}$	3.6
3.3	5.0	$3.1^{2.3}_{-1.1}$	$2.65^{1.94}_{-0.96}$	1.5
5.0	12.0	$0.39^{0.27}_{-0.15}$	$0.34^{0.23}_{-0.13}$	0.2
η^μ range		$d\sigma/d\eta^\mu$ [pb]		
-1.30	-0.55	$1.58^{0.96}_{-0.51}$	$1.12^{0.68}_{-0.36}$	0.8
-0.55	-0.15	$3.6^{2.2}_{-1.3}$	$2.90^{1.76}_{-1.07}$	2.1
-0.15	0.25	$4.7^{3.1}_{-1.7}$	$4.2^{2.8}_{-1.5}$	2.8
0.25	0.65	$5.5^{3.9}_{-2.0}$	$5.3^{3.8}_{-1.9}$	3.3
0.65	1.10	$5.8^{4.6}_{-2.1}$	$5.9^{4.6}_{-2.1}$	3.4
1.10	1.50	$5.5^{4.4}_{-2.1}$	$5.8^{4.7}_{-2.2}$	2.9
p_t^{jet1} range [GeV]		$d\sigma/dp_t^{jet1}$ [pb/GeV]		
7	10	$1.86^{1.52}_{-0.71}$	$1.81^{1.52}_{-0.70}$	0.8
10	14	$1.04^{0.76}_{-0.37}$	$0.84^{0.56}_{-0.29}$	0.6
14	25	$0.237^{0.140}_{-0.078}$	$0.165^{0.084}_{-0.052}$	0.1
$\delta\phi^{jets}$ range [deg]		$d\sigma/d\delta\phi^{jets}$ [pb/deg]		
90	150	$0.064^{0.043}_{-0.022}$	$0.0220^{0.0131}_{-0.0072}$	0.05
150	165	$0.186^{0.131}_{-0.066}$	$0.119^{0.073}_{-0.039}$	0.1
165	180	$0.50^{0.38}_{-0.18}$	$0.51^{0.40}_{-0.19}$	0.2

Table A.12: Predicted differential beauty dijet muon cross sections in photoproduction at next-to-leading order as a function of p_t^μ, η^μ, p_t^{jet1}, x_γ^{obs} and $\delta\phi^{jets}$ on hadron (Had) and on parton (Part) level calculated with FMNR and MC@NLO.

Appendix B

Fit Results

The following histograms depict the transverse momentum p_t^{rel} of the muon relative to the associated jet axis (left column) and the impact parameter δ (right column) in the analysis bins of the transverse momentum p_t^{μ} of the muon, the pseudorapidity η^{μ} of the muon, the transverse momentum p_t^{jet1} of the leading jet, the angular separation $\delta\phi^{jets}$ of the two selected jets and the obsverable x_{γ}^{obs}. The respective range of the variables is written on the upper left side of each figure. The fractions of events containing charm, beauty and light quarks are determined with the combined fit. The sum of the three quark contributions is compared to the data to demonstrate the quality of the fit results.

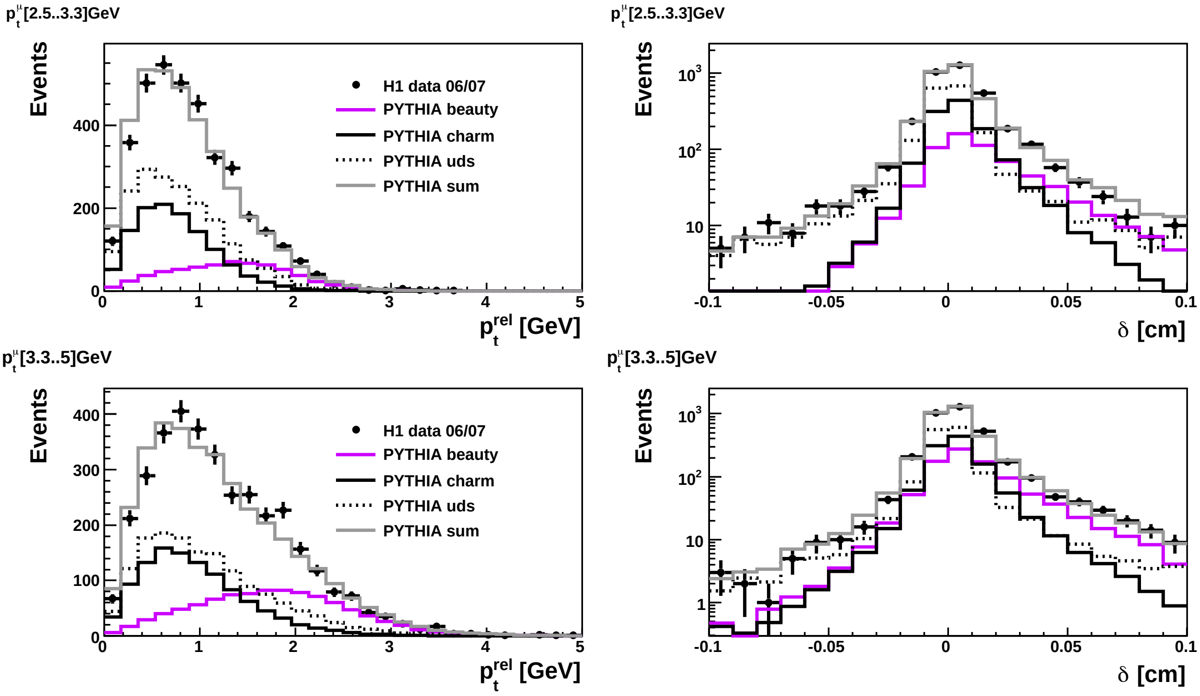

Figure B.1: The variables p_t^{rel} (left column) and δ (right column) in the analysis bins of p_t^{μ} for the data (points) and the PYTHIA simulation in comparison.

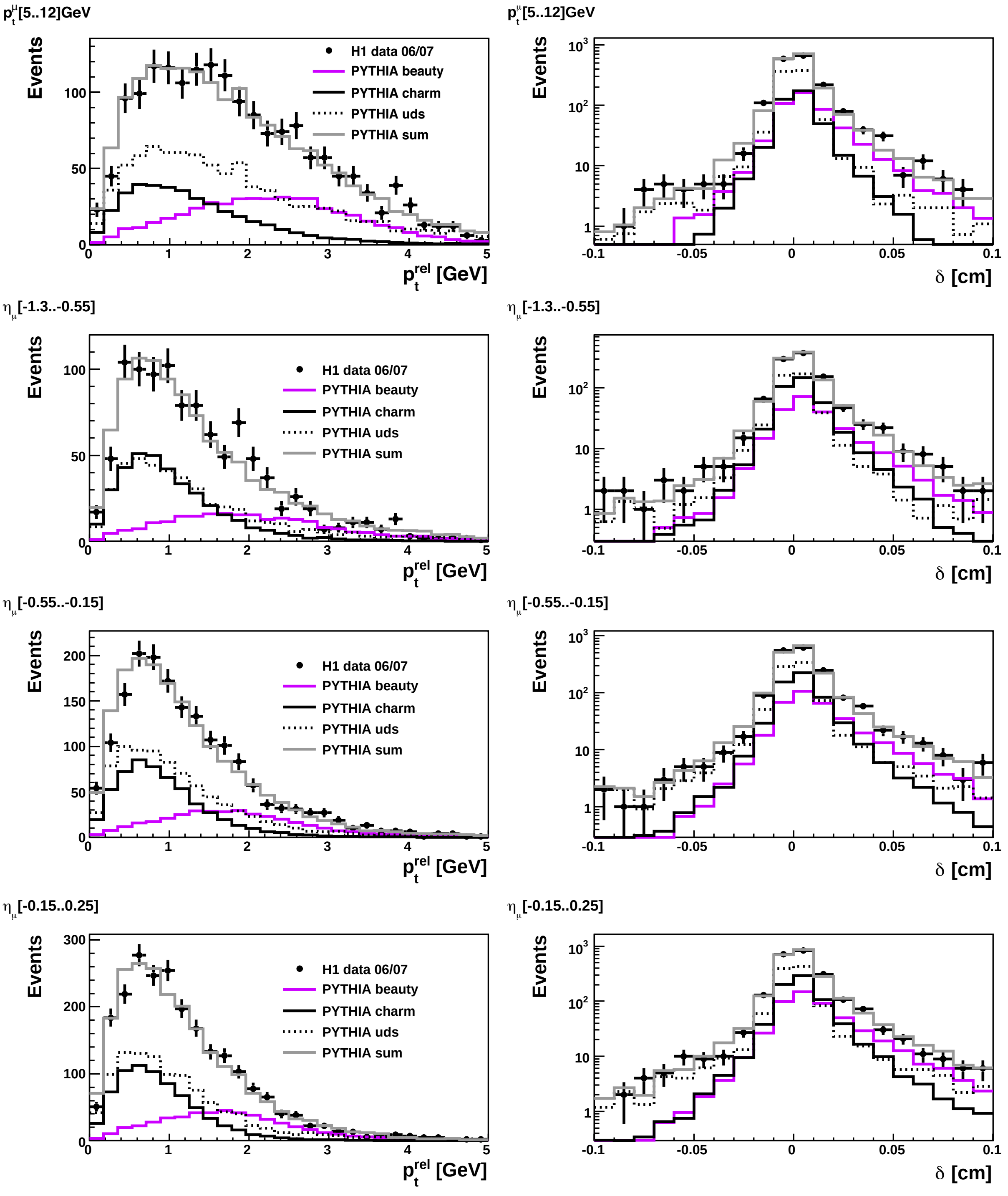

Figure B.2: The variables p_t^{rel} (left column) and δ (right column) in the analysis bins of p_t^{μ} and η^{μ} for the data (points) and the PYTHIA simulation in comparison.

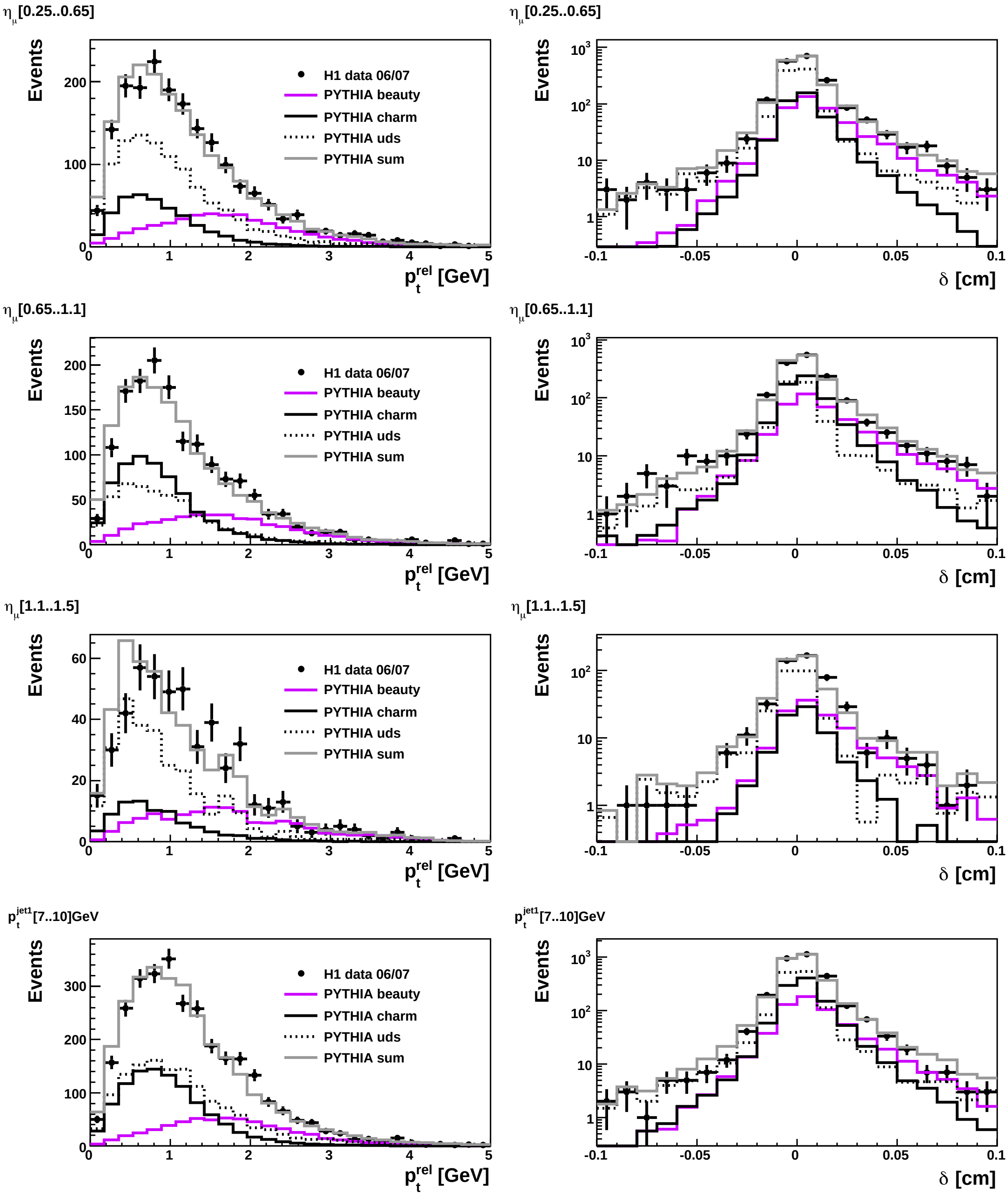

Figure B.3: The variables p_t^{rel} (left column) and δ (right column) in the analysis bins of η^{μ} and p_t^{jet1} for the data (points) and the PYTHIA simulation in comparison.

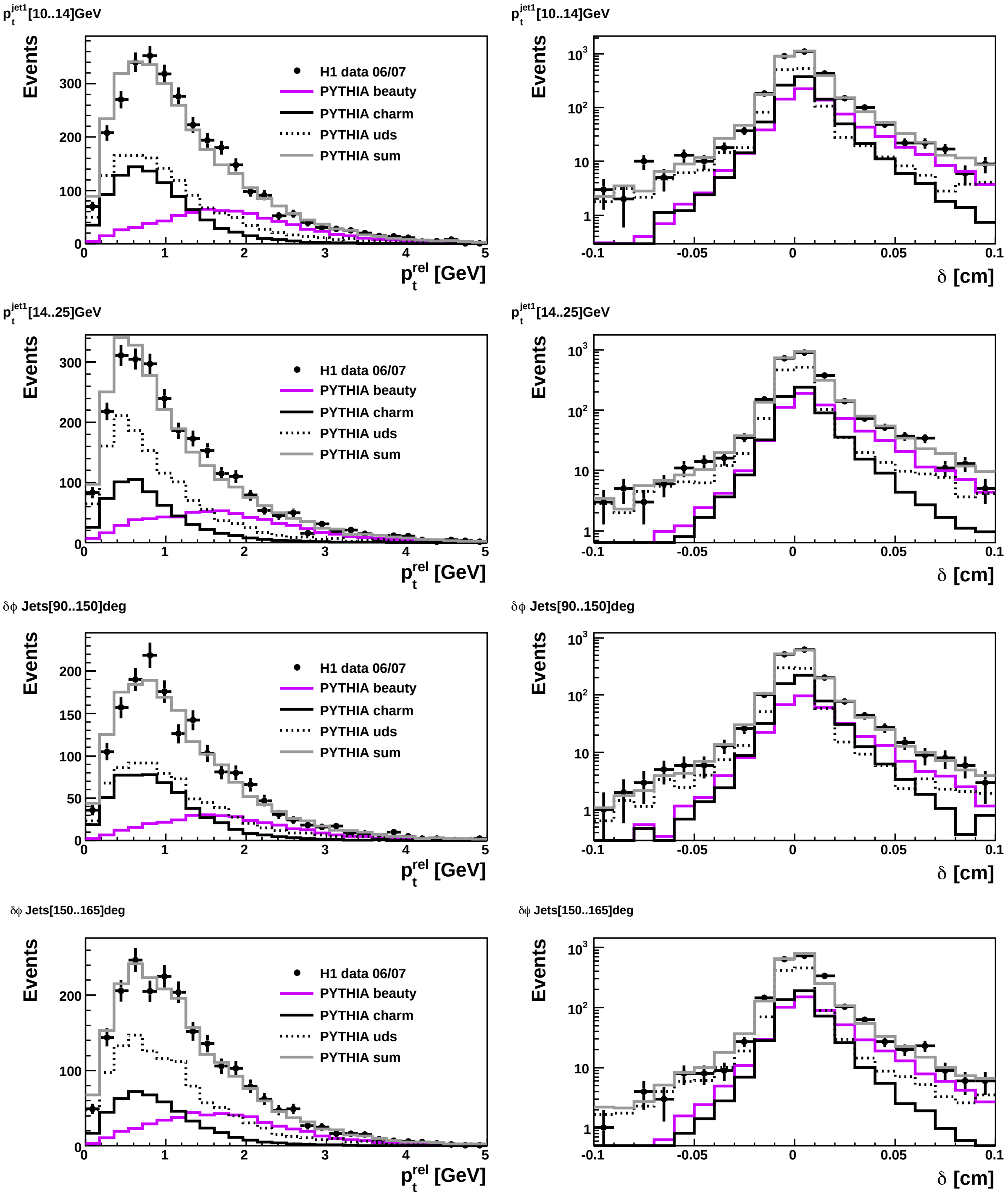

Figure B.4: The variables p_t^{rel} (left column) and δ (right column) in the analysis bins of p_t^{jet1} and $\delta\phi^{jets}$ for the data (points) and the PYTHIA simulation in comparison.

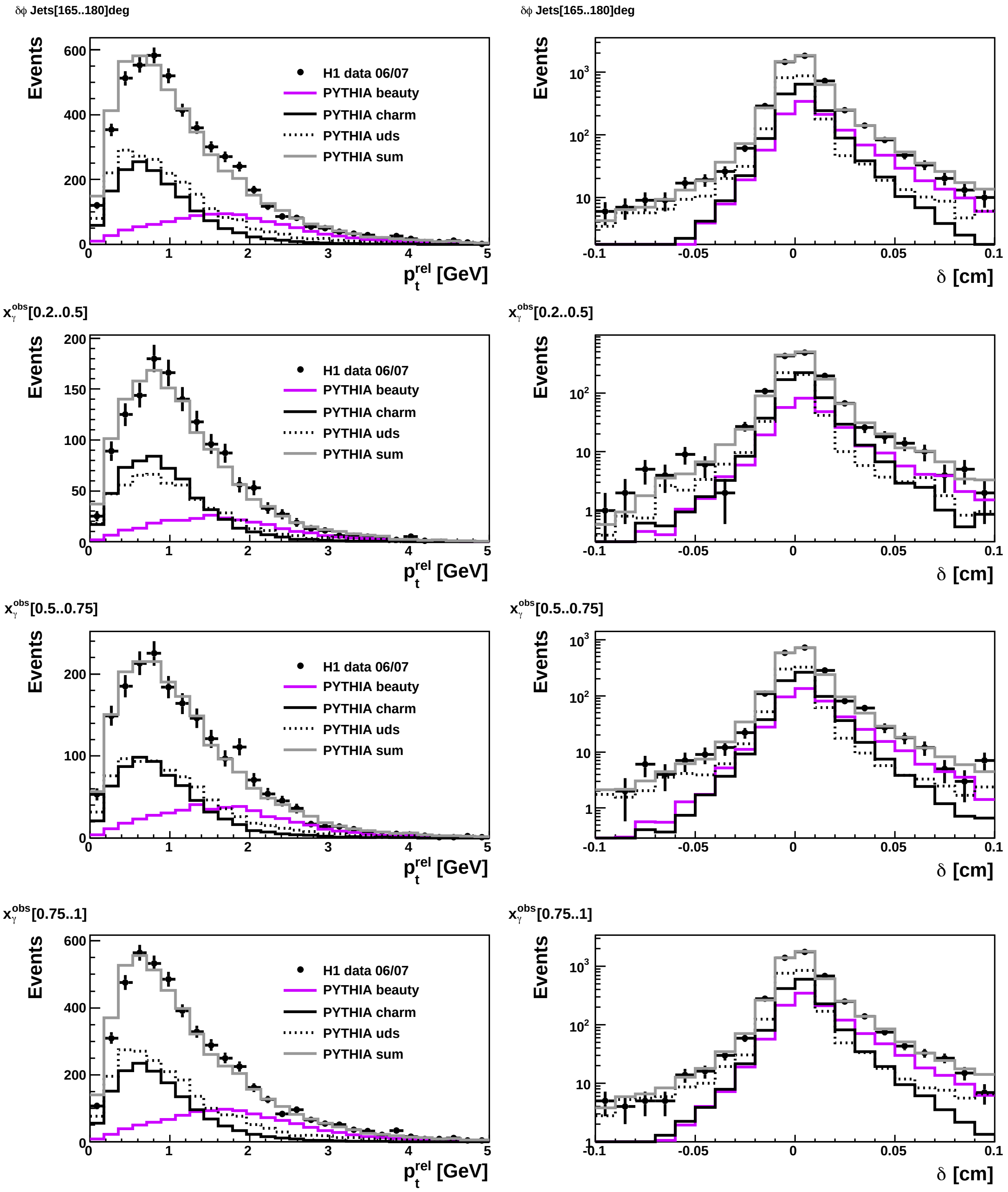

Figure B.5: The variables p_t^{rel} (left column) and δ (right column) in the analysis bins of $\delta\phi^{jets}$ and x_γ^{obs} for the data (points) and the PYTHIA simulation in comparison.

Bibliography

[1] M. E. Peskin and D. V. Schroeder. *An Introduction to Quantum Field Theory.* The Advanced Book Program, 1995.

[2] C. Glasman. Precision Measurements of α_s at HERA. *AIP Conf. Proc.*, 792:689–692, 2005.

[3] J. D. Bjorken. Asymptotic Sum Rules at Infinite Momentum. *Phys. Rev.*, 179:1547–1553, 1969.

[4] R. P. Feynman. Very High-Energy Collisions of Hadrons. *Phys. Rev. Lett.*, 23:1415–1417, 1969.

[5] J. D. Bjorken and E. A. Paschos. Inelastic Electron Proton and Gamma Proton Scattering, and the Structure of the Nucleon. *Phys. Rev.*, 185:1975–1982, 1969.

[6] C. G. Jr. Callan, M. Cronau, A. Pais, E. Paschos, and S. B. Treiman. Light Cone Approach to Structure Function Inequalities. FERMILAB-PUB-72-029-T.

[7] J. I. Friedman and H. W. Kendall. Deep inelastic Electron Scattering. *Ann. Rev. Nucl. Part. Sci.*, 22:203–254, 1972.

[8] D. J. Fox et al. Test of Scale Invariance in High-Energy Muon Scattering. *Phys. Rev. Lett.*, 33:1504, 1974.

[9] J. G. H. de Groot et al. Inclusive Interactions of High-Energy Neutrinos and Anti-Neutrinos in Iron. *Zeit. Phys.*, C1:143, 1979.

[10] J. C. Collins, D. E. Soper, and G. Sterman. Factorization for Short Distance Hadron - Hadron Scattering. *Nucl. Phys.*, B261:104, 1985.

[11] A. D. Martin. Proton structure, Partons, QCD, DGLAP and beyond. *Acta Phys. Polon.*, B39:2025–2062, 2008.

[12] J. Feltesse and A. Cooper-Sarkar [H1 and ZEUS Collaboration]. Extraction of the Proton Parton Density Functions using a NLO-QCD Fit of the combined H1 and ZEUS inclusive DIS Cross Sections. *H1prelim-08-045*, 2008.

[13] J. Pumplin, D. R. Stump, J. Huston, H. L. Lai, M. Pavel, M. Nadolsky, and W. K. Tung. New Generation of Parton Distributions with Uncertainties from global QCD Analysis. *JHEP*, 07:012, 2002.

[14] E. Witten. Anomalous Cross-Section for Photon - Photon Scattering in Gauge Theories. *Nucl. Phys.*, B120:189–202, 1977.

[15] R. Nisius. The Photon Structure from deep inelastic Electron Photon Scattering. *Phys. Rept.*, 332:165–317, 2000.

[16] G. A. Schuler and T. Sjöstrand. Low and high Mass Components of the Photon Distribution Functions. *Z. Phys.*, C68:607–624, 1995.

[17] V. V. Gribov and L. N. Lipatov. e+e- Pair Annihilation and deep inelastic ep Scattering in perturbation Theory. *Sov. J. Nucl. Phys.*, 15:438 and 675, 1972.

[18] L. N. Lipatov. The Parton Model and perturbation Theory. *Sov. J. Nucl. Phys.*, 20:94, 1975.

[19] G. Altarelli and G. Parisi. Asymptotic Freedom in Parton Language. *Nucl. Phys.*, 126:298, 1977.

[20] Y. L. Dokshitzer. Calculation of the Structure Functions in deep inelastic Scattering and e+e- Annihilation by perturbative Theory in Quantum Chormodynamics. *Sov. Phys. JETP*, 46:641, 1977.

[21] E. A. Kuraev, L. N. Lipatov, and V. S. Fadin. Multi - Reggeon Processes in the Yang-Mills Theory. *Sov. Phys. JETP*, 44:443, 1976.

[22] E. A. Kuraev, L. N. Lipatov, and V. S. Fadin. The Pomeranchuk Singularity in nonabelian Gauge Theories. *Sov. Phys. JETP*, 45:199, 1977.

[23] I. I. Balitsky and L. N. Lipatov. The Pomeranchuk Singularity in Quantum Chromodynamics. *Sov. J. Nucl. Phys.*, 28:822, 1978.

[24] M. Ciafaloni. Coherence Effects in initial Jets at small Q^2/s. *Nucl. Phys. B*, 296:49, 1988.

[25] S. Catani, F. Fiorani, and G. Marchesini. QCD coherence in initial state radiation. *Phys. Lett. B*, 234:339, 1990.

[26] S. Catani F. Fiorani, and G. Marchesini. Small x behaviour of initial state radiation in perturbative QCD. *Nucl. Phys. B*, 336:18, 1990.

[27] G. Marchesini. QCD Coherence in the Structure Function and associated Distributions at small x. *Nucl. Phys. B*, 445:49, 1995.

[28] J. Smith and W. K. Tung. Heavy Flavor Production. NIKHEF-H-93-20.

[29] L. M. Jones and H. W. Wyld. Charmed Particle Production by Photon Gluon Fusion. *Phys. Rev.*, D17:759, 1978.

[30] M. Cacciari, S. Frixione, and P. Nason. The p_T Spectrum in Heavy-Flavor Photoproduction. *JHEP*, 03:006, 2001.

[31] B. Andersson, G. Gustafson, G. Ingelman, and T. Sjostrand. Parton Fragmentation and String Dynamics. *Phys. Rept.*, 97:31–145, 1983.

[32] M. G. Bowler. e+ e- Production of Heavy Quarks in the String Model. *Zeit. Phys.*, C11:169, 1981.

[33] C. Peterson, D. Schlatter, I. Schmitt, and P. M. Zerwas. Scaling Violations in Inclusive e+e- Annihilation Spectra. *Phys. Rev.*, D27:105, 1983.

[34] R. Brun, F. Bruyant, M. Maire, A. C. McPherson, and P. Zanarini. GEANT3. CERN-DD/EE/84-1.

[35] T. Sjostrand, S. Mrenna, and P. Skands. PYTHIA 6.4 Physics and Manual. *JHEP*, 05:026, 2006.

[36] H. Jung. The CCFM Monte Carlo Generator CASCADE. *Comput. Phys. Commun.*, 143:100–111, 2002.

[37] H. Jung. Un-integrated uPDFs in CCFM. *Proceedings of 12th International Workshop on Deep Inelastic Scattering (DIS 2004)*, 2004.

[38] S. Frixione, M. L. Mangano, P. Nason, and G. Ridolfi. Total Cross Sections for Heavy Flavour Production at HERA. *Phys. Lett.*, B348:633–645, 1995.

[39] M. Martisikova. *Jet Shapes in Charm Photoproduction at HERA*. PhD thesis, Universität Hamburg, 2005. DESY-THESIS-2005-047.

[40] T. Sjostrand. The PYTHIA and JETSET Programs. Prepared for Particles and Fields 92: 7th Meeting of the Division of Particles Fields of the APS (DPF 92), Batavia, Illinois, 10-14 Nov 1992.

[41] S. Alekhin et al. HERA and the LHC - A Workshop on the Implications of HERA for LHC Physics: Proceedings Part B. 2005.

[42] H. L. Lai et al. [CTEQ Collaboration]. Global QCD Analysis of Parton Structure of the Nucleon: CTEQ5 Parton Distributions. *Eur. Phys. J.*, C12:375–392, 2000.

[43] M. Glück, E. Reya, and A. Vogt. Photonic Parton Distributions. *Phys. Rev.*, D46:1973–1979, 1992.

[44] T. Toll. *MC@NLO*. PhD thesis, (in preparation), Universität Hamburg, 2009.

[45] G. et al Corcella. HERWIG 6.5: An Event Generator for Hadron Emission Reactions With Interfering Gluons (including supersymmetric Processes). *JHEP*, 01:010, 2001.

[46] C. Amsler et al [Particle Data Group]. Review of Particle Physics. *Phys. Lett.*, B667:1, 2008.

[47] O. Behnke. Production of Charm and Beauty Quarks at HERA. *Habilitationsschrift, Ruprecht-Karls Universität Heidelberg*, 2005.

[48] A. B. Meyer. Heavy Quark Production at HERA. *Habilitationsschrift, Universität Hamburg*, 2005.

[49] L. Finke. *Measurement of Charm and Beauty Dijet Cross Sections in Photoproduction.* PhD thesis, Universität Hamburg, 2006. DESY-THESIS-2006-035.

[50] J. E. Augustin et al. Discovery of a Narrow Resonance in e+ e- Annihilation. *Phys. Rev. Lett.*, 33:1406–1408, 1974.

[51] J. J. Aubert et al [E598 Collaboration]. Experimental Observation of a Heavy Particle J. *Phys. Rev. Lett.*, 33:1404–1406, 1974.

[52] J. Rademacker. Charm (and Beauty) Production at the Tevatron. 2007.

[53] A. Aktas et al [H1 Collaboration]. Inclusive D*-Meson Cross Sections and D*- Jet Correlations in Photoproduction at HERA. *Eur. Phys. J.*, C50:251–267, 2007.

[54] S. Chekanov et al [ZEUS Collaboration]. Inclusive Jet Cross Sections and Dijet Correlations in D*- Photoproduction at HERA. *Nucl. Phys.*, B729:492–525, 2005.

[55] S. W. Herb et al. Observation of a Dimuon Resonance at 9.5-GeV in 400-GeV Proton - Nucleus Collisions. *Phys. Rev. Lett.*, 39:252–255, 1977.

[56] M. D'Onofrio [CDF and D0 Collaboration]. Beauty Production Cross Section Measurements at E(cm)=1.96-TeV. *Proceedings of 40th Rencontres de Moriond on QCD and High Energy Hadronic Interactions, La Thuile, Aosta Valley*, 2005.

[57] D. E. Acosta et al [CDF Collaboration]. Measurement of the J/ψ Meson and $b-$Hadron Production Cross Sections in $p\bar{p}$ Collisions at $\sqrt{s} = 1960$ GeV. *Phys. Rev.*, D71:032001, 2005.

[58] C. Adloff et al [H1 Collaboration]. Measurement of Open Beauty Production at HERA. *Phys. Lett.*, B467:156–164, 1999.

[59] A. Aktas et al [H1 Collaboration]. Measurement of Beauty Production at HERA using Events with Muons and Jets. *Eur. Phys. J.*, C41:453–467, 2005.

[60] S. Chekanov et al [ZEUS Collaboration]. Bottom Photoproduction measured using Decays into Muons in Dijet Events in ep Collisions at s**(1/2) = 318-GeV. *Phys. Rev.*, D70:012008, 2004.

[61] S. Frixione, P. Nason, and G. Ridolfi. Differential Distributions for Heavy Flavor Production at HERA. *Nucl. Phys.*, B454:3–24, 1995.

[62] I. Abt et al [H1 Collaboration]. The Tracking, Calorimeter and Muon Detectors of the H1 Experiment at HERA. *Nucl. Instrum. Meth.*, A386:348–396, 1997.

[63] B. List. The H1 Central Silicon Tracker. *Nucl. Instrum. Meth.*, A501:49–53, 2001.

[64] D. Pitzl et al. [H1 Collaboration]. The H1 Silicon Vertex Detector. *Nucl. Instrum. Meth.*, A454:334–349, 2000.

[65] D. Pitzl et al [H1 Collaboration]. Evaluation of double sided, AC coupled, double Metal Silicon Strip Detectors for H1 at HERA. *Nucl. Instrum. Meth.*, A348:454–460, 1994.

[66] C. Kleinwort et al [H1 Collaboration]. H1 Alignment Experience. Technical report, H1 Collaboration, 4-6 Sep. 2006 Prepared for the 1st LHC Detection Alignment Workshop, Geneva, Switzerland.

[67] M. Hilgers and R. Horisberger. Development of a Radiation Hard Version of the Analog Pipeline Chip APC 128. *Nucl. Instrum. Meth.*, A481:556–565, 2002.

[68] R. Horisberger and D. Pitzl. A Novel Readout Chip for Silicon Strip Detectors with analog Pipeline and digitally controlled analog Signal Processing. *Nucl. Instrum. Meth.*, A326:92–99, 1993.

[69] M. Kausch-Blecken von Schmeling. *The Silicon Microvertex Detector of the H1 Experiment: Readout, Event Reconstruction, and Studies on Heavy Quark Decays.* PhD thesis, Universität Hamburg, 1998. DESY-THESIS-1998-033.

[70] B. Andrieu et al. [H1 Collaboration]. The H1 Liquid Argon Calorimeter System. *Nucl. Instrum. Meth.*, A336:460–498, 1993.

[71] B. Andrieu et al [H1 Calorimter Group]. Results from Pion Calibration Runs for the H1 Liquid Argon Calorimeter and Comparisons with Simulations. *Nucl. Instrum. Meth.*, A336:499–509, 1993.

[72] R. D. Appuhn et al [H1 Spacal Group]. The H1 Lead/Scintillating-Fibre Calorimeter. *Nucl. Instrum. Meth.*, A386:397–408, 1997.

[73] C. Kleinwort and U. P. Krüger. Track Reconstruction in the IRON. *H1 Software Note*, 1992.

[74] E. Elsen. Aspects of the H1 Trigger and Data Acquisition System. Prepared for 2nd Annual Conference on Electronics for Future Colliders, Chestnut Ridge, N.Y., 19-21 May 1992.

[75] M. Goettlich. *Study of Charm and Beauty Production at HERA / H1 using Dilepton Events.* PhD thesis, Universität Hamburg, 2007. DESY-THESIS-2007-012.

[76] B. Naroska, S. Schieck, and G. Schmidt. Lepton Identification in the H1 Detector at low Momenta. H1 Internal Note, H1-IN-518, 1997.

[77] D. Schmidt. *Diffraktive Photoproduktion von Charmonium im H1-Detektor bei HERA*. PhD thesis, Universität Hamburg, 2001. DESY-THESIS-2001-029.

[78] M. Steder. *Measurement of inelastic Charmonium Production at HERA*. PhD thesis, Universität Hamburg, 2008. DESY-THESIS-2008-023.

[79] O. Behnke and J. Kroseberg. CSTLIN: Combined CJC-CST Track Fit. H1 internal note, 1998.

[80] T. Kuhr and M. Kausch-Blecken von Schmeling. CSPRIM: Primary Vertex Determination using CST Measurements. H1 internal Note, 1999.

[81] M. Krämer. Tuning the Vertex Detector Simulation of H1. Proceedings of the international School of Subnuclear Physics: 45th course, 2007.

[82] C. Gerlich. *Messung der Produktion schwerer Quarks in inklusiven Zweijet-Ereignissen mit einem Myon unter Anwendung einer Multi-Impaktparameter Methode am H1 Experiment bei HERA*. PhD thesis, Ruprecht-Karls-Universität Heidelberg, 2005.

[83] D. Pitzl. private communication.

[84] D. Pitzl. H1 Detector Performance. Talk at H1 CrossTalk 2008.

[85] M. Peez, B. Portheault, and E. Sauvan. An Energy Flow Algorithm for Hadronic Reconstruction in OO: Hadroo2.

[86] J. E. Huth et al, editor. *Proceedings of the 1990 Summer Study on High Energy Physics*, volume World Scientific, Singapore. Snowmass, Colorado, edited by E. L. Berger, 1992.

[87] S. Catani, Y. L. Dokshitzer, M. H. Seymour, and B. R. Webber. Longitudinally invariant K(t) Clustering Algorithms for Hadron Hadron Collisions. *Nucl. Phys.*, B406:187–224, 1993.

[88] A. A. Glazov. *Measurement of the Proton Structure Functions $F_2(x, Q^2)$ and $F_L(x, Q^2)$ with the H1 Detector at HERA*. PhD thesis, Humboldt Universität Berlin, 1998. DESY-THESIS-1998-005.

[89] V. V. Arkadov. *Measurement of the deep-inelastic ep scattering Cross Section using the backward Silicon Tracker at the H1 Detector at HERA*. PhD thesis, Humboldt Universität Berlin, 2000. DESY-THESIS-2000-046.

[90] M. Jacquet, Z. Zhang, V. Brisson, S. Kermiche, and C. Vallee. Absolute Hadronic Jet Calibration of the H1 Liquid Argon Calorimeter. H1 internal Note, H1-0499-571.

[91] S. Osman and D. Salek. The Low Pt HFS Jet Energy Calibration. H1 internal Note, H1-02/09-631.

[92] F. Jacquet and A. Blondel. Report from the Study Group on Detectors for Charged Current Events. *in Proceedings of the Study for an ep Facility for Europe, edited by U. Arnaldi*, 377(DESY-79-048), 1979.

[93] V. Blobel. Help for LOOK, a Program System for Graphics. H1 internal Note, H1-IN-102, 1988.

[94] F. D. Aaron et al [H1 Collaboration]. Strangeness Production at low Q^2 in Deep-Inelastic ep Scattering at HERA. 2009.

[95] R. J. Barlow and C. Beeston. Fitting using finite Monte Carlo Samples. *Comput. Phys. Commun.*, 77:219–228, 1993.

[96] R. Brun. ROOT: An object-oriented Data Analysis Framework.

[97] F. James. Minuit, Function Minimization and Error Analysis, CERN Program Library Long Writeup D506. Technical report, CERN, Geneva.

[98] V. Michels. *Measurement of Beauty Production in Deep inleastic Scattering at HERA.* PhD thesis, Universität Hamburg, 2008. DESY-THESIS-2008-022.

[99] S. Levonian. Status of the Offline Lumi Corrections for ep HERA2 Data, 2006.

[100] S. Z. Habib. *Proton Structure Functions at High Inelasticity.* PhD thesis, (in preparation), Universität Hamburg, 2009.

[101] M. Krämer. A Measurement of Beauty Photoproduction through Decays to Muons and Jets at HERA-II. *H1prelim-08-071*, 2008.

[102] S. Chekanov et al [ZEUS Collaboration]. Measurement of Beauty Photoproduction using Decays into Muons in Dijet Events at HERA. 2008.

[103] J. Breitweg et al [ZEUS Collaboration]. Measurement of inclusive $D^{*\pm}$ and associated Dijet Cross Sections in Photoproduction at HERA. *Eur. Phys. J.*, C6:67–83, 1999.

Danksagung

Als erstes möchte ich mich bei allen bedanken, die mich während meiner Zeit bei H1 unterstützt haben. Mein besonderer Dank gilt Frau Prof. Dr. Beate Naroska, die den Abschluss meiner Arbeit zu meinem tiefem Bedauern nicht mehr erleben kann. Ich danke ihr für die freundliche Aufnahme in ihre Arbeitsgruppe und das entgegengebrachte Vertrauen, um meine Promotion am H1 Experiment durchzuführen. Mit ihrem unermüdlichen Arbeitseifer und der ansteckenden Begeisterung für die Teilchenphysik wird sie mir als großes Vorbild in Erinnerung bleiben.
Herrn Prof. Dr. Robert Klanner danke ich sehr für das schnelle Korrekturlesen dieser Arbeit, die hilfreichen Korrekturvorschläge, sowie die Übernahme des Erstgutachtens.
Bei PD Dr. Andreas Meyer bedanke ich mich sehr für die geduldige Betreuung der Analyse, das gründliche Korrekturlesen, sowie die Übernahme des Gutachtens der Dissertation. Ich bin ihm vor allem sehr dankbar, dass er trotz seiner Doppelbelastung immer Zeit für mich fand und meine Analyse mit wertvollen Anregungen vorangebracht hat.
PD Dr. Olaf Behnke danke ich für die vielen hilfreichen Hinweise zur Analyse, das gründliche Korrekturlesen und die Übernahme des Disputationgutachtens. Für seine beruhigenden Kommentare und die freundliche Unterstützung bin ich sehr dankbar.
Ich danke Tobias Toll für die Berechnung der MC@NLO Vorhersagen für die Charm und die Beauty Messung. Bei Dr. Benno List bedanke ich mich für die Zusammenarbeit während des Preliminary Requests und des CST Monte Carlo Tunings. Für seine FMNR NLO Berechnungen der Beauty Wirkungsquerschnitte bin ich ebenfalls sehr dankbar.
Sehr zur besseren Verständlichkeit und Lesbarkeit dieser Arbeit haben außerdem Dr. Michael Steder, Dr. Marcel Kossow, PD Dr. Hannes Jung, Shiraz Habib und Lena beigetragen. Für die Korrekturvorschläge danke ich euch sehr. Alle verbleibenden Unstimmigkeiten gehen natürlich zu meinen Lasten.
Mein Dank gilt außerdem allen Mitgliedern der H1 Kollaboration für die angenehme und wertvolle Zusammenarbeit. Dies gilt insbesondere für die Mitglieder der Heavy Flavour Gruppe.
Bei Dr. Maria Martisikova bedanke ich mich herzlich für die anfängliche Betreuung meiner Analyse. Bei Dr. Volker Michels, Dr. Michael Steder, Martin Brinkmann und Brian Grell bedanke ich mich für die gute Zusammenarbeit, sowie für die angenehme Büroatmosphäre.
Bei Shiraz Habib bedanke ich mich für die vielen lehrreichen Tandemstunden, für die spaßigen Shoppingtouren und für zahlreiche Diskussionen.
Tiefsten Dank empfinde ich gegenüber Marcel, der mit seiner ausdauernden und liebevollen Unterstützung sehr zur Entstehung dieser Arbeit beigetragen hat.
Meinen Eltern danke ich von ganzem Herzen für die fortwährende Unterstützung aller meiner Vorhaben während der letzten 28 Jahre.